ABOUT THE BOOK

In the current era of AI, researchers are focusing on advanced research across all branches of science. Each new material discovered by science leads to new applications, which, in turn, foster growth in technology. There has been significant development in research in all fields of science and technology. Advances in the use of materials based on scientific knowledge have been particularly impactful. However, it is the application of this science to create practical objects i.e., technology-that makes new materials widely popular.

This edited book, titled, "Current Research in Science and Technology," has been reviewed by experts and published on the occasion of National Science Day by the national Publisher, RUSHI Publication, Chhatrapati Sambhajinagar (M.S.), India. It is intended as a guideline to promote researchers in various disciplines of Science, Engineering, Medicine, and Technology. The authors, hailing from different parts of the country, have contributed their research work to motivate budding researchers. Most of the manuscripts in this book focus on current scientific research conducted by the authors during their research work. These manuscripts are written in simple and accessible language, complemented by photographs, tables, and graphs. The book includes chapters from various research fields, and every effort has been made to cover a wide range of scientific disciplines.

RUSHI PUBLICATION
B-115, Gajanan Colony, Garkheda
Aurangabad. (M. S.) INDIA, 431 005
E-mail: *rushipublication27@gmail.com*

ISBN: 978-81-970491-8-7

ISBN:978-81-970491-8-7

Current Research in Science and Technology

Editor: Dr. C. M. Kale

Current Research in
Science and Technology
An Edited Book

Current Research in
Science and Technology
An Edited Book

Editor

Dr. Chandrashekhar M. Kale

Head and Professor

Department of Physics

Indraraj Arts, Commerce and Science College, Sillod

Dist. Chhatrapati Sambhajinagar, (M.S.) India-431112

Rushi Publication

A National Publisher

Current Research in Science and Technology

Chief Editor
Dr. Chandrashekhar M. Kale
Head and Professor
Dept. of Physics
Indraraj Arts, Commerce and Science College, Sillod
Dist. Chhatrapati Sambhajinagar (M.S.) India-431112

Co-Editor
Dr. Mahesh K. Babrekar
Department of Physics,
Indraraj Arts, Comm. and Science College,
Sillod. Dist. Chhatrapati Sambhajinagar

Review Editor
Dr. Veerabhadrayya M.
University College of Science,
Tumkur University, Tumakuru.
Pin-572103, Karnataka, India

Dr. J. M. Bhandari
Principal and Head
Department of Physics,
Smt. S. K. Gandhi Arts, Amolak Sci. and P. H. Gandhi Comm. College,
Kada. Tal. Ashti. Dist. Beed.

Dr. Suchita V. Deshmukh
Department of Physics,
Indraraj Arts, Comm. and Science College, Sillod
Dist. Chhatrapati Sambhajinagar

Edition
28 February 2025, Friday
(National Science Day)

Typesetter
Shravani Graphics, Sillod
Dist. Chhatrapati Sambhajinagar

Publisher
Rushi Publication
Garkheda, Chhatrapati Sambhajinagar -431005
E-mail: *rushipublication27@gmail.com*
Contact: 9975080017

Printed at
Rajkamal Print, Chikalthana
Chhatrapati Sambhajinagar -(M.S.) India

Total pages
158

Price
Rs. 400 /-

Cover design
Rushi Arts, Chhatrapati Sambhajinagar

ISBN: 978-81-970491-8-7

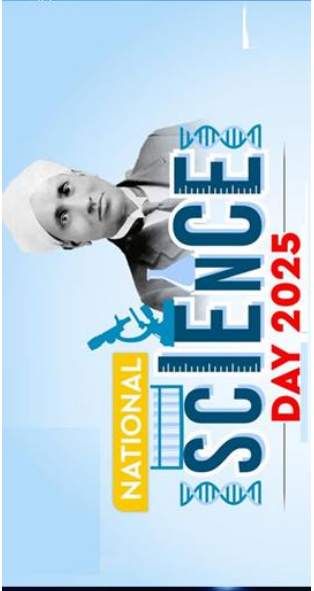

Preface...

I am very pleased to introduce the fourth edited book published by Rushi Publication, Chhatrapati Sambhajinagar, entitled *"Current Research in Science and Technology,"* and to present it to new researchers. Every year, National Science Day is celebrated in India on February 28 to mark the discovery of the Raman Effect by Indian physicist Sir C.V. Raman on February 28, 1928.

In this current era of AI, Science and Technology are crucial components of our daily lives and survival. Combined, both disciplines have facilitated the creation of a comfortable environment and lifestyle. Therefore, every year we plan to publish a research article in a book on the occasion of National Science Day to encourage the budding potential of researchers in their work. *Current Research in Science and Technology* is an interdisciplinary edited book that provides a platform for the latest research and developments across a wide range of scientific and technological fields. This book also serves as a reference for students at all levels of research, offering guidance while writing theses or papers.

The book comprises a total of 33 chapters from different branches of science. The corresponding author has honestly tried to describe the advanced research ideas, making it a platform for exchanging acquired knowledge in all aspects of science and technology. The authors have submitted their original, unpublished work related to numerous disciplines, communicating current and advanced research.

The most important feature of this book is that it motivates and stimulates curiosity and research interest among students, helping them gain a clearer understanding of their concepts.

At the outset, I would like to express my deep gratitude to Hon'ble Shri. Uttamsingh Pawar, President of our education society (Former Member of Parliament, Jalna, MS, India) for his blessings and support. I also take this opportunity to sincerely thank Hon'ble Shri. Ashok Deore, Secretary of our education society, and the In-charge Principal of our college, Dr. V. B. Lamb, for their continuous support.

I would also like to express my sincere thanks to my mentor, Prof. K. M. Jadhav (Emeritus Professor, Head, Department of Basic and Applied Sciences, MGM University, Chhatrapati Sambhajinagar), Dr. S. J. Shukla (Deogiri College, Aurangabad), Dr. D. R. Shengule (Principal, Vivekanand College, Chhatrapati Sambhajinagar), and Dr. Ashok Pandit (Principal, Yashwant College, Sillod), who inspired me greatly for this work.

I am deeply thankful to my dear friends, Dr. Mahesh K. Babarekar, who played the role of co-editor, and Dr. Veerabhadrayya M., Dr. J. M. Bhandari, and Dr. Suchita V. Deshmukh for their reviews, suggestions, and corrections in this regard. I also express my sincere thanks to the National Publisher, Dr. Mrs. Surekha S. Lakkas (Rushi Publication, Chhatrapati Sambhajinagar), who trusted me to play the role of editor and published this book within a short timeframe.

Finally, I express my thanks to my friends, college colleagues, and research students who supported and encouraged me throughout the editing process of this book. Last but not least, I would like to thank all the co-authors for their huge response and trust in me, which enabled me to complete this reference book in a short period of time and give it a beautiful shape. This accomplishment was only possible because of the spontaneous and continuous support from everyone involved.

Dr. Chandrashekhar M. Kale
(**Chief Editor**)

Current Research in
Science and Technology

An Edited Book (ISBN: 978-81-970491-8-7)

INDEX

*****

Recent Technological Advancements and Applications of Biomedical Nanoparticles

Dr. Atul Pandurag Keche

Department of Physics, Shri Muktanand college, Gangapur. Chhatrapati Sambhajinagar. (M.S.) India
Email: *meet.atulkeche@gmail.com*

ABSTRACT

Biomedical nanoparticles have emerged as a transformative force in healthcare, offering unparalleled opportunities for diagnostics, therapeutics, and advanced drug delivery systems. Their unique physicochemical properties, such as nanoscale size, high surface area, and customizable surface functionalities, enable precise interaction with biological systems at the molecular and cellular levels. Recent technological advancements have further amplified their potential, paving the way for innovations in targeted drug delivery, imaging, biosensing, and tissue engineering. Advances in fabrication techniques, including top-down and bottom-up approaches, have facilitated the production of nanoparticles with precise size, shape, and functionalization, ensuring optimal performance in clinical settings. The integration of nanotechnology with emerging fields such as artificial intelligence and precision medicine is discussed. Challenges such as scalability, regulatory approval, and potential long-term effects are also addressed, underscoring the need for multidisciplinary collaboration to translate laboratory successes into real-world applications.

Keywords: *Nanoparticles; Synthesis techniques; Biomedical applications*

1. INTRODUCTION

The advent of nanotechnology has revolutionized various scientific fields, with biomedicine being one of its most impactful beneficiaries. Nanoparticles, defined as particles with dimensions less than 100 nanometers, exhibit unique properties that are not observed in their bulk counterparts. These include enhanced reactivity, quantum effects, and the ability to penetrate biological barriers. Biomedical nanoparticles, in particular, have garnered significant attention due to their potential to address complex healthcare challenges such as targeted drug delivery, non-invasive imaging, and regenerative medicine. They provide a platform for combining multiple functionalities, such as therapeutic and diagnostic capabilities, into a single system, enhancing their versatility and utility. This paper delves into the technological advancements and applications of biomedical nanoparticles, analyzing their role in transforming healthcare practices. The interest of the scientific community in biomedical nanoparticles is increasing day by day due to its uncompensated demand for the labeling materials and tracking agents [1], imaging methods [2], drug delivery [3], pharmaceutical [4], development of vaccines, surgical implants [5], diagnostic techniques [6], biological sensing, antibacterial [7], genetic engineering [8], surgery [9], hyperthermia treatments and therapies [10], photo-thermal therapy, medical appliances [11] sterilization process [12], thus have a significant potential for applications in the field of biomedicine [13, 14]. The discussion spans their synthesis, functionalization, applications, and challenges, providing a comprehensive overview of their current and future potential.

2. SYNTHESIS AND FUNCTIONALIZATION OF BIOMEDICAL NANOPARTICLES

2.1 Synthesis Techniques

The synthesis of biomedical nanoparticles is a critical step that determines their properties and functionality. Two primary approaches are employed: Top-down approaches involve the breakdown of bulk materials into nanoparticles through techniques such as milling, lithography, and laser ablation. While effective for achieving precise size control, these methods often result in irregular shapes and surface defects, which can limit their efficiency in biomedical applications. Conversely, bottom-up approaches involve the assembly of nanoparticles from atomic or molecular precursors through methods. The researchers have invented several synthesis methods for the production of nanoparticles like the wet-chemical method [15], the ceramic method [16], the micro-emulsion method [17], a hydrothermal method [18], auto-clave method [19], etc. These techniques typically yield more uniform particles with well-defined morphologies, ensuring reproducibility and functionality. Innovations such as microfluidics and green synthesis methods have further advanced the field by enabling scalable and environmentally friendly production processes.

2.1 Functionalization Strategies

Functionalization enhances the biocompatibility and specificity of nanoparticles. Common strategies include surface coating, which involves using polymers like polyethylene glycol (PEG) to reduce immunogenicity and prolong circulation time in the bloodstream. Ligand attachment, such as adding targeting ligands like antibodies or peptides, enables nanoparticles to selectively bind to specific cells or tissues, enhancing their therapeutic and diagnostic precision. Additionally, encapsulation protects therapeutic agents within nanoparticles, ensuring controlled release at the target site. Advanced functionalization methods now integrate stimuli-responsive features, where nanoparticles release their payload in response to specific triggers such as pH, temperature, or enzymes, further improving their efficacy and reducing side effects.

3. APPLICATIONS OF BIOMEDICAL NANOPARTICLES

3.1. Drug Delivery

Nanoparticles have revolutionized drug delivery by enabling targeted transport of therapeutic agents to specific tissues or cells. Liposomes, dendrimers, and polymeric nanoparticles are widely used for encapsulating drugs, improving bioavailability, and reducing side effects. For instance, nanoparticles loaded with chemotherapeutic agents like doxorubicin have demonstrated enhanced efficacy by preferentially accumulating in tumor tissues through the enhanced permeability and retention (EPR) effect. Similarly, nanoscale vectors such as lipid nanoparticles (LNPs) are employed for delivering genetic material like siRNA and mRNA, exemplified by their pivotal role in COVID-19 mRNA vaccines. Recent developments include the creation of hybrid nanoparticles that combine organic and inorganic components to achieve multifunctionality, such as simultaneous drug delivery and real-time monitoring of therapeutic outcomes [20].

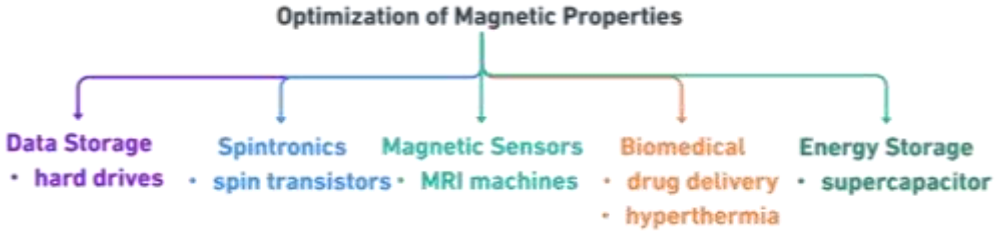

Fig.1: Various types of biomedical nanoparticles

3.2. Imaging and Diagnostics

Biomedical nanoparticles serve as contrast agents in imaging modalities such as magnetic resonance imaging (MRI), computed tomography (CT), and fluorescence imaging.

Superparamagnetic iron oxide nanoparticles (SPIONs) and quantum dots are prominent examples, offering superior sensitivity and resolution for disease detection. These nanoparticles enhance imaging capabilities, enabling earlier and more accurate diagnosis of medical conditions. Efforts are ongoing to develop multimodal nanoparticles that combine imaging capabilities with therapeutic functions, creating integrated solutions for theranostics. This approach has shown promise in conditions like cancer, where simultaneous diagnosis and treatment are critical [21-24].

3.3. Biosensing

Nanoparticles have enabled the development of highly sensitive biosensors for detecting biomolecules such as proteins, nucleic acids, and pathogens. Gold nanoparticles and carbon nanotubes are commonly used in these applications, leveraging their optical and electrical properties for precise signal transduction. These biosensors hold immense potential for early disease detection and monitoring, offering rapid and accurate diagnostic capabilities in resource-limited settings. Advances in biosensor technology are focusing on wearable and implantable devices that integrate nanoparticle-based sensors, paving the way for continuous health monitoring and data acquisition [25-27].

3.4. Tissue Engineering

Nanoparticles play a crucial role in tissue engineering by serving as scaffolds or delivery vehicles for growth factors. For example, hydroxyapatite nanoparticles are widely used in bone regeneration due to their similarity to natural bone mineral. By facilitating the repair and regeneration of damaged tissues, nanoparticles contribute significantly to advancements in regenerative medicine. Current research is exploring the use of nanoparticles in combination with 3D bioprinting techniques to create complex tissue structures with enhanced functionality and precision [26].

3.5. Integration with Emerging Technologies

The convergence of nanotechnology with fields such as artificial intelligence (AI) and precision medicine is shaping the next frontier of biomedical applications. AI-driven data analysis accelerates nanoparticle design and optimization, allowing for the identification of optimal properties and configurations for specific applications. Precision medicine approaches leverage nanoparticles for patient-specific therapies, tailoring treatments based on individual genetic and physiological profiles. These synergies are fostering the development of innovative solutions that are tailored to individual patient needs, enhancing the efficacy and safety of medical interventions. The integration of IoT-enabled devices with nanoparticle-based systems is also gaining traction, enabling remote monitoring and management of therapeutic outcomes [21-24].

4. CHALLENGES AND FUTURE DIRECTIONS

Despite their immense potential, biomedical nanoparticles face several challenges. Scalability remains a significant technical hurdle, as the large-scale production of nanoparticles with consistent quality is complex. Regulatory approval processes are stringent, often slowing down the clinical translation of nanoparticle-based therapies. Additionally, the potential for accumulation and toxicity of nanoparticles in the body necessitates thorough long-term studies. Addressing these challenges requires advancements in manufacturing technologies, comprehensive safety assessments, and the establishment of standardized protocols for nanoparticle characterization and testing. Future research should focus on addressing these challenges through interdisciplinary collaborations, fostering innovation, and expediting the translation of nanoparticle-based solutions to clinical practice [28-30].

5. CONCLUSION

Biomedical nanoparticles are at the forefront of a technological revolution in healthcare. Their unique properties and versatile applications are redefining disease diagnostics, treatment, and prevention. From targeted drug delivery to advanced imaging and tissue engineering, these nanostructures are opening new avenues for innovation in medicine. While challenges remain, continued advancements in nanoparticle synthesis, functionalization, and integration with emerging

technologies promise a transformative impact on personalized medicine and global healthcare outcomes. By addressing current limitations and leveraging interdisciplinary expertise, the potential of biomedical nanoparticles to revolutionize modern healthcare can be fully realized

REFERENCES

[1]. N.T. Thanh, L.A. Green, Nano Today, 5 (2010) 213-230.

[2]. G. Choi, N.S. Rejinold, H. Piao, J. H. Choy, Chemical Science, (2021).

[3]. S. Bhatia, Nanoparticles types, classification, characterization, fabrication methods and drug delivery applications, Natural polymer drug delivery systems, Springer2016, pp. 33-93.

[4]. M. Jyothi, V.J. Angadi, T. Kanakalakshmi, M. Padaki, B.R. Geetha, K. Soontarapa, Journal of Polymers and the Environment, 27 (2019) 2408-2418.

[5]. B. Mues, E.M. Buhl, T. Schmitz-Rode, I. Slabu, Journal of Magnetism and Magnetic Materials, 471 (2019) 432-438.

[6]. H.A. Adeola, S. Sabiu, T.A. Adekiya, C.E. Aruwa, B.E. Oyinloye, Heliyon, 6 (2020) 04890.

[7]. K. Atacan, M. Özacar, M. Özacar, International journal of bio macromolecules, 109 (2018) 720-731.

[8]. X. Zhao, Z. Meng, Y. Wang, W. Chen, C. Sun, B. Cui, J. Cui, M. Yu, Z. Zeng, S. Guo, Nature plants, 3 (2017) 956-964.

[9]. A.S. Garanina, V.A. Naumenko, A.A. Nikitin, E. Myrovali, A.Y. Petukhova, S.V. Klimyuk, Y.A. Nalench, A.R. Ilyasov, S.S. Vodopyanov, A.S. Erofeev, Nanomedicine: Nanotechnology, Biology and Medicine, 25 (2020) 102171.

[10]. F. Brero, M. Albino, A. Antoccia, P. Arosio, M. Avolio, F. Berardinelli, D. Bettega, P. Calzolari, M. Ciocca, M. Corti, Nanomaterials, 10 (2020) 1919.

[11]. F.M. Bojin, V. Paunescu, Pros and cons on magnetic nanoparticles use in biomedicine and biotechnologies applications, Nanoparticles' Promises and Risks, Springer2015, pp. 103-135.

[12]. S. Dutz, S. Wojahn, C. Gräfe, A. Weidner, J.H. Clement, Nanomaterials, 7 (2017) 453.

[13]. K.R. Reddy, P.A. Reddy, C.V. Reddy, N.P. Shetti, B. Babu, K. Ravindranadh, M.V. Shankar, M.C. Reddy, S. Soni, S. Naveen, Methods in microbiology, 46 (2019) 227-254.

[14]. Y. Tao, H.F. Chan, B. Shi, M. Li, K.W. Leong, Advanced Functional Materials, 30 (2020) 2005029.

[15]. G.P. Nethala, R. Tadi, G.R. Gajula, P.P. Madduri, A. Anupama, V. Veeraiah, Materials Chemistry and Physics, 238 (2019) 121903.

[16]. O. Caltun, I. Dumitru, M. Feder, N. Lupu, H. Chiriac, Journal of magnetism and magnetic materials, 320 (2008) e869-e873.

[17]. J. Khan, H. Ullah, M. Sajjad, A. Ali, K.H. Thebo, Inorganic Chem. Communications, 98 (2018) 132-140.

[18]. Y. Hammiche-Bellal, A. Djadoun, L. Meddour-Boukhobza, A. Barama, Sumy State University2013.

[19]. L. Ajroudi, S. Villain, V. Madigou, N. Mliki, C. Leroux, J. of Crystal Growth, 312 (2010) 2465-2471.

[20]. O. Gamucci, A. Bertero, M. Gagliardi, G. Bardi, Coatings, 4 (2014) 139-159.

[21]. I. Robinson, Synthesis, characterisation and functionalisation of magnetic nanoparticles for biomedical applications, The University of Liverpool (United Kingdom)2009.

[22]. C.R. Vestal, Z.J. Zhang, Journal of the American Chemical Society, 125 (2003) 9828-9833.

[23]. X. Li, J. Wei, K.E. Aifantis, Y. Fan, Q. Feng, F.Z. Cui, F. Watari, Journal of Biomedical Materials Research Part A, 104 (2016) 1285-1296.

[24]. K. McNamara, S.A. Tofail, Advances in Physics: X, 2 (2017) 54-88.

[25]. T.V. Tran, D.T.C. Nguyen, P.S. Kumar, A.T.M. Din, A.A. Jalil, D.-V.N. Vo, Environmental Chemistry Letters, (2022) 1-23.

[26]. R. Remya, A. Julius, T. Suman, V. Mohanavel, A. Karthick, C. Pazhanimuthu, A.V. Samrot, M. Muhibbullah, Journal of Nanomaterials, 2022 (2022).

[27]. H.-V. Tran, N.M. Ngo, R. Medhi, P. Srinoi, T. Liu, S. Rittikulsittichai, T.R. Lee, Mater, 15 (2022) 503.

[28]. Y. Gao, W. Yuling, International Journal of Biological Macromolecules, (2022).

[29]. M. Nadeem, R. Khan, N. Shah, I.R. Bangash, B.H. Abbasi, C. Hano, C. Liu, S. Ullah, S.S. Hashmi, A. Nadhman, Nanomaterials, 12 (2022) 130.

[30]. M.G. Montiel Schneider, M.J. Martín, J. Otarola, E. Vakarelska, V. Simeonov, V. Lassalle, M. Nedyalkova, Pharmaceutics, 14 (2022) 204.

*****

ISBN: 978-81-970491-8-7
2
Current Research in
Science and Technology
(An Edited Book)

Dynamic Viscosity of Allyl Halide with Ketone at Temperature 303.15 K

Dr. Y. S. Sudake

Dept. of Physics, New Arts, Commerce and Science College, Shevgaon, (M.S.) India
Email: *ysudake@gmail.com*

ABSTRACT

In summer, at room temperature 303.15 k, the viscosity of a binary mixture of Allyl halide (Allyl Bromide, Allyl Chloride) with Ketone (Acetone, 2-Butanone, 2-Pentanone and 2-Heaxanone) are determined by simple viscometer. These are used to determine the viscosity deviation of a binary mixture of Allyl halide and the carbonyl group of ketones at the same temperature. Viscosity deviation is employed to identify the type and strength of intermolecular interaction between Allyl hallide and Ketone. The viscosity deviation shows the opposite tendency in ketone rich region and Allyl halide rich region. The effect of increase in carbon chain length of ketone on viscosity is also reported. It is also noted that functional groups Br and Cl affect intermolecular interaction. The viscosity deviation is fitted to Redlich- Kister equation.

Keywords: *Viscosity, Allyl halide, Ketone.*

1. INTRODUCTION

When two or more liquids are mixed the resultant formation of the mixture shows different behavior from the ideal expected. The properties of a binary mixture of liquid are more interesting in the point of view of theoretical and practical in many fields. The fundamental properties such as density and viscosity are also key to the extraction of strength and type of intermolecular and intramolecular interaction among the parent liquids. The knowledge of these properties of the mixture is essential in engineering, pharmaceutical and industry applications [1,2]. The allyl bromide (ALB) and allyl chloride (ALC) are Allyl halide and polar molecules. Ketone is an organic liquid having a carbonyl group(C=O) attached to R and Ṙ, where, R and Ṙ are the same or different. Ketone is used from synthesis to paint. Kemeakegha et.al [3] reported the density and viscosity of Ethyl acetoacetate with ketone at temperatures 303.15K and 308.15K. As part of our ongoing research [4-7] on Allyl halide with ketone, the present paper reports the viscosity of Allyl Bromide and Allyl Chloride with Ketone (Acetone, 2-Butanone, 2-Pentanone and 2-Hexanone) at room temperature 303.15 K in summer season.

2. EXPERIMENTAL METHOD

The chemicals used in this present work are Allyl Chloride, Allyl Bromide, Acetone (ACE), 2-butanone (2-BU), 2-pentanone (2-PE) and 2-hexanone (2-HE) of AR grade and used without further purification. The 5 mL solutions were prepared at eleven different volume percentages by adding ketone in Allyl hallide starting from 0 to 100 % in steps of 10 %, by micropipette with an accuracy of ± 0.0006 mL. The viscosity of pure liquid and binary mixture is determined by a simple Ostwald Viscometer at room temperature 303.15K in the summer season. The viscosity of one liquid is

compared with viscosity of another standard liquid. This is done by comparing the time flow of equal volumes of these liquids through the same capillary viscometer.

The viscometer is cleaned with acetone and dried it before is used to measure of viscosity of liquids. The viscometer is hung exactly vertically by using the stand. Referring to Figure 1, the sample under test is introduced into bulb B up to mark Z, and then forced, under pressure liquid is sucked into bulb A up to mark X. The liquid is then allowed to fall freely back to bulb B at room temperature. The time required to meniscus of liquid from mark X to Y is measured with a digital stopwatch and noted down. This is repeated at least five times for one sample to approach the exact time flow. The average time is used to determine viscosity. The capillary tube is cleaned with acetone each time before using another sample. Water is used as a reference liquid to determine the viscosity of unknown liquids.

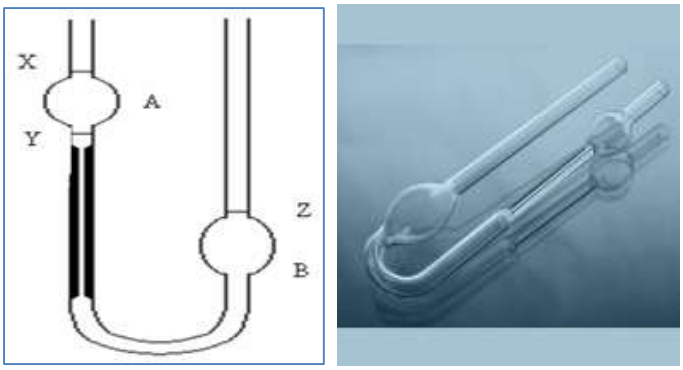

Fig. 1: Ostwald Viscometer

3. RESULTS AND DISCUSSIONS

The viscosity of binary mixture is determined by using equation

$$\frac{\eta_1}{\eta_2} = \frac{\rho_1 t_1}{\rho_2 t_2} \quad (1)$$

Where ρ_1, ρ_2, η_1 and η_2 are density and viscosity of liquid and water respectively. t_1 and t_2 are measured time of flow of liquid and water respectively. Water is always taken as standard or reference liquid.

Table1: Viscosity of binary mixture of Allyl Chloride with ketone systems at temperature 303.15k

Volume Fraction of ALC	ALC+ACE	ALC+2-BU	ALC+2-PE	ALC+2-HE
1.0	0.3835	0.3835	0.3835	0.3835
0.9	0.3784	0.3829	0.3852	0.3860
0.8	0.3728	0.3828	0.3895	0.3916
0.7	0.3676	0.3833	0.3977	0.4028
0.6	0.3655	0.3839	0.4059	0.4161
0.5	0.3659	0.3856	0.4131	0.4313
0.4	0.3636	0.3887	0.4193	0.4465
0.3	0.3598	0.3884	0.4206	0.4605
0.2	0.3524	0.3866	0.4231	0.4708
0.1	0.3455	0.3852	0.4251	0.4795
0.0	0.3376	0.3793	0.4272	0.4838

The viscosity of pure liquid and binary mixture of systems ALC+ACE, ALC+2-BU, ALC+2-PE and ALC+2-HE are determined by the above equation and tabulated in Table 1 The value of viscosity of all systems shows non-linear variation which the result of intermolecular interaction take place between Allyl halide and Ketone. The viscosity of the binary mixture ALC+ACE and ALC+2-BU decreases as the volume fraction of ALC decreases while the viscosity of ALC+2-PE and

ALC+2-HE increases as the volume fraction of ALC decreases. At every volume fraction, the viscosity of the system increases as we move from ALC +ACE to ALC+2-HE. This may be due to the carbon chain length of ketone increase so the viscosity of mixture increases. This trend is confirmed by observing increasing viscosity from ACE to 2-HE.

The viscosity of pure liquid and binary mixture of system ALB+ACE, ALB+2-BU, ALB+2-PE and ALB+2-HE are determined by the above equation and tabulated in Table 2. The value of viscosity of all systems shows non-linear variation is the result of intermolecular interaction take place between Allyl halide and Ketone. The viscosity of the binary mixture of all systems decreases as the volume fraction of ALB decreases.

Table 2: Viscosity of binary mixture of Allyl Bromide with ketones systems at temperature 303.15k

Volume Fraction of ALB	ALB+ACE	ALB+2-BU	ALB+2-PE	ALB+2-HE
1.0	0.5489	0.5489	0.5489	0.5489
0.9	0.5251	0.5269	0.5301	0.5325
0.8	0.4958	0.5084	0.5164	0.5250
0.7	0.4755	0.4933	0.5067	0.5228
0.6	0.4621	0.4821	0.5020	0.5303
0.5	0.4479	0.4730	0.5006	0.5333
0.4	0.4335	0.4622	0.4936	0.5353
0.3	0.4193	0.4519	0.4856	0.5353
0.2	0.3975	0.4304	0.4746	0.5293
0.1	0.3691	0.4061	0.4574	0.5096
0.0	0.3375	0.3794	0.4272	0.4839

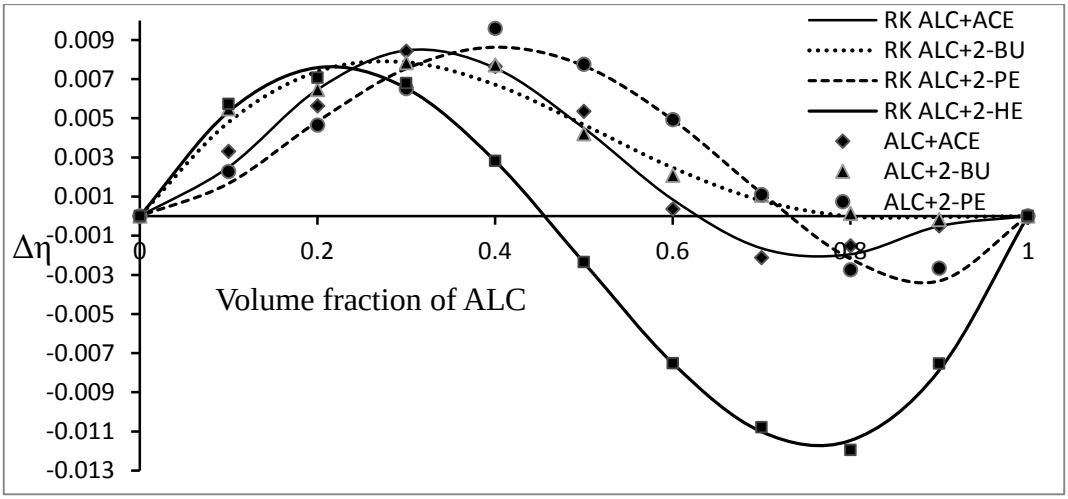

Fig. 1: Viscosity deviation of binary mixture at temperature 303.15K.

The viscosity deviation of binary mixture is determined by equation

$$\Delta\eta = \eta_{mix} - (v_1\eta_1 - v_2\eta_2) \quad (2)$$

Where η_{mix}, η_1 and η_2 is viscosity of mixture pure liquid 1 and pure liquid 2 respectively v_1, v_2 volume fraction of liquid 1 and liquid 2 respectively. The viscosity deviation of Allyl chloride with ketone is plotted in Fig. 1. This shows a positive deviation in ketone ketone-rich region indicating strong specific interaction due to dipolar association force being predominant in complex formation. The negative deviation in the ALC-rich region due to differences in molecular size and shape of components causes the loss of dipolar association in pure components [8,9]. The viscosity deviation of Allyl Bromide with ketone is depicted in Fig. 2.

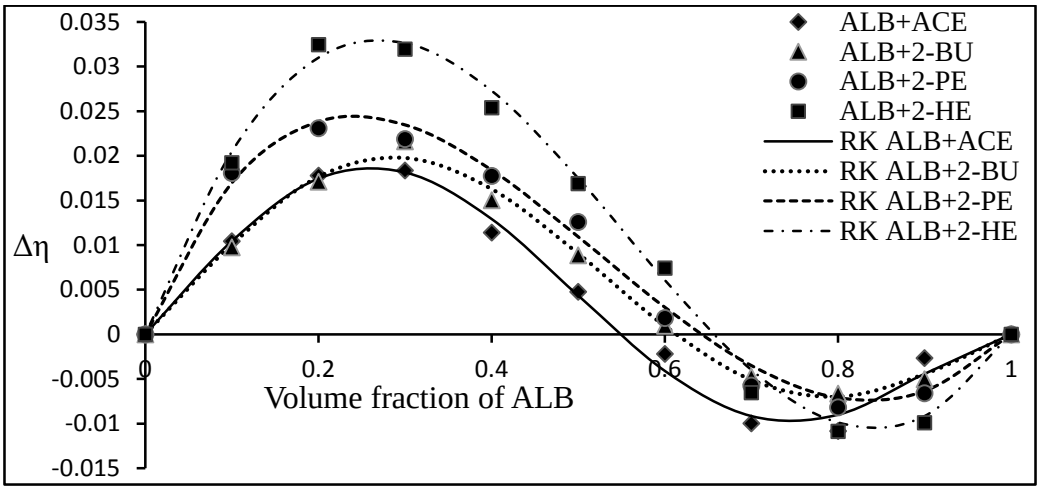

Fig. 2: Viscosity deviation (Δη) of binary mixtures at temperature 303.15K.

The nature of the graph is somewhat similar to trends observed in binary mixture of Allyl chloride with ketone. The positive deviation in the ketone-rich region also indicates strong specific interaction dominant in mixing components while the negative deviation of viscosity in ALB and ALC-rich regions indicates dispersion force dominant between mixing components. It is also noticed that the magnitude of viscosity deviation increases with increases in the carbon chain of ketones in allyl bromide with the ketone system. The viscosity deviation is fitted to Redlich – Kister [10-11] equation and standard deviation is determined by following equation. The value of a_j coefficient and standard deviation are tabulated in table 3.

The aj coefficient

$$Y^E = x\ .(1-x).\sum_{j=0}^{n} a_j.(2x\ -1\ )^j \tag{3}$$

$$\sigma = \sqrt{\frac{[\sum Y^E{}_{cal} - Y^E{}_{expt}]^2}{(n-1)}} \tag{4}$$

Table 3: a_j coefficient and standard deviation (б) of viscosity deviation

System	a_0	a_1	a_2	a_3	σ
ALC+ACE	0.0180	0.0733	-0.0108	-0.0817	0.0006
ALC+2-BU	0.0187	0.0449	0.0121	-0.0177	0.0006
ALC+2-PE	0.0307	0.0389	-0.0623	-0.0066	0.0007
ALC+2-HE	-0.0094	0.1087	-0.0074	-0.0262	0.0004
ALB+ACE	0.0173	0.1822	0.0249	-0.1234	0.0014
ALB+2-BU	0.0362	0.1637	-0.0082	-0.0985	0.0009
ALB+2-PE	0.0438	0.1600	0.0240	0.0030	0.0013
ALB+2-HE	0.0699	0.2218	-0.0109	-0.0251	0.0014

5. CONCLUSION

The present paper successfully reported the study of the viscosity of Allyl chloride with Ketone (ACE, 2-BU, 2-PE and 2-HE) and Allyl Bromide with ketone (ACE,2-BU,2-PE and 2-HE). Viscosity deviation of both systems suggests that there is strong intermolecular interaction between Allyl halide (ALC and ALB) and carbonyl group ketone (ACE,2-BU, 2-PE and 2-HE). Deviation will increase as the carbon chain length of ketone increases.

REFERENCES

[1]. K. Sreekanth, D. Sravana Kumar, M. Kondaiah, D. Krishna Rao, Physica B 406 (2011) 854.

[2]. E. D. Dikio, Simphiwe M. Nelana, David A. Isabirye, Eno E. Ebenso , Int. J. Electrochem. Sci., 7 (2012) 11101.

[3]. A. J. Kemeakegha, B. A. Jumbo, Int. J. of Innovative Science and Research Technology, 5(6), 1598 (2020).

[4]. A. P. Maharolkar, Y. Sudke, S. Kamble & A Tidar, A. G. Murugkar, S.S. Patil & P. W. Khirade, International Journal of Chemistry (2)2, 250, (2010).

[5]. Y. S. Sudake, S. P. Kamble, S. S. Patil, P. W Khirade and S. C. Mehrotra J Korean Chem. Society 56(1),20, (2012).

[6]. Y. S. Sudake, S. P. Kamble, A. P. Maharolkar, S. S. Patil, P. W. Khirade and S. C. Mehrotra, Bulletin of the Korean Chemical Society, 33(10),3423(2012).

[7]. Y.S. Sudake**,** S. P. Kamble, and P. W. Khirade J. of Applied Sci. and Computation VI (1), 875-882(2019).

[8]. R.J. Fort and W. R.Moore, Trans.Faraday Soc., **62**, 1112,(1966).

[9]. R. A. Clara, C. G. Marigliano, and H. N. Solimo, J Chem. Eng. Data **51**, 1473, (2006).

[10]. M. I. Aralaguppi, T. M. Aminabhavi, R. H. Balundgi and S. S. Joshi, J. Phys. Chem., 95, 5299, (1991).

[11]. O. Redlich and A. Kister, Ind. Eng. Chem., 40, 348, (1948).

*****

Soil Pollution and Ecosystem

Dr. Manisha D. Dhiware

Department of Physics, KVN's Naik Arts, Commerce and Science College,
Canada corner, Nashik, 422002
Email: *manishasalunke73@gmail.com*

ABSTRACT

Soil is one of nature's most incredible assets. World Soil Day, observed every December 5th, is a global call to recognize the indispensable role of soil in our lives and the urgent need to protect it. Soil is home to a quarter of our planet's biodiversity, making it a lively, dynamic ecosystem teeming with activity. Most of the food we consume is grown in soil. It is the foundation of our agricultural systems. Soil captures and stores carbon, playing a pivotal role in combatting climate change. As water passes through, soil acts as a filter, removing impurities and ensuring clean water supply. Despite its crucial role, soil faces threats from erosion, pollution, deforestation, and unsustainable agricultural practices. The main anthropogenic sources of soil pollution are the chemicals used in or produced as byproducts of industrial activities, domestic, livestock and municipal wastes (including wastewater), agrochemicals, and petroleum-derived products.

Keywords: *Soil Pollution, Chemical contamination, Food safety, Health*

1. INTRODUCTION

Soil pollution is defined as the presence of toxic chemicals (pollutants or contaminants) in soil, in high enough concentrations which causes a risk to human health and the ecosystem. In the case of contaminants which occur naturally in soil, even when their levels are not high enough to cause a risk, soil pollution is still said to occur if the levels of the contaminants in soil exceed the levels that should naturally be present. The sources of soil pollution can occur from various point and non-point sources. The most common sources are domestic wastes, untreated or insufficient treatment of industrial discharges, husbandry wastes and agricultural uses of fertilizers, pesticides and herbicides. Soil pollution is a global issue that poses serious threats to human and ecosystem health. [1] Anthropogenic activities are the primary source of soil contaminants. Both organic and inorganic pollutants can enter the soil matrix through various pathways, including the application of fertilizers and pesticides, improper disposal of wastewater, pharmaceuticals, plastics, and the burning of fossil fuels. [2] Additionally, these organic and inorganic pollutants have been linked to serious illnesses in humans. Trace toxic metals like arsenic, lead, and cadmium have been associated with various types of cancers, while organic substances like polychlorinated biphenyls, polycyclic aromatic hydrocarbons, insecticides, and herbicides have been linked to various human diseases. [3] Physical methods involve the physical removal, washing, encapsulation, and electro kinetic extraction contaminates in soil [4].

All soils, whether polluted or unpolluted, contain a variety of compounds (contaminants) which are naturally present. Such contaminants include metals, inorganic ions and salts (e.g. phosphates, carbonates, sulphates, nitrates), and many organic compounds (such as lipids, proteins, DNA, fatty acids, hydrocarbons, PAHs, alcohols, etc.). These compounds are mainly formed through soil

microbial activity and decomposition of organisms (e.g., plants and animals). Additionally, various compounds get into the soil from the atmosphere, for instance with precipitation water, as well as by wind activity or other types of soil disturbances, and from surface water bodies and shallow groundwater flowing through the soil. When the amounts of soil contaminants exceed natural levels (what is naturally present in various soils), pollution is generated. Soil pollution consists of pollutants and contaminants. The main pollutants of the soil are the biological agents and some of the human activities. Soil contaminants are all products of soil pollutants that contaminate the soil. Human activities that pollute the soil range from agricultural practices that infest the crops with pesticide chemicals to urban or industrial wastes or radioactive emissions that contaminate the soil with various toxic substances. The alarming reality is that we have been witnessing a rapid loss of the quality of our soils and the invaluable benefits they offer [5]. For example, it has been estimated that 16.1% of soils are contaminated in China, as reported by the Chinese Ministry of Environmental Protection [6].

2. MATERIALS AND METHOD

Causes of Soil Pollution:

Soil pollution can harm ecosystems by reducing biodiversity, contaminating food, and degrading soil quality. Soil pollution can be natural or due to human activity. The activities of the human that causes the majority of soil pollution such as industries, or use of pesticides in agriculture.

1. Industrial Activity:

Mining, manufacturing, and the use of synthetic products (e.g. pesticides, paints, batteries, industrial waste, and land application of industrial or domestic sludge) can result in heavy metal contamination of urban and agricultural soils. The incorrect way of chemical waste disposal from different types of industries can also cause for contamination of soil.

2. Agricultural Activities:

Chemical utilization has gone up tremendously since technology provided us with modern pesticides / herbicides and fertilizers. They are full of chemicals that are not produced in nature and cannot be broken down by it. Plants absorb many of these pesticides and when they decompose, it may cause soil pollution.

- **Pesticides:** Pesticides (DDT, Aldrin and Dieldrin) are synthetic toxic chemicals that definitely kill different types of pests and insects causing damage to agriculture but it has contaminated the soils. They are non-biodegradable chemicals. Therefore, these chemicals will not gradually decompose and keep on accumulating in the soil. Hence, the concentration of these chemicals will increase in food chain through contaminated soils, it will cause many metabolic and physiological disorders in humans.
- **Herbicides:** Slowly, the industries began production of herbicides like sodium arsenite (Na_3AsO_3), sodium chlorate ($NaClO_3$), etc. for the weed control but they are also not environmentally friendly. Herbicides are not as harmful as pesticides but most of the herbicides are toxic. Research suggested that the spraying herbicides causes more insect attack and diseases of plants in comparison to manual weeding.
- **Inorganic Fertilizers:** Excessive use of inorganic nitrogen fertilizers leads to acidification of soil and contaminate the agricultural soil. Also known as agrochemical pollution. Large quantities of fertilizers are regularly added to soils in intensive farming systems to provide adequate N, P, and K for crop growth. The compounds used to supply these elements contain trace amounts of heavy metals (e.g., Cd and Pb) as impurities. Continuous application of inorganic fertilizers may significantly increase the heavy metals content in the soil.

3. Waste Disposal:

Industrial waste is sure to cause soil contamination. Disposal of plastics, cans, and other solid waste falls into the category of soil pollution. Leaking of sewerage system can also affect soil quality and cause soil pollution by changing the chemical composition of the soil.

3. RESULTS AND DISCUSSIONS

Effect of Soil Pollution

It causes harmful effect on the soil and the environment. Contamination of soil will decreases the agricultural output. Major soil pollution effects are:

- **Inferior Crop Quality:** It can decrease the quality of the crop. Regular use of chemical fertilizers, pesticides will decrease the fertility of the soil at a rapid rate and alter the structure of the soil. This will lead to decrease in soil quality and poor quality of crops. Over the time the soil will become less productive due to the accumulation of toxic chemicals in large quantity.
- **Harmful Effect on Human Health**: It will increase the exposure to toxic and harmful chemicals thus increasing health threats to people living nearby on the degraded land. Living, working or playing in the contaminated soil can lead to respiratory diseases, skin diseases, and other diseases. Also, it can cause other health problems.
- **Water Sources Contamination:** The surface run-off after raining will carry the polluted soil and enter into different water resource. Thus, it can cause underground water contamination thereby causing water pollution. This water after contamination is not fit for human as well as animal use due to the presence of toxic chemicals.

1. Remediation of Polluted Soils

- ❖ Phytoremediation: During recent years the concept of using plants to remediate contaminated sites has received greater attention. It consists of the Greek prefix phyton (Plant), attached to the Latin root remedium (to correct or to remedy).
- ❖ Phytoextraction
- ❖ Phytostabilisation
- ❖ Rhizofiltration
- ❖ Phytovolatilization
- ❖ Phytodegradation

2. Soil scraping

Replacement of uppermost contaminated soil (0-15 cm depth) from cultivated field has been possible. The maximum amount of lead was absorbed / adsorbed by soil in clay – humus complexes. By scraping of contaminated soil highest quality of heavy metals can be removed from the soil and become suitable from growing the crops.

3. Prevention/Management of Soil Pollution

- ❖ Recycling of waste before disposal.
- ❖ Proper disposal method of household and industrial waste.
- ❖ Proper maintenance of sewage system.
- ❖ Use of organic manures /pesticides instead of chemical fertilizers and pesticides.
- ❖ Encouraging the integrated application of inorganic fertilizers, organic manures and bio-fertilizers (INM system)
- ❖ Avoiding deforestation and promoting forestation.
- ❖ Encouraging plantation by social and agro forestry programs.
- ❖ Suitable and safe disposal of including nuclear wastes.
- ❖ Conducting many pollution awareness programs.

4. CONCLUSION

Therefore, human activities are responsible for the majority of the soil pollution. We as humans buy things that are harmful and not necessary, use agricultural chemicals (fertilizers, pesticides, herbicides, etc.), drop waste here and there. Hence, it is very important to educate people around you the importance of environment if they are not aware. Soil pollution can cause an imbalance of the ecosystem of the soil. The soil is an important habitat and is the house of different type of microorganisms, animals etc. Thus, soil pollution can negatively impact the lives of the living

organisms and can result in the gradual death of many organisms. It can cause health threats to animals grazing in the contaminated soil or microorganisms residing in the soil.

5. ACKNOWLEDGEMENT

We would like to extend our heartfelt appreciation to the Principal K. V. N. Naik College, Nashik for his time to assist us in enhancing our work and providing lab facility.

REFERENCES

[1]. Singh, S. P., and Singh, M. K. (2020). "Soil pollution and human health," in Plant responses to soil pollution. Editors P. Singh, S. K. Singh, and S. M. Prasad (Singapore: Springer).

[2]. Peña, A. (2022). A comprehensive review of recent research concerning the role of low molecular weight organic acids on the fate of organic pollutants in soil. J. Hazard. Mat. 434, 128875. doi:10.1016/j. jhazmat. 2022.128875

[3]. Rahman, M. M., Dong, Z., and Naidu, R. (2015). Concentrations of arsenic and other elements in groundwater of Bangladesh and West Bengal, India: Potential cancer risk. Chemosphere 139, 54–64. doi: 10.1016/j.chemosphere.2015.05.051

[4]. Liu, L., Li, W., Song, W., and Guo, M. (2018). Remediation techniques for heavy metal- contaminated soils: Principles and applicability. Sci. Total Environ. 633, 206–219.doi: 10.1016/j.scitotenv.2018.03.161

[5]. Jie, C., Jing, Z. C., Man, Z. T., and Zi, T. G. (2002). Soil degradation: A global problem endangering sustainable development. J. Geogr. Scie. 12, 243–252. doi:10.1007/bf02837480

[6]. Ministry of Environmental Protection (MEP) (2014). National soil contamination survey report. Beijing, China: Ministry of Env. Protection. at: http://www.mep.gov.cn/gkml/hbb/qt/201404/t20140417_270670.

*****

ISBN: 978-81-970491-8-7
4
Current Research in
Science and Technology
(An Edited Book)

Growth Techniques of NLO Crystals: SEST and Unidirectional SR Methods for Optoelectronic and Photonic Applications

Yogesh Balwantrao Rasal

Department of Physics, Smt. S. K. Gandhi Arts, Amolak Science, and P. H. Gandhi Commerce College Kada, Tal. Ashti, Dist. Beed, Maharashtra, India
Email: *rasyog1975@gmail.com*

ABSTRACT

Crystal growth is a critical area of research with applications in materials science, chemistry, and physics, particularly in the fabrication of semiconductors, pharmaceuticals, and advanced materials. Researchers use various methods to control the nucleation, growth rate, and final properties of crystals, and the Shankar Narayan and Ramasamy (SR) method could be an approach tailored to enhancing these processes. Thiourea Complex doped potassium dihydrogen phosphate single crystal was successfully grown by SR method. In this method, a thermal gradient is maintained between the bottom and top of the ampoule, in which a seed of the grown crystal is fixed at the bottom of the ampoule. The grown Thiourea Complex doped potassium dihydrogen phosphate crystal was characterized by different techniques. The SR method is an advanced experimental technique used to grow NLO crystals, enabling the unidirectional growth of large, transparent, and defect-free single crystals for optoelectronic and photonic applications.

Keywords: *Slow evaporation method, SR method, seed crystal, Unidirectional growth, UV-visible*

1. INTRODUCTION

The second harmonic generation (SHG) single crystal has been one of the most sought-after properties in the field of semi-organic nonlinear optical materials for the past three decades. Various methods have been developed for growing single and bulk crystals, each with different growth conditions and applications [1-4]. The slow evaporation solution method is the most fundamental technique for crystal growth. Other methods, such as the melt growth technique, have been explored for semi-organic crystal growth. In the melt growth process, the material is crystallized through fusion and solidification as the liquid cools below its freezing point [5]. This process leads to the formation of crystals that are generally free of defects and impurities, as the crystallization reaction occurs more rapidly compared to other methods. Melt growth can be further divided into several techniques, with the two most common being the Bridgman and Czochralski methods [6-7].

Another widely used technique for crystal growth is the solution growth method, which is the simplest and oldest approach for growing crystals from an aqueous solution. This method is particularly useful for growing large crystals and can be further classified into low-temperature solution growth, high-temperature solution growth, hydrothermal growth, and gel growth [8-11]. In this study, potassium thiourea complex-doped potassium dihydrogen phosphate (PTCKDP) crystals were grown using the Sankaranaryanan-Ramasamy (S-R) method at 35°C. Figures 1a and 1b show the crystals grown by the slow evaporation solution method and the S-R method, respectively.

Despite the various crystal growth methods, each has its own limitations, including thermal stress, internal defects, challenging growth conditions, difficulty in growing large crystals, long waiting periods, complicated equipment, and multi-step processes. Therefore, in this research, the unidirectional Sankaranaryanan-Ramasamy (S-R) crystal growth method was employed to overcome these drawbacks. This method uses less sophisticated equipment to grow unidirectional single crystals. One of its main advantages is that it allows crystals to be grown at any desired temperature along any axis, with all solute material being converted into crystal form.

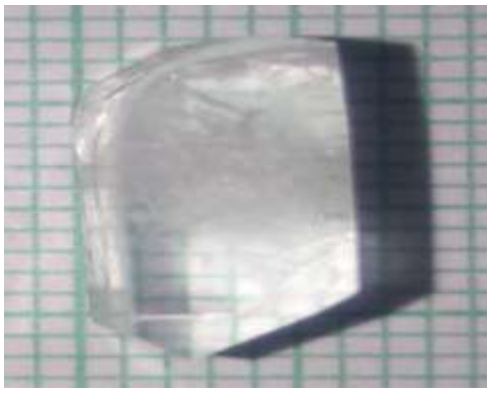

Fig.1: Photograph of 0.2 mol% PTC doped KDP crystal by SEST Method.

Fig.2: Photograph of 0.2 mol% PTC doped KDP crystal by SR Method.

2. MATERIALS AND METHOD

Tetra thiourea potassium chloride (TTPC) - doped potassium dihydrogen phosphate (KDP) crystals were synthesized using both the slow evaporation solution technique (SEST) and the Sankaranaryanan-Ramasamy (SR) method.

1.1. Slow evaporation solution technique

Initially tetra thiourea potassium chloride (TTPC) crystals were grown using the slow evaporation solution technique (SEST) method. The synthesis process began with the preparation of potassium thiourea chloride (PTC) crystals by dissolving potassium chloride (≥ 99%, Merck) and thiourea (≥ 99%, Merck) in a1:4 ratios in deionized water (conductivity ≤ 1.0 μmhos/cm) called as tetra thiourea potassium chloride for three different molar concentrations. The resulting solutions was stirred for five hours, filtered using Whatman filter paper (I), and left undisturbed for slow evaporation.

Fig. 3. Photograph of growth in CTB

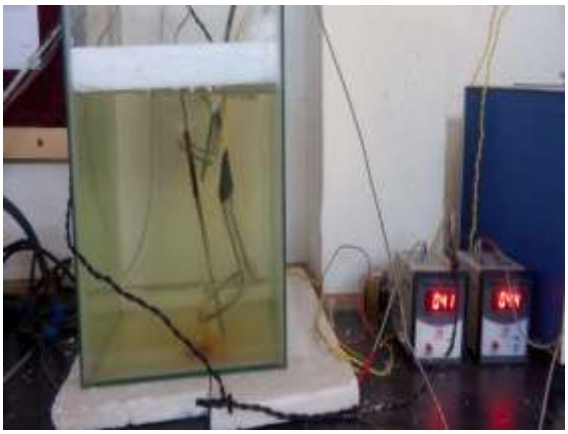

Fig.4. Photograph of SR Method.

Next, 0.1, 0.5 and 1.0 mole % of the PTC yield was doped into a supersaturated solution of potassium dihydrogen phosphate (KDP, ≥ 99%, Merck) to produce PTCKDP crystals. This mixture was stirred for 8 hours to ensure uniformity and then placed in a constant temperature bath at 40°C. High-quality seed crystals were then selected for SR growth. The purity of the PTCKDP crystals was

further improved through successive recrystallization using the SEST method. After 20 days, a high-quality transparent whitish PTCKDP single crystal was harvested. The resulting PTCKDP crystal, measuring 15×6×5 mm^3, grown by the SEST method, is shown in Fig. 1(a).

2.2. Sankaranarayanan - Ramasamy method

The setup for growing unidirectional crystals using the Sankaranaryanan-Ramasamy (SR) method consists of ring heaters placed at both the top and bottom of a growth ampoule, which is connected to a temperature controller. The ampoule is designed to meet the experimental requirements and to achieve the desired crystal dimensions. The top heater is maintained at a higher temperature to facilitate slow evaporation, while the position of the heater can be adjusted to regulate the crystal growth rate. A seed crystal, measuring 4 mm x 4 mm x 2 mm, was selected from crystals grown using the slow evaporation technique and chosen for growth along the (1 1 0) plane. This selected plane was mounted at the bottom of the ampoule. The setup for growing unidirectional crystals using the Sankaranaryanan-Ramasamy (SR) method consists of ring heaters placed at both the top and bottom of a growth ampoule, which is connected to a temperature controller. The ampoule is designed to meet the experimental requirements and to achieve the desired crystal dimensions. The top heater is maintained at a higher temperature to facilitate slow evaporation, while the position of the heater can be adjusted to regulate the crystal growth rate. A seed crystal, measuring 4 mm x 4 mm x 2 mm, was selected from crystals grown using the slow evaporation technique and chosen for growth along the (1 1 0) plane. This selected plane was mounted at the bottom of the ampoule.

A 300 ml saturated solution of 0.2 mole % PTCKDP was prepared at 40°C, filtered using Whatman filter paper, and carefully transferred to the growth vessel. The vessel was then sealed and placed in a dust-free chamber. The growth process began with the top ring heater maintaining a temperature of 44°C, while the bottom of the ampoule was kept at 40°C, creating a temperature gradient between the top and bottom regions. This temperature differential facilitated nucleation near the surface of the solution throughout the growth period. Under these conditions, transparent crystals began to grow at a rate of approximately 1 mm per day. After 35 days, a high-quality crystal with dimensions of 38 mm by 18 mm was harvested. The SR method improves by eliminating the need for suspension threads, which can negatively impact crystal quality. Additionally, unlike conventional solution growth techniques that require large volumes of solution in a large container, the SR method efficiently converts a significant portion of the solute into a bulk single crystal. Fig.1(b) shows the PTCKDP crystal grown using the SR method, with dimensions of 35×20×15 mm^3.

1. Optimizing Crystal Growth Conditions

The Shankarnarayan and Ramasamy method could be focused on optimizing the environmental and chemical conditions that affect crystal growth. These conditions include temperature, supersaturation, solution concentration, and the presence of solvents or additives.Researchers could use this method to refine growth parameters, ensuring that crystals grow with desired qualities, such as size, shape, and purity. The goal might be to control the kinetics of nucleation and growth to produce high-quality single crystals.

2. Facilitating Controlled Nucleation

Nucleation is the initial phase in crystal growth where atoms or molecules come together to form a stable cluster. The Shankarnarayan and Ramasamy method might focus on controlling the nucleation rate to ensure uniformity and reproducibility of crystal formation. Researchers could apply this method to suppress unwanted spontaneous nucleation (which leads to polycrystalline or flawed crystals) and promote homogeneous nucleation. This leads to the growth of large, single crystals, which is important in fields like pharmaceuticals (e.g., for the crystallization of active drug compounds) and optics (e.g., in the development of laser crystals).

3. Modulating Growth Rate and Morphology

Crystal growth rates can often be controlled through the manipulation of solution concentration, temperature, and the addition of growth modifiers. The Shankarnarayan and Ramasamy method could

include techniques for adjusting these factors to control not just the size of the crystals but also their morphology and surface structure. Researchers in materials science might use this method to direct crystals to grow in specific directions, allowing for the fabrication of anisotropic crystals that possess desirable mechanical, electrical, or optical properties.

4. Crystallization from Non-Aqueous Solvents

The Shankarnarayan and Ramasamy method may involve optimizing the use of non-aqueous solvents or melts for crystallization. Non-aqueous crystallization is useful when crystallizing compounds that are insoluble or poorly soluble in water. Researchers may focus on organic crystal growth or crystallization of inorganic compounds that require solvents like alcohols, acetone, or ionic liquids. This method could help in improving crystal size and purity, particularly for organic compounds used in organic electronics or pharmaceuticals.

5. Control of Defects and Impurities

Crystal defects (like dislocations, vacancies, and interstitial impurities) are often undesirable as they can impair the physical properties of the crystals. The Shankarnarayan and Ramasamy method could be tailored to minimize or control these defects during crystal growth. By modifying growth conditions, such as cooling rate, pressure, or solvent composition, researchers can reduce the incorporation of unwanted defects and ensure that the resulting crystals have high structural integrity.

In contrast, the slow evaporation method relies on free convection to control the growth process, creating a surface boundary layer where diffusion occurs. In the SEST method, the solution's rotation thins the boundary layer, enhancing the transport of solute to the crystal surface. In the SR method, gravity governs the concentration near the crystal surface, causing solutes to approach the surface directly. This results in the crystal surface attracting solute atoms more effectively. The SR method allows for crystal growth under stable and controlled conditions [12-17].

3. RESULTS AND DISCUSSIONS

The PTCKDP crystal sample was analyzed using various characterization techniques. Single crystal X-ray diffraction (XRD) analysis was performed with an Enraf Nonius CAD4-MV31 X-ray diffractometer. The results revealed that the crystal belongs to the tetragonal (I) crystal system, with lattice parameters a = b = 7.48 Å, c = 7.00 Å, and a unit cell volume of 391 Å^3.

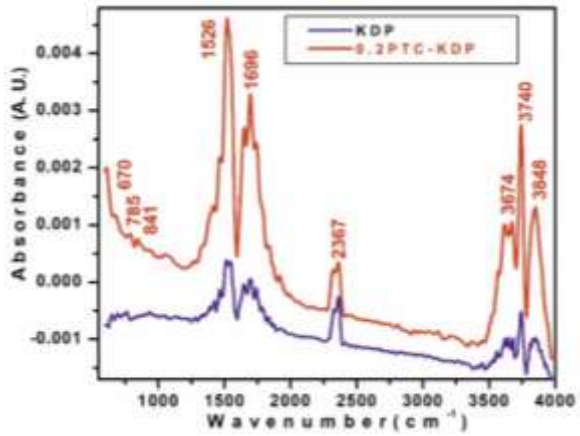

Fig.5: FT-IR plot of the doped crystal

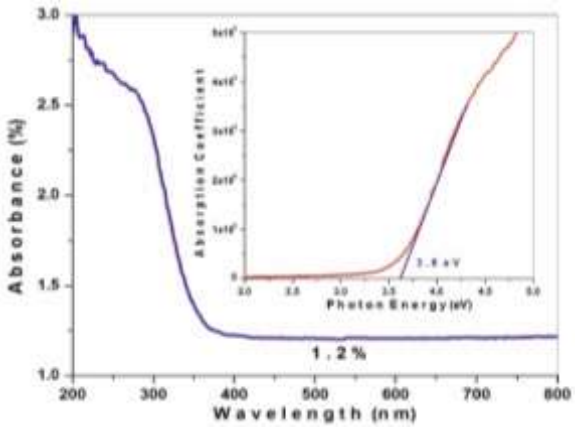

Fig. 6: Absorbance vs. wavelength and Tauck's plot.

The Fourier transform infrared (FT-IR) spectrum of PTCKDP was analyzed using a Bruker α-ATP spectrophotometer, with the results shown in Figure 5. The P-Cl stretching vibration was observed at 670 cm^{-1}, while the absorption peak at 785 cm^{-1} corresponds to P-O-C stretching. A peak at 841 cm^{-1} was attributed to C-Cl bond stretching, and the C=C stretching and NH2 bending vibrations were identified at 1526 cm^{-1} and 1696 cm^{-1}, respectively. Absorption peaks at 2364 cm^{-1} and 3678 cm^{-1} were assigned to phosphorus acid ester O-H stretching and O-H asymmetric

stretching, respectively. Additionally, the peaks at 3740 cm^{-1} and 3848 cm^{-1} were related to O-H stretching vibrations [18].

The PTCKDP crystal was analyzed using UV-visible spectroscopy to assess its absorbance. A sample with a thickness of 3 mm was examined using a Shimadzu UV-2450 spectrophotometer, and the analysis was conducted over a wavelength range of 200 to 900 nm. The obtained data was used to calculate various optical parameters. The transmittance spectrum, shown in Fig. 6, indicates that the PTCKDP crystal has a low absorbance of just 1.2% across the entire visible spectrum, which is a promising characteristic for applications in frequency conversion devices. The optical band gap (Eg) of the crystal was determined using the relation $\alpha h\nu = A(h\nu - Eg)^{1/2}$, where α is the linear absorption coefficient. The value of Eg was found to be 3.6 eV. These optical properties suggest that the PTCKDP crystal is suitable for optical limiting and photonic applications [19-20].

To investigate the second harmonic generation (SHG) properties, the Kurtz-Perry powder test was performed. Before testing, the 0.2 mol% PTCKDP crystal was crushed into a fine powder with uniform particle size. The powdered sample was placed in a microcapillary tube and irradiated with a Q-switched Nd-YAG laser operating at a wavelength of 1064 nm. The laser had energy of 4.7 mJ per pulse, a repetition rate of 10 Hz, and a pulse width of 10 ns. The green emission from the sample confirmed the nonlinear optical behavior of the PTCKDP crystal. The output voltage of the beam from the powdered sample was measured using an oscilloscope (CRO). The measured output for the 0.2 mol% PTCKDP crystal was 141 mV, while the output from pure KDP was 114 mV. This indicates that the SHG efficiency of PTCKDP is 1.25 times greater than that of KDP, demonstrating its potential for nonlinear optical (NLO) applications [21-22].

4. CONCLUSION

The Shankarnarayan and Ramasamy method for crystal growth can be seen by researchers as a comprehensive approach to optimizing conditions that control crystal size, morphology, purity, and defect structures. This method can find significant applications across various industries, including semiconductor manufacturing, pharmaceuticals, materials science, and nanotechnology. It is a tool for advancing the precision and efficiency of crystal growth techniques, improving material properties, and enabling the development of high-performance devices and applications in fields like electronics, optics, and medicine. The Potassium Thiourea Chloride-doped KDP crystal was grown using the SR method, a novel technique for unidirectional crystal growth. This method allows the entire solute to be converted into a single crystal, which measures 35 mm in length and 15 mm in diameter. Characterization results from XRD, FT-IR, UV, and SHG analyses confirm the effectiveness of this method in producing nonlinear optical materials.

5. ACKNOWLEDGEMENT

The authors are also thankful to Prof. P. K Das, Department of Physical Chemistry, Indian Institute of Science (IISc), Bangalore, India for SHG Test. The authors are also thankful to Dr. Senthilkumar Pandian, SSN Chennai, India for SR set up support.

REFERENCES

[1]. A. Senthil, P. Ramasamy, Synthesis, J. Crystal Growth 312 (2010), 276–281,

[2]. J. Uma, V. Rajendran, Progress in Natural Science: Materials International 26 (2016), 24-31,

[3]. P. Rajesh, P. Ramasamy, Materials Letters 63 (2009) 2260–2262,

[4]. M. Arivanandhan et al, J. Crystal Growth 281 (2005) 596-603,

[5]. N. Vijayan, N. Balamurugan, R. Ramesh,Babu, R. Gopalakrishnan, P. Ramasamy, J. Crystal Growth, 275, 1–2, 15 (2005)

[6]. Krishnamoorthy Aunkumar, S. Kalainathan, Applied Physics B 125 (2019)

[7]. Kalaivanan Raju, Mythili Aruchamy, Srinivasan Karuppannan, Cryst. Res. Technol. (2020), 1900234,

[8]. S. Nandhini, K. Sudhakar, S. Muniyappan, P. Murugakoothan, Materials Today: Proceedings 8 (2019) 256–263, https://doi.org/10.1016/j.matpr.2019.02.109.
[9]. Colin D. McMillen, Joseph W. Kolis, Journal of Crystal Growth, 310 (2008) 2033-2038,
[10]. Nianrui Qu et al, *Mater. Res. Express* 6 (2019) 016201
[11]. Jiasong Zhong et al, Materials Research Bulletin, 47 (2012) 3691-3696,
[12]. P. Rajesh, P. Ramasamy, Spectrochimica Acta Part A 74 (2009) 210–213,
[13]. K. Sethuramana , R. Ramesh Babua , R. Gopalakrishnana,, P. Ramasamy Journal of Crystal Growth 294 (2006) 349–352
[14]. G. Anandha Babu and P. Ramasamy, Cryst. Res. Technol., (2008) 1 – 8, https://DOI 10.1002/ crat. 20071 1076.
[15]. A. Senthil, P. Ramasamy, Journal of Crystal Growth 312 (2010) 276–281,
[16]. Y. B. Rasal, R. N. Shaikh, M. D. Shirsat, S. Kalainathan, S. S. Hussaini, Mater. Res. Express 4 036202,
[17]. S. Balamurugana, P. Ramasamy, S.K. Sharma, Yutthapong Inkong, Prapun Manyum, Materials Chemistry and Physics 117 (2009) 465–470
[18]. Stuart Barbara, Infrared Spectroscopy: Fundamentals and Applications, John Wiley and Sons, Chichester, 2004.
[19]. Sheen Kumar, N. Rayar, S. L., Indian Journal of Physics 96(2022) p.79-87,
[20]. Anandaraj Louis, Jothi Lakshmanan, Synthesis, J. Minerals Mater. Character. Engine. 10 (2022),
[21]. S.K. Kurtz, T.T. Perry, J. of Appli. Physi.39 (1968)3798-3813
[22]. R.S. Priyadharshini, M. Saravanan, Optics Laser Technol. 164 (2023) 109512,

*****

ISBN: 978-81-970491-8-7
5 Current Research in Science and Technology
(An Edited Book)

Crystallographic and Dielectric Properties of Cadmium (Cd^{2+}) Substituted Ni-Cu Spinel Ferrites

Dr. R. B. Kavade

Department of Physics, Bhagwan Mahavidyalaya (Arts, Commerce and Science), Ashti Dist. Beed. (MS) India
Email: *kavade.ramdas@gmail.com*

ABSTRACT

The Cadmium (Cd^{2+}) ions substituted samples of mixed nickel- copper ferrites having the compositional combination $Ni_{0.5}Cu_{0.5-x}Cd_xFe_2O_4$ (x = 0.0, 0.1, 0.3, 0.5) have been synthesized using AR grade oxides by standard solid state reaction technique. The formation of single-phase cubic spinel structure of all the samples under investigation have been carried out using X-ray diffraction technique at room temperature. Using LCR–Q meter the dielectric constant (ε′), dielectric loss (ε″), dielectric loss tangent (tanδ) was measured as a function of frequency. The frequency dependence of dielectric parameters measurements was carried out within the range 100 Hz to 1 MHz. The values of dielectric parameters (ε′,ε″and tanδ)are much higher at lower frequencies but decreases with increase in frequency. At very high frequencies, its values become so small that it becomes independent of frequency. The decrease in dielectric parameters with increase of frequency may be due to the fact that beyond a certain frequency of the external electric field, the electronic exchange between ferrous and ferric ions cannot follow the alternating field. It is observed that dielectric constant (ε′), dielectric loss (ε″) and dielectric loss tangent (tanδ) appreciably increases with cadmium concentration x but decreases with increases in frequency.

Keywords: *Mixed spinel ferrites, XRD, dielectric properties.*

1. INTRODUCTION

Ferrites are ferromagnetic materials with good magnetic, dielectric properties and a large number of technological applications in satellite communication, memory device, computer, components, filter components, antenna rods, transformer core etc, because of their excellent electrical and magnetic properties [1].The high electrical resistivity, low eddy current and dielectric losses, moderate saturation magnetization, easy and low cost of preparation, high Curie temperature and high permeability are the remarkable characteristics of a ferrite material which makes them useful in variety of applications. The properties of ferrite depend on magnetic interaction, cation distribution in the two sub lattice, method of preparation, preparative parameters, type and amount of dopant [2-4]. The dielectric properties of ferrites are dependent upon several factors including the method of preparation, chemical composition and grain structure. Among the spinel ferrites, nickel ferrite is having special attraction because of their useful properties such as inverse spinel nature, high saturation magnetization and Curie temperature, high electrical resistivity and chemically most stable. In the literature very few studies on cadmium substituted nickel-copper ferrite are reported.

Here, we report our results on dielectric studies of the prepared $Ni_{0.5}Cu_{0.5-x}Cd_xFe_2O_4$ for the values of x = 0.0, 0.1, 0.3, 0.5samples.

2. EXPERIMENTAL

The polycrystalline samples of $Ni_{0.5}Cu_{0.5-x}Cd_xFe_2O_4$ (x = 0.0, 0.1, 0.3, 0.5) were prepared using the standard ceramic technique [5]. A.R. grade oxides of corresponding ions (NiO, CuO, CdO and Fe_2O_3) were mixed in stoichiometric proportion. Grinding using agate mortar (4 h) was carried out for each sample. The samples were pre-sintered at 1293 K for 12 h. The sintered powder is again reground and sintered at 1353 K for 14 h. Then the powder of samples compressed into pellets of 10 mm diameter using a hydraulic press with pressure 6 ton/inch^2 and sintered at 1273K for 12 h. The samples were furnace cooled to room temperature. The prepared samples were characterized by X-ray powder diffract-meter in the 2θ range 20°-80°at room temperature to confirm single phase spinel structure. Dielectric constant (ε′) dielectric loss (ε″) and loss tangent (tanδ) as a function of frequency at room temperature were measured by LCR Meter. For dielectric measurements the pellets were coated with silver paste for good ohmic contact.

3. RESULTS AND DISCUSSION

3.1 XRD (X-Ray Diffraction)

The XRD patterns of mixed spinel ferrites system $Ni_{0.5}Cu_{0.5-x}Cd_xFe_2O_4$ (x = 0.0, 0.1, 0.3, 0.5) under investigation shows that the samples have single phase cubic spinel structure. The figure 1 shows typical XRD pattern for x = 0.1. The Bragg's peaks are sharp and intense. Lattice constant calculated using XRD data increases with increase in cadmium content 'x'. The variation in the lattice constant with cadmium substitution can be explained on the basis of ionic radii of nickel (0.69Å) , copper (0.72Å) and cadmium(0.97 Å) [6].The ionic radii of nickel and copper are very close to each other but ionic radii of cadmium is relatively large hence there is much increment in the lattice constant.

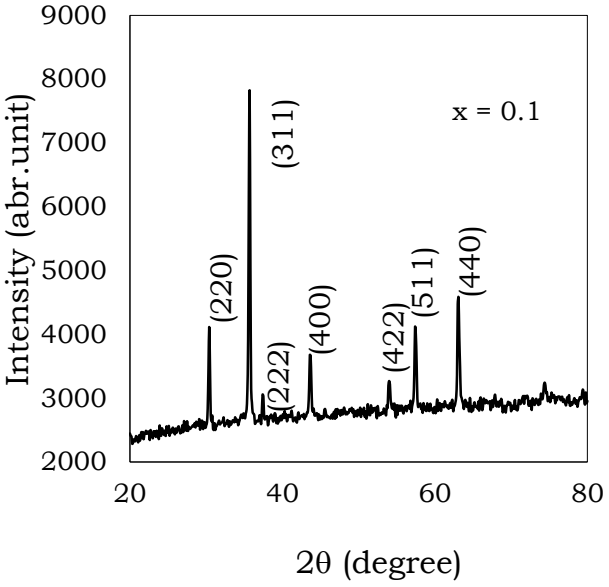

Fig. 1: Typical XRD Pattern of $Ni_{0.5}Cu_{0.5-x}Cd_xFe_2O_4$ (x=0.1)

3.2 Dielectric Constant (ε′)

Variation of dielectric constant (ε′) of $Ni_{0.5}Cu_{0.5-x}Cd_xFe_2O_4$ (x = 0.0, 0.1, 0.3, 0.5) with frequency and cadmium content x is shown in Fig.2. It is observed from Fig.2 that dielectric constant increases with the increase in Cd^{2+} concentration. In Ni–Cu-Cd ferrites, copper ions occupy tetrahedral (A) sites and octahedral [B] sites, cadmium ions occupy tetrahedral (A) sites where as Ni^{2+} ions prefer to go to octahedral [B] sites. Fe^{3+} ions which exist in 2+ as well as in 3+ states, occupy both A and B sites. When Cd^{2+} is added in place of Cu^{2+} ions, some of the Fe^{3+} ions are converted to Fe^{2+} ions to maintain the charge neutrality.

As a result, hopping between Fe^{3+} and Fe^{2+} ions increases hence the resistance of grains decreases. This increases the probability of electrons to reach the grain boundary. Consequently, polarization and dielectric constant increase [7]. The value of ε′ is much higher at lower frequencies.

It decreases with the increase in frequency. At very high frequencies, its value becomes so small that it becomes independent of frequency. Other researchers have also observed similar kind of behavior [8, 9]. The variation in dielectric constant may be explained on the basis of space charge polarization. According to Maxwell and Wagner two-layer model [10, 11], space charge polarization is because of inhomogeneous dielectric structure of the material. It is formed by large number of well conducting grains separated by thin poorly conducting intermediate grain boundaries. The electronic exchange between Fe^{2+} and Fe^{3+} is due to the local movement of electrons in the direction of electric field which determines the polarization in ferrites. Polarization decreases with the rise in frequency and then attains a constant value. It is because of the fact that beyond a certain value of frequency of external field, the electron exchange $Fe^{2+} \leftrightarrow Fe^{3+}$ cannot follow the alternating field [12, 13].

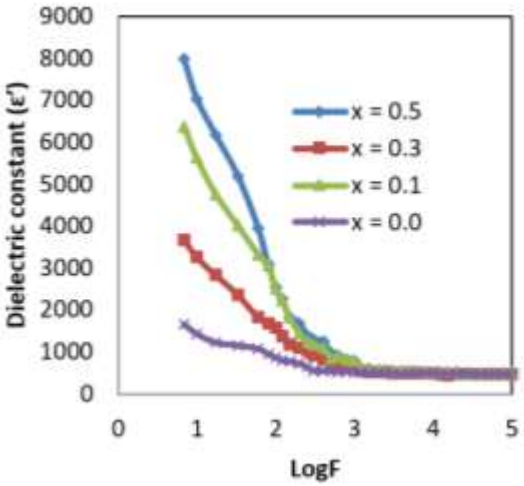

Fig.2: Variation of dielectric constant (ε′) with logarithm of frequency (Log F) of $Ni_{0.5}Cu_{0.5-x}Cd_xFe_2O_4$

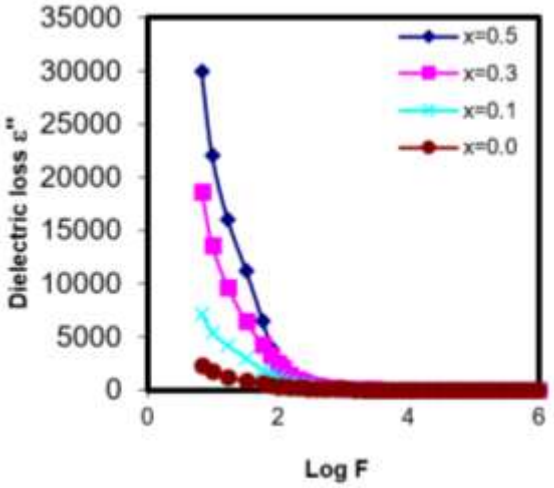

Fig.3: Variation of dielectric loss (ε″) with logarithm of frequency (Log F) of $Ni_{0.5}Cu_{0.5-x}Cd_xFe_2O_4$

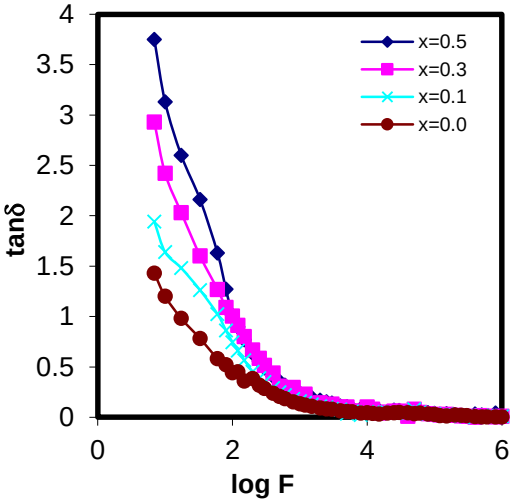

Fig.4: Variation of dielectric loss tangent (tanδ) with logarithm of (Log F) of $Ni_{0.5}Cu_{0.5-x}Cd_xFe_2O_4$

3.3 Dielectric Loss (ε″)

The variation of dielectric loss (ε″) is shown in **Fig. 3**. The variation of dielectric loss (ε″) with frequency can be explained on the basis of dispersion due to the Maxwell–Wagner interfacial polarization with Koop's phenomenological theory [14]. Dielectric loss decreases with the increase of frequency. It is because of decrease in polarization with the increase in frequency. Ultimately, it reaches a constant value. Other researchers [15] have quoted a similar kind of trend with the change in frequency. Rabinkin and Novikova [16] pointed out that polarization in ferrites is similar to that of conduction. The electron exchange between $Fe^{2+} \leftrightarrow Fe^{3+}$ results the local displacement of electrons in

the direction of the applied field that determines the polarization. Polarization decreases with the increase in value of frequency and then reaches a constant value. Dielectric loss (ε″) has large value at lower frequency. It is because of the predominance of species like Fe^{2+} ions, oxygen vacancies, grain boundary defects, interfacial dislocation pile-ups, voids, etc. [14- 17]. The decreasing trend in (ε″) with the increase in frequency is natural due to the fact that any species contributing to polarizability is found to show lagging behind the applied field at higher frequencies [7].

3.4 Dielectric Loss Tangent (Tanδ)

The values of tanδ depend on a number of factors such as stoichiometry, Fe^{2+} content and structural homogeneity, which in turn depend on the composition and sintering temperature of the samples [18, 19]. The variation of dielectric loss tangent (tanδ) is shown in **Fig. 4.** The initial decrease of tanδ with an increase in frequency may also be explained on the basis of Koop's phenomenological model [15]. Table 1 shows comparison of dielectric constant (ε′), dielectric loss (ε″) and dielectric loss tangent (tanδ) at room temperature at 100 Hz, and 1 MHz frequencies for $Ni_{0.5}Cu_{0.5-x}Cd_xFe_2O_4$ system. It revealed from Table 1 that dielectric constant, dielectric loss and dielectric loss tangent increases with cadmium content and decreases with frequency.

Table: 1 Room temperature dielectric constant (ε′), dielectric loss (ε″) and dielectric loss tangent (tan**δ)** at100 Hz and 1 MHz of $Ni_{0.5}Cu_{0.5-x}Cd_xFe_2O_4$

x	Frequency					
	100 (Hz)			1(MHz)		
	ε′	**ε″**	tan**δ**	**ε′**	**ε″**	tan**δ**
0.0	862	379	0.44	494	0.64	0.0013
0.1	1557	1161	0.77	495	3.80	0.0070
0.3	2513	2517	1.00	521	3.89	0.0079
0.5	3214	4500	1.15	580	4.56	0.0098

4. CONCLUSIONS

1. Single phase cubic spinel structured samples of $Ni_{0.5}Cu_{0.5-x}Cd_xFe_2O_4$were obtained successfully using ceramic technique.
2. Substitution of (Cd^{2+}) ions increases the dielectric parameters of the system.
3. The values of dielectric parameters (ε′,ε″and tanδ) are high at low frequencies but decreases with increase in frequency.

REFERENCES

[1]. P. P. Hankare, S.D. Jadhav, U.B. Sankpal. S.S. Chavan, K.J.Waghmare,B.K. Chougule, J. Alloys and Compounds 475 (2009) 926

[2]. D. G. Mitchell, J. Magn. Reson. Imaging,7 (1997) 1

[3]. E. V. Shevchenko, D.V. Talapin, A.J. Rogach, A. Kornowski, M. Haase, H. Weller J. Am. Chem. Soc. 124 (38) (2002) 11480

[4]. M. H. Kryder, MRS Bull. 21 (9) (1996) 17.

[5]. D. Ravinder, SrinivasaRao,P. Shalini Mater.Lett. 57 (2003) 4040.

[6]. A. M. Sankpal, S. R. Sawant, A. S. Vaingankar, I. S. Pure, App. Phys. 26(1988) 459.

[7]. A. K. Singh, T. C. Goel, R. G. Mendiratta, J. Appl. Phys. 91 (2002) 6626.

[8]. R. Manjula, V. R. K. Murthy, J. Sobhanadri, J. Appl. Phys. 59 (1986) 2929.

[9]. K. Deepika, P. Sumitra, J. S. Baijal, J.Mater. Sci. 25 (1990) 5142.

[10]. J. C. Maxwell, Electricity and Magnetism, vol. 1, Oxford University Press, 1929 (section 328).

[11]. K. W. Wagner, Ann. Phys. 40 (1913) 817.

[12]. R. G. Kharabe, R. S. Devan, C. M. Kanamadi, B. K. Chougule, Smart Mater. Struct. 15 (2006) N36.
[13]. C. F. Jafferson, C. K. Baker, IEEE Trans. Magn. 4 (1968) 460
[14]. C. G. Koops, Phys. Rev. 83 (1951) 121.
[15]. A. M. Shaikh, S. S. Bellad, B. K. Chougule,J. Magn. Magn. Mater.195 (1999) 384.
[16]. I. T. Rabinkin, Z. I. Novikova, Ferrites, Izv Acad, Nauk USSR Minsk, 1960, p. 146.
[17]. J. C. Maxwell, Electricity and Magnetism, vol. 2, Oxford University Press, New York, 1973, p. 828.
[18]. S.S. Shinde and K. M. Jadhav, J. Mat. Lett.1998)63
[19]. S. F. Mansour, Egypt. J. Solids 28 (2) (2005) 263.

*****

Sol-Gel based Low Temperature Synthesis of Tin Oxide Nanoparticles for photo-electrochemical Solar Cells

Dr. Sambhaji S. Bhande

Department of Physics, Baburaoji Adaskar Mahavidyalaya, kaij. Dist. Beed, Maharashtra, India.
Email: *sambhajibhande@gmail.com*

ABSTRACT

The tin chloride precursor initiated sol-gel chemical method for synthesizing tin oxide (SnO_2) nanoparticles electrode is envisaged in dye-sensitized solar cells. Three steps; synthesis of nanoparticles, formation of paste using suitable surfactants and film development using doctor-blade method, are adopted for obtaining SnO_2 electrode. The films of SnO_2 nanoparticles formed onto glass and indium-tin-oxide substrates are annealed at 450 °C for 3 h. Influence of indium-tin-oxide on the structural elucidation, morphological evaluation, grain size confirmation and Raman shift analysis of the SnO_2 nanoparticles is eliminated by considering glass as the depositing substrate. Enhanced light absorbance at 500 nm due to the N719 dye molecules adsorption compared to pristine SnO_2 electrode has showed 1.62% solar-to-electrical conversion efficiency.

Keywords: *Photo-electrochemical Cells, Sol-gel, Tin Oxide, DSSCs.*

1. INTRODUCTION

Since the achievement of a solar to electrical energy conversion efficiency of over 11% achieved using a nano-crystalline TiO_2 electrode [1], large band gap semiconducting materials are enormously under investigation for their possible applications in dye-sensitized solar cells (DSSCs). The large band gap materials include TiO_2, SnO_2, WO_3, MgO, ZnO, Nb_2O_5, etc. [2, 3].

The tin oxide (SnO_2) is a chronic candidate when these semiconducting metal oxides are considered. Large surface area SnO_2 has many advantages including a faster rate of electron interception by the redox electrolyte, higher electronic mobility, low sensitivity to UV degradation due to its larger band gap and hence the better long-term stability [4], etc. Moreover, the lower conduction band edge (more positively located) position of SnO_2 facilitates the high efficiency of electron injections from the adsorbed dye molecules [5]. Along with these interesting properties several applications such as good adhesion to many polycrystalline and amorphous substrates including glasses, metals and oxides for the use of polycrystalline SnO_2 as transparent electrodes and thin film solid state gas sensor for different gases with high sensitivity, photovoltaic devices, transparent conductive films for display and solar cells, catalysis, and anode materials of secondary lithium ion battery etc., of SnO_2 have been numerously documented in the literature [6-11]. Several chemical and physical methods including chemical vapor deposition, chemical bath deposition, electro-deposition, high temperature thermal deposition, molten salt synthesis, laser ablation, dc and rf -sputtering etc. for synthesizing SnO_2 nanostructures including nanoparticles, nanoribbons, nanorods, nanowires and nanotubes etc. [11-15] are preferred as on today [16-21]. Implication of SnO_2 nanoparticles in DSSCs is limited by its open circuit voltage (V_{oc}), less than 400 mV [22] making it

less attractive compared to TiO_2 and ZnO semiconductors. Conventional nanoparticles of SnO_2 have produced comparatively small conversion efficiencies of around 1–2% because of the inherent low conduction band edge and the fast recombination process [23].

In the present study, porous SnO_2 nanoparticles were procured from a simple, cost effective and low temperature sol-gel method. Two substrates viz. glass and ITO were preferred for avoiding confusion of results between SnO_2 nanoparticles film and ITO substrate. To avoid ITO substrate contamination the film of SnO_2 nanoparticles onto glass substrate was preferred for structural elucidation, morphological evolution and Raman shift analysis. For grain-size identification SnO_2 powder was scratched from the glass substrate and then mounted on the copper grid using fine-tipped syringe with acetone as a solvent. Change in absorbance, due to N719 dye molecules loading, was confirmed from an optical absorbance studies. The elemental chemical analysis was carried out from the energy dispersive X-ray (EDX) analysis. Prior to DSSCs use, the SnO_2 electrode was dipped in N719 dye for 3 h followed by acetonitrile rinsing. The current density-applied voltage (J-V) measurement of SnO_2 electrode of about two micrometer thickness and 0.25 cm^2 area was employed using 100 mW/cm^2 light intensity which was controlled with Si diode.

.

2. MATERIALS AND METHODS

Preparation of SnO_2 nanoparticles films onto glass and ITO substrates was divided into three parts; (a) synthesis of nanoparticles powder using sol-gel method, (b) formation of homogeneous paste followed by doctor blading scotch tape of two micron thickness, and (c) step-wise annealing in auto-controlled oven at 450 °C for 3 hr. All the chemicals were purchased from Sigma-Aldrich and used without further purification. For the synthesis of SnO_2 nanoparticles, initially 0.3 M tin tetrachloride ($SnCl_4$) was taken in ethanol solvent for 100 ml, after dissolving it, 0.6 M thioacetamide was further added to the same solution. The solution was then sealed in a falcon tubes of 100 ml with a magnetic sturrer inserted. The solgel deposition was carried out at 80 ºC for 3 hrs. It must be noted that, if the time period exits above 3 hrs. The SnO_2 starts increase its particle size. The gel thus obtained were washed with ethanol and naturally dried in air and then annealed at 450 ºC for 1 hr.

In second step, 0.5 gm crystalline SnO_2 nanoparticles powder was mixed with polyethylene glycol (0.5 ml), 0.5 ml 10wt% diluted acetyl acetone, one to two drops of triton X-100, 0.5 ml ethanol and 0.5 ml water while continuous stirring. Slurry was mixed well by continues crushing in the mortar. The viscosity of the paste was controlled by ethanol and water followed by doctor-blading onto normal and ITO coated glass substrates using two micrometer thickness scotch tape. These prepared samples were annealed at 500ºC for 1hr for crystallinity improvement. Prior to characterizations these samples were cooled naturally to room temperature.

3. RESULTS AND DISCUSSION

Fig. 1 shows the XRD spectrum with intense and distinct peaks of SnO_2 nanoparticles film deposited onto glass substrate. Observed reflection peaks were coppered with JCPDS (41-1445), and confirmed the presence of pure crystalline SnO_2. No peaks corresponding to tin metal or any other phase as impurity peaks were identified. The obtained peaks were with characteristic diffraction peaks of SnO_2 corresponding to (110), (101), (200), (111), (211), (220), (002), (310), (112), (301), (202), and (321) reflection planes. The grain size calculated from (110) peak was ~ 15 nm which later was confirmed from the high resolution transmission electron microscopy (HR-TEM) analysis fringes. Surface morphological evolution was confirmed from the SEM images recorded at different magnifications [**Fig. 1 b**]. The identical SnO_2 spherical nanoparticles were seen in both photo-images. This morphology would be interesting for DSSCs due to its larger surface area and relatively smaller crystallite size. The calculated grain size of the SnO_2 nanoparticles was comparable to Debye length which can occupy the space charge region of SnO_2 completely by controlling its band structure [24]. Thus, the charge transportation should be easy which would reduce the charge recombination rate to

great extent. The highly porous nature on its surface generally allows maximum dye adsorption for efficient solar-to-electricity conversion by maximum light harvesting. The EDX study of SnO_2 nanoparticles onto glass substrate was carried out for Sn and O elements. The wt. % ratio of Sn and O was 57:33, confirming the formation of stoichiometric SnO_2 using this method.

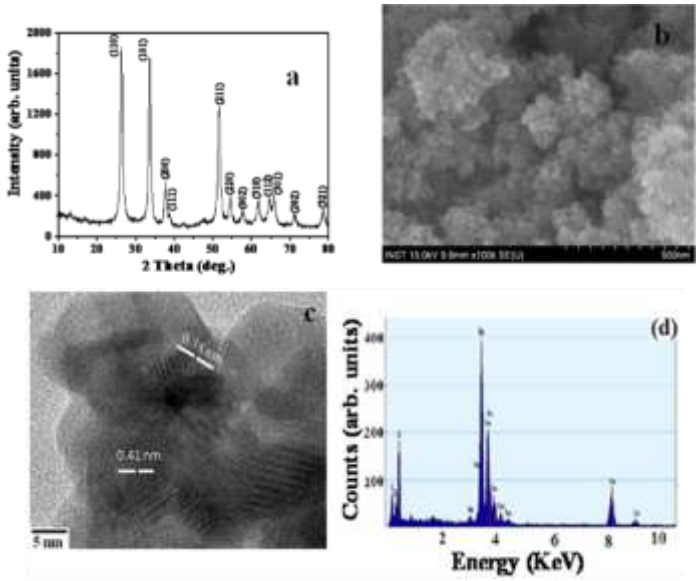

Fig.1.a: XRD pattern of SnO_2 b) SEM analysis c) TEM d) EDAX

In Fig. 1 (c) HR-TEM images of SnO_2 nanoparticles are also presented. Spherical nanoparticles of SnO_2, consistent to the SEM images, were identical. Nearly 50 nanometer area was considered for obtaining the reflection fringes. Presence of spotted-lines instead of points or continuous lines has proved the nanostructure of SnO_2. The calculated inter planar 0.41 and 0.39 nm spacing's were closely matched to inter planar spacing's of (110) and (101) reflection planes (0.411 and 0.391 nm), respectively, of SnO_2. Unclear but uniform reflection circles are due to Nano crystalline form of SnO_2 as for amorphous metal oxides fuzzy pattern is dominant whereas, dis distinct regular spots are seen in crystalline metal oxides. The EDAX pattern (**Fig.1-d**) recorded while TEM analysis has confirmed existence of Sn and O in 56 and 34 wt% ratio.

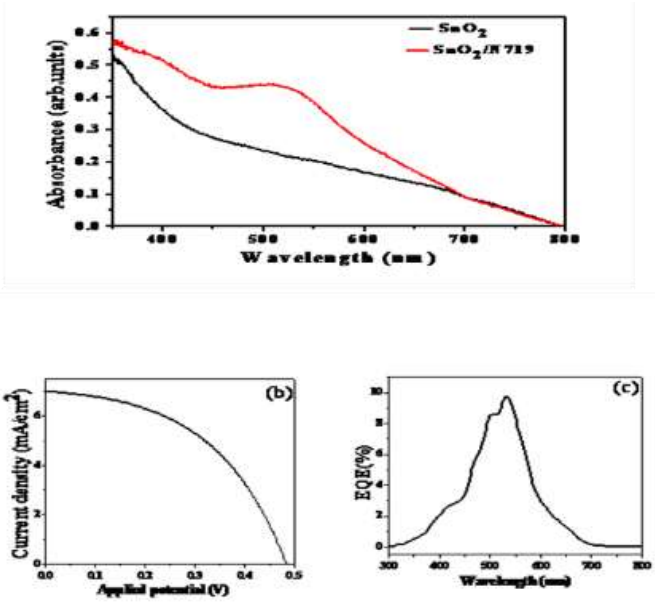

Fig. 2: UV -Vis spectra b) JV curve c) IPCE curve

The UV-visible absorbance spectrum was carried out in order to study optical behavior of the SnO_2 electrode as the quantum confinement effect is expected if the semiconductor dimensions become smaller than the Bohr radius of the exciting, and the absorbance edge will be shifted to the

higher energy [25]. The absorbance spectrum of pristine SnO_2 electrode and SnO_2 electrode after the dye loading was taken for the analysis. The absorbance edge in case of Pristine SnO_2 electrode is 515 nm whereas the electrode with N719 dye loaded on its surface shows the absorbance edge at 655 nm and 695 nm, respectively (**Fig.2-a**).

The *J-V* measurement of the SnO_2 nanoparticles-N719 electrode, prepared by the sol-gel method, was tested for DSSCs application (Figure 2b). For the measurement, an electrolyte solution consisting of 15 mL iodide-tri-iodide solution was used. Obtained V_{oc} in the present case was superior to that of 150 mV reported earlier [26]. The uniformly distributed spherical SnO_2 nanoparticles could be responsible for 1.62% conversion efficiency, which is competitive to ZnO nanostructures [27, 28], one of the widely used metal oxides so far. The SnO_2 nanoparticles electrode with fill factor (*FF=0.48*), current density (J_{sc}=6.94), mA/cm^2, and (V_{oc}=0.47 V) was certainly inevitable. This is attributed to porous and nanocrystalline texture of SnO_2. High surface area and porous nature of SnO_2 nanoparticles must be responsible for efficient dye molecules absorbance followed moderate solar-to-electricity conversion efficiency. Contrary, in spite of high current density, IPCE (Figure 2c) value was close to 10, indicating that there was dominant recombination either at dye/electrolyte or conduction band of SnO_2 (-4.0 vs Normal hydrogen Electrode)/electrolyte interfaces. By surface engineering monitoring [29] or by using dyes of higher extinction coefficients [30, 31] SnO_2 nanoparticles device performance can be increased, which is underway.

4. CONCLUSION

Using sol-gel and doctor blade methods two micrometer thick SnO_2 nanoparticles electrodes were prepared onto glass and indium-tin-oxide substrates and explored for structural, optical and morphological properties and used in DSSCs application. The 57:33 stoichiometry, confirming the formation of SnO_2, for Sn and O elements was obtained from the EDX analysis. Phase confirmation was also carried out by X-ray diffraction. In spite of weak IPCE value, solar-to-electrical conversion efficiency of 1.66% was obtained due enhanced optical absorbance caused by N719 dye molecules adsorption onto SnO_2 nanoparticles. The IPCE value can be increased either by surface engineering monitoring or by using dyes of higher extinction coefficients, which is underway.

REFERENCES

[1]. M. Gratzel, (2004) Conversion of sunlight to electric power by nanocrystalline dyesensitized solar cells. J Photochem Photobiol A: Chem 164, 3-14.

[2]. D. Kuang, Je´ re´mie Brillet, P. Chen, M. Takata, S. Uchida, H. Miura, K. Sumioka, M.Z. Shaik, M. Gratzel, (2008) Application of Highly Ordered TiO_2 Nanotube Arrays in Flexible Dye-Sensitized Solar Cells. ACS nano 2, 1113-1116.

[3]. A. Zaban, S.G. Chen, S. Chappel, B.A. Gregg, (2000) Nanoporous Electrodes for Dye Sensitized Solar Cells. Chem Commun 22, 2231– 2232.

[4]. S. Gubbala, V. Chakrapani, V. Kumar, M.K. Sunkara, (2008) Band-Edge Engineered Hybrid Structures for Dye-Sensitized Solar Cells Based on SnO_2 Nanowires. Adv. Funct. Mater 18, 2411-2418.

[5]. K. Hara, T. Sato, R. Katoh, A. Furube, Y. Ohga, A. Shinpo, S. Suga, K. Sayama, H. Sugihara, H. Arakawa, (2003) Molecular Design of Coumarin Dyes for Efficient Dye-Sensitized Solar Cells. J Phys Chem B 107 597-606.

[6]. Z. Li, H. Wang, P. Liu, B. Zhao, Y. Zhang (2009) Synthesis and field-emission of aligned SnO_2 nanotubes arrays. Appl Surf Sci 255 4470-4473.

[7]. Y. Liu, M. Liu,(2005) Growth of Aligned Square-Shaped SnO_2 Tube Arrays.Adv Funct Mater 15,57-62.

[8]. Y.J. Ma, F. Zhou, L. Lu, Z. Zhang, (2004) Low-temperature transport properties of individual SnO_2 nanowires. Solid State Commun. 130, 313-316.

[9]. Z.R. Dai, Z.W. Pan, Z.L. Wang, (2001) Ultra-long Single Crystalline Nanoribbon of Tin Oxide. Solid State Commun 118, 351-354.

[10]. Z.R. Dai, J.L. Gole, J.D. Stout, Z.L. Wang, (2002) Tin Oxide Nanowires, Nanoribbons, and Nanotubes. J Phys Chem B 106, 1274-1279.

[11]. X. Jiang, Y. Wang, T. Herricks, Y. Xia, (2004) Ethyledne Glycol-Mediated Synthesis of Metal Oxide Nanowires. Mater Chem 14, 695-703.

[12]. Y. Liu, C. Zheng, W. Wang, C. Yin, G. Wang, (2001)Synthesis and Characterization of Rutile SnO_2 Nanorods. Adv Mater 13, 1883-1887.

[13]. R.S. Dale, C.S. Rastomjee, F.H. Potter, R.G. Egdell, (1993) Sb and Bi implanted SnO_2 thin films: photoemission studies and application as gas sensors. Appl Surf Sci 70/71, 359-362.

[14]. A. Martel, F.C. Briones, J. Fandino, R.C. Rodriguez, P.B. Perez, A.Z. Navarro, M.Z. Torres, J.L. Pena, (1999) Chemical and phase composition of SnOx:F films grown by DC reactive sputtering. Surf Coat Technol 122, 136-142.

[15]. P. Thangadurai,A.C. Bose, S. Ramasamy, R. Kesavamoorthy, T.R. Ravindran, (2005)High Pressure effects on electrical resistivity and dielectric properties of nanocrystalline SnO_2, J. Phys. and Chem. of Solids. 66, 1621-1627.

[16]. J.A.T. Antonio, R.G. Baez, P.J.Sebastian, A.J. Vàzquez, (2003)Thermal stability and structural deformation of rutile SnO_2 nanoparticles. J. Solid State Chem 174, 241-248.

[17]. F. Legendre, S. Poissonnet, P. Bonnailie, (2007) Synthesis of nanostructured SnO_2 materials by reactive ball-milling. J Alloys Compd 434, 400-404.

[18]. F. Gu, S.F. Wang, M.K. Lü, X.F. Cheng, S.W. Liu, G.J. Zhou, D. Xu, D.R. Yuan, (2004) Luminescence of SnO_2 thin films prepared by spin-coating method. J Cryst Growth 262, 182-185.

[19]. W. Kim, S.H. Shim, (2006)Synthesis and characteristics of SnO_2 needle-shaped nanostructures, J Alloys and Compd 426, 286-289.

[20]. S. Chappel, A. Zaban, (2002)Nanoporous SnO_2 electrodes for dye-sensitized solar cells:improved cell performance by the synthesis of 18 nm SnO_2 colloids. Sol Energy Mater Sol Cells 71, 141-152.

[21]. K. Sayama, H. Sugihara, H. Arakawa. (1998) Photoelectrochemical properties of a porous Nb_2O_5 electrode sensitized by a ruthenium dye. Chem Mater 10, 3825-3832.

[22]. Y. Fukai, Y. Kondo, S. Mori, E. Suzuki, (2007) Highly efficient dye-sensitized SnO_2 solar cells having sufficient electron diffusion length. Electrochem Commun 9, 1439-1443.

[23]. J.h. Lee, N.G. Park, Y.J. Shin, (2011) Nano-grain SnO_2 electrodes for high conversion efficiency SnO_2–DSSC. Sol Engy Mater sol Cells 95, 179-183.

[24]. N. Yamazoe, (1991) New approaches for improving semiconductor gas sensors. Sens Actuators B Chem 5, 7-19.

[25]. V.G. Kravets, (2007) Photoluminescence and Raman spectra of SnO_x nanostructures doped with Sm ions, Opt Spectrosc 103, 766-771.

[26]. S. Gubbala, V. Chakrapani, V. Kumar, M.K. Sunkara, (2008) Band-edge engineered hybrid structures for dye-sensitized solar cells based on SnO_2 nanowires. Adv Funct Mater 8, 12411-2418.

[27]. M. Kruk, M. Jaroniec, (2001) Gas adsorption characterization of ordered organic inorganic nanocomposite materials. Chem Mater 1, 3169-3183.

[28]. A. Umar, A.A. Hajry, Y.B. Hahn, D.H. Kim, (2009) Rapid synthesis and dye sensitized solar cell applications of hexagonal-shaped ZnO nanorods. Electrochimica Acta 54 5358-5362.

[29]. C. Prasittichai, J.T. Hupp, (2010) Surface modification of SnO_2 photoelectrodes in dyesensitized solar cells: Significant improvements in photovoltage via Al_2O_3 atomic layer deposition. J Phys Chem Lett 1, 1611-1615.

[30]. M. I. Baraton, (2001) FTIR spectrometry as a quality control method for surface engineering of nanomaterials. Mater Res Soc Proc 636, D811-D8110.

[31]. D. Kuang, C. Klein, S. Ito, J.E. Moser, R.H. Baker, S.M. Zakeeruddin, M. Gratzel, (2007) High molar extinction coefficient Ion-coordinating Ruthenium sensitizer for efficient and stable mesoscopic dye sensitized solar cells. Adv. Func. Mater. 17, 154-160.

***

ISBN: 978-81-970491-8-7
7
Current Research in
Science and Technology
(An Edited Book)

Recent Reports on Biologically Active Pyridoxal Derived Schiff Base Complexes

Samik Gupta

Department of Chemistry, Sambhu Nath College, Labpur, Birbhum. West Bengal, PIN- 731303
Email: *samikgpt@gmail.com*

ABSTRACT

Ever since the role of vitamin B6 has been established as cofactor of a range of enzymes, Schiff base complex of one of its vitamers, the pyridoxal (or its phosphorylated derivative) are being studied with increased interest in order to gain better understanding of its bio-significance. In recent years pyridoxal derived complexes are finding use in a wide variety of biological processes and therapeutics fueled by their good bio-availability.

Keywords: *Pyridoxal, Vitamin B6, Schiff base, metal complex, biological activity*

1. INTRODUCTION

Vitamin B6 is the only vitamin essential for the metabolism of vital nutrients like protein, fat and carbohydrate in many organisms. It exists as six vitamers which are water soluble. These are pyridoxine, pyridoxal, pyridoxamine and their 5-phosphate derivatives. The activity of 5-phosphorylated pyridoxal (PLP) as a coenzyme is well established [1]. The transamination, decarboxylation and racemization reactions catalyzed by enzymes in which PLP exist as coenzyme depends strongly on the aldehyde group of the PLP molecule. Snell and coworkers had earlier discovered a non-enzymatic trans-amination reaction between topyridoxaland certain amino acids leading pyridoxal amine [2]. Subsequently, they also demonstrated that rates of these non-enzymatic trans-amination reactions could be increased by involving metal ions like Cu (II), Al (III) or Fe (III) in water at a near neutral pH[3]. This observation signaled at the possibility of formation of a Schiff base during the reaction and the catalytic role of a Schiff base metal complex formed in-situ in these reactions. Very recently, Tanaka and coworkers has shown that an enzyme serine dehydrates which has PLP as a coenzyme involves coordinated zinc in a catalytic reaction [4].

Therapeutic use of Vitamin B6 in rheumatoid Arthritis, Parkinson's disease and lead poisoning [5, 6, 7] has been established. It also functions as an antioxidant in fungi [8]. Deficiency of Vit B6 may lead to colorectal cancer [9]. There has been a large volume of research on the pyridoxal derived Schiff base complexes of transition metal as these complexes give important insight as to how PLP containing enzymes work inside the body as well as their structural features. Pyridoxal, being a biocompatible molecule, its Schiff base complexes are often appreciably water soluble and shows a variety of biological activities. These complexes have been studied for mimicking enzymes like peroxidase, superoxide dismutase and phosphatase inhibitor. Interaction with DNA has also been studied by several research groups. Their cytotoxicity to different human cancer cell lines have shown promising results. These complexes also had antimicrobial and antioxidant properties. In this review we have concentrated on the biological activity of recently published pyridoxal based Schiff base complexes. I have tried to incorporate reports under each of these categories to the best of our ability.

2. RESULTS AND DISCUSION

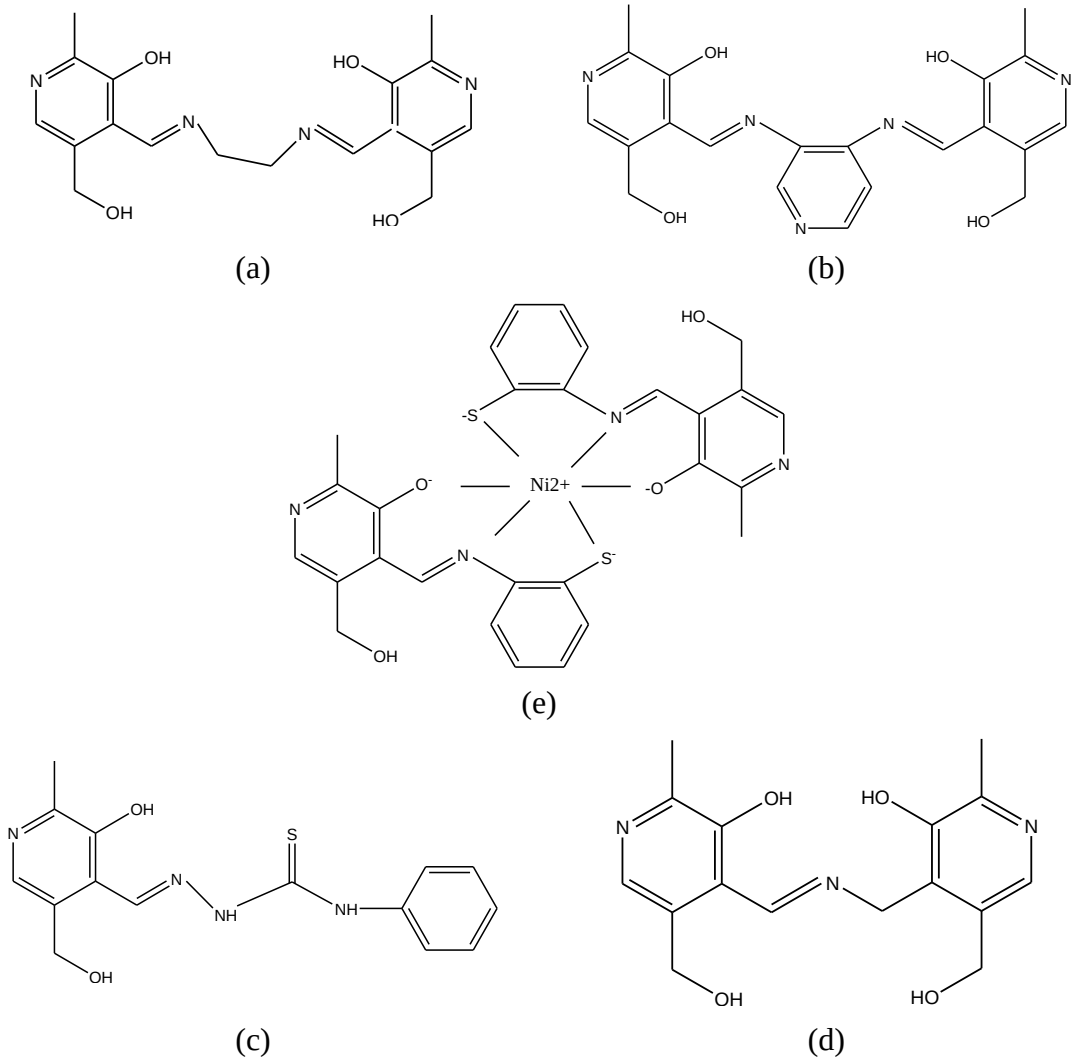

Fig. 1: (a) ligand used for the preparation of complex 1 (b) ligand used for the preparation of complex 16, (c) ligand used for the preparation of complex 22, (d) ligand used for the preparation of complexes 84-88, (e) representative structure of the anionic complex 89.

2.1. SOD mimetic property

Sandra Signorella and coworkers prepared a series of pyridoxal derived Schiff bases with ethylene diamine, propylene diamine and butylene diamine. The bis- Schiff base ligands produced this way were named as H_2pyr_2en, H_2pyr_2pn and H_2pyr_2bn and their Mn (II) complexes (1-4) were studied for SOD activity. Complexes were able to catalyze the dismutation of superoxide efficiently with IC_{50} values in the range of 1.22–2.15 μM, as measured by the NBT photo-reduction inhibition superoxide dismutase assay, in water solution at pH 7.8. The length of the alkyl chain in the diamine portion of ligand plays an important role in the antioxidant activity of these complexes, with $[Mn(pyr_2pn)(H_2O)_2]ClO_4$(3) showing the lowest IC_{50} value [10].

A series of Cu (II) complexes (5-9) of Schiff base prepared from pyridoxal and aromatic o- halo amines were tested for SOD mimetic property in the same manner as the earlier set.One of the complexes showed an expressive IC_{50} of 0.4 μM. In addition, catecholase-like activity and cleavage of plasmid DNA were also evaluated. The complex bearing iodine substituent with the amine ligand gave the best results [11].

Reaction of pyridoxal with tris(2-aminoethyl) amine, the tripodal amine, yielded a tripodal Schiff base ligand, its subsequent complexation with the manganese(II)(12) was studied by Patrícia

Regina Ebani and coworkers. This complex was also found to catalyze the dismutation of superoxide efficiently with IC_{50} equal to 3.38 μM, by standard NBT photo-reduction inhibition superoxide dismutase assay in water solution of pH 7.8 [12].

2.2. Phosphatase and phosphatase inhibitor property

Senjuti Mondal and coworkers reported a complex (11) which has shown positive response for phosphatase activity towards 4-NPP (4-NPP=N-Phenethyl-4-piperidinone) substrate.[13]. In order to evaluate the potential of the two dioxidovanadium(V) complexes as protein tyrosine phosphatase inhibitors, one a pyridoxal and other a resorcinol based Schiff base complex(14,15), they were tested towards a panel of tyrosine phosphatases of single concentration of 25 μM. The pNPP hydrolysis by the phosphatases were measured at pH 7.0 and 37°C.The former complex inhibited more than 70% of PtpB, YopH and PTP1B activity, but had no effect against PtpA, PTP-PEST and LYP, under these conditions. Conversely, the latter complex showed a lower inhibition of PTPs activity, inhibiting less than 40% of enzyme activity as reported by Josieli D. Siqueira [14]

2.3. Antibacterial and anti-microbial activity

Pseudomonus aeruginosa bacterial infection may cause pneumonia and septic shock in human beings. The virulence of such an infection is controlled by a quorum sensing regulatory system. A pyridoxal lactohydrazone Schiff base was found to be effective in inhibiting quorum sensing related virulence factor of the bacteria [15].

Schiff base ligand prepared from pyridoxal and 3, 4-diaminopyridine was used as a tetradendate ligand in dianionic form to prepare Cu (II) and Zn(II) complexes(16,17) . The structure of the complexes was explored using spectral and density functional theory calculations. The Schiff base and the complexes were found to have antibacterial properties [16]. Schiff base prepared by pyridoxal and 4-amino pyridine an used as a bidentate ligand to prepare complexes Mn(II), Cu(II) and Zn(II) (18, 19, 20). These complexes were studied for antibacterial activity [17]

2.4. DNA binding and molecular docking properties

Rajendran Manikandan and coworkers found that substitution (CH_3 or C_6H_5) on terminal N(4)-nitrogen of thiosemicarbazone had an influence on the potential binding and cleavage ability with DNA and binding of BSA (bovine serum albumin)(21,22)[18].Tirtha Mukherjee and coworkers studied a few first transition metal complexes which were found to be classical grove binders to DNA and also got bound to HSA(human serum albumin)(23, 24, 25)[19].Another set of Cu(II) complexes (26-30)were found to be good binders to DNA and HSA[20]

A ligand prepared from pyridoxal and p- nitro benzyl ethylene diamine, which is optically active in nature, was employed for preparation of a oxovanadium (IV) complex(31).This complex was found to be able to cleave the supercoiled plasmid DNA, pBR322 DNA. This was also observed that the oxovanadium (IV) complex performed better than $VOSO_4$ in its DNA cleavage property[21].

In keeping with the recent developments in metallo-pharmaceuticals, vanadium complexes of Schiff base ligands derived from p-substituted aromatic benzohydrazides (OH, CH_3, H, NO_2, and NH_2) and pyridoxal hydrochloride were prepared (32-36). For therapeutic application, the complexes must be able to bind with DNA and HSA. The molecular docking studies were performed on these five complexes for their interactions with calf thymus deoxyribonucleic acid and human serum albumin by spectroscopic assays and molecular docking calculations [22].

Ni(II) nitrate complexes with pyridoxal-semi, thiosemi, and isothiosemicarbazone ligands ($[Ni(PLSC)(H_2O)_3]\cdot 2NO_3^-$, $[Ni(PLTSC)_2]\cdot 2NO_3^- \cdot H_2O$, and $[Ni(PLITSC)(H_2O)_3]\cdot 2NO_3^-$) (37-39) were prepared and Human Serum Albumin (HSA) and the DNA-binding properties of these complex cations were measured by molecular docking simulations. It was observed that the presence of water molecules and various substituents affects the thermodynamics of the processes [23].

2.5. Cytotoxicity studies

Photocytotoxicity in visible light for Copper (II) pyridoxal Schiff base complexes $[Cu(L_1/L_2)(B)]ClO_4$((40-43)). Here HL_1 is 4-(((2-(1H-imidazol-4-yl)ethyl)imino)methyl)-5-

(hydroxymethyl)-2-methylpyridin-3-ol (in 40,41), HL_2 is 2-(((2-(1H-imidazol-4-yl)ethyl)imino) methyl) Phenol (in 42, 43), B is 11-(9-acridinyl)dipyrido[3,2-a:2′,3′-c]phenazine (acdppz) (in 40 and 42), dipyrido [3,2-a:2′,3′-c]phenazine (in 41) and 1,10-phenanthroline (in 43). Among these complexes Phenol ligated complexes showed significant photocytotoxicity in visible light for HeLa and MCF7 cells reaching IC_{50} value of <0.6 μM, while being relatively non-toxic in dark[24].Another set of Cu(II) complexes(44-49) were good binders to DNA and HSA ad were cytotoxic towards MCF-7 breast and CF prostate cancer cell lines as well[25].

Iron(III) complexes of Schiff bases prepared from dipicolylamines and pyridoxal or salicylaldehyde, namely, $[Fe(B)(L)](NO_3)$ (50-54), where B is phbpa in 50, anbpa in 51, 53 and pybpa in 52,54(H_2L^1 is3-hydroxy-5-(hydroxymethyl)-4-(((2-hydroxyphenyl)imino)methyl)-2-methyl pyridine and H_2L^2 is 2-[(2-hydroxyphenyl-imino)methyl]phenol), were prepared and their uptake in cancer cells and photocytotoxicity were studied in a publication in Inorganic chemistry. Complexes 51 and 52 showed photo-cytotoxicity in a remarkable way in various cancer cells with IC_{50} values of 0.4 to 5 μM. The cytotoxicity in dark was 10 fold lower. Light exposure caused formation of reactive oxygen species.The cell death progressed through apoptotic pathway The non-vitamin complexes 53 and 54 were comparatively much lower cytotoxic (3-fold lower photo cytotoxicity) than vitamin B6 counterparts, possibly due to faster uptake of the vitamin B6 based complexes inside the cancer cells. Complexes 51 and 52 show significant uptake in the endoplasmic reticulum, while complexes 53 and 54 are distributed throughout the cells without any specific localization pattern [26]. Penta coordinated diorganotin(IV) complexes(55-68) derived from pyridoxal hydrochloride and 4- or 5-*R*-substituted *ortho*-aminophenols were prepared and cytotoxic activity of all complexes against human cell lines U-251 (glioblastoma), K-562 (chronic myelogenous leukemia), HCT-15 (human colorectal cancer), MCF-7 (human breast cancer) and SKLU-1 (non-small-cell lung cancer) were evaluated. The inhibitory percentage values indicated better activity than standard chemotherapeutic drug cisplatin[27].A Vanadium (IV) complex $Pyr_2enV(IV)$ (69) evaluated for cytotoxicity was able to induce 93% and 57% of cell mortality in A375 (human melanoma) and A549 (human lung carcinoma) cells, respectively; the mortality was <24% in other studied cell lines and in human normal epidermal keratinocytes, lung cells and peripheral blood mononuclear cells[28].Cu(II) complexes with pyridoxal *S*-allyl dithiocarbazate and pyridoxal thiosemicarbazones were prepared and one of them studied for cytotoxicity(70-74). The Hoechst 33342/PI dual-staining assay showed the typical apoptotic morphology of cancer cells, and the RT-qPCR analysis revealed that the expressions of *Bax*, *Casp3*, *Casp8*, *Casp9* and *TP53* were markedly increased in both the Ehrlich and S-180 cells exposed to 10 μMcomplex for 3 h. According to these results, this complex induces cell death through apoptosis, showing potential as a future drug against cancer [29].

Four vanadium complexes (75-78) and a molybdenum complex (79) of pyridoxal hyrdrazone ligand were evaluated for cytotoxicity against lung cancer cell line (A549 cell line). It was found that after 48 hours 77 had the lowest IC_{50} value, 65.32 ± 9.95 μM and compound 78 had the highest value. (75.28±32.09μM).In-vivo studies in the zebrafish model was performed on compounds 77, 78 and 79 revealed that the molybdenum complex showed higher toxic effects than the others [30].

Fe, Co, Ni, Cu complex es of pyridoxalthiosemicarbazide (80-83) were investigated for DNA and BSA binding capacity. The copper complex showed highest interaction with proteins. When cytotoxicity of these complexes were studied with HCT116, A375, MCF-7, A2780, and MCF5 cell lines, it was found that the copper complex induced the highest toxicity[31].

Schiff base (H_2L) obtained by the condensation of pyridoxamine with pyridoxal and its novel copper(II) and oxovanadium(IV) complexes: $[Cu(HL)Cl]$ (84), $[Cu(LH_2)(phen)]Cl_2$ (85), $[Cu(LH_2)(amphen)]Cl_2$ (86), $[V^{IV}O(HL)Cl]$ (87), and $[V^{IV}O(LH_2)(phen)]Cl_2$ (88), (phen= 1,10-phenanthroline and amphen=5-amino 1,10-phenanthroline).The Cu(II) complexes (84 and 85) hindered cell viability of human osteosarcoma cell line (MG-63) (IC_{50} values of 3.6 ± 0.6 and 7 ± 1.9 μM for 84 and 85), while 86 and the $V^{IV}O$ complexes (87,88) had no anticancer property [32].

2.6. Other biological activities

Liniquer Andre Fontana and coworkers examined the peroxidase activity of Ni (II) complexes of Schiff base ligands prepared from pyridoxal] (89-91). With these complexes accelerated reactions, solution stability and high selectivity of the peroxidase mimetic reaction was observed [33]. Antioxidant activity of Vanadium (IV), Mo (VI)/(IV) and Ru (II) complexes (92-98) by DPPH were tested. The results obtained revealed that the scavenging activity of the complexes towards DPPH is high for the oxovanadium (IV) complexes as evident by lower IC_{50} values. The scavenging activity is comparable to ascorbic acid as a standard antioxidant. The EC_{50} concentration ratio together with other antioxidant parameters also support the results[34]
Two series of pyridoxal Schiff base complexes of Co(III) with aniline containing thioether function one is $[Co^{III}(LnC)(L0C)]$ (n = 1–4, 99-102) with a LnC ligand and another ligand formed in-situ (L0C) and the other is $[Co^{III}(LnC)_2]PF_6$ (n = 1–4, 102--105).The complexes were evaluated by in silico calculations on viable biological targets one among them being severe acute respiratory syndrome coronavirus 2 (SARS-CoV-2).Results suggested that all the inorganic complexes under study are potential anticancer/antiviral agents; however, 102 and 105 are the best candidates for future in vitro assays[35].

5. CONCLUSION

Schiff base complexes are generally has appreciable water solubility. Pyridoxal Schiff base ligands bearing the Vitamer performs better in this regard. This is why complexes of these ligands show high bioavailability and hence can be utilized for a range of biological activities. With the understanding obtained about their structure-function relationship, improved structural design of these complexes will lead to more therapeutic application in future.

REFERENCES

[1]. S. Sharif, D. Schagen, M.D. Toney, H.-H. Limbach, J. Am. Chem. Soc. 129 (2007) 4440-4455.
[2]. E. Ritter, P. Przybylski, B. Brzezinski, F. Bartl, Curr. Org. Chem. 13 (2009) 241-249.
[3]. D.E. Metzler, E.E. Snell, J. Am. Chem. Soc. 74 (1952) 979-983
[4]. H. Tanaka, M. Senda, N. Venugopalan, A. Yamamoto, T. Senda, T. Ishida, K.Horlike, J. Biol. Chem. 286 (2011) 27548-27558.
[5]. S.-C. Huang, J.C.-C. Wei, D.J. Wu, Y.-C. Huang, Eur. J. Clin. Nutr. 64 (2010) 1007-1013.
[6]. M.F. Camiña, J.S. Casas, M.V. Castaño, M.D. Couce, A. Gato, P. Herbello-Hermelo, A. Sánchez, J. Sordo, M.D. Torres, J. Inorg. Biochem. 104 (2010)599-610.
[7]. K. Murakami, Y. Miyake, S. Sasaki, K. Tanaka, W. Fukushima, C. Kiyohara, Y.Tsuboi, T. Yamada, T. Oeda, T. Miki, N. Kawamura, N. Sakae, H. Fukuyama, Y.Hirota, M. Nagai, Fukuoka Kinki Parkinson's Disease Study Group, Br. J. Nutr.104 (2010) 757-764.
[8]. S. Mooney, H. Hellmann, Phytochemistry 71 (2010) 495-501.
[9]. S.C. Larsson, N. Orsini, A. Wolk, JAMA 303 (2010) 1077-1083.
[10]. S. Signorella, V. Daier, G. Ledesma, C. Palopoli, P. C. Piquini Polyhedron 102 (2015) 176-184.
[11]. V. Murašková, N. Szabó, M. Pižl, I. Hoskovcová, D. Sedmidubský Inorg. Chim. Acta, 461(2017) 111-119.
[12]. P. R. Ebani, L. A. Fontana, P. T. Campos, E. F. Rosso, D. F. Back J. Mol. Struct. 1120(2016) 163-170.
[13]. S. Mandal, Y. Sikdar, R. Sanyal, S. Goswami J. of Mol. Struct. 1128(2017) 471-480.
[14]. J. D. Siqueira, A. C. Menegatti, H. Terenzi, M. B. Pereira, D. F. Back Polyhedron, 130 (2017) 184-194.
[15]. A. Heidari, N. Noshiranzadeh, F. Haghi, R. Bikas, Microb. Pathog. 112 (2017)103–110
[16]. R. Omidinia, S. A. Beyramabadi, S. Allameh, A. Morsali, M. Pordel. Journal of Molecular Structure, 1248 (2022) 131452
[17]. M. Aleshahidi, M. Gholizadeh, S. M. Seyedi Research on Chemical Intermediates 48(11)(2022) 1-26
[18]. R. Manikandan, P.Vijayan, P. Anitha, G. Prakash, R. Nandhakumar. Chim. Acta, 421, (2014) 80-90.
[19]. T. Mukherjee, J. C. Pessoa, A. Kumar, A. R. Sarkar Inorg. Chim. Acta. 426 (2015) 150-159.
[20]. N. Ribeiro, S. Roy, N. Butenko, I. Cavaco, I. Correia J. Inorg. Biochem. 174(2017) 63-75.

[21]. PanwarHazari, P.; Pandey, A. K.; Chaturvedi, S.; Tiwari, A. K.;Chandna, S.; Dwarakanath, B. S.; Mishra, A. K. Synthesis of oxovanadium(IV) Schiff base complexes derived from C-substituted diamines and pyridoxal-5-phosphate as antitumoragents. Chem. Biol. Drug Des. 79(2012) 223–234

[22]. L. P. Fioravanço , J. B. Pôrto, F. M. Martins , J. D. Siqueira , B. A. Iglesias , B. M. Rodrigues , O. A. Chaves , D. F. Back J. Inorg. Biochem. 239(2023)11207010.Doi:1016/j.jinorgbio.2022.112070

[23]. V. Jevtovic, A. Rakić, O. A. O. Alshammari,M. S. Alhar,T. Alenezi,V. Rakic,D. Dimić, Inorganics, 12(9) (2024) 251

[24]. N. Mukherjee, S. Podder, S. Banerjee, S. Majumdar, A. R. Chakravarty Eur. J. Med. Chem. 122 (2016) 497-509.

[25]. N. Ribeiro, S. Roy, N. Butenko, I. Cavaco, I. Correia J. Inorg. Biochem. 174 (2017) 63-75.

[26]. U. Basu, I. Pant, A. Hussain, P. Kondaiah, A.R. Chakravarty*Inorg. Chem.* 54 (8) (2015) 3748

[27]. J. M. Galván-Hidalgo, G. M. Chans, T. Ramírez-Apan, A. Nieto-Camacho, S.Hernández-Ortega, E. Gómez, Appl.Organomet. Chem31(9) (2017) e3704

[28]. M. Strianese, A. Basile, A. Mazzone, S. Morello, , M. C.Turco, C.Pellecchia, J. Cellular Physiology 228(11), (2013). 2202–2209

[29]. C.C.Gatto, M.A.S.Chagas, I.J. LimaF. M. Andrade, H. D. Silva, G. R. Abrantes E. P. S. Lacerda Trans. Met. Chem 44 (2019) 329.

[30]. Mato-López , A. Sar-Rañó , M. R. Fernández , M. L. Díaz-Prado , A. Gil , Á. Sánchez-González, N.Fernández-Bertólez , J. Méndez , V. Valdiglesias , F. Avecilla, J Inorg Biochem 235(2022) 111937,

[31]. V. Jevtovic , A. K. Alshamari , D. Milenković , J. D.Marković, Z. Marković, D. Dimić Int J Mol Sci. 25 (2023) 24(15),11910

[32]. L. M. Balsa, V. Ferretti, M. Sottile, P. Nunes, J. C. Pessoa, I. Correia and I. E. León Dalton Trans., , 53 (2024) 3039-3051

[33]. L. A. Fontana, M. Stüker, G. M. Oliveira, B. A. Iglesias, D. F. Back Inorg. Chem. Commun., 62, (2015) 55-59

[34]. S. A. Elsayed, A. M. Noufal, A. M. El-Hendawy J. Mol. Struct. 1144 (2017) 120-128.

[35]. L. A. Fontana, F. M. Martins, J. D. Siqueira, C. Serpa, O. A. Chaves, D. F. Back, *Inorganics 12*(6) (2024) 171

*****

Parameterization of Nuclear Potential in Reaction Dynamics Studies: Role of AI & ULSI Based Technologies

Alpna Ojha*, Sunita Gupta[#]

Department of Physics, Agra College, Agra-282002, U.P. India
Email:*iwa2008@rediffmail.com, [#]sunitagupta1823@gmail.com*

ABSTRACT

In the modern era of low carbon policies, nuclear energy has certain benefits over conventional energy sources. Nuclear energy, generated by the nuclear reaction process in reactors is a complex one. At present, the fifth generation of computers having ultra-large-scale integration (ULSI) technology along with artificial intelligence (AI) is being increasingly used in nuclear physics to accelerate research, improve data analysis, and develop new technologies. The studies of nuclear reactions with advanced statistical based computer codes provide the details of the dynamical processes resulting in scattering or transmutation as well as the richness of advanced nuclear data. Apart from other reaction mechanisms, complete fusions (CF) along with incomplete fusion (ICF) are some of the dominant modes of reactions induced by heavy ion (HI) at the low/medium energy range ≤ 7 MeV/nucleon. The dynamics of these processes may be explained quite well by the optical model of nuclear reactions. The estimation of fractional incomplete fusion in a reaction system induced by HI depends on theoretical excitation functions in some experimental techniques in keeping with offline measurements of excitation functions. These theoretical excitation functions are predicted by statistical model-based computer codes with ULSI technology using optical model potential (OMP) parameters to calculate the reaction cross sections. With a slight alteration in the selection of OMP parameters may affect the depth of nuclear potential as well as its shape. Further, this change in potentials influences the shape elastic scattering and the reaction probabilities, which in turn, alters the theoretical differential reaction cross-sections predicted by statistical code. The OMP parameters for HI-induced reactions are not universal, and distinct sets of these parameters may be utilized for various spans of mass number A and incident energy E. For all reaction systems, a solitary set of OMP parameters is insufficient. The study of the dependence of nuclear reaction dynamics on the parameter systematics of emitted particles in the shell of statistical model based advanced fifth-generation computer codes has been described in this chapter.

Keywords: *ULSI technology, HI induced nuclear reactions, OMP parameters*

1. INTRODUCTION

The mysterious and highly dense entity, the nucleus, carries almost all the mass of the atom ≈ 99.95% but occupies an extremely tiny space inside the atom. One way of getting the hidden features and information of the nucleus is through the comparative study of experimental results with proposed theoretical models i.e. the study of nuclear reactions between desired nuclei under appropriate experimental conditions. These statistical models are the highly idealized version of a nuclear reaction system. Computer codes are used to implement statistical models of nuclear reactions. These codes are used to calculate the reaction cross-sections of nuclear reactions for a broad range of incident particles and target nuclei.

Fifth-generation computers can handle the vast amounts of data required to study nuclear reactions. They are also able to run complex simulations of nuclear reactions, which will help

scientists to better, understand how these reactions work. ULSI technology [1] allows fifth- generation computers to be built with millions of transistors on a single chip. This makes them much faster and more powerful than current computers, which allows them to handle even the most demanding nuclear reaction simulations. Together, fifth-generation computers and ULSI technology revolutionize the study of nuclear reactions. They allow scientists to study nuclear reactions in much greater detail than ever before, and they will help us to develop new nuclear technologies. Fifth-generation computers are heavily reliant on Artificial intelligence (AI) [2, 3], which are used to automate tasks, improve decision-making, and interact with humans more naturally. AI is being used to develop new models of nuclear reactions that can be used to simulate the behavior of nuclear matter under extreme conditions.

2. STATISTICAL MODEL

The initial and final stages of the nuclear reaction processes are well described, but the picture of the complex mechanism of the process throughout the interaction period is not well described. In order to characterize such a phenomenon, there is a need for theoretical models. To explain the mysterious reaction mechanism, various simplified theories and models have been proposed in the present literature. These statistical models are the highly idealized version of a nuclear reaction system and an alternative method to describe the nuclear reaction in terms of two body interaction that encapsulates a set of statistical assumptions about the data-gathering process. As a function of incident energy or the energy of the residual nucleus and the angles at which the emitted particles are measured, statistical models provide the absolute values of reaction cross-sections. Some of the nuclear reaction models put out in the literature include the compound nucleus model, optical model, direct reaction model, and pre-equilibrium model.

3. OPTICAL MODEL

In the optical model, a potential is used in place of the incident particle and nucleus interaction. Instead of many bodies problem, the interaction process resembles a two-body problem. Bethe and several others first proposed the idea of replacing the target nucleus with a square potential well in the year 1935 [4, 5]. As the reaction cross sections predicted by this model appeared to be too small, it did not provide a satisfactory fit to the experimental results. To resolve this discrepancy, Woods & Saxon replaced the square well with the complex spherical potential [6], given as

$$"V = -(V_0 + iW_0)[1 + \exp\{(r - R)/a\}]^{-1}"$$

The complex optical potential is, generally, represented as [7];

$$"U(r) = V_c - Vf(x_v) + \left(\frac{h}{m_\pi c}\right)^2 V_{so}(\sigma.l)\frac{1}{r}\frac{d}{dr}f(x_{so}) - i\left[Wf(x_W) - 4W_D\frac{d}{dx_D}f(x_D)\right]"$$

Where symbols have their usual meaning.

The optical model delineates the interaction between the incident projectile and the target nucleus which is treated in analogy to the transmission of light through a partially absorbing medium. The OMP parameters of the optical model are used to compute the transmission coefficients (TCs) for emitting particles: neutron, proton, and alpha particles in Hauser-Feshbach statistical theory and are used for the statistical predictions of cross-sections of reaction for evaporated residues of reaction systems by statistical model-based computer codes. In general, nuclear reaction computer codes are based on the statistical compound reaction mechanism of the fusion of heavy ions.

4. COMPUTER CODES

Computer codes based on theoretical models are needed for advanced nuclear physics and nuclear data to describe the various features of the nucleus and nuclear reaction dynamics. Nuclear processes involved in the astrophysical field, an extension of the periodic table by the synthesis of

super-heavy elements, etc. demand huge nuclear data with wide ranges of energies and mass numbers. Data for the stable nuclei under appropriate conditions can be obtained directly via experiments. However, the nuclear data for the targets far from the stability may not be measured directly. Statistical models of nuclear reactions provide the only way to estimate the different data values for such cases, as with the use of nuclear-model based predictions, data can be generated for wide energy ranges and important channels, for which experimental data are not available. In the existing literature, various computer codes are available to describe the decay process of excited nuclei in HI induced nuclear reactions. Some of them are ALICE, GNASH, EMPIRE, TALYS, PACE4, and CASCADE. Present work has been analyzed within the frame work of code PACE4.

In order to calculate the TCs using Hauser-Feshbach calculations, code PACE4 [8] by default uses phenomenological OMP parameter systematics. The potential provided by Wilmore and Hodgson [9] is utilized as the neutron potential. For proton, the potential given by Becchetti-Greenlees [10] is used as an inbuilt parameter in PACE4, which is appropriate for medium weight nuclei with an intermediate range of incident energy. Fixed OMP parameters for alpha-particles has used in PACE4 provided by Huizenga [11].

The combination of above mentioned sets of OMP parameter systematics for nucleons and α-particles has been utilized to predict the theoretical reaction cross-sections by code PACE4 in a default manner, generally for almost all the reaction systems of different targets & projectile combinations and incident energy ranges in the existing literature, although, a sole set of OMP parameter systematics might not be sufficient for the whole span of mass numbers of targets and the entire span of projectile energies. The OMP parameters systematics is not unique, they are phenomenologically determined from elastic scattering fittings having various kinds of ambiguities. Several sets of phenomenological OMP parameter systematics have been published in the literature for distinct spans of mass numbers of targets and broad ranges of incident energies [7]. Although, some global parameterizations of the nucleon-nucleus OMP have also been reported in the literature for a broad range of mass numbers and low/intermediate energies for (n, n) and (p, p) type reactions by Varner et al in 1991 [12] and A. J. Koning et al in 2003 [13]. These global OMP parameter sets are not appropriate choices for complex HI induced reaction systems. For nucleus-nucleus optical model potentials in HI induced nuclear reactions, global parameterization is still a topic of research.

5. RESULT AND DISCUSSION

The OMP parameter systematics for heavy targets and incident energies well above the Coulomb barrier may not be the same as for light targets and low energies. The OMP parameters for proton described by J.J.H. Menet et al in 1971 [14] may be more accurate in the higher energy range of incident particles and wide range of target mass numbers, $A \geq 100$. The changed OMP parameter systematics for proton, using systematics given by J.J.H. Menet et al in the place of systematics given by Becchetti-Greenlees, may be used for the prediction of theoretical EFs of ERs populated in a reaction system, for example, the system $^{12}C + ^{165}Ho$ [15] and the impact of this change on the reaction dynamics may analyze by observing the change in predicted theoretical EFs. The reaction system $^{12}C + ^{165}Ho$ is induced by Carbon-12 and has a heavy target Holmium- 165 with mass number 165 ($A >$ 100). The experimental data of excitation functions for numerous populated evaporation residues (ER) during interaction of system $^{12}C + ^{165}Ho$ is already available in the literature [15], which have been measured experimentally by utilizing the activation technique at the energies 55, 62, 71, and 80 MeV. The available experimental data of reaction cross-sections has been analyzed theoretically by the code PACE4 at the above mentioned energies along with the predictions at some more energy points to get a clear analysis. It is important to note that PACE4 ignores ICF channels and pre-equilibrium (PE) channels when predicting theoretical cross-sections and only considers complete fusion channels.

By comparing existing experimental EFs with corresponding theoretical EFs predicted by code PACE4 using various sets of parameters of optical model potential, it has been possible to analyze the

effects of variations in these parameters on the predictions of statistical cross sections and, consequently, their impact on the contribution of ICF in the reaction system $^{12}C + ^{165}Ho$. Various sets of OMP parameter systematics other than the default set have been formed by using OMP parameter systematics for proton described by J.J.H. Menet et al [14] instead of systematics given by Becchetti-Greenlees [10] for proton. Systematics given by Wilmore and Hodgson [9] used as the potential for neutron and systematics given by Huizenga [11] for α-particles have been taken the same for all sets of OMP parameter systematics. Comparative study between experimental existing data of EFs of populated ERs for multiple neutron and proton emitting channels (xn and pxn channels) of reaction system $^{12}C + ^{165}Ho$ and theoretical EFs predicted by PACE4 using distinct sets of OMP parameters has been analyzed. Out of various sets of OMP parameters, which one set gives a good agreement between the experimental and theoretical EFs for multiple neutron and multiple neutron-proton channels that set becomes the proper or appropriate choice of OMP parameters for the reaction system $^{12}C + ^{165}Ho$. The fair agreement between the experimental and theoretical EFs for x_n and px_n channels indicates that these channels are populated due to complete fusion.

The resulting proper choice of OMP parameters for reaction system $^{12}C+^{165}Ho$ is used for predicting theoretical EFs, corresponding to alpha and two alpha (α and 2α) emitting channels with multiple emission of neutrons, and then estimating the corresponding strength of ICF of the system. By comparing the existing experimental cross sections to the predicted theoretical cross sections of the alpha and two alpha emitting channels with additional emission of one or more neutrons (αxn and 2αxn channels), the ICF fraction of the reaction system may be extracted in certain experimental techniques in keeping with offline measurements of excitation functions (EFs). As a result, in some methodologies, the theoretical predictions produced by the statistical model are an essential component in the calculation of the ICF percentage for specific chosen systems. It has been found that the strength of the ICF varies with the increasing value of beam energy. The major contribution of the production of ERs corresponds to α and 2α emitting channels comes from the ICF of carbon-12 with the target Ho-165 nuclei. Here, ^{12}C may break up into ^{8}Be and α-fragment and only one part of the broken fragment fuses with the target nucleus leaving the remaining part of the projectile as a spectator.

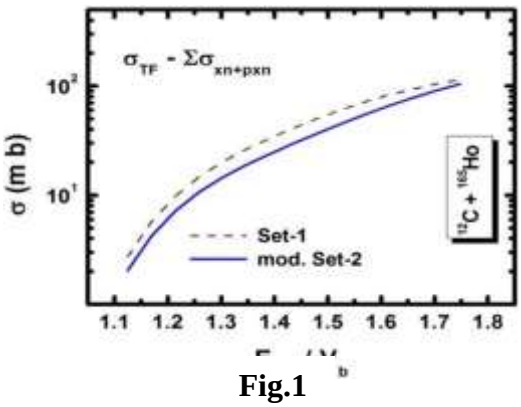

Fig.1

Fig.1: Sum total of the theoretically computed cross-sections of all channels other than xn/pxn channels (σ_{TF}- $\Sigma\sigma_{xn/pxn}$) of the reaction system $^{12}C + ^{165}Ho$ predicted by PACE4 utilizing Set-1 as well as modified Set-2 of OMP parameters.

The impact of variations in OMP parameter systematics can be analyzed by the study of the sum total of all the theoretically computed cross sections other than multiple neutrons and multiple neutron-proton channels (σTF- $\Sigma\sigma xn+pxn$), which is actually the sum total of the theoretically computed by cross Sections for αxn and 2αxn channels, predicted by the PACE4 using two sets of the OMP parameters, "Set-1" with Becchetti-Greenlees systematics for proton, and "modified Set-2" with systematics given by Menet et al for proton. For the selected system $^{12}C + ^{165}Ho$, it has been discovered that alternation in the OMP parameters makes a difference in the sum total of the theoretical cross sections of αxn and 2αxn channels by around 10% to 30% [16].

5. CONCLUSION

The nuclear interaction potentials are the keys to understanding the complex fusion processes. The dynamics of these processes may be explained quite well by optical model of nuclear reactions. Alternations in these parameters significantly make differences in the theoretically computed cross-sections anticipated for a variety of channels, which in turn alters the estimated fractional incomplete

fusion. The OMP parameter systematics affects the end results of the theoretical predictions of the interaction process in the case of HI induced nuclear reactions to an appreciable extent. Comparative analyses of experimental data with the corresponding theoretical predictions created by statistical model-based computer code with ULSI technology utilizing distinct sets of OMP parameters can be used to determine the effects of alterations of the OMP parameters on the theoretical predictions. The estimated ICF fraction of the reaction systems is also affected by the developed systematics and hence this systematics need to be deeply studied. Large trials involving the computer code PACE4, AI of fifth-generation computers, and ULSI technology revolutionize the study of nuclear reactions. They allow scientists to study nuclear reactions in much greater detail and help to develop new nuclear technologies. This information can then be used to improve the design and operation of nuclear reactors.

REFERENCES

[1]. Nicholas R. White, Nuclear Instruments and Methods in Physics Research Section B: Beam Interactions with Materials & atoms, 55, 1-4, 287-295 (1991).

[2]. Paulo Bedaque et al., "A.I. for nuclear physics" Eur. Phys. J. A, 57 (2021).

[3]. Qingyu Huang et al., "A review of the application of artificial intelligence to nuclear reactors: Where we are and what's next" Heliyan, 9, 3 (2023), https://doi.org/10.1016/j.heliyon.2023.e13883

[4]. Bethe H. A., "Theory of Disintegration of Nuclei by Neutrons" Phys. Rev. 47, 747 (1935).

[5]. Becker J. A., "Thermionic Electron Emission and Adsorption Part I. Thermionic Emission" Rev. Mod. Phys. 7, 95 (1935).

[6]. Woods R. D. and Saxon D. S., "Diffuse Surface Optical Model for Nucleon-Nuclei Scattering", Phys. Rev. 95, 577 (1954).

[7]. Perey C. M. and Perey F. G., At. "Compilation of phenomenological optical-model parameters 1954–1975", Data Nucl. Data Tables 17, 1 (1976).

[8]. Gavron A., "Statistical model calculations in heavy ion reactions", Phys. Rev. C 21, 230 (1980).

[9]. Wilmore D. and Hodgson P. E., "The calculation of neutron cross-sections from optical potentials", Nucl. Phys. 55, 673 (1964).

[10]. Becchetti F. D, Jr. and Greenlees G. W., "Nucleon-Nucleus Optical-Model Parameters, A>40, E<50 MeV", Phys. Rev. 182, 1190 (1969).

[11]. Huizenga J. R. and Igo G., "Theoretical reaction cross sections for alpha particles with an optical model", Nucl. Phys. 29, 462 (1962).

[12]. Varner. R. L et al., "A global nucleon optical model potential", Phys. Reports 201, 2, 57- 119 (1991).

[13]. Koning A. J. and Delaroche J. P., "Local and global nucleon optical models from 1 keV to 200 MeV", Nucl. Phys. A 713, 231 (2003).

[14]. Menet, J. J. H. et al., "Total reaction cross-section measurements with 60-mev protons", Phys. Rev. C 4, 1114 (1971).

[15]. Gupta S. et al., "Complete and incomplete fusion of ^{12}C with ^{165}Ho below 7 MeV/nucleon: Measurements and analysis of excitation functions", Phys. Rev. C 61, 064613 (2000).

[16]. Ojha A. et al., "Mass-number dependence of statistical model parameters and its impact on incomplete fusion fraction calculations", Phys. Rev. C 104, 034615 (2021).

*****

Dielectric Study of Ti-Zn Substituted Ni-Ferrite Nanoparticles

Dr. Ramesh T. Ubale

Department of Physics, Siddharth Arts, Commerce and Science College, Jafrabad-431206
Email: *rameshubale1971@gmail.com*

ABSTRACT

Investigation of dielectric properties of, Ti-Zn doped $CoFe_2O_4$ spinel ferrite with the formula $NiFe_{2-2x}Ti_xZn_xO_4$ (x = 0.00, 0.05, 0.10, 0.15 and 0.20) were synthesized by using well-known standard sol-gel auto combustion synthesis method. The X-ray diffraction technique was used to investigate the crystal structure for the determination of structural morphological parameters. After the confirmation of the samples, then it is used for the study of dielectric properties with varying frequencies from 20Hz to 1MHz with the help of an LCR-Q meter. Dielectric properties vary with frequency because of the way dipoles reverse direction. The dielectric constant (ε′), dielectric loss (ε′′) and dielectric loss tangent (tan δ) by measuring the capacitance 'C' using the LCR-Q meter at room temperature and as a function of frequency was calculated and this dielectric analysis can help characterize materials and understand their electrical behavior. This can help with their potential applications in electronics and energy conversion.

Keywords: *Sol-gel method, X-ray diffraction, dielectric constant, dielectric loss, dielectric loss tangent.*

1. INTRODUCTION

Nanocrystalline magnetic ferrites have recently attracted a lot of attention due to their wide range of technical applications in various fields, such as magnetic fluids for information storage [1], ferrofluids [2], magnetic-driven drug delivery [3], sensors [4], catalyst [5], and magnetic resonance imaging enhancement [6]. The chemical, electrical, mechanical, structural, and magnetic properties of ferrite nanoparticles are special and have a range of promising technological applications in high-density recording equipment, color photography, ferrofluids, high-frequency devices, and magnetic refrigerators [7]. The tetrahedral (A) and octahedral (B) interstitial sites in the crystal structure of spinel ferrite are where cations of different valences and types can be accommodated depending on their site preference energies. Cations with higher radii often occupy the tetrahedral A site, whereas those with lower radii typically occupy the octahedral B site. Since the previous eight decades, several researchers from various laboratories have been studying spinel ferrite for a variety of uses [8].

Spinel ferrite was synthesized throughout the past several decades using a variety of techniques, and its structural, electrical, dielectric, and magnetic characteristics were optimized by adding several dopant ions [9-10]. The characteristics of spinel ferrite can be significantly tailored by incorporation of divalent or trivalent cations [11]. Additionally, doping of tetravalent ions is promising to enhance the electrical and magnetic characteristics of bulk spinel ferrite. Due to their exceptional characteristics, which differ from those of bulk spinel ferrites, nanocrystalline spinel ferrites have become increasingly important as nanoscience and nanotechnology have advanced in recent years. Greater chemical stability, a high surface-to-volume ratio, and ease of preparation at low

cost and temperature are all characteristics of nanocrystalline ferrites. Nanocrystalline ferrites are found beneficial in many applications, including sensors, catalysts, targeted medication delivery, hyperthermia, water purification, etc. because of these exceptional features [12]. They draw the attention of numerous researchers because of their multifunctional qualities.

Thus, this chapter focuses on the synthesis, structural, and dielectric behavior of Ti^{4+}-Zn^{2+} co-substituted nickel ferrite ($NiFe_2O_4$) nanoparticles with the composition given as $NiFe_{2-2x}Ti_xZn_xO_4$ (x = 0.00, 0.05, 0.10, 0.15 and 0.20).

2. EXPERIMENTAL DETAILS

2.1. Materials

Nickel nitrate [Ni $(NO_3)_2 \cdot 6H_2O$], ferric nitrate [Fe $(NO_3)_2 \cdot 9H_2O$], zinc nitrate [Zn $(NO_3)_2 \cdot 6H_2O$], titanium tetra-butoxide (Ti $(OCH_2CH_2CH_2CH_3)_4$), citric acid [$C_6H_8O_7 \cdot H_2O$], ammonia solution [$NH_3.H_2O$], acetone, and distilled water were used as a primary chemical. All chemicals used were of analytical grade (AR grade) and the solutions were prepared with distilled water.

2.2. Synthesis of $NiFe_{2-2x}Ti_xZn_xO_4$ Nanoparticles

A well-known sol-gel procedure was adopted for the preparation of $NiFe_{2-2x}Ti_xZn_xO_4$ nanoparticles in which nickel nitrate [Ni $(NO_3)_2 \cdot 6H_2O$], ferric nitrate [Fe $(NO_3)_2 \cdot 9H_2O$] and zinc nitrate [Zn $(NO_3)_2 \cdot 6H_2O$], titanium tetra-butoxide were used as a raw material. All the nitrates were dissolved together in a minimum amount of distilled water to get a clear solution. The citric acid was used as a fuel. The citric acid to nitrate ratio was considered to be 1:3. An aqueous solution of citric acid was mixed with a metal nitrate solution. The solution was transformed into a sol and then a gel was formed by evaporation of the water (condensation reactions). The ammonia solution was slowly added to maintain the pH at 7 of the mixed homogeneous solution. The temperature after the gel formation is increased to 120°C. At this temperature, the gel gets burnt converting into fine loose powder of $NiFe_{2-2x}Ti_xZn_xO_4$ nanoparticles. The resultant's as obtained nanoparticles were annealed at 650°C for 4 h to remove the moisture and impurity if any present in the sample.

2.3. Characterizations

The structural properties were studied by characterizing the samples by X-ray diffractometer using CuK_α (λ = 0.15418 nm) radiation in the 2θ range of 20° to 80°. The dielectric properties were studied with varying frequencies from 20Hz to 1MHz with the help of an LCR-Q meter

3. RESULTS AND DISCUSSIONS

3.1. X-ray Diffraction (XRD) Analysis

The X-ray diffraction pattern of $NiFe_{2-x}Ti_xZn_xO_4$ (typical sample x = 0.00 and 0.05) nanoparticles was used to investigate the crystal structure for the determination of structural morphological parameters as shown in **Fig.1(a)** and **Fig.1(b).**

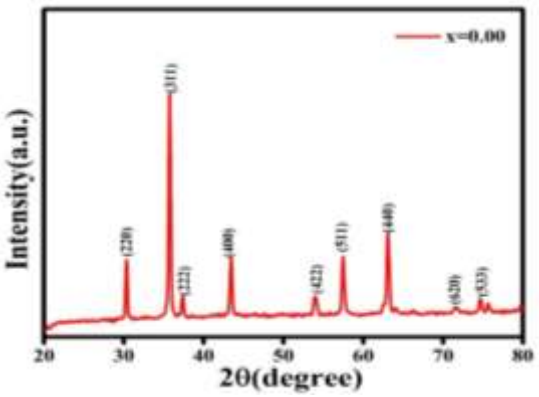

Fig. 1: (a) XRD pattern of $NiFe_{2-x}Ti_xZn_xO_4$ (x = 0.00) nanoparticles

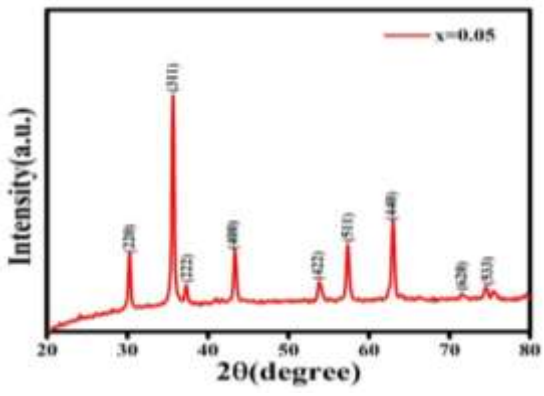

Fig.1: (b) XRD pattern of $NiFe_{2-x}Ti_xZn_xO_4$ (x = 0.05) nanoparticles

Using an X-ray diffractometer (XRD), the prepared nanoparticle samples in powder form were utilized to examine the structural characteristics. All of the prepared samples are well crystallized, as evidenced by the well-defined, sharp, and strong diffraction peaks that emerge in the XRD patterns. For each composition, the XRD pattern displays the diffraction peaks (220), (311), (222), (400), (422), (511) and (440). Lattice constant of the prepared series was given in Table 1.

Table 1: Lattice constant of $NiFe_{2-2x}Ti_xZn_xO_4$ (x = 0.00, 0.05, 0.10, 0.15 and 0.20) nanoparticles.

Composition (x)	**0.00**	**0.05**	**0.10**	**0.15**	**0.20**
a (Å)	8.327	8.338	8.352	8.357	8.365

The formation of a single-phase cubic spinel structure is demonstrated by the presence of all these peaks in the XRD pattern. The absence of any other peaks in the XRD patterns demonstrates the exceptional purity of the prepared samples. Similar results on nickel ferrite nanoparticles are reported in the literature [13-14].

3.2. Dielectric Analysis

The dielectric properties for the present $NiFe_{2-2x}Ti_xZn_xO_4$ (x = 0.00, 0.05, 0.10, 0.15, and 0.20) nanoparticles can be explained based on the mechanism of the polarization process in ferrite nanoparticles. The dielectric properties of all the samples of $NiFe_{2-2x}Ti_xZn_xO_4$ (x = 0.00, 0.05, 0.10, 0.15 and 0.20) nanoparticles were studied in the present work by determining the dielectric constant (ε′), dielectric loss (ε″) and dielectric loss tangent (tan δ) by measuring the capacitance 'C' using the LCR-Q meter at room temperature and as a function of frequency.

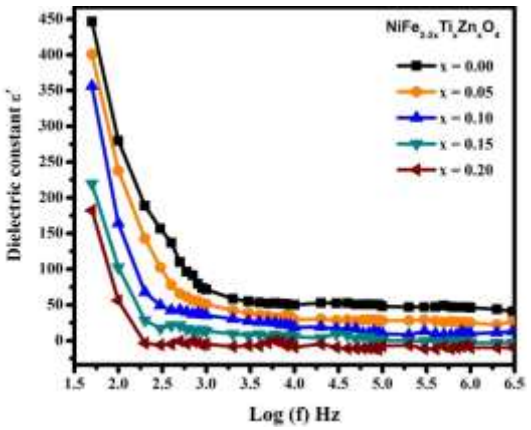

Fig. 2: Dielectric constant plot of $NiFe_{2-x}Ti_xZn_xO_4$ (x = 0.00, 0.05, 0.10, 0.15, 0.20) nanoparticles

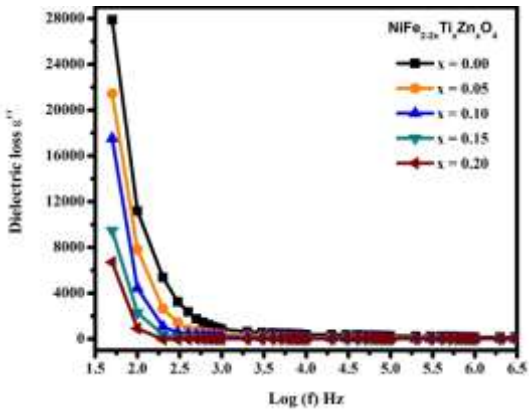

Fig. 3 Dielectric loss plot of $NiFe_{2-x}Ti_xZn_xO_4$ (x = 0.00, 0.05, 0.10, 0.15, 0.20) nanoparticles

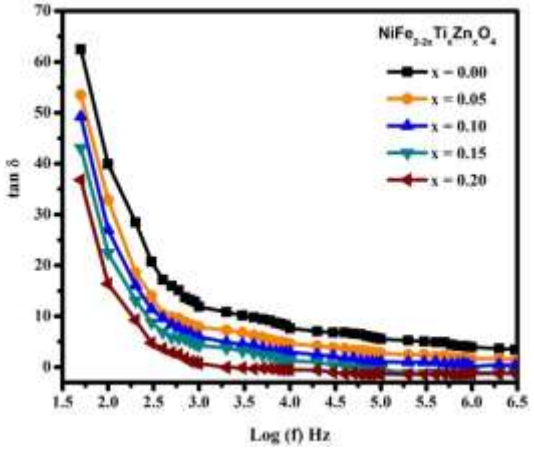

Fig. 4: Dielectric loss tangent plot of $NiFe_{2-x}Ti_xZn_xO_4$ (x = 0.00, 0.05, 0.10, 0.15, 0.20) nanoparticles

The variation of dielectric constant (ε') with applied frequency for all $NiFe_{2-2x}Ti_xZn_xO_4$ (x = 0.00, 0.05, 0.10, 0.15, and 0.20) nanoparticles samples was observed as shown in **Fig. 2**. It is observed from **Fig. 2** that the dielectric constant decreases continuously with increase in frequency for all the samples followed by a frequency independent behavior. The plot illustrates that the dielectric constant decreases with an increase in frequency and reaches the constant value at higher frequencies. The decrease in dielectric constant with an increase in frequency may be due to the relaxation of the electrical dipole. At higher frequencies, the relaxation process ceases due to the short time. In the X-band frequency range, all materials showed a gradual increase and decrease in permittivity. Fe^{2+} ions play an important role in the high-frequency permittivity of ferrite materials [15]. It is observed that the dielectric constant is high in the range of low frequency and it decreases with frequency. The reason for the high value of the dielectric constant at low frequencies may be due to dislocations, voids, and defects present in the crystal structure of nano ferrites. The decrease in dielectric constant with increasing frequency is because at higher frequencies any effect contributing to polarization is found to show lagging behind the applied field. When the frequency is increased beyond a certain frequency limit, the electron hopping cannot follow the electric field fluctuations and causes a decrease in the dielectric constant. At high frequencies, the value of the dielectric constant is low because it comes from the grains having a small value of dielectric constant due to low resistivity and becomes less dependent on frequency. The observed variation of dielectric constant with frequency can be attributed to the space charge polarization, which is due to an inhomogeneous dielectric structure as discussed by Maxwell and Wagner and is in agreement with Koop's phenomenological theory.

The variation of dielectric loss as a function of frequency is shown in Figure **Fig. 3**. It can be observed from **Fig.3** that dielectric loss (ε") decreases exponentially with increase in frequency. The dielectric loss (ε") factor is considered to be the most important part of the total core loss in ferrites. The decrease in dielectric loss is almost similar to that of the dielectric constant. The decrease in the imaginary part of the dielectric constant i.e. dielectric loss is pronounced more in comparison to the real dielectric constant. The values of dielectric loss depend on several factors such as Fe^{2+} contents, structural homogeneity, and stoichiometry, which in turn depends on the synthesis methods and composition. The dielectric loss tangent (tan) is a function of frequency calculated from the dielectric constant and dielectric loss. The variation of dielectric loss tangent is shown in **Fig. 4** which shows an exponential decreasing trend with increasing frequency. The observed behavior of dielectric loss tangent can be explained based on Maxwell-Wagner interfacial polarization. The values of tan δ depend on several factors such as carrier concentration and structural homogeneity. The compositional dependence of various dielectric parameters such as dielectric constant, dielectric loss, and dielectric loss tangent shows that all parameters decrease as Ti-Zn content x increases.

4. CONCLUSION

The Ti^{4+}-Zn^{2+} co-doped nickel ferrite nanoparticles with compositions as $NiFe_{2-2x}Ti_xZn_xO_4$ (x = 0.00, 0.05, 0.10, 0.15, and 0.20) were successfully prepared using sol-gel auto combustion method. X-ray diffraction data revealed the pure phase formation with cubic spinel structure for all the compositions. The dielectric properties show a decreasing behavior with increasing frequency at room temperature. The co-doping of Ti^{4+}-Zn^{2+} ion leads to a fascinating change in the properties of nickel ferrite nanoparticles which can be useful for many technological and industrial applications.

REFERENCES

[1]. P. Morais, R. Santos, A. Pimenta, R. Azevedo, E. Lima, Prep. and chara.of ultra-stable biocompatible magnetic fluids using citrate-coated Co-ferrite nanoparticles, Thin solid films, 515 (2006) 266-270.

[2]. M. Kole, S. Khandekar, Engineering applications of ferrofluids: A review, Journal of Magnetism and Magnetic Materials, 537 (2021) 168222.

[3]. A. Nigam, S. Pawar, Structural, magnetic, and antimicrobial properties of zinc doped magnesium ferrite for drug delivery applications, Ceramics International, 46 (2020) 4058-4064.

[4]. R. Srivastava, B.C. Yadav, Ferrite materials: introduction, synthesis techniques, and applications as sensors, International Journal of Green Nanotechnology, 4 (2012) 141-154.

[5]. B.I. Kharisov, H.R. Dias, O.V. Kharissova, Mini-review: Ferrite nanoparticles in the catalysis, Arabian Journal of Chemistry, 12 (2019) 1234-1246.

[6]. N. Akhlaghi, G. Najafpour-Darzi, Manganese ferrite (MnFe2O4) Nanoparticles: From synthesis to application-A review, Journal of Industrial and Engineering Chemistry, 103 (2021) 292-304.

[7]. K.K. Kefeni, T.A. Msagati, B.B. Mamba, Ferrite nanoparticles: synthesis, characterization, and applications in an electronic device, Materials Science and Engineering: B, 215 (2017) 37-55.

[8]. K.K. Kefeni, B. B. Mamba, T.A. Msagati, Application of spinel ferrite nanoparticles in water and wastewater treatment: a review, Separation, and Purification Technology, 188 (2017) 399-422.

[9]. T.N. Pham, T.Q. Huy, A.-T. Le, Spinel ferrite (Fe 2 O 4)-based heterostructured designs for lithium-ion battery, environmental monitoring, and biomedical applications, RSC advances, 10 (2020) 31622-31661.

[10]. M. Abdellatif, G. El-Komy, A. Azab, Magnetic characterization of rare earth doped spinel ferrite, Journal of Magnetism and Magnetic Materials, 442 (2017) 445-452.

[11]. M. Hasan, M. Arshad, A. Ali, K. Mahmood, N. Amin, S. Ali, M. Khan, G. Mustafa, M. Khan, M. Saleem, Mg and La co-doped ZnNi spinel ferrites for low resistive applications, Materials Research Express, 6 (2018) 016302.

[12]. M. Mahmood, M.A. Yousuf, M.M. Baig, M. Imran, M. Suleman, M. Shahid, M.A. Khan, M.F. Warsi, Spinel ferrite magnetic nanostructures at the surface of graphene sheets for visible light photocatalysis applications, Physica B: Condensed Matter, 550 (2018) 317-323.

[13]. B.P. Jacob, A. Kumar, R. Pant, S. Singh, E. Mohammed, Influence of preparation method on structural and magnetic properties of nickel ferrite nanoparticles, Bulletin of Mater. Science, 34 (2011) 1345-1350.

[14]. S. Joshi, M. Kumar, S. Chhoker, G. Srivastava, M. Jewariya, V. Singh, Structural, magnetic, dielectric and optical properties of nickel ferrite nanoparticles synthesized by co-precipitation method, Journal of Molecular Structure, 1076 (2014) 55-62.

[15]. S. Mansour, Frequency and composition dependence on the dielectric properties for Mg-Zn ferrite, Egypt. J. Solids, 28 (2005) 263-273.

*****

ISBN: 978-81-970491-8-7
10
Current Research in
Science and Technology
(An Edited Book)

Preparation Methods of Ferrites

Prashant P. Chikode

Department of Physics, Jaysingpur College, Jaysingpur, Maharashtra, India, 416101
Email: *prashantchikode@gmail.com*

ABSTRACT

Ferrites are an essential class of magnetic materials widely used in electronic, biomedical, and industrial applications due to their excellent electrical and magnetic properties. Various preparation methods have been developed to tailor their structural, morphological, and magnetic characteristics. This paper provides a comprehensive overview of the key synthesis techniques for ferrites, including solid-state reaction, sol-gel, co-precipitation, hydrothermal, and microwave-assisted methods. The sol-gel and co-precipitation methods offer better control over particle size and composition at lower temperatures. The choice of synthesis route significantly influences the final properties of ferrites, making method selection crucial for specific applications. This review highlights recent advancements and emerging trends in ferrite preparation, providing insights into optimizing synthesis techniques for enhanced performance in various technological fields.

Keywords: *Ferrites, Synthesis methods, Solid-state reaction, Sol-gel, Co-precipitation, Hydrothermal, Microwave-assisted synthesis, Magnetic materials.*

1. INTRODUCTION

Ferrites are a significant class of ceramic materials with remarkable magnetic, electrical, and optical properties, making them essential in various technological applications. These materials, primarily composed of iron oxides combined with other metal oxides, exhibit a spinel, hexagonal, or garnet structure, which governs their physical and chemical behavior. Ferrites are widely employed in electronics, telecommunications, biomedical applications, and energy storage systems due to their high resistivity, excellent magnetic properties, and low eddy current losses.

The synthesis of ferrites is a critical step in tailoring their structural, morphological, and magnetic properties to suit specific applications. Over the years, several preparation methods have been developed, each offering distinct advantages and challenges. Traditional and modern synthesis routes influence the phase purity, particle size, crystallinity, and overall performance of ferrite materials. The most commonly employed techniques for ferrite synthesis include the solid-state reaction method, sol-gel method, co-precipitation technique, hydrothermal synthesis, and microwave-assisted synthesis, among others. Each of these methods affects the material's final properties, impacting its usability in various applications.

The solid-state reaction method is a conventional approach widely used in large-scale production due to its simplicity and cost-effectiveness. However, it requires high-temperature processing, which may result in grain growth and reduced control over particle size. In contrast, wet chemical methods such as sol-gel and co-precipitation offer better control over homogeneity, purity, and fine particle size, making them suitable for advanced technological applications. Hydrothermal and microwave-assisted methods have gained attention for their energy efficiency, shorter reaction times, and improved control over particle size and morphology.

Understanding the influence of different synthesis methods on ferrite properties is crucial for optimizing their performance. This paper provides a comprehensive review of the preparation techniques used for ferrite synthesis, highlighting their principles, advantages, limitations, and applications. The discussion aims to offer insights into selecting appropriate synthesis routes based on the desired material properties and application requirements. Additionally, recent advancements and emerging trends in ferrite synthesis are explored to provide a futuristic perspective on this evolving field. By examining the diverse preparation methods of ferrites, this paper aims to guide researchers and industry professionals in optimizing synthesis techniques for improved material performance and broader technological applications.

2. BRIEF SURVEY ON THE SYNTHESIS OF HIGH-DENSITY FERRITE

Ferrites are synthesized by many researchers, and for this, they use several methods such as

1. Ceramic method [1,2]
2. Chemical method [3,4]

These methods are classified depending nature of the final product,

1. Ceramic methods which were suitable for conventional powder.
2. Precursor methods and chemical methods are non-conventional powder methods [6].

The well-known chemical reaction for the preparation of ferrite is

$MCl_2 + Na_2 Fe_2 O_4 <=> MaFe_2O_4 + 2Nacl.$

2.1. Ceramic method

A ceramic method is the most useful method, to obtain ferrite powder because of its low economic condition. In the ceramic method metal oxides and ferrous oxides are taken in good proportion and they are mixed with suitable techniques. Such materials are well mixed by using a liquid that is water, alcohol, kerosene, acetate, etc. in a steel ball mill or vibrating systems. The mixture is filtered by a ceramic crucible and prefiltered at a suitable temperature to avoid the decomposition of carbonates and oxides so that there is no change of other gases at the time of final sintering [5].

2.2. Precursor method

This method is a short-time process for obtaining fine ferrite material at the lowest possible temperature. The most important advantage of the Precursor method is that the resultant material should be good stoichiometry [6, 7].

The citrate precursor method was used by J. Madhuri Sailaja et al [8] to prepare ferrite composition $Ni_{0.65}Zn_{0.35}Fe_2O_4$. They investigate that the phase structure of prepared ferrite was a single-phase spinel crystal structure.

2.3. Oxalates Precursor

Oxalate is used to obtain ferrite material with the help of the precursor method, to obtain ferrite material of size 100 to 200 nm at which oxalate is decomposed thermally at temperature 390^0C. The oxalate precursor method was used by A. T. Raghavender et al [8] to prepare nanocrystalline ferrite of composition $Ni_{0.5+1.5x}Cu_{0.3}Zn_{0.2}Fe_{2-x}O_4$ ($0 \leq x \leq 0.5$) at a small amount of temperature.

2.4. Wet chemical method

To obtain ferrite powder with a high level of homogeneity, small grain size, small porosity, and bigger surface area, the wet chemical method is used. The wet chemical method contains several steps to obtain the final product,

1) Reactions to spray
2) Freeze drying.
3) Hydrothermal oxidation.
4) Co- precipitation. [9, 10]

The wet chemical Coprecipitation method was used by M, B. Tahir et al to synthesize substituted nickel ferrite, where the concentration of nickel varies from 0.02, 0.04, 0.06, 0.08.

Structural properties of prepared ferrite were studied from scanning electron microscope, and X-ray diffraction. The size of prepared ferrite nanoparticles was observed that 250nm to 400nm.

3. COMBUSTION SYNTHESIS

To obtain nanoparticles with good chemical homogeneity, high purity, and lower calcination temperature, the auto combustion method is applied [11,12]. This method is one of the most important for the synthesis of nanomaterials. The reaction is exothermic which is used to produce nanoparticles. There are many types of combustion synthesis

1) Self-propagating high temperature.
2) Low-temperature combustion synthesis.
3) Solution composition synthesis.
4) Gel combustion.
5) Sol-gel combustion.
6) Emulsion combustion.
7) Volume combustion etc.

3.1. Sol-Gel Combustion Method for Preparation of Ferrites

The sol-gel combustion method is an efficient and widely used technique for synthesizing ferrites with controlled particle size and high purity. This method involves dissolving metal precursors in a solution containing a suitable fuel, such as citric acid or glycine, to form a homogeneous sol. The sol undergoes gelation, forming a network that traps metal ions uniformly. Upon heating, the gel experiences a self-propagating combustion reaction, leading to the rapid formation of ultrafine ferrite powders. The sol-gel combustion method offers several advantages, including low synthesis temperatures, short processing times, and excellent chemical homogeneity. Additionally, it enables the production of nanostructured ferrites with tailored magnetic and electrical properties, making it ideal for applications in sensors, catalysts, and electromagnetic devices. The ability to control composition and morphology at the nanoscale makes this method particularly useful for advanced ferrite-based technologies.

4. SYNTHESIS OF FERRITE MATERIALS

The Mg [(Sm) 0.4 (Dy)0.6]$_x$Fe$_{2-x}$O$_4$, Mg [(Sm)0.5(Dy)0.5]xFe$_{2-x}$O$_4$, Mg [(Sm) 0.6(Dy)0.4]x Fe$_{2-x}$O$_4$ (x = 0.05 to 0.3 in steps of 0.05) ferrite materials were synthesized by chemical combustion route, in which starting reagents were used of AR grade magnesium, ferrous, samarium and dysprosium nitrates and glycine. The magnesium nitrate (Mg $(NO_3)_2$), ferrous nitrate ($Fe(NO_3)_2$), samarium nitrate ($Sm(NO_3)_2$), and dysprosium nitrate ($Dy(NO_3)_2$) were weighted in the required proportion and dissolved in double distilled water. The solution was heated until the ignition process of the material is completed. The as-synthesized powder is ground using agate mortar to get a fine powder of samples and then calcined in air at 600ºC for 1 hr. and in the end sintered at 1000ºC for 1hr.

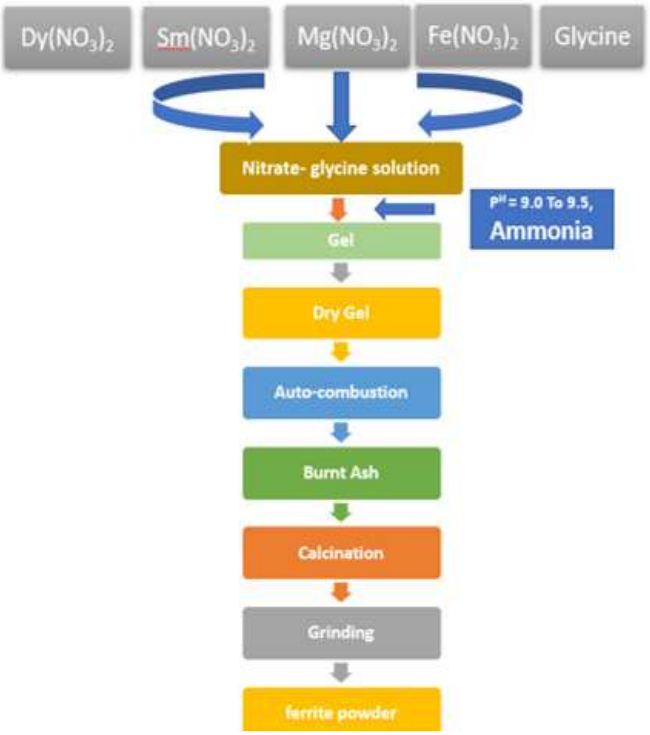

Fig. 1: Flowchart for preparation of ferrite

Fig 2: Preparation of ferrite powder

4.1. Preparation of pellet.

At first, the die was washed with acetone. The prepared powder is mixed with a binder then it is ground using its agate mortar. Acetone can be evaporated. The only dry powder is in the die of size 1.5 cm diameter which can be pressed with a load of 16 per inch square for some time [13].

4.2. Formation of toroid

Initially die was cleaned by using acetone, and the Powder of 5 gram weight is taken which can be added with a binder then it is ground with an agate motor. The dry powder was inserted into a die of size 2cm. The inner diameter of the toroid is about 1 cm, the Powder can place with a load of 6 tons per inch square for 5 minutes. The average height of the toroid is about 0.2 to 0.4 cm Solenoid is bent in a circular ring it becomes to toroid it is used as an inductance coil in many applications.

4.3. Final sintering

The final powder and pellet are sintered in the atmosphere at a temperature of about 10000C for 1 hour. The schedule for final sintering is as below,

1) At a rate of 30C per minute temperature was given for material and it was increased up to 1000 0C.
2) Then it is kept for 1 hour.
3) The temperature is decreased at a rate of 20C per minute.
4) The product is at room temperature.

5. CONCLUSIONS

The preparation methods of ferrites play a crucial role in determining their structural, morphological, and magnetic properties. Various synthesis techniques, including solid-state reaction, sol-gel, co-precipitation, hydrothermal, and microwave-assisted methods, offer unique advantages and challenges. While traditional methods provide large-scale production, wet chemical approaches enable better control over particle size and composition. The sol-gel combustion method, in particular, offers an efficient route for synthesizing nanostructured ferrites with enhanced properties. As research advances, optimizing these preparation techniques will be key to improving the performance of ferrites in diverse applications, from electronics to biomedical fields, paving the way for innovative technological developments.

6. ACKNOWLEDGEMENT

Author is thankful to Shivaji University, Kolhapur for availing laboratory facilities

REFERENCES

[1]. Young R.J., Wu T.B., and Lin I.N., Mat. Res. Bull., 22 (1987), 1472.
[2]. Patil R.S., Kakatkar S.V., Sankpal A.M., Sawant S. R., Suryavanshi S.S., Ghodake U.R. and Kamat R.K., IJAP. 32 (1994), 193.
[3]. Martin J.L., Rojas R.M., Vila E., Martinez O.G., Mat. Res. Bull. 29, No.111994, 1163-1173.
[4]. Gallagher P.K., Schrey F., Amm. Ceram. Soc. 47. (1964), 434.

[5]. Reijnen P.J.L., Science of ceramics, 4, 169, (1968)

[6]. J.M. Longo, H. S Horowitz, and L.R. Clavenna, "Solid State Chemistry-a Contempiry overview," Edited by Smith L. Holt, Joseph B. Milstein and Murry Robbins Advances in Chemistry Series, 186, American Chemical Society's

[7]. A. Verma, T. C. Goel, R. G. Mendiratta, and P. Kishan, J. of Mag. and Mang Mat 208 (2000), 13-1.

[8]. J. Madhurisailaja "Synthesis and Properties of Ni-Zn Nano Ferrite by Citrate Precursor Method for High Frequency Applications" International Journal of Engineering Research and Technology (IJERT) vol 12,2013.

[9]. A. T. Raghavender, Sagar E. Shirsath, K. Vijaya Kumar "Synthesis and study of nanocrystalline Ni–Cu–Zn ferrites prepared by oxalate based precursor method" Journal of Alloys and Compounds, Volume 509, Issue 25, 23 June 2011, Pages 7004-7008.

[10]. P.S. Anil Kumar, J. J. Shrotri, C.E. Deshpande, S.K. Date, Appl. Phys. Vol.81No.8 (199) 4788-4790.

[11]. B. K. Das, "Preparation and Characterization of Materials," Edited by J. M. Honig and C.N.R Rao, September 2017 Academic Press, New York (1981) 77-99

[12]. Jeevan S. Ghodake, Permeability and microwave absorption properties of dysprosium substituted magnesium ferrite, Journal of Emerging Technologies and Innovative Research, Vol.6, Issue 4 (2019) 354-360.

[13]. U. R. Ghodake, N. D. Chaudhari, R. C. Kambale and S. S. Suryawanshi, Initial permeability studies of Mn substituted Mg-Zn ferrites synthesized by oxalate precursors, Physics Procedia, 54 (2014) 152-158.

*****

Interferometric Method: A Tool for Study of Molecular Behaviour

Dr. Pawan S. Kachave

Department of Physics, DSM's College of Arts, Commerce and Science, Parbhani. (M.S.) India
Email: *pkachave3@gmail.com*

ABSTRACT

Interferometry, a technique that exploits the wave-like nature of light, has emerged as a powerful tool in the study of molecular behaviour. By precisely measuring the interference patterns generated by light waves, scientists can glean invaluable insights into the structure, dynamics, and interactions of molecules. This chapter will delve into the fundamental principles of interferometry and explore its diverse applications in molecular research.

Keywords: *Ultrasonic, Interferometry, Molecular Behaviour, Ultrasonic velocity.*

1. INTRODUCTION

1.1 Principles of Interferometry

At its core, interferometry relies on the superposition of two or more coherent light waves. Coherence, in this context, refers to the consistent phase relationship between the waves. When these waves overlap, they interfere, either constructively (resulting in amplified intensity) or destructively (resulting in diminished intensity). This interference pattern, a series of bright and dark fringes, carries information about the path difference travelled by the interfering waves.

1.2 Types of Interferometers

Several types of interferometers are employed in molecular studies, each with its own unique advantages:

Michelson Interferometer: This classic design splits a single beam of light into two paths, which are then recombined after traversing different distances. The resulting interference pattern is highly sensitive to changes in the optical path length, making it suitable for measuring small displacements or refractive index variations.

Mach-Zehnder Interferometer: Similar to the Michelson interferometer, but with a more robust configuration, the Mach-Zehnder interferometer offers greater flexibility in controlling the optical path lengths and allows for more complex experimental setups.

Sagnac Interferometer: This ring-based interferometer is particularly sensitive to rotations, making it useful in applications such as gyroscopes and optical sensors.

2. METHODOLOGY

2.1 Spectroscopy

Fourier Transform Infrared (FTIR) Spectroscopy: FTIR spectroscopy utilizes Michelson interferometry to analyze the infrared absorption or emission spectra of molecules. By measuring the interference pattern generated by the sample, FTIR spectrometers can accurately determine the

vibrational frequencies of molecular bonds, providing valuable information about molecular structure and dynamics.

Fourier Transform Raman Spectroscopy: Similar to FTIR, Fourier Transform Raman spectroscopy employs interferometry to analyze Raman scattering, an inelastic scattering of light by molecules. This technique provides complementary information to infrared spectroscopy, enabling a more comprehensive understanding of molecular vibrational modes.

2.2 Microscopy

Interferometric Microscopy: Interferometric microscopy techniques, such as differential interference contrast (DIC) microscopy and phase contrast microscopy, enhance the contrast of transparent or weakly absorbing samples by converting phase shifts induced by the sample into intensity variations. This allows for visualization of subtle details in biological cells and tissues.

Atomic Force Microscopy (AFM): While not strictly an optical interferometer, AFM utilizes a sharp tip to probe the surface of a sample. The deflection of the tip, measured interferometrically, provides information about the topography and mechanical properties of the sample at the atomic level.

2.3 Refractive Index Measurements

Interferometry is highly sensitive to changes in refractive index. This property is exploited in a variety of applications, including:

Concentration Measurements: By monitoring the refractive index of a solution, interferometric techniques can accurately measure the concentration of solutes, enabling real-time analysis of chemical reactions and biochemical processes.

Gas Analysis: Interferometers can be used to detect and quantify trace gases in air or other gaseous mixtures, finding applications in environmental monitoring and industrial process control.

2.4 Surface Plasmon Resonance (SPR)

SPR, a label-free technique, utilizes the interaction of light with surface plasmons (collective oscillations of electrons at a metal-dielectric interface) to detect and quantify biomolecular interactions. Interferometric detection enhances the sensitivity and accuracy of SPR measurements, enabling the study of protein-protein interactions, antibody-antigen binding, and DNA hybridization.

2.5 Advantages of Interferometric Methods

High Sensitivity: Interferometric techniques are inherently sensitive to small changes in optical path length, enabling the detection of minute variations in refractive index, displacement, or other physical parameters.

High Resolution: The high spatial resolution of interferometric microscopy allows for detailed imaging of cellular structures and subcellular components.

Versatility: Interferometric methods can be adapted to a wide range of applications, from spectroscopy and microscopy to chemical sensing and biomolecular interaction analysis.

Non-Destructive: In many cases, interferometric measurements can be performed without altering or damaging the sample, making them suitable for the study of delicate biological specimens.

2.6 Challenges and Future Directions

Despite their numerous advantages, interferometric methods also face certain challenges:

Environmental Sensitivity: Interferometric measurements can be susceptible to environmental disturbances, such as vibrations and temperature fluctuations, which can introduce noise and artifacts into the data.

Data Analysis: Analyzing and interpreting complex interference patterns can be challenging, requiring sophisticated data processing and analysis techniques.

Cost: High-end interferometers and associated equipment can be expensive, limiting their accessibility to some research groups. Despite these challenges, ongoing research and development efforts are continuously improving the performance and expanding the capabilities of interferometric methods. Advancements in materials science, nanotechnology, and computational techniques are paving the way for new and innovative applications in molecular research. For example, the

development of integrated photonic circuits is enabling the miniaturization and integration of interferometers into compact and portable devices, opening up new possibilities for point-of-care diagnostics and field-based measurements.

3. RESULT AND DISCUSSION

3.1 Ultrasonic Interferometer: A Specific Case

Ultrasonic interferometry provides a unique approach to studying molecular behavior by utilizing high-frequency sound waves. In this technique, a piezoelectric transducer generates ultrasonic waves that propagate through the medium under investigation. These waves are reflected back from a fixed reflector, and the resulting interference pattern is analyzed to determine the speed of sound in the medium.

The speed of sound in a medium is influenced by various factors, including temperature, pressure, and the presence of dissolved substances. By precisely measuring the speed of sound, ultrasonic interferometry can be used to:

Determine the concentration of solutes: The speed of sound in a solution changes with the concentration of dissolved substances. By calibrating the instrument with known concentrations, ultrasonic interferometry can be used to accurately determine the concentration of various analytes, such as electrolytes, sugars, and proteins.

Study molecular interactions: Changes in the speed of sound can provide insights into molecular interactions, such as solute-solvent interactions, molecular association, and complex formation.

Investigate thermodynamic properties: Ultrasonic interferometry can be used to determine various thermodynamic properties of liquids, such as adiabatic compressibility, density, and molar volume.

3.2 Experimental Setup

A typical ultrasonic interferometer consists of:

A piezoelectric transducer: This device generates and receives ultrasonic waves.

A sample cell: The sample under investigation is placed in a temperature-controlled sample cell.

An electronic circuit: This circuit generates and amplifies the ultrasonic signal, detects the received signal, and processes the data.

A data acquisition system: The data acquisition system records the interference pattern and processes it to determine the speed of sound.

3.3 Applications of Ultrasonic Interferometry

Ultrasonic interferometry has found widespread applications in various fields, including:

Analytical chemistry: Concentration determination in various solutions, such as blood serum, pharmaceutical formulations, and industrial process streams.

Biochemistry: Study of protein-ligand interactions, enzyme kinetics, and bio-molecular association.

Physical chemistry: Determination of thermodynamic properties of liquids, such as adiabatic compressibility and density.

Food science: Quality control and analysis of food products, such as milk, juices, and alcoholic beverages.

4. CONCLUSION

Ultrasonic interferometry is a technique that uses ultrasonic waves to measure the velocity of sound in liquids. Ultrasonic interferometry provides a sensitive and non-destructive method for studying molecular behaviour. By precisely measuring the speed of sound in a medium, this technique can provide valuable insights into the concentration of solutes, molecular interactions, and thermodynamic properties. An Ultrasonic Interferometer is a simple and direct device to determine the ultrasonic velocity in solids, liquids and gases with a high degree of accuracy. Continued advancements in transducer technology, electronic circuitry, and data analysis techniques are expected to further enhance the capabilities of ultrasonic interferometry in the years to come.

REFERENCES

[1]. Mason, W. P. (1964). Physical Acoustics: Principles and Methods. Academic Press.
[2]. Beyer, R. T. (1997). Physical Acoustics and the Properties of Solids. Springer-Verlag.
[3]. Carlin, B. (1949). Ultrasonic Technology. McGraw-Hill.
[4]. Balachandran, W. (1980). Ultrasonic Methods for Process Control. Elsevier.

*****

Study of Properties of NiS Thin Films for Optoelectronic Applications

Dr. V. B. Sanap

Department of Physics, Yeshwantrao Chavan College, Sillod, Dist. Chh. Sambhajinagar (M.S.), India
Email: *vbs.research@gmail.com*

ABSTRACT

Nickel Sulphide (NiS) thin films have been deposited on glass substrate by a simple chemical technique known as chemical bath deposition (CBD) technique. The films have been synthesized using grade I chemicals like Nickel sulphate, thiourea and ammonia solution. The as-deposited films have been prepared for varying deposition parameters such as concentration of solution, deposition time, pH of solution, temperature, etc. The obtained films were characterized for the study of structural, morphological and optical properties using X-ray diffraction (XRD), scanning electron microscopy (SEM), UV-visible spectroscopy (UV-VIS). The XRD study confirms the cubic structure of as-deposited NiS thin film with good crystallinity. The grain size obtained is in the range of 54nm to 78nm. The optical study reveals the good quality nano-crystalline films with energy band gap ranging from 1.31eV to 1.43eV. Overall study indicates the prepared NiS thin film has a good crystallinity with uniform morphology which is useful for optoelectronic applications.

Keywords: *Chemical bath deposition, Nickel sulphide, thin films, NiS.*

1. INTRODUCTION

Nickel sulphide (NiS) is a semiconductor material belongs to VIII–VI compound materials. It is one of the most attractive materials due to its high reflection in the infrared range, electron mobility and low toxicity. NiS thin films have a number of applications in various devices such as solar selective coatings, solar cells, photoconductors, sensors, IR detectors, as an electrode in photo electrochemical storage device etc. [1-3]

A variety of methods like electro-deposition, SILAR, thermal and photochemical chemical vapour deposition, pulsed laser ablation, metal-organic chemical vapour deposition can be used for the preparation of nickel sulphide thin films. [4-7]

Recently, chemical bath deposition technique has become more popular, due to its numerous advantages. Chemical bath deposition technique is easy, inexpensive and convenient method for large area preparation of thin films. Another advantage is to deposit thin films at close to room temperature on different kinds, shapes and sizes of substrates [8-11].

In this study, the effect of various deposition parameters on the properties of thin films were studied by characterising the deposited films using X-ray diffractometer, scanning electron microscopy and UV-Visible Spectrophotometer techniques. The obtained results are very useful for many scientific, technological and industrial applications in the field of optoelectronic devices.

2. EXPERIMENTAL DETAILS

Grade I chemicals have been used for the deposition of NiS thin film. Solutions of various concentration of nickel sulphate and thiourea prepared in double distilled water is used for deposition

of nickel sulphide films. The pH of solution was adjusted by adding ammonia solution slowly in it. The solution was stirred and transferred to another container containing substrate. The resulting solution was kept at 70±2ºC for different deposition time. Commercial soda lime glass slides were used as substrate for the deposition. Cleaning of substrate is important in deposition of thin films; cleaning steps and growth procedure is reported elsewhere [12-14].

The crystallographic structure of films was analysed with a diffracto-meter (EXPERT-PRO) by using Cu-Kα lines (λ=1.542Å). The average grain size in the deposited films was obtained from a Debye-Scherrer's formula. Surface morphology was examined by JEOL model JSM-6400 scanning electron microscope (SEM). Optical properties were measured at room temperature by using Perklin-Elmer UV-VIS lambda-35 spectrometer, at normal incidence of light in the wavelength range 200-1000nm.

3. RESULT AND DISCUSSION

3.1. Structural and morphological properties

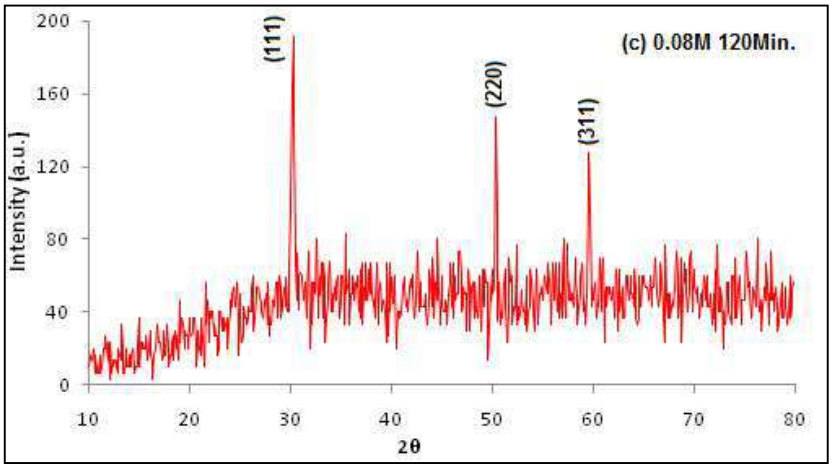

Fig. 1: XRD pattern of nickel sulphide thin film.

Fig. 1 shows the XRD pattern of nickel sulphide thin film. The nickel sulphide film shows dominant crystalline peaks at 2θ = 30.2°, 50.3° and 59.5° positions correspond to the (111), (220) and (311) planes for higher deposition time. A comparison of peak position with the standard data (JCPDS Reference code: 00-052-1027) confirms the cubic structure of nickel sulphide films [15]. XRD graph shows highest intensity diffraction peak along (111) plane indicating smooth surface with small grain size and high degree of homogeneity. It is also observed that the intensity of peaks increases with deposition time. Diffraction peak along (311) plane is observed for higher deposition time. The average grain size (g) has been obtained from the XRD patterns using the Debye-Scherrer's formula [13-15],

$$g = K\lambda / \beta \cos\theta$$

Where, K = constant taken to be 0.94,

λ = wavelength of x-ray used (1.542Å)

β = FWHM of the peak and

θ = Bragg's angle

The morphological study shows smoother and more uniform films for 0.08M concentration. The grain size obtained is in the range of 54nm to 78nm. The grain size evaluated from SEM matches with the grain size obtained by XRD.

3.2. Optical Properties

Optical properties are the properties of a material that relate to light. These properties include absorption, dispersion, dielectric polarization, luminescence, refraction, and refractive index. **Fig. 2** shows the optical absorbance spectra of nickel sulphide thin film deposited for various

deposition time. The as-deposited thin film shows gradual decrease in absorbance with the increase in wavelength of radiation. The absorbance spectra clearly indicate the higher absorbance for thicker films. This may be due to more deposition of film on the surface of substrate providing better absorption properties.

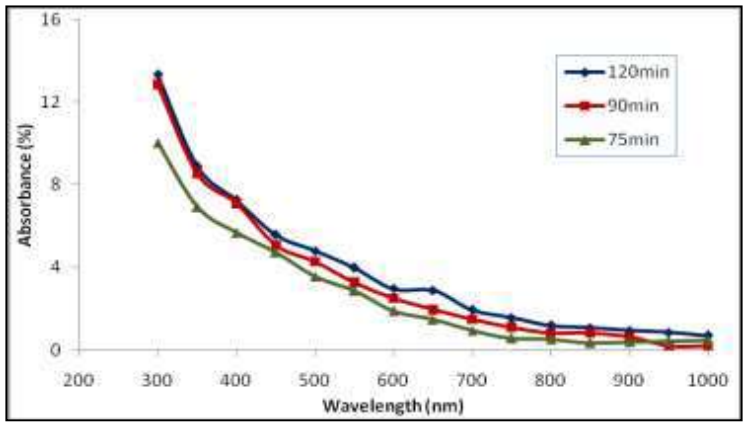

Fig. 2 Optical absorbance of nickel sulphide thin films for different deposition time.

From the absorbance data, the absorption co-efficient α was calculated using Lamberts law [16-17],

$$\ln (I_0/I_t) = 2.303\ A = \alpha\ d$$

Where, I_0 and I_t are the intensity of incident and transmitted light respectively.

A is absorbance and

d is the film thickness.

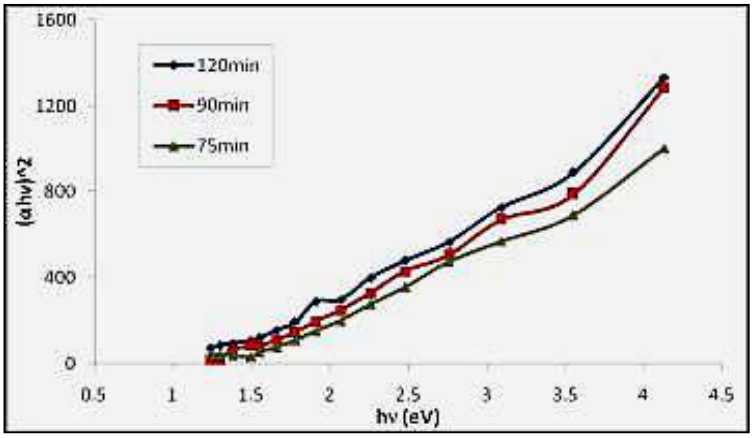

Fig. 3: Plot of $(\alpha\ h\nu)^2$ versus hν for nickel sulphide thin films

The absorption co-efficient α was found to follow the relation, [16-17]

$$\alpha h\nu = A\ (h\nu - Eg)^{1/2}$$

The band gap Eg was determined from each film by plotting $(\alpha\ h\nu)^2$ versus hν and then extrapolating the straight-line portion to the energy axis at α =0.

A band gap is the energy range in a solid where no electronic states exist. It's also known as an energy gap. The band gap energy Eg obtained is in between 1.31eV and 1.43eV for various deposition time as shown in **Fig. 3**.

CONCLUSIONS

Nanostructured NiS thin films have been successfully deposited by using low cost, simple CBD technique. The XRD patterns showed the films were polycrystalline in nature with cubic structure. The effects of deposition parameters on different properties of as-deposited thin films have been discussed. The films have been characterized using optical measurements as absorbance spectra, optical band gap energy as well as thickness, structure, surface morphology. Results obtained from characterization shows obtained films are of good quality and suitable for optoelectronic applications.

ACKNOWLEDGEMENTS

The authors are grateful to Head, DME, VNIT Nagpur for providing XRD and SEM facilities. We would also like to acknowledge Head of Instrumentation Cell, SGBAMU for UV-VIS-Near IR facilities.

REFERENCES

[1]. A. Gahtar et. Al. (2020) Advances in Materials Science, Vol. 20, No. 3(65).
[2]. Pramanik P and Biswas S (1986) J. Solid State Chem. 65 145
[3]. Anuar K., Zulkarnain Z., Saravanan N., Zuriyatina A., Sharin R., (2004) Materials Science (Medziagotyra), 10, p. 157-161.
[4]. Sartale S.D., Lokhande C.D. (2001) Materials Chemistry and Physics, 72, p. 101-104.
[5]. Lee H.Y., Kanai M., Kawai T., Kawai S. (1993) Japan Journal of Applied Physics, 32, p. 2100-2101.
[6]. Nomura R., Hayata H. (2001) Transactions of the Materials Research Society of Japan, 26, p. 1283-1286.
[7]. Cheon J.W., Talaga D.S., Zink J.I. (1997) Chemistry of Materials, 9, p. 1208-1212.
[8]. S.H.Pawar, C.H. Bhosale (1986) Bull. Matter Sci., Vol.8, No.3, 419-422.
[9]. Y.A.Salazar et al. (2006) Brazilian Journal of Physics, vol.36, No.3B.
[10]. Myeong-Hee Ko, Bonggeun Shong et.al (2018) Ceram. Int., 041.
[11]. J.G.Vazquez Luna et al. (1999) Cryst. Res. Technol. Vol.34, No.8, 949-958.
[12]. P.K.Nair, M.T.S. Nair et al (1989) J. Phys, D22, 829.
[13]. G.Kitaev, S.Mokrushin, A. Uritskaya, (1965) Kolloidn.Z.27, 51.
[14]. I. Oladeji, I.Chow, (1997) J.Electrochem. Soc. 144, 2342.
[15]. Kitakaze A., Sugaki A. (2001) Neues Jahrbuch Mineralogie Monatshefte, 41-48,
[16]. M.Maleki, M. Sasani Ghamsari, sh Mirdamadi, R. Ghasemzadeh (2007) Semi-conductor Physics-Quantum Electronics and Optoelectronics 10, 30.
[17]. M.S. Sonawane, M.S. Shinde and R.S. Patil (2015) Indian Journal of Pure & Applied Physics, Vol. 53, 686-690.

*****

ISBN: 978-81-970491-8-7
13
Current Research in
Science and Technology
(An Edited Book)

Morphological Behaviour Study & Dielectrical Properties of Indium (In^{3+}) Substituted Yttrium Iron Garnet

Dr. Raghunath G. Vidhate

Department of Physics, Anandrao Dhonde Alias Babaji Mahavidyalaya, Kada, Dist. Beed. (M.S.) India
Email: *rgvidhate@rediffmail.com*

ABSTRACT

The garnet series having the general formula $Y_3In_xFe_{5-x}O_{12}$ (x = 0.0, 0.2 and 0.4) were synthesized by using double sintering solid state reaction method. The samples were characterized by X-ray diffraction technique (XRD). The X-ray diffraction studies of compositions revealed the formation of single phase cubic structure with lattice constant ranging from 12.37 to 12.43 Å up to x = 0.4. The dielectric properties were investigated using LCR-Q meter (hp HEWLETT) in the frequency range 100 Hz to 1 MHz. The dielectric constant (ε′), dielectric loss (ε″) and dielectric loss tangent (tan δ) were measured as a function of frequency by using LCR-Q meter. The frequency dependence of dielectric measurements was carried out for given samples.

Keywords: *garnet, YIG, XRD, dielectric.*

1. INTRODUCTION

Ferrites represent an important category of materials, which are in great demands due to their numerous applications in many fields. The electrical and magnetic properties of ferrites are strongly dependent on their chemical composition and their method of preparation [1, 2]. It is important to optimize the electrical and magnetic properties of ferrites, for desired applications. Due to their interesting properties scientists, researchers and engineers are still interested in designing the various types of ferries material substituted with different cations with different valences and prepared by different techniques.

Among the various types of ferrites rare earth garnet especially yttrium iron garnet (YIG) is of great importance for scientist and technologist because of their applications in microwave communication devices such as circulators, gyrators and phase shifters because of its small ferromagnetic resonance line-width, high electrical resistivity and low dielectric loss in microwave regions in many fields [3]. Yttrium iron garnet (YIG) is microwave ferrite, which in polycrystalline form has specific characteristics. The magnetic and crystallographic properties of the magnetic iron garnet have been studied by many workers [4-7]. Substituted iron garnets have found extensive use in wide band non-reciprocal microwave devices [8].

2. EXPERIMENTAL

The samples of In^{3+} substituted $Y_3In_xFe_{5-x}O_{12}$ garnets with x = 0.0,0.2 and 0.4 were prepared by well-known double sintering ceramic method in which a molar ratio of analytical Y_2O_3, Fe_2O_3 and In_2O_3 (all 99.99% pure AR grade chemicals, Mumbai) were mixed thoroughly in stoichiometric proportions and then ground to very fine powder by using agate mortar for about 3hr. These mixtures in powder form were pre-sintered in a programmable muffle furnace at 1200 ^{0}C for 24 h and cooled to

room temperature slowly at the rate of 2 ^{0}C/min. The samples were reground and re-fired at 1350 ^{0}C for 30 h and slowly cooled to room temperature at the rate of 2^0 C/min., and then reground for 1 h. The fine powdered sample was pelletized under the pressure 5 ton/inch^2.

3. RESULTS AND DISCUSSION

Mixed garnet ferrites system under investigation has been structurally investigated by X-ray diffraction technique. Typical XRD pattern for x = 0.2 sample in shown in **Fig.1.**

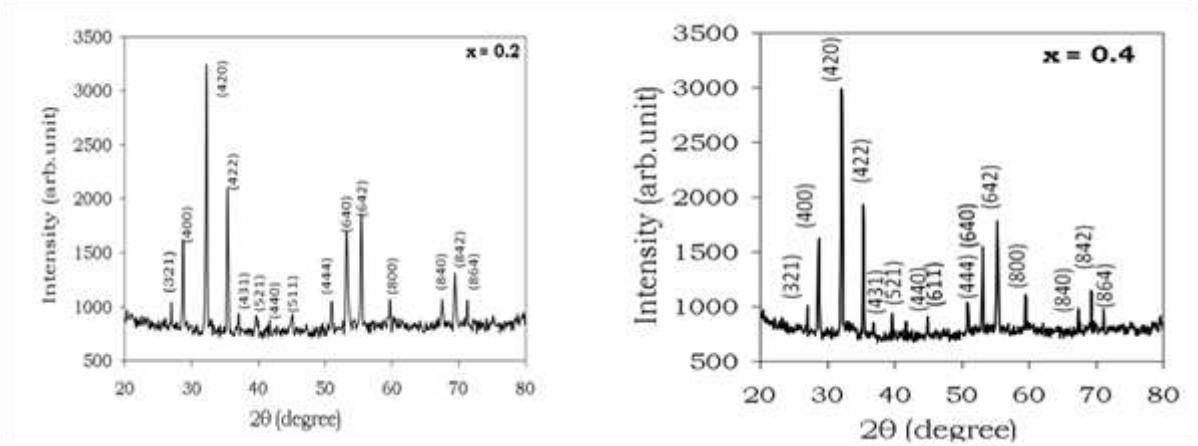

Fig. 1: XRD pattern of $Y_3In_xFe_{5-x}O_{12}$ for x = 0.2 and x=0.4 sample.

The XRD pattern shows the reflections namely (321), (400), (420), (422), (431), (521), (611), (444), (640), (642), (800) and (842). No extra peaks other than cubic structure have been observed in the XRD pattern. The Bragg peaks are sharp and intense. The lattice parameters are calculated using XRD data and are given in table-1. It is observed from table-1 that lattice constant increases with increase in indium content 'x' as shown in **Fig.1.** The ionic radii of yttrium (0.89Å) Fe^{3+} is (0.67Å) and indium (0.81Å) hence we observe variation in the lattice parameter with indium substitution. The bulk density of all samples was measured using Archimedes principle and values are tabulated in table-1. Bulk density increases with increase in indium content 'x'. Using the values of molecular weight and volume of the sample X-ray density was calculated. The values of X-ray density are also listed in **Table 1.** X-ray density increase with composition 'x' as shown in **Fig.3**.

Table 1: Lattice constant (a), X-ray density (dx), bulk density (d_B), porosity (P) and particle size (t) of $Y_3In_xFe_{5-x}O_{12}$.

x	a (Å)	dx (gm/cm^3)	d_B (gm/cm^3)	P (%)	t (μm)
0.0	12.370	5.179	4.13	20.25	3.42
0.2	12.401	5.224	4.19	19.97	3.25
0.4	12.433	5.264	4.26	19.07	3.17

The observed variation in X-ray density is attributed to increase in volume of the samples. The crystallographic parameters (lattice constant, X-ray density) are in good agreement with reported values [9] .The most intense peak (4 2 0) of XRD pattern was used to evaluate particle size of the samples. The particle size was calculated by using Scherer's formula, the values of particle size for all the composition is listed in **Table 1**.

Dielectric Measurements

The dielectric constant measurements were carried out on disc shaped pellets as a function of frequency by using two probe method. The real ε′ and imaginary ε″ parts of the dielectric constant and loss tangent tan δ of $Y_3In_xFe_{5-x}O_{12}$ were computed according to Smith and Wijn [10, 11]. The variation of the dielectric constant ε′ and dielectric loss ε″ with respect to frequency at room

temperature is shown in **Fig 4 (a).** It can be observed from **Fig 4 (a**) that dielectric constant (ε′) and **Fig.4 (b)** dielectric loss (ε′′) both decreases with increase in frequency.

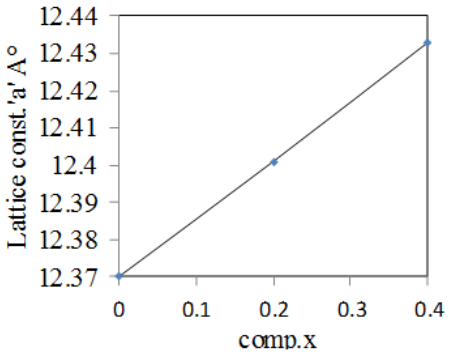

Fig. 2: Lattice constant of $Y_3In_xFe_{5-x}O_{12}$ (x = 0.0, 0.2 and x=0.4)

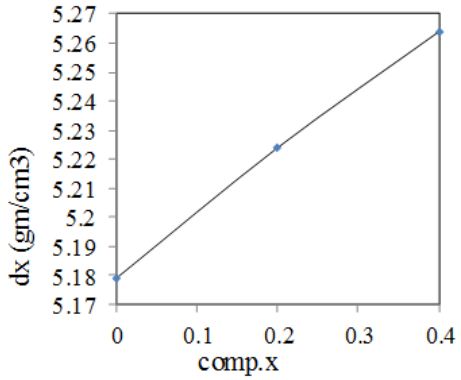

Fig. 3: X-ray density of $Y_3In_xFe_{5-x}O_{12}$ (x = 0.0,0.2 and x=0.4)

It can also be observed that dielectric loss (ε′′) decreases with increasing frequency much more rapidly than (ε′). This behaviour of dielectric constant is attributed by assuming that mechanism of polarization in ferrite is similar to that of conduction mechanism. Iwauchi [12] reported strong co-relation between the conduction mechanism and dielectric behaviour of the ferrites. **Fig. 4(c)** shows the variation of dielectric loss tangent with frequency at 300 K for all the values of 'x'. It is observed from **Fig. 4(c)** that, the parameter tan δ decreases exponentially with the increase of frequency.

Table 2: Room temperature dielectric constant (ε′), dielectric loss (ε′′) and dielectric loss tangent (tan δ) at 100 Hz, 10 KHz and 1 MHz of $Y_3In_xFe_{5-x}O_{12}$

x	Frequency								
	100 (Hz)			10 (kHz)			1(MHz)		
	ε '	ε "	tan δ	ε '	ε "	tan δ	ε '	ε "	tan δ
0.0	864	268	0.31	714	120	0.28	487	112	0.23
0.2	892	374	0.42	854	341	0.40	505	172	0.34
0.4	926	444	0.48	892	392	0.44	518	191	0.37

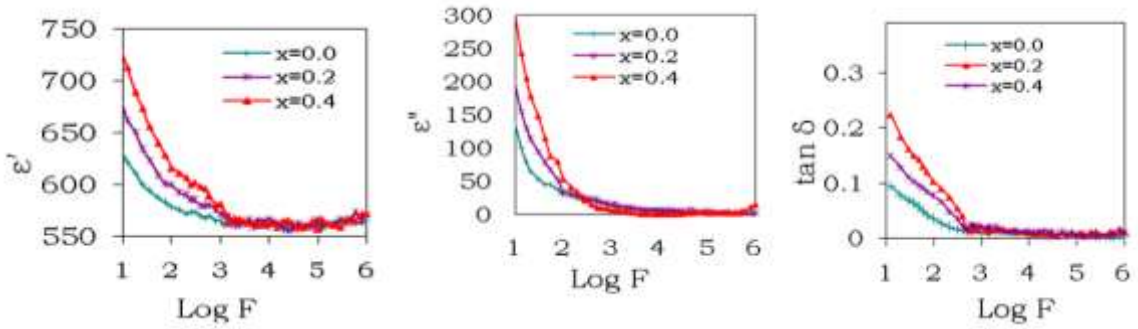

(a) (b) (c)

Fig.4: Variation of (a) dielectric constant (ε'), (b) dielectric loss (ε'') and (c) dielectric loss tangent (tanδ) with logarithm of frequency (log f) of $Y_3In_xFe_{5-x}O_{12}$ (x = 0.0, 0.2 and 0.4).

4. CONCLUSION

The garnet system $Y_3In_xFe_{5-x}O_{12}$ (x = 0.0, 0.2 and 0.4) have been successfully prepared by standard ceramic technique. The lattice parameter increases slightly with In^{3+} substitution. The dielectric constant (ε′) and dielectric loss (ε′′) both decreases with increase in frequency. It can also be

observed that dielectric loss (ε″) decreases with increasing frequency much more rapidly than (ε′). The dielectric loss tangent (tan δ) also decreases exponentially with the increase in frequency.

REFERENCES

[1]. Ibetombi Soibam, Sumitra phanjoubam, H. B. Sharma, H N K Sharma and Chandra Prakash. Ind. J. Phys. 83 (3) (2009) 285.

[2]. B. K. Kuanr, P. K. Singh, P. Kisan, N. Kumar, S.L.N. Rao, G.P. Srivastava. J. Appl. Phys. 8 (1986) 63

[3]. Guo Cuijing, Zhang Wei, Ji Rongjin, Zeng Yanwei. J.Magn. Magn. Mater. 323 (2011) 611.

[4]. S. Geller and M. A. Gilleo J. Phys. chem. Solids 3 (1957) 30.

[5]. M. A. Gilleo and Geller S.Phys. Rev. 110, (1958) 73.

[6]. M. A.Gilleo, J. Phys. Chem. Solids 13 (1960) 33.

[7]. E. E. Anderson, J. Phys. Soc. Japan Suppl. 17 (1962) 365.

[8]. B. Lax and K. Button, "Microwave ferrites and ferri-magnetics", McGraw-Hill Book Co. Inc New York (1962).

[9]. J. Richard Cunningham and Elmer, E. Anderson J.Appl.Phys.32,(1961)S388

[10]. J. Smit and H. P. J. Wijn, Ferrites, New York, Wiley, 1959.

[11]. Hongjie Zhao Ji Zhou Yang Bai Zhilun Gui Longtu Li, J. Magn. Magn. Mater. 280 (2004) 208.

[12]. K. Iwauchi, Jap. Appl. Phys. 10 (1971) 1520.

*****

ISBN: 978-81-970491-8-7
14
Current Research in
Science and Technology
(An Edited Book)

Reduced Potential Curves for the Diatomic Mercury Halides

Dr. Suchita V. Deshmukh

Department of Physics, Indraraj Arts, Commerce and Science College, Sillod
Chhatrapati Sambhajinagar. (M.S.) India
Email: *deshsuchita@gmail.com*

ABSTRACT

The reduced potential curves (RPC) of the ground electronic states of HgCl, HgBr and HgI are constructed. These curves obey the rules of RPC scheme and also show similarity to respective RKR curves.

Keywords: *Potential energy curves, Reduced potential functions for diatomic molecules*

1. INTRODUCTION

Diatomic mercury halides HgX (X = Cl, Br and I) are used in laser. The experiment on photo-dissociation [1] of HgX_2 vapour and electron-beam excitation [2] of a mixture of Hg, Ar and halogen-bearing hydrocarbons have shown that strong lasing action in the bound-state transitions $B^2\Sigma+ - X\ ^2\Sigma+$ may be used in high-power lasers. Recently dissociation energies of HgCl, HgBr and HgI from potential energy curves reported by Bhartiya et al [3].

The potential energy curves are important in the studies of dissociation energies, Franck-Condon factors, chemical physics, laser physics etc. The potential functions can be drawn using RKR [4-6] method, which is based on an experimental data. Recently Jenc and Brandt [7] have developed a method of calculating potential energy curves, which is known as RPC. In the present study this method has been employed to construct the RPC's for the ground states of HgCl, HgBr and HgI.

2. THE REDUCED POTENTIAL ENERGY CURVES

The method suggested by Jenc and Brandt [7] uses the RKR data. The reduced potential energy curves are drawn between two parameters namely ρ on X axis and u +1 on Y axis

$$u = U/De \text{ where } U = \Sigma\ Ci\ (v+ ½)i \quad (1)$$

Ci are vibrational constants like $C_1 = \omega e$, $C_2 = - \omega exe$, $C_3 = \omega eye$ etc. De is dissociation energy.

$$\rho = \frac{r - [1-\exp(-r / \rho_{ij})]\ \rho_{ij}}{r_e - [1-\exp(-r / \rho_{ij})]\ \rho_{ij}} \quad (2)$$

Where re is equilibrium inter nuclear separation and ρij can be calculated as follows,

$$\rho_{ij} = \frac{r_e - [(3.96)\ D_e/\kappa_e]^{½}}{1 - \exp(-r_e / \rho_{ij})} \quad (3)$$

Where Ke is a force constant.

The reduced quantities fulfill following conditions.

1. $\rho \geq 0$
2. $\rho = 0$ for $r = 0$
3. $\rho = 1$ for $r = re$
4. $\rho \rightarrow \infty$ for $r = \rightarrow \infty$
5. $u \leq 0$ for $U \leq 0$
6. $u = 0$ for $U = 0$
7. $u \rightarrow \infty$ for $U \rightarrow \infty$
8. $u = -1$ for $U = -De$

3. PROPERTIES OF RPC

1) The RPC's of different molecules never intersect.

2) The RPC's of diatomic molecules slightly differing in both atomic numbers coincide.

3) While keeping one atomic number constant a considerable change in the values of other effect than a relatively small change in the values of both atomic numbers. This fact is clear in the RPC's of heavy hydrides.

4) In general the shape of RPC turns slowly to the right around the minimum while becoming broader.

5) Rare gas molecules does not follow the rule number 2, 3 and 4. The RPC's of rare gas molecules coincide approximately to each other and form a right hand boundary of the admissible RPC region.

6) All RPC's including excited state lie in RPC region.

7) The approximate coincidence mentioned in rule 2 and 5 is very accurate in repulsive limb.

It was found that deviations from the above rule in the RPC's of the diatomic molecules might appear suggesting the possible existence of perturbation in the state or because of erroneous extrapolation of the RKR potential.

4. MOLECULAR CONSTANTS

The latest spectroscopic constants are used to construct RKR and RPC curves. All these constants are summarized in **Table 1.** Along with references [3, 8, 9, 10]. The ρ_{ij} are calculated using expression (3). For the calculation of RKR curves, the vibrational as well as rotational constants are also needed which are listed in **Table 1**.

Table1: Molecular constants of $X^2\Sigma$ of HgCl, HgBr and HgI

Constants	HgCl	HgBr	HgI
μ	29.807955	57.771192	77.935295
ωe	298.973	188.249	126.071
ωexe	2.15130	1.0359	1.27.4
ωeye	0.010112	-0.0015068	0.0159
ωeze	-0.00050562	-0.00024809	-----
αe	0.0007239	0.0003274	0.00018024
Be	0.09674	0.04345	0.02747
De	8350	5500	2750
re	2.4180	2.5916	2.80629
ρij	3.668477	4.696022	6.224255
Reference	[3,8, 9]	[3,8,10]	[3, 8,10]

Note: All constants are in cm-1 except re and ρij, which are in Å and μ, is in amu

5. VERIFICATION OF RPC

The individual RKR and RPC of HgCl, HgBr and HgI are shown in **Fig. 1** (a,b,c and a', b', c') respectively. RKR and RPCs of respective molecules have similarity.

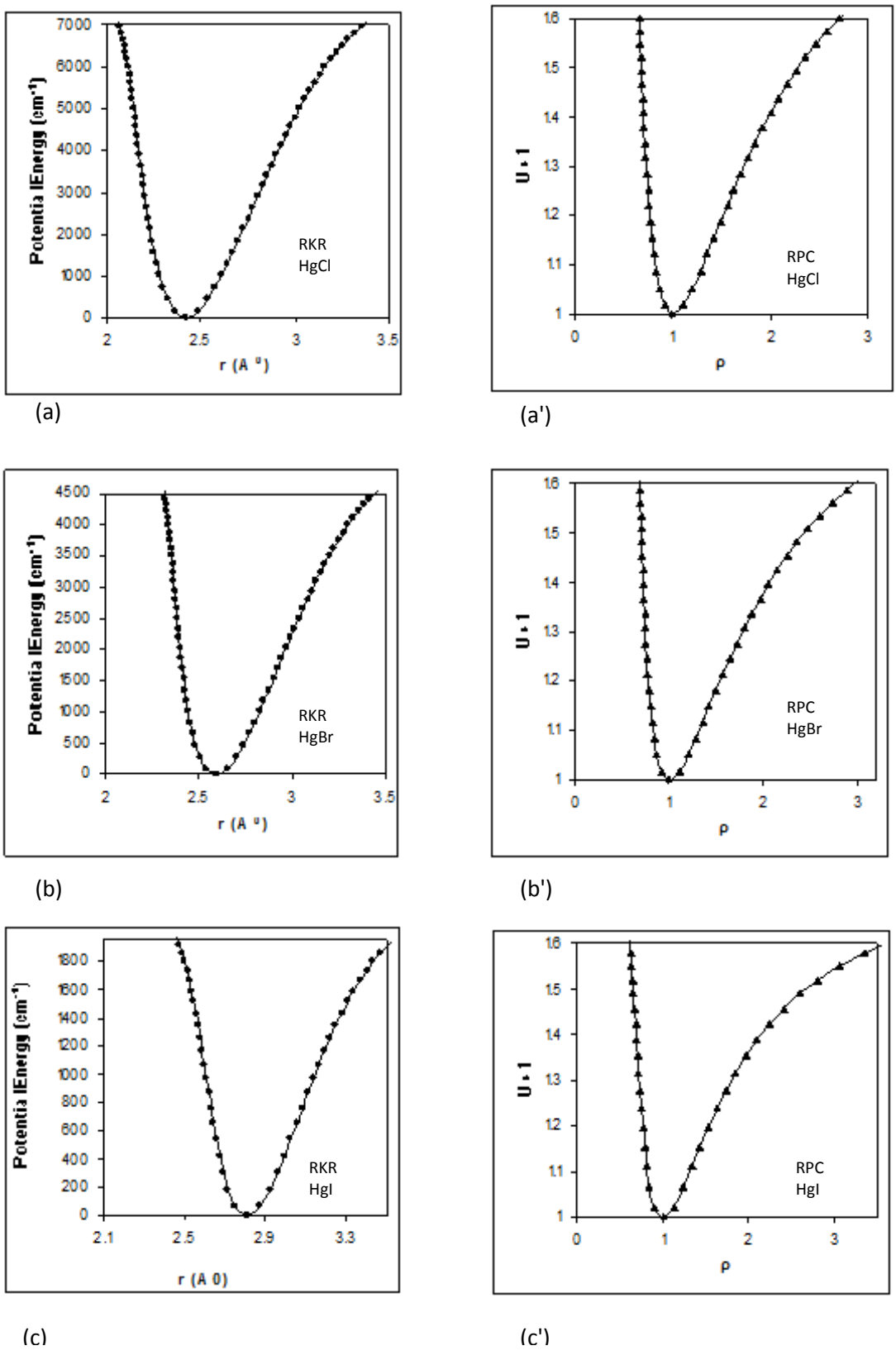

Fig. 1: The RKR of HgCl, HgBr and HgI are shown in (a, b, and c) whereas RPC are shown in (a', b', land c') respectively.

Secondly the combined RPCs of HgCl, HgBr and HgI which are shown in **Fig. 2**, the RPC of lighter molecule HgCl is in side where as the RPC of heavier molecule HgI is outside which is as expected.

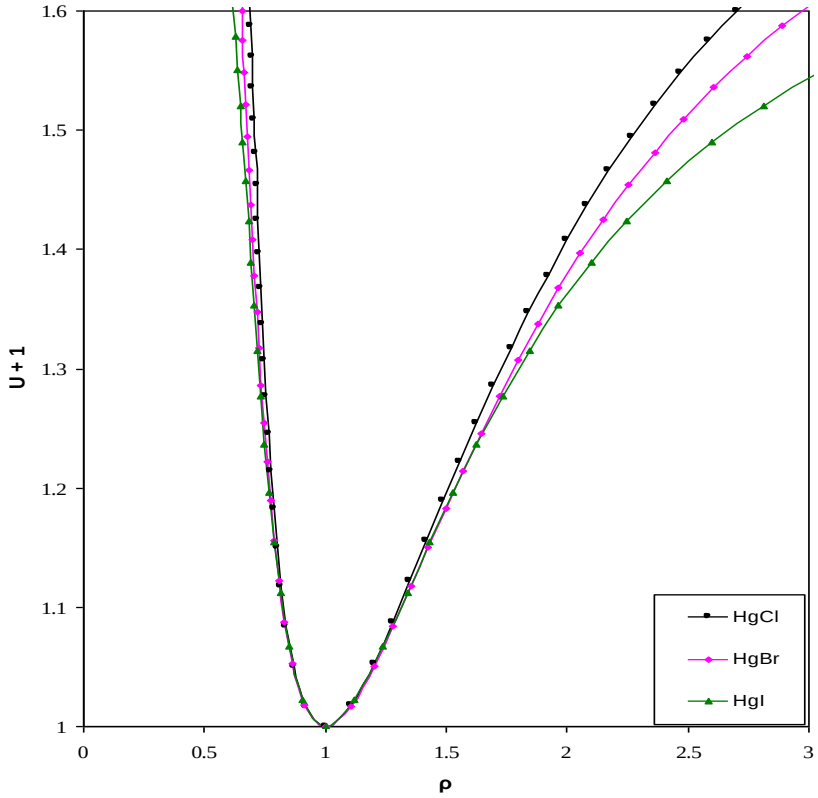

Fig.2: Combined RPC of ground state of HgCl, HgBr and HgI.

The applications of RPC could be as follows:

1. It can detect the errors in the construction of RKR.
2. It can be used to detect errors in molecular constants.
3. It can detect the errors in analysis of a spectrum due to perturbations or otherwise.

It is shown that the behavior of this group of chemically related molecules is fully in accord with the overall regularities observed for many other groups of diatomic molecules [11].

6. CONCLUSION

The RPC scheme is verified for the ground states ($X^2\Sigma$) of HgCl, HgBr and HgI molecules. The RPC scheme seems to lead to a picture that might be called, 'a periodic system of diatomic molecules'.

REFERENCES

[13]. E. J. Schimitscheck and J. E Celto.; Opt. Lett, 2, 64 (1978)
[14]. W. T. Whitney; Appl. Phys. Lett., 32, 239(1978)
[15]. J. B Bhartiya, S. H. Behere and M. .L P.Rao; J. Quant. Spectrosc. Radiat. Transfer, 43,1,95 (1990).
[16]. R.Rydberg; Z Phys, 80,514 (1933)
[17]. O. Klein; Z Phys, 76,226 (1932)
[18]. A. L. G. Rees; Proc Phys Soc., 59,998 (1947)
[19]. F. Jenc, B. A. Brandt; J. Mole. Spectrosc., 165, 590 (1994).
[20]. G. Herzberg, Spectra of diatomic molecules, Van Nostrand Reinhold Company, New York. (1950)
[21]. N. H. Cheung and T. A. Cool; J. Quant. Spectrosc. Radiat. Transfer , 21, 397 (1979)
[22]. B. E. Wilcomb and R. B. Bernstein ; J. Mol. Spectrosc., 62, 442 (1976)
[23]. S. H. Behere, M. D. Saksena, M. N. Deo and A. S. Jadhav; J. Quant. Spectrosc. Rad Trans. 97, 1-9, (2006)

*****

ISBN: 978-81-970491-8-7
15
Current Research in
Science and Technology
(An Edited Book)

Study of Laser Irradiation on Js-335 Soybean Seeds of Four Different Aged Seeds

Dr. R. R. Mistry

Department of Physics, Deogiri College, Chhatrapati Sambhajinagar (M.S.) India
Email: *ranjeetphy18@gmail.com*

ABSTRACT

This study was to determine whether the germination and electrical conductivity was related to their aged and exposure of laser light. We have taken four ages of seeds (fresh, 6 months old, 12 months old and 18 months old seeds). He-Ne laser of wavelength λ=632.8nm and intensity of beam is 5 mW/mm^2 were irradiation on seeds of time duration was 2, 4, 6, 8, 10, 12 minutes. The results indicate a positive impact of laser irradiation on seed metabolism. Growth characteristics such as germination, seedling length and speed of germination have been found to be significantly increased by laser irradiation. We recorded maximum percentage of germination of JS-335 Soybean seeds was 97.32%, 92.32%, 88.65% and 81.98 for 10 min. irradiation in fresh, 6 months old, 12 months old and 18 months old seeds respectively.

Keywords: *Laser irradiation, germination percentage, vigour index and electrical conductivity.*

1. INTRODUCTION

The laser discovery in the past century has been of great impact and application in the society from its conception until today. Among the outstanding achievements of science in the 20th century, the laser occupies a pivotal position. The characteristics of the laser radiation, such as monochromatic, coherence, polarization and high density, can be used not only in all sphere of engineering but also in medical and plant biology. Among its applications it is used in agriculture as a biostimulator device [1]. The laser light of low intensity produces biostimulation when used on seeds, seedlings and plants [2]. The basis of the stimulation mechanism in any plants physiological stage is the synergism between the polarized monochromatic laser beam and the photoreceptors that, when triggered, activate numerous biological reactions. There are many facts that indicate the biostimulating action of laser radiation on various organs and tissues in animals and plants [3]. The plants absorb light via their photoreceptors. They control all stages of plant development laser activation of plants results in an increase in their bioenergetics potential, and fermentative systems, as a stimulation of their biochemical and physiological process [3, 4].

The last 50 years different chemical additives are used for fertilizing crops and controlling pests helping to develop highly successful farm system ensuring an abundant food production. Their application causes the contamination of raw material for food production with toxins, decrease soil yielding capacity [1]. Light play a major role in growing plant. The effect of light during germination process and plant growth is undeniable

Soybean is the world's most popular oil seed crops, cultivated in more than 100 countries. Soybean seed mainly comprised of protein, fiber, vitamin, minerals and source of organic compound, which are most important factors. Establishing the quality of seed lot is a crucial step, whether for cultivation or research activities. In order to obtain the highest crop production yield and quality,

seeds of high quality that produce rapid and uniform seedling emergence are required. Germination of seeds depends on seed quality, environment, seed born pathogen and quality of soil. To increase percentage of germination by using medicine and chemical fertilizer are harmful for environment and society. The bio-stimulating agent such as laser light is the best method to increase percentage of germination. Various workers in the field provided possibility of accelerating germination of seeds, plant growth, increase their resistance to disease, enzymatic activities and concentration of chlorophyll in the seeds of several plants using LED light, micro-wave and laser light [5- 7]. The present study is conducted to study the effect of He-Ne irradiation on germination percentage, speed of germination, growth of seedling and electrical conductivity.

2. METHOD & MATERIAL

A. Seed Materials

Soybean Seeds (Glycine max., JS-335) used in this work was supplied by college of agricultural engineering and technology, Marathwada Krishi Vidyapeeth, Parbhani, India.

B. Treatments

Continuous laser irradiation at λ= 632.8nm was obtained from He-Ne and intensity of beam is 5mW/mm^2. JS-335 Soybean seeds of four different aged seeds were irradiated to 2, 4, 6, 8, 10 and 12 minutes by He-Ne laser. The irradiation treatment of seeds was performed in the dark room to avoid the influence of the Sun rays.

C. Germination Test

Seed germination capability is measured by standard germination method. The emerging normal seedlings under favorable conditions were different for different seed lot, which can be manifest in storage or in the field [8]. For germination period favourable conditions are necessary to be provided and controlled. These conditions enhance metabolic activity and which results germination.

Treated seeds were placed in petri dishes with equidistance then incubated in a germinator with $(25\pm2)^0$C temperature for 7 days. Germinated seeds were counted daily for 7 days. A seed is considered to be germinated when radicle emergence is about 5mm [9-11]. At the end of 7th day seedling length were measured. The procedure was repeated thrice for all ages of the seeds.

D. Seed Vigour Index

Seed vigour index was calculated by determining the germination percentage and seedling length of the same seed lot. We were selected randomly 10 germinated seeds and measured seedling length. The seed vigour index was calculated by using the formula

Vigour Index= Germination % x Average Seedling length (in mm.)

E. Electrical Conductivity Test

A seed sample of 10gm was sterilized with distilled water for 2-3 minutes. The clean sample was immersed in 100ml of water at 25 ± 1^0C temperature for 12hr. After that the seeds were removed by a clean forcep. The steep water left was decanted and was termed as leachate. The conductivity meter was warmed about 30 minutes before testing by Deeping in distilled water. First the conductivity of distilled water was measured then leachate was measured. The formula for calculate the electrical conductivity of seed extract was as follows.

E.C. = [Actual E.C. meter reading-E.C. of distilled water] × Cell constant factor.

3. RESULT AND DISCUSSION

3.1. Germination Test on Soybean Seeds

Improvement of seed quality and germination rate by He-Ne Laser treatment on pre-sowing Soybean seeds under laboratory condition has been analyzed in detail. In this study we have analyzed the impact of He-Ne Laser irradiation with different doses on germination rate, vigour index and electrical conductivity of leakage solution of JS-335 Soybean seeds for four different ages of seeds

(Fresh, 6 months old, 12 months old and 18 months old seeds).

The results indicate a positive impact of laser irradiation on seed metabolism. Growth characteristics such as germination, seedling length, speed of germination and vigour index have been found to be significantly increased by laser irradiation. We recorded maximum percentage of germination of JS-335 Soybean seeds was 97.32%, 92.32%, 88.65% and 81.98 for 10 min. irradiation in fresh, 6 months old, 12 months old and 18 months old seeds respectively. For high aged seeds shows lower germination percentage due to detonation. Similar results of enhanced germination percentage, seedling length and speed of germination have also been recorded in Scorzonera hispanica L. seeds by Marcela et al. (2016). St. Dinoev et al. (2004) reported that low power Laser irradiation on wheat and Maize seeds that the photon light was stored in seeds and plants utilized this stored energy during growth process and it can be seen in their development.

3.2. Electrical Conductivity of JS-335 Soybean Seeds.

Tables 5 shows the effect of Laser irradiation on Germination percentage and electrical conductivity of seed leachate of JS-335 Soybean seeds of fresh seeds, 6 months old, 12 months old and 18 months old seeds respectively. We observed electrical conductivity of fresh, 6 months old, 12 months old and 18 months old seeds where controlled seeds show 7.66, 9.31, 12.07 and 14.40µS.Cm.$^{-1}$gm.$^{-1}$ml.$^{-1}$ and for 12min. irradiation seeds shows 4.21, 5.62, 9.06, and 11.93µS.Cm.$^{-1}$gm.$^{-1}$ml.$^{-1}$ respectively. The experimental data shows that electrical conductivity was higher in controlled as well as in higher age seeds. However, the lowest electrical conductivity value for 12min. irradiation and fresh seeds.

Table 1 Effect of pre-germination exposure with different dose of He-Ne Laser on JS-335 Soybean Seed (Fresh Seeds)

Treatment	Germination %	MGT	SOG	Seedling Length	Vigour Index	E.C. (µS.cm.$^{-1}$gm.$^{-1}$ml.$^{-1}$)
Controlled	82.31	3.12	28.03	11.50	946.56	7.66
2 min.	84.98	3.15	28.84	11.80	1002.76	6.69
4 min.	92.98	3.01	35.17	12.06	1121.33	5.86
6 min.	94.65	2.84	37.09	12.13	1152.10	5.23
8 min.	96.98	2.82	38.09	12.20	1183.15	4.70
10 min.	97.65	2.50	44.49	12.33	1204.02	4.36
12 min.	97.31	2.49	45.68	12.30	1197.88	4.21

Table 2: Effect of Pre-Germination Exposure with Different Dose of He-Ne Laser on JS-335 Soybean Seed (6 months old seeds).

Treatment	Germination %	MGT	SOG	Seedling Length	Vigour Index	E.C. (µS.cm^{-1}gm^{-1}ml^{-1})
Controlled	77.32	3.11	26.28	11.03	852.83	9.31
2 min.	79.32	3.09	27.24	11.16	885.21	8.19
4 min.	81.64	2.92	31.47	11.33	924.98	7.32
6 min.	84.98	2.80	33.43	11.90	1011.26	6.15
8 min.	87.98	2.76	35.09	12.20	1073.35	5.62
10 min.	92.32	2.48	42.31	12.50	1154	4.99
12 min.	90.31	2.42	43.13	12.73	1149.64	4.51

We notice that electrical conductivity of seed leachate is correlated to germination percentage, speed of germination and seed vigour index. Simona-Laura Lasar et al. (2014) conducted experiments on germination and electrical conductivity tests on artificially aged seed lots of two wall-rocket species. Electrical conductivity was determined by using 0.1 gm of seeds in 10ml of deionized water at 25^0C for 24 hours. If seeds have low electrical conductivity, then they have high germination power, high seed vigour index. Electrolyte losses were related to decrease in seed germination capacity.

Table 3: Effect of Pre-Germination Exposure with Different Dose of He-Ne Laser on JS-335 Soybean Seed (12 months old seeds).

Treatment	Germination %	MGT	SOG	Seedling Length	Vigour Index	E.C. ($\mu S.Cm.^{-1}gm.^{-1}ml.^{-1}$)
Controlled	74.98	3.12	25.56	10.50	787.29	12.07
2 min.	78.31	3.12	26.84	10.43	816.77	11.20
4 min.	79.31	2.91	30.65	10.63	843.06	10.47
6 min.	81.98	2.79	32.28	10.83	887.84	10.03
8 min.	85.31	2.77	33.95	10.86	926.46	9.11
10 min.	88.65	2.50	40.09	11.03	977.80	9.11
12 min.	84.64	2.40	40.28	11.26	953.04	9.06

Table 4: Effect of Pre-Germination Exposure with Different Dose of He-Ne Laser on JS-335 Soybean Seed (18 months old seeds).

Treatment	Germination %	MGT	SOG	Seedling Length	Vigour Index	E.C. ($\mu S.Cm.^{-1}gm.^{-1}ml.^{-1}$)
Controlled	67.31	3.92	16.59	7.33	493.38	14.40
2 min.	71.65	4.10	18.09	7.46	534.50	14.16
4 min.	72.64	3.91	19.56	8.06	585.47	13.53
6 min.	76.31	3.50	21.09	8.20	625.74	13.14
8 min.	79.98	3.49	22.17	8.43	674.23	12.46
10 min.	74.98	3.48	24.66	8.60	705.02	12.02
12 min.	81.64	3.45	24.97	8.93	729.04	11.93

Table 5: Germination percentage and electrical conductivity of seed leachate for different aged seeds

Sample	Fresh Seeds		6 Months old Seeds		12 Months old Seeds		18 Months old Seeds	
	Germination %	E.C. ($\mu S.\ Cm^{-1}\ gm.^{-1}ml.^{-1}$)	Germination %	E.C. ($\mu S.Cm.^{-1}\ gm.^{-1}ml.^{-1}$)	Germination %	E.C. ($\mu S.Cm.^{-1}\ gm.^{-1}ml.^{-1}$)	Germination %	E.C. ($\mu S.Cm.^{-1}\ gm.^{-1}ml.^{-1}$)
Controlled	82.31	7.66	77.32	9.31	74.98	12.07	67.31	14.40
2min.	84.98	6.69	79.32	8.19	78.31	11.20	71.65	14.16
4min.	92.98	5.86	81.64	7.32	79.31	10.47	72.64	13.53
6min.	94.65	5.23	84.98	6.15	81.98	10.03	76.31	13.14
8min.	96.98	4.70	87.98	5.62	85.31	9.11	79.98	12.46
10min.	97.65	4.36	92.32	4.99	88.65	9.11	74.98	12.02
12min.	97.31	4.21	90.31	4.51	84.64	9.06	81.64	11.93

4. CONCLUSION

The germination of each seed is considered as one of the first and most fundamental life stage of a plant, so that the success in growth and yield production is also dependent on this stage. Based on the results obtained from this study it can be conclude that the Laser irradiation on seeds is more beneficial in order to obtain the maximum crop production and quality, seeds germinate quickly and have uniform seedling. The electrical conductivity method is the best and quick method as compared to other vigour test methods to predict the quality of seeds.

REFERENCES

[1]. Aladjadjiyan A. (2007) the use of Physical Methods for Growth Stimulation in Bulgari. Journal of Central European Agriculture, 8(3), 369-380.

[2]. Chen Y.P., Liu Y.J., Wang X.L., Ren Z.Y.,and Yue M. (2005). Effect of microwave and He-Ne laser on enzyme activity and biophoton emission of Isatis indigotica. Fort. J. Integr. Plant Biol., 47, 849-855.

[3]. Hernandez AC, CarballoC.A, Cruz Orea A, Ivanov R.,E. San Martin, Michtchenko, (2005)Photoacoustic Spectroscopy Applied to the Study of the Influence of Laser Irradiation on Corn Seeds. J. Physique IV (France), 125, 853-855.

[4]. Gladyszewska B (2006) Pre-sowing laser biostimulation of cereal grais, Tech. Sci., 6, 33-38.

[5]. Durkova E. (1993) the activity of Wheat grains and the effect of laser radiation. Acta Phytotech, 49, 59-66.

[6]. Gladyszewska B (2006) Pre-sowing laser biostimulation of cereal grais, Tech. Sci., 6, 33-38.

[7]. Govil S.R. Agrawal, O.C. Rai, K.P. and Thakur S.N. (1991) Physiological responses of Vigna radiate L. to nitrogen and argon laser irradiation. Ind. J. Pl. Physiol., 34 (1), 72-76.

[8]. D. C. F. S. Dias and J. Marcos Filho (1996) Electrical conductivity to assess seed vigor of soybean (Glycine max (L.) Merrill). Scientia Agricola, vol. 53, no. 1, Article ID 31-42.

[9]. N. M. Carvlho and J. Naakagawa (2000) Seeds: Science, Technology and Production, FUNEP, Jaboticabal, Brazil.

[10]. Marcela Krawiec, Agata Dziwulska-Hunek, Sawina Palonka, Magdalena Kaplan and Piotr Bayla (2016) Effect of Laser Irradiation on Seed germination

[11]. Huize Chen and Rong Han (2014) He-Ne laser treatment improves the photosynthetic efficiency of wheat exposed to enhanced UV-B radiation. Laser Physics-Elsevier, 24, 1-6.

*****

ISBN: 978-81-970491-8-7
16
Current Research in
Science and Technology
(An Edited Book)

Gas Sensing Properties of $Zn_{1-X}Ag_x O$ (X = 0.01, 0.10) Thick Films Synthesized Using Hydrothermal Route

Dr. A.V. Rajgure[a]*, Dr. L. P. Chikhale[b]

[a*]*Department of Physics, G. S. Tompe Arts, Commerce & Science College*
Chandur Bazar, Dist. Amravati (M.S.), 444704 (India)
[b]*Department of Physics, Venkatesh Mahajan Senior College, Dharashiv*
Dist. Dharashiv (M.S.), 413501 (India)
Email: *rajgure@gmail.com*

ABSTRACT

Pure and Ag-doped ZnO nanostructured powders were synthesized using the hydrothermal method. These powders were employed to fabricate sensor elements via the screen-printing technique. The synthesized sensors were characterized by X-ray diffraction (XRD) and their gas response properties were systematically analyzed. Compared to pure ZnO nanostructures, Ag-doped ZnO sensors exhibited enhanced sensitivity toward acetone at an optimal operating temperature of 300°C. Moreover, the Ag-doped sensors demonstrated notable response even at low acetone concentrations with excellent selectivity. The response and recovery times were determined to be 12 seconds and 25 seconds, respectively.

Keywords: *ZnO, Gas sensor, Hydro-thermal synthesis, Screen-printing*

1. INTRODUCTION

In recent years, there has been a growing interest in the development and investigation of nanostructured gas sensors. These sensors play a pivotal role in monitoring chemical and toxic gases in industrial settings, effectively mitigating the emission of hazardous pollutants. Metal oxide semiconductor gas sensors are particularly advantageous, offering high sensitivity and selectivity for specific analytes. Among the commonly studied materials, SnO_2 , WO_3 , and TiO_2 have been widely employed for gas sensing applications.

Zinc oxide (ZnO), an II-VI compound semiconductor with a direct band gap of 3.3 eV at room temperature, has emerged as a promising material in sensor research due to its unique electronic and structural properties. To improve the sensitivity, selectivity, and response times of ZnO-based sensors, researchers have explored doping with metallic species such as Al, Cu, and Pd. While these modifications enhance sensor performance, challenges related to synthesis complexity and the need for advanced characterization techniques often hinder the scalability of such systems [1-5].

The hydrothermal synthesis method offers a straightforward, cost-effective approach to producing high-purity, structurally uniform oxide nanostructures with controlled size and shape. The resulting materials are environmentally friendly and highly suitable for sensor applications [6].

Acetone, a highly volatile and flammable organic solvent, is extensively used in the production of plastics, fibers, and pharmaceuticals. However, prolonged exposure to acetone can pose severe health risks, including liver, kidney, and nervous system damage. Notably, acetone is also a biomarker for diabetes, making its detection critical for non-invasive medical diagnostics. These factors

emphasize the necessity of developing reliable sensors capable of detecting acetone with high sensitivity and selectivity [7-13].

In this study, we synthesized pure and Ag-doped ZnO nanostructures using the hydrothermal method and fabricated thick films via the screen-printing technique. The Ag-doped ZnO sensors demonstrated exceptional acetone sensing performance, characterized by high sensitivity, rapid response and recovery times, and strong selectivity.

2. MATERIALS AND METHODS

2.1 Synthesis of $Zn_{1-x}Ag_xO$

Pure and Ag-doped ZnO powders were synthesized using the hydrothermal method. Analytical-grade zinc acetate dihydrate ($Zn(CH_3COO)_2 \cdot 2H_2O$), silver nitrate ($AgNO_3 \cdot 6H_2O$), and sodium hydroxide (NaOH, purity 99.9%) were used as precursors without further purification.

In a typical synthesis, zinc acetate and 1.6 mmol of silver nitrate were dissolved in 160 mL of deionized water. A 1M NaOH solution was then added drop wise under vigorous stirring until the pH of the solution reached 10. The resulting mixture was transferred to a sealed Teflon-lined autoclave and heated at 95°C for 3 hours. After cooling to room temperature, the precipitates were centrifuged and washed three times with deionized water. The resulting powder was air-dried at 50°C for 2 hours to obtain Ag-doped ZnO. Pure ZnO was synthesized following the same procedure without the addition of silver nitrate.

The synthesized powders were analyzed using XRD for structural characterization for analysis. The powders were printed on alumina substrates via the screen-printing technique, and the resulting films were sintered at 700°C for 2 hours. Silver-patterned electrodes were applied to the sintered films for gas sensing studies.

Table 1: Samples identification $Zn_{1-X}Ag_XO$

Mol % Ag doping	Sample Code	Crystal size
Pure ZnO	S1	68
X=0.01	S2	55
X=0.10	S3	62

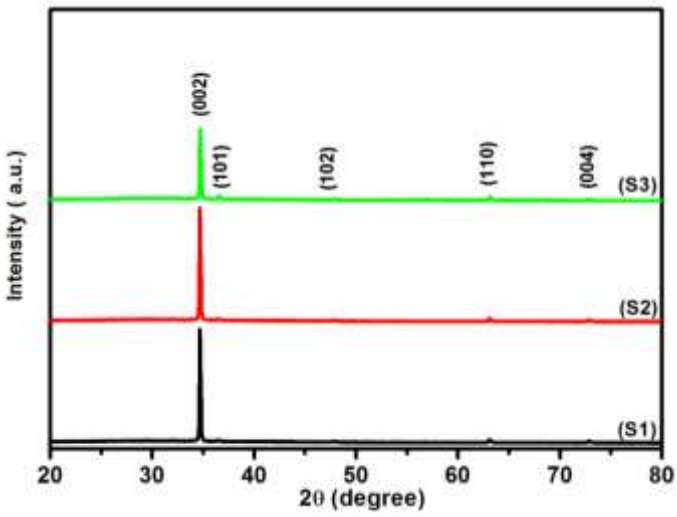

Fig. 1: The XRD patterns of the sintered samples

3. RESULTS AND DISCUSSION

3.1 Structural Properties

The XRD patterns of the sintered samples (S1, S2, S3) are shown in **Fig. 1**. The diffraction peaks correspond to planes (100), (002), (101), (102), (110), (103), (200), (112), and (201), confirming the hexagonal wurtzite structure of ZnO. Weak peaks corresponding to Ag doping were observed, consistent with JCPDS data (36–1451). The average crystallite size, calculated using

Scherrer's formula, ranged from 60–100 nm. Doping with Ag increased the crystallite size, likely due to the larger ionic radius of Ag^{2+} (122 pm) compared to Zn^{2+} (74 pm).

3.2 Gas Sensing Properties

The gas sensing performance of the films was evaluated for acetone, ethanol, and LPG at various operating temperatures. The response was calculated using the relation:

$$S(\%) = \frac{(R_a - R_g)}{R_a} \times 100$$

Where Ra and Rg represent the sensor resistance in air and upon exposure to the target gas, respectively.

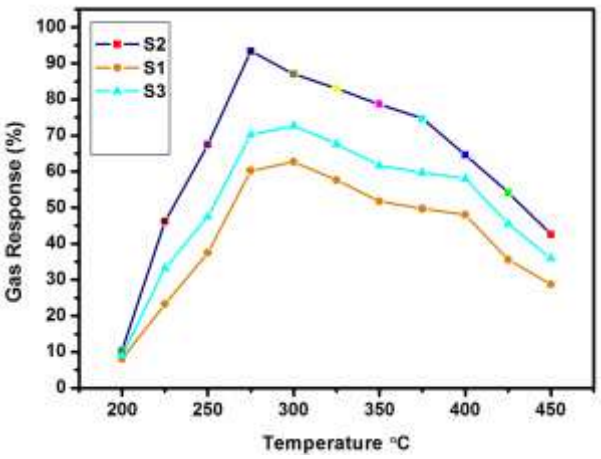

Fig.2: Acetone Gas Sensitivity

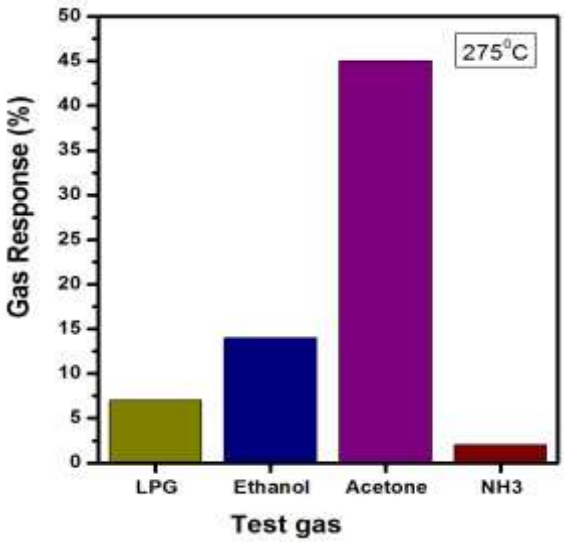

Fig. 3: The response of undoped and Ag doped ZnO to different test gases for 100ppm concentration at the optimum operating temperatures

Fig.2 shows that the gas response of various surfactant ZnO thin films for different reducing gas was studies at temperature range 200–450°C. ZnO N-type semiconductor, so primary shows reducing gas responses increases with operating temperature attained maximum value then further decrease with future rise in operating temperature [14-17]. The 2000 ppm acetone gas sensor response toward undoped and Ag doped ZnO Samples shows. The response value of 94, 70, and 60% to S1, S2, S3 respectively, the gas response across the acetone gas for the S2 sample shows maximum gas response.

Fig.3 shows the response of undoped and Ag doped ZnO to different test gases for 100 ppm concentration at the optimum operating temperatures for acetone. The ZnO sensor exhibited gas response 7, 15, 45, 3% response toward LPG, Ethanol, Acetone and NH_3 respectively. Acetone, ethanol show increase response and LPG and NH_3show low gas response. S2 Sample show good response to acetone gas 100ppm concentration, at low operating temperature 275°C.

Fig.4. Shows the transit response towards acetone gas as function of time for S2. The entire sensor sample shows fast response and recovery time toward acetone gas. Sample shows fast response and recovery time 12s and 28s respectively compared to other reducing gas. Sample S2 shows noticeable applicant for acetone gas response.

3.3. Stability and Reproductively S2 Samples

Stability and reproductively sensor consistency is strongly depend on the sensor material (**Fig.6)**. The sample S2 stability and reproductively gas response measure numerous times. The response of S2 Sample measure 10^{th}, 20^{th}, 30^{th}, 40^{th}, $50^{th}$and 60^{th} days after the first measured the gas

sensor response. It was also confirmed that the selectivity of sensor at operating temperature 275°C continuously constant last two months.

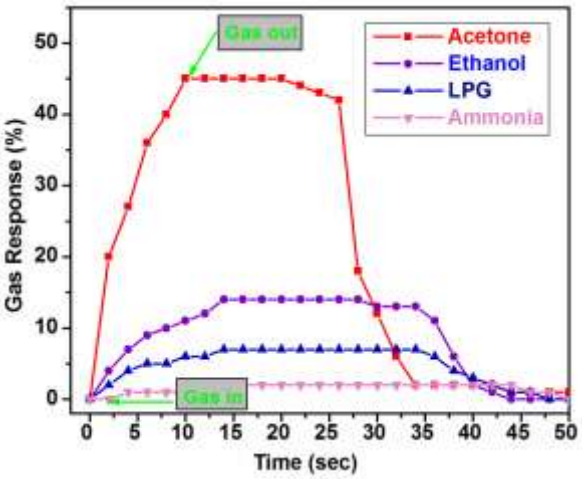

Fig.4: Transit response studies

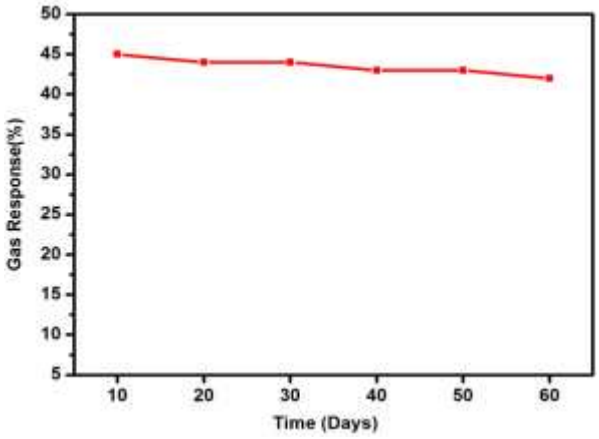

Fig.6: Stability and Reproductively S2 Sample

The gas sensing mechanism is based on carrier concentration of electron. N-type semiconductor such ZnO, the electron concentration of conduction electrons can be change either oxidation or reduction process. When ZnO film surrounding temperature in air, the chemisorbed reaction, adsorption of atmospheric oxygen generated on film surfaces O^{2-}, 0^{-}, or 0_2^{-} .When the reducing gas injected to the surrounding atmosphere, Such as acetone ,acetone molecule react between the oxygen species and vapor molecule as follows [15-22].The reducing gas acting on the ZnO sensor surface can be explained as:

$$R + O^{-} \leftrightarrow RO + e^{-}$$

Where, R representing the reducing gas. As reaction species and vapor molecule , re-injected oxygen species into surface films so that the carrier concentration were changed ,so reduced resistances of thin films[23-24].

For acetone, S2 exhibited the highest response (94%) at 275°C, outperforming both S1 (60%) and S3 (70%) at their respective optimal temperatures. The enhanced performance of S2 was attributed to its smaller grain size and increased surface area. Transient response measurements for S2 showed response and recovery times of 12 seconds and 25 seconds, respectively. The sensor maintained 94% of its initial performance after two months, indicating high stability and reliability.

4. CONCLUSION

Pure and Ag-doped ZnO nanostructures were successfully synthesized using the hydrothermal method, and their gas sensing properties were systematically studied. The Ag-doped ZnO sensor exhibited superior acetone sensing performance, characterized by high sensitivity, rapid response and recovery times, and excellent selectivity. These findings highlight the potential of Ag-doped ZnO nanostructures for industrial and medical gas sensing applications.

REFERENCES

[24]. G. Eranna, B.C. Joshi, D.P. Runthala, R.P. Gupta, Oxide materials for development of integrated gas sensors- a comprehensive review, Crit. Rev. Solid State Mater.Sci. 29 (2004) 111–188.

[25]. A.D. Brailsford, E.M. Logothetis, Selected aspects of gas sensing, Sens. Actuators B 52 (1998) 195–203.

[26]. Y. Liu, E. Koep, M.L. Liu, A highly sensitive and fast-responding SnO2 sensor fabricated by combustion chemical vapor deposition, Chem. Mater. 17 (2005) 3997–4000.

[27]. Effects of NiO addition in WO3-based gas sensors prepared by thick film process Whyoshup Noh, Yongjin Shin, Jintae Kim, Woosun Lee, Kwangjun Hong,

[28]. Sheikh A. Akbar, Jinseong Park a, Solid State Ionics 152– 153 (2002) 827– 832

[29]. Y.H. Gui, S.M. Li, J.Q. Xu, C. Li, Study on TiO2-doped ZnO thick film gas sensors enhanced by UV light at room temperature, Microelectronics J. 39 (2008) 1120–1125.

[30]. N. Kumar, A. Dorfman, J. Hahm, Fabrication of optically enhanced ZnO nanorods and microrods using novel biocatalysts, J. Nanosci. Nanotechnol. 5 (2005) 1915–1918.

[31]. P. Mitra, A.P. Chatterjee, H.S. Maiti, ZnO thin film sensor, Mater. Lett. 35 (1998) 33–38.zno

[32]. Influence of Al, In, Cu, Fe and Sn dopants on the response of the ZnO thin film gas sensor to ethanol vapour has been studied by Paraguay et al.

[33]. H. Gonga, J.Q. Hu, J.H.Wang, C.H. Ong, F.R. Zhu, Nano-crystalline Cu-doped ZnO thin film gas sensor for CO, Sens. Actuators B: Chem. 115 (2006) 247–251.

[34]. Influence of Pd-loading on gas sensing characteristics of SnO2 thick films,L.K. Bagal , J.Y. Patil , I.S. Mulla , S.S. Suryavanshi ,Ceramics International 38 (2012) 4835–4844

[35]. Zhang X Y, Dai J Y, Ong H C, Wang N, Chan H L and Choy C L 2004 Chem. Phys. Lett. 393 17

[36]. Actone gasAgency for Toxic Substances and Disease Registry, Division of Toxicology, 1600 Clifton Road NE, Mailstop F-32, Atlanta, GA 30333. Report from Department of Health and Human Services, US. Available on http://www.atsdr.cdc.gov/. P.P. Sahay, Zinc oxide thin film gas sensor for detection of acetone, J. Mater. Sci. 40 (2005) 4383–4385.

[37]. M.S. Wagh, G.H. Jain, D.R. Patil, S.A. Patil, L.A. Patil, Modified zinc oxide thick film resistors as NH3 gas sensor, Sens. Actuators B 115 (2006) 128–133.

[38]. B.D. Cullity, S.R. Stock, Elements of X-ray Diffraction, 2nded., Prentice-Hall New Jersey, 2001, 388.

[39]. Ag zno refEffect of Ag on the microstructure and electrical properties of ZnO Shu-Ting Kuo, Wei-Hsing Tuan, Jay Shieh , Sea-Fue Wang , Journal of the European Ceramic Society 27 (2007) 4521–4527

[40]. E. Comini, Metal oxide nano-crystals for gas sensing, Anal. Chim. Acta 568 (2006) 28–40.

[41]. C. Li, Z. Du, H. Yu, T. Wang, Low-temperature sensing and high sensitivity of ZnO,nanoneedles due to small size effect, Thin Solid Films 517 (2009) 5931–5934.

[42]. J.Y. Patil, M.S. Khandekar, I.S. Mulla, S.S. Suryavanshi, 2012, Combustion synthesis of magnesium ferrite as liquid petroleum gas (LPG) sensor: Effect of sintering temperature. Current Applied Physics 12, 319-324.

[43]. Small coverage low sense Al-doped zinc oxide thin films for liquid petroleum gas (LPG) sensors, P.P. Sahay∗ , R.K. Nath, Sensors and Actuators B 133 (2008) 222–227

[44]. M.E. Franke, T.J. Koplin, U. Simon, Metal and metal oxide nanoparticles in chemiresistors: does the nanoscale matter Small 2 (2006) 36–50. (recover gas)

[45]. I. Lundstrëm, Approaches and mechanisms to solid state-based sensing, Sens. Actuators B: Chem. 35–36 (1996) 11–19.

[46]. T.J. Hsueh, C.L. Hsu, S.J. Chang, I.C. Chen, laterally grown ZnO nanowire ethanol gas sensors, Sens. Actuators B: Chem. 126 (2007) 473–477.

[47]. L.J. Bie, X.N. Yan, J. Yin, Y.Q. Duan, Z.H. Yuan, Nanopillar ZnO gas sensor for hydrogen and ethanol, Sens. Actuators B: Chem. 126 (2007) 604–608.

*****

ISBN: 978-81-970491-8-7
17
Current Research in
Science and Technology
(An Edited Book)

Investigation of Structural properties of Bulk and Thin Film of Cobalt Ferrite

Dr. Mahesh K. Babrekar

Department of Physics, Indraraj Arts, Commerce and Science College, Sillod
Dist. Chhatrapati Sambhajinagar. (M.S.) India
Email: *maheshkb1973@gmail.com*

ABSTRACT

The present work has been carried out on magnetic ferrite materials to study their structural properties in most of the studies the sample is in bulk form prepared by usual ceramic technology. Recently, nano-particle ferrites are gaining importance because of their unusual properties. The reduction in the particle size from micrometer level to nanometer level greatly influenced the properties of ferrite. Several chemical methods have been employed to produce nano-particles. Nano sized ferrites with uniform particle size are desirable for a verity of applications like drug delivery, ferro-fluids, data storage, biomedical applications. Thin film ferrites are also gaining importance because of their easy preparation

Keywords: *Bulk materials, thin film, structural properties, nanoparticles*

1. INTRODUCTION

Recently nanotechnology gained tremendous attention in the research community. From the last decade remarkable research activities found to be extensively carried out in nano-science and nanotechnology. The novel nanometer scale materials with excellent and unique physical and chemical properties have been developed. Semiconductor natured polycrystalline spinel ferrites are most important magnetic materials because of their interesting magnetic and electrical properties as well as low eddy current and dielectric losses. The spinel ferrites find applications in a wide range of frequencies (microwave to radio frequency). Nanostructure have attached huge interest as rapidly growing class of materials for many applications several techniques have been used to characterize the size, crystal structure, elemental composition and variety of other physical properties of nanoparticles. Nanomaterial is important for understanding their properties and application which is about 1 to 100 mm nano-science can be used across other field like chemistry, electronic engineering, physic and material science. The polycrystalline soft ferrites show high resistivity and due to their dielectric nature are used in microwave applications [1]. The magnetic properties of spinel phase oxides are rich and complex. The important electrical and magnetic properties of spinel ferrite depend on method of preparation, type and amount of dopants etc. [2-3]. Cobalt ferrite is a well-known hard magnetic material having high magneto-crystalline anisotropy, high coercivity and moderate saturation magnetization. The principal objective of this research h article is to summarize the present knowledge on the use, advance advantages and weakness of large number of experimental techniques that are available for the characterization of nanoparticles [4].

Cobalt ferrite possesses inverse spinel structure and degree of inversion depends on method of preparation and also to study the bulk and thin film structural properties of cobalt ferrite.

2. EXPERIMENTAL

The samples of cobalt ferrite ($CoFe_2O_4$) have been prepared by standard ceramic technique using AR grade oxides of cobalt oxide, ferric oxide and nickel oxide. The powders of CoO and Fe_2O_3, NiO and Fe_2O_3 were mixed in stoichiometric proportion and wet ground. The mixed powders of CoO and Fe_2O_3 are then pre-sintered at 900^0C and 950^0C respectively. After pre-sintering the powders were reground for about two hours and then pelletized. In making the pellets polyvinyl alcohol (PVA) was used as a binder. The disc shaped pellets of cobalt ferrite and nickel ferrite were finally sintered at 1050^0C and 1100^0C respectively. The samples were then cooled slowly to the room temperature.

Thin film of Cobalt ferrite was prepared by spray pyrolysis technique on glass substrate. Solutions of ferric chloride are prepared in a molar proportion. The solutions were prepared in 1:2 ratio and mixed together and stirred for a long time. After this the mixed solution is sprayed uniformly on a glass substrate through a nozzle of 0.5mm bore under a constant pressure of 5 kg/cm^2. The temperature of the glass substrate was maintained at around 450^0C. The thin film of nickel ferrite was annealed at 550^0C for 2 hours.

The bulk samples of cobalt ferrite were characterized by X-ray diffraction (XRD) technique. The X-ray diffraction patterns were recorded taken in the 2θ range of 20^0-80^0, using Cu-Kα radiation. The XRD data was collected at room temperature.

3. RESULTS AND DISCUSSION

3.1. Structural analysis

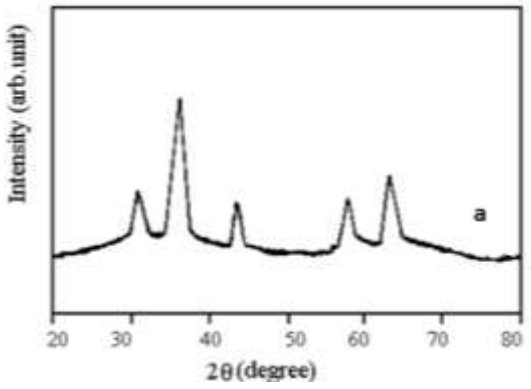

Fig. 1 XRD patterns of as prepared thin film samples of cobalt ferrite

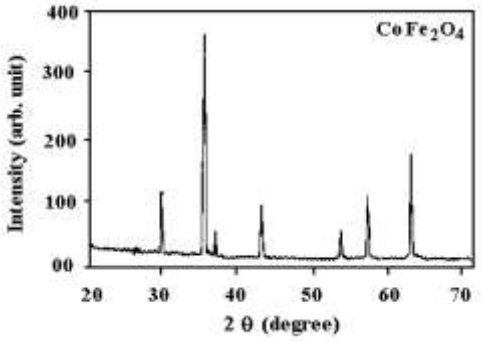

Fig. 2 X-ray diffraction pattern of bulk cobalt ferrite

X-ray Diffraction is one of the most extensively used techniques for the characterization of nanoparticle typically XRD provides information regarding the crystalline structure, nature of the phase the lattice structure of crystalline substance like unit size dimensions, bond angles, chemical composition and crystallographic structure of nature and manufactured material. XRD is a based on the constructive interference of X-Ray and the sample concern which should be crystalline. **Fig. 1** and **Fig 2** depicts the X-ray diffraction patterns of cobalt ferrite ($CoFe_2O_4$) respectively. X-ray diffraction (XRD) patterns contain Bragg peaks corresponding to cubic spinel structure. No extra peaks have been detected in the XRD patterns clearly indicate the formation of single phase cubic spinel ferrite materials. No extra peak were found in the pictograph shows the phase purity of the sample in both the samples prepared by solid state reaction method and pray pyrolysis methods. The investigated samples in the pictograph of XRD. The peak are broad is in thin film and sharp intense pick are obtained in bulk cobalt ferrite. The values obtained from X-ray Diffraction used to find inter planer spacing 'd', Bragg angle '2θ'. The values of inter planer spacing 'd', Bragg angle '2θ' are given in **Table 1** for cobalt ferrite. The lattice constant 'a' of cobalt ferrite was determined using XRD data and the values are given in **Table 1**. The values of lattice constant are in the reported range [5-6].

Table 1: Inter planer spacing (d) and Bragg angle (2θ) of cobalt ferrite

Plane (hkl)	Cobalt ferrite	
	Inter planer spacing (d)	Bragg angle (2θ)
(220)	2.958	30.33
(311)	2.524	35.80
(222)	2.416	36.42
(400)	2.094	43.52
(422)	1.71	54.05
(440)	1.52	62.90

Inter-planer spacing (d), Bragg angle (2θ) of bulk cobalt ferrite sample. Using the molecular weights and lattice constant, the X-ray density d_x of cobalt ferrite have been obtained. The value of X-ray density for cobalt ferrite also given in **Table 2.**

Table 2: Lattice constant (a), X-ray density (d_x), Particle size (t), Bulk density and Porosity (P) of bulk cobalt ferrite sample

Parameter	**Cobalt ferrite**
Lattice constant 'a' (Å)	8.383
X-ray density 'd_x' (gm/cm^2)	5.352
Particle size 't' (μm)	48
Bulk density	4.228
Porosity 'P' (%)	21

X-ray powder diffraction (XRD) is Rapid analytical technique primarily used for Phase identification on the crystalline material and can provide information on unit cell dimension and atomic spacing. The X-ray generated by cathode ray tube, filtrate to produce nano-chromatic radiation, collineated concentrated and directed towards the sample. The interaction incidence monochromatic rays with the sample interference when condition satisfy Bragg's law,

$$n\lambda = 2d \sin\theta.$$

This equation wavelength (λ) electromagnetic radiation to the diffraction angle(θ) and lattice Spacing(d) in a crystalline sample through arrangement of 2θ angles. All possible diffraction directions on of the lattice are attend to the random orientation of the powered materials. The particle size was obtained using full width at half maxima (FWHM) of most intense Bragg peak in XRD pattern using Scherrer equation [7]. The values of particle size for cobalt ferrite is summarized in Table 5.2.The bulk density was measured using mass and volume of the sample and the values are given in Table 5.2.The percentage porosity 'P' was obtained from bulk density and X-ray density and the values are given in **Table 2.** The porosity 'P' of the samples of cobalt ferrite is below 15% [8].

3.1. Thin film studies

The X-ray diffraction patterns of nickel ferrite film and cobalt ferrite film prepared at 550^0C are shown in **Fig. 1** and **Fig. 2**. No extra peak has been observed in XRD pattern. An analysis of XRD patterns indicates that sample possesses single phase cubic spinel structure. The most intense peak of (311) is clearly seen in the XRD patterns of as deposited thin film. The other peaks of cubic spinel structure are appeared when films are annealed at 550^0C [9-10]. The values of lattice constant for thin films of nickel ferrite and cobalt ferrite are given in **Table 3.** The crystallite size for (311) plane is of the order of 50-60nm and values are reported in **Table 3.**

Table 3: Lattice constant (a) and Particle size (t) for nickel and cobalt ferrite thin film

Parameter	Cobalt ferrite
Lattice constant 'a' (Å)	8.375
Particle size 't' (nm)	54

4. CONCLUSIONS

The role of several different techniques for the characterization of nanomaterial though this Compressive summary of nanoparticle characterization methods we demonstrated the use of each one of them emphasizing on their advantages and limitations as well as on explaining how they can complement each other. The bulk samples of nickel ferrite and cobalt ferrite prepared by ceramic technique. Are well characterized by X-ray diffraction technique. The structural parameter like lattice constant of nickel ferrite and cobalt ferrite is in the reported range. The sample in the form of thin film of nickel ferrite and cobalt ferrite are successfully prepared by spray pyrolysis technique. The X-ray diffraction analysis reveals the formation of single phase cubic spinel structure of the prepared materials. The resistivity obtained from current voltage characteristics is of the order of 15×10^7 ohm-cm and 7×10^7 for nickel ferrite and cobalt ferrite.

REFERENCES

[1]. L. I. Robkin and Z. I. Novikova, Ferites IZS Acad. Nauk Mink (1960) 146.
[2]. Souad Ammar, Arnaud Helfel et. al. J. Mat. Chem. 11 (2001) 186.
[3]. B.P. Ladgoankar, C.B. Kolekar, P.N. Vasamberkar and A.S. Vaingankar, Ind.J. Eng.Matt. Sci. 7 (2000) 419.
[4]. Dainius Perednis, Ludwic J. Gauckler,J. Elect. Cerm. 14 (2005) 103.
[5]. Xu Zuo, Shaloni Yan, Bernardo Barbiellini, Vincent G. Harris, C. Vittoria, J. Mag. Mag. Mat.303(2000)
[6]. B. D. Cullity, "Elements of X-ray diffraction" (Addison Wesley Public Inc. Reading, mass) (1956), 262.
[7]. P. C. Fannin, S. W. Charles and J. L. Bormann,J. Magn. Magn. Mater 201 (1999) 98.
[8]. Z. Yue, J. Zhou, Lil, H. Zhang and Z Gui,J. Magn. Magn. Mater 208 (2000) 55.
[9]. E.J.W. Verwey and J.H. de BoesRec. Trav. Chim. Pay. Bas. 55 (1936) 531
[10]. G. H. Jonker,J. Phys. Chem. Solids, 9 (1959) 105.

*****

Structural and Morphological Studies of Green Synthesised Nickel Doped Titanium Dioxide Nanoparticles Using Aloe Vera Gel as a Fuel

Dr. Veerabhadrayya M.

University College of Science, Tumkur University, Tumakuru-572103, Karnataka, India
Email: *veerabhadrayyam1974@gmail.com*

ABSTRACT

Nanocrystalline pure and Nickel (Ni) doped tin oxide (TiO_2) powders were green synthesized using Aloe vera gel as a fuel by combustion method. Prepared samples were characterized by PXRD and FESEM. The PXRD analysis revealed the tetragonal rutile phase. The grain size was estimated using Debye-Scherrer equation and Williamson-Hall method. The cell parameters were found using Rietveld refinement. The morphology study was made using FESEM pictures.

Keywords: *Titanium Dioxide, PXRD, Rietveld refinement.*

1. INTRODUCTION

Titanium dioxide (TiO_2) known as Titanium Oxide or titanium IV oxide or Titania, is naturally occurring oxide of titanium [1]. Nanocrystalline TiO_2 has shown excellent performance by comparison to other semiconductors such as ZnO and SnO_2 [2]. Titanium dioxide (TiO_2) nanoparticles are ideal semiconducting materials with large band gap for various applications such as photo catalyst, pigments, paints, toothpaste, ointments, sun/ultraviolet light screen and self-cleaning surface [3]. The high surface areas bring the beneficial to many TiO_2-based applications as it facilitates reaction/interaction [4]. Consequently the performance of TiO_2-based devices is largely influenced by the sizes of the particles. The TiO_2 play an important role in the field of green energy development. Various methods are developed for synthesis of TiO_2 nanoparticles [5-7]. But many methods are required complex equipment and complicated operations. The simple solution combustion method is an ideal method for rapid and facile preparation of metal oxides nanoparticles in air at ambient pressure. One of the primary environmental benefits of Aloe vera bio fuel is its potential to significantly reduce greenhouse gas emissions. Ethanol produced from Aloe vera can be considered a carbon-neutral fuel, as the CO_2 released during its combustion. The present work deals with the synthesis, structural and morphological study of nickel doped TiO_2 prepared by low temperature solution combustion method using *Aloe Vera* gel as a fuel.

2. EXPERIMENTAL

2.1 Materials

The raw materials used in this study are Titanium Tetrabutoxide [Ti $(OC_4H_9)_4$, 97 %, Sigma Aldrich], Nitric acid (HNO_3, 70%, SD fine), nickel nitrate [Ni $(NO_3)_2$. $6H_2O$, 99.9% sd fine] and Aloe Vera gel. All the reagents used in the synthesis were of analytical grade and used as received without further purification.

2.2 Extraction of Aloe Vera Gel

Aloe Vera leaves were collected from the plants grown in garden of the Tumkur University, Tumkur, India. Leaves were washed thoroughly with double distilled water to remove the dust particles. The rough outer green part of *Aloe vera* leaves was stripped off to get the transparent gel (Fig. 1). The gel was cut into small pieces and grounded to get uniform concentration.

Fig. 1: Extraction of *Aloe Vera* gel

2.3 Preparation of Titanium Dioxide Nanoparticles

The titanium tetrabutoxide solution was mixed with 1:1 solution of nitric acid to get titanium tetra nitrate [Ti $(NO_3)_4$] solution. Stoichiometric amount of titanium tetra nitrate and nickel nitrate [Ni $(NO_3)_2$. $6H_2O$] (2-10 mol %) were dissolved in double distilled water separately. The quantity of *Aloe Vera* gel was kept at 10 ml for all the samples. These three solutions were added to a pyrex vessel. The mixed solution was heated under constant stirring at a temperature of about 100°C on a hot plate. Then the concentration of the solution slowly became higher and eventually a gel was formed. When the temperature of the hot plate was raised to about 300°C, the gel underwent a strong, self-sustaining combustion reaction with evolution of gases in a large volume and pale yellow powder was formed. The entire combustion process ended in a few seconds. The resulting powder was then fired at a temperature higher than 400°C in a muffle furnace until complete decomposition of the carbonaceous residues was achieved. The nanopowders produced are kept in alumina crucibles and calcinated at 800 ^oC for 3 hours. The following **Fig. 2** shows the flowchart of preparation of nickel doped titanium dioxide nanoparticles.

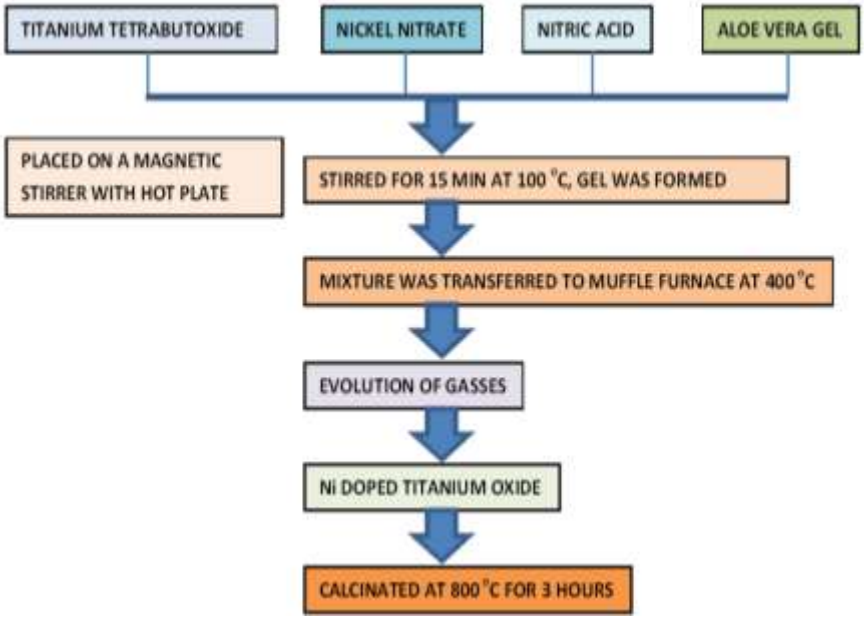

Fig. 2: Flowchart of preparation of nickel doped titanium dioxide nanoparticles

2.4 Characterization

The structural characterization of TiO_2 nanoparticles was performed using Rigaku powder X-ray diffractometer (PXRD). The diffraction patterns are recorded at room temperature (RT) using

CuKα (1.541 Å) radiation with nickel filter in the range 5°-90° at a scan rate of 2° min^{-1}. Morphology of the synthesized TiO_2 nanoparticles was examined by FESEM by Carl Zeiss Supra 55 (Germany) microscope.

3. RESULT AND DISCUSSION

3.1 Powder XRD (PXRD) studies: Indexing

PXRD patterns of undoped and Ni doped TiO_2 powder is shown in Fig. 3. All the X-ray diffraction peaks of the samples were matched with JCPDS card No.21-1276 and belong to a space group P42/mnm.

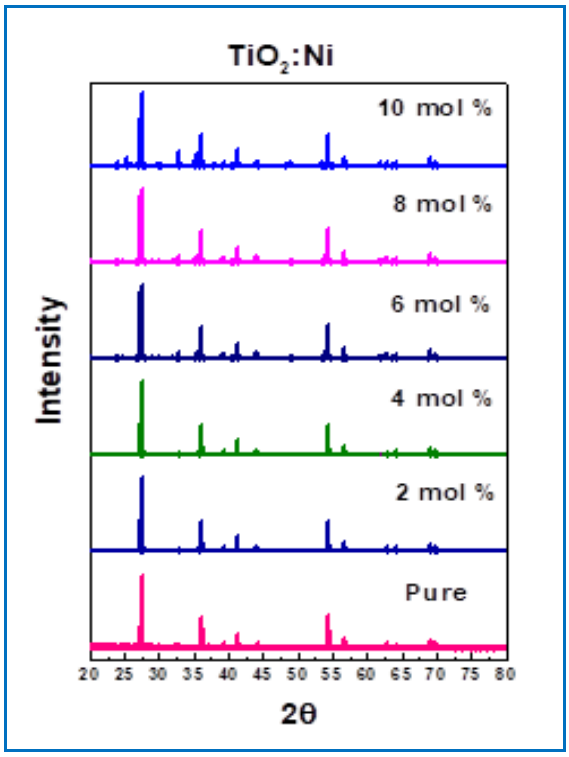

Fig. 3: PXRD patterns of Pure and Ni (2-10 mol %) doped TiO_2 nanoparticles

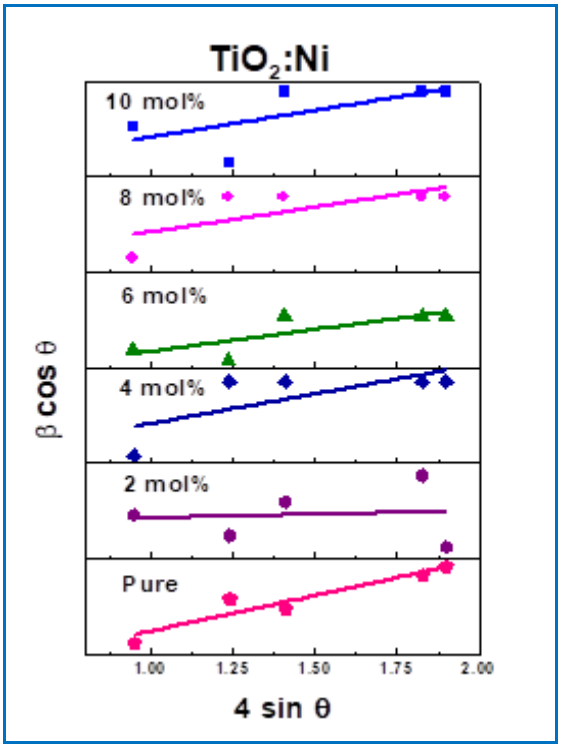

Fig. 4: W-H plots of Pure and Ni (2-10 mol %) doped TiO_2 nanoparticles

Particle size calculation

Particle size is the measurement of the diameter of individual particles that make up a material. The average particle size (D) was estimated using the Scherrer equation [8]

$$D=\frac{0.9\lambda}{\beta\cos\theta} \quad (1)$$

Where, D is the crystallite size,

λ is the X-ray wavelength,

β is the full width at half maximum of the diffraction peak, and

θ is the Bragg diffraction angle of the diffraction peaks.

Further, strain present and grain size of TiO_2 nanoparticles were estimated using Williamson-Hall [9] plots given by,

$$\beta\cos\theta = \frac{0.9\lambda}{D} + 4\varepsilon\sin\theta \quad (2)$$

Where, ε is the strain associated with the nanoparticles.

Equation (2) represents a straight line between 4 sinθ (X-axis) and β cosθ (Y-axis). The intercept of this line on Y-axis was used to calculate grain size (D).

The **Fig.4** shows the W-H plots of the TiO_2: Ni (2-10 mol %) nanopowders.

The values of particle size are tabulated in the following **Table 1.**

Table 1: Particle size of TiO_2: Ni Nano-powders

Sample	Particle Size (nm)	
	Scherrer Method	**W-H Plot**
TiO_2: Pure	50.21	53.26
TiO_2: Ni 2mol%	49.95	50.49
TiO_2: Ni 4mol%	45.22	48.85
TiO_2: Ni 6mol%	42.65	45.24
TiO_2: Ni 8mol%	41.95	43.85
TiO_2: Ni10mol%	40.15	41.97

3.2 Rietveld Refinement

To get exact lattice parameters, Rietveld refinement analysis (Fig. 5) was performed by using FULLPROF software assuming P42/mnm space group for tetragonal type structure. Pseudo-voigt function was utilized to fit the various parameters to the data point (one scale factor, one zero shifting, four background, three cell parameters, five shape and width of the peaks, one global thermal factor and two asymmetric factors). Diamond software was utilized for extracting the possible packing diagram which is shown in Fig. 6. The refined parameters and atomic functional positions are displayed in Table 2. The fitting parameters (R_p, R_{wp} and χ^2) indicate a good agreement between the refined and observed PXRD patterns.

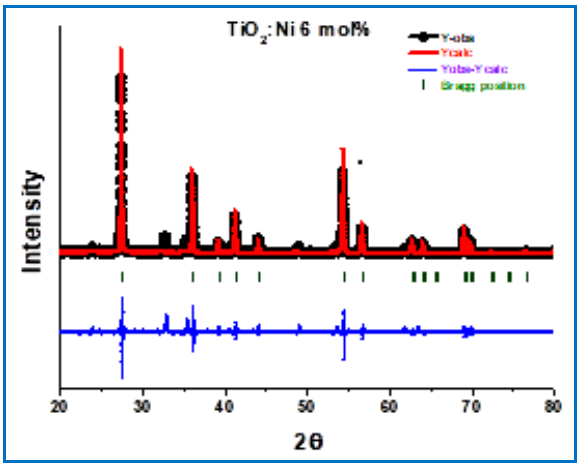

Fig. 5: Rietveld refinement of TiO_2: Ni (6 mol %) Nano powder

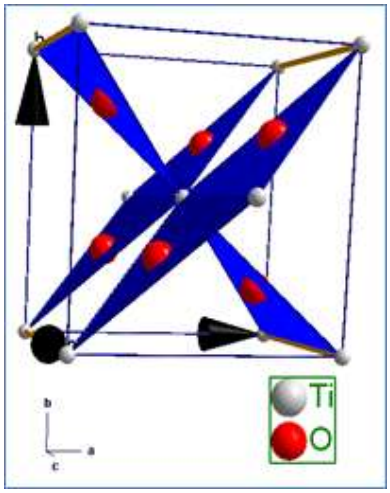

Fig. 6: Packing diagram of TiO2: Ni (6 mol %) Nano powder

From the Rietveld refinement analysis, it is revealed that the value of cell parameter (*a*) and unit cell volume decreased while that of density increased as the doping concentration increases. This has been depicted in the **Fig.7** and **Fig. 8.**

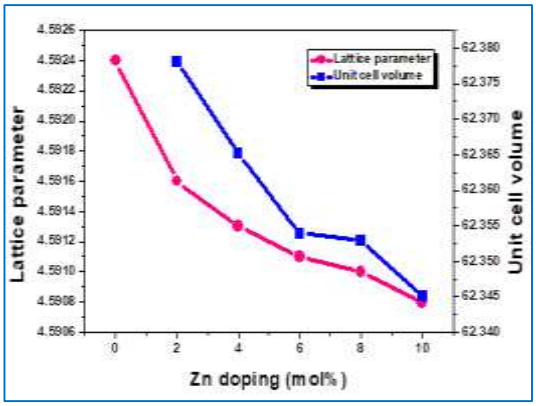

Fig. 7: Lattice parameter and unit cell volume of TiO_2 nanoparticles with Ni doping concentration

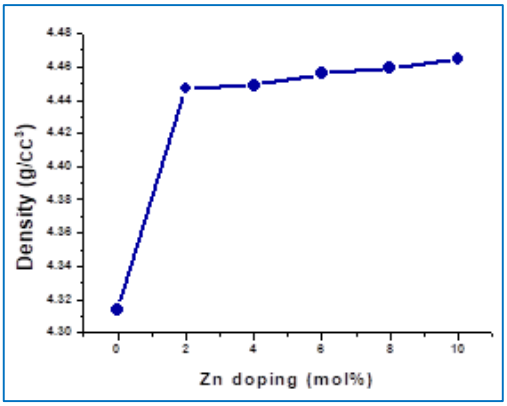

Fig. 8: Density of TiO_2 nanoparticles with Ni doping concentration

Table 2: Rietveld refined structural parameters for TiO_2: Ni nanoparticles

Compound	Pure	2 mol%	4 mol%	6 mol%	8 mol%	10 mol%
Crystal system	Tetragonal	Tetragonal	Tetragonal	Tetragonal	Tetragonal	Tetragonal
Space group	P42/mnm	P42/mnm	P42/mnm	P42/mnm	P42/mnm	P42/mnm
Lattice parameters (A°)						
a =b c	4.5924 2.9595	4.5916 2.9588	4.5913 2.9585	4.5911 2.9584	4.5910 2.9582	4.5908 2.9580
$\alpha= \beta= \gamma$	90^O	90^O	90^O	90^O	90^O	90^O
Unit cell volume ($A^{\circ 3}$)	62.3864	62.3781	62.3652	62.3539	62.3529	62.3451
Atomic coordinates						
Ti x	0.00000	0.00000	0.00000	0.00000	0.00000	0.00000
y	0.00000	0.00000	0.00000	0.00000	0.00000	0.00000
z	0.00000	0.00000	0.00000	0.00000	0.00000	0.00000
O_2 x	0.29218	0.30602	0.30615	0.30453	0.30512	0.30501
y	0.29218	0.30602	0.30615	0.30453	0.30512	0.30501
z	0.00000	0.00000	0.00000	0.00000	0.00000	0.00000
Refinement parameters						
R_P	19.4	17.0	18.2	18.8	16.6	23.7
R_{WP}	26.0	22.4	22.8	25.6	25.8	32.8
R_{Exp}	24.3	19.7	19.9	19.4	19.9	18.5
χ^2	1.14	1.29	1.25	1.75	1.78	3.14
GoF	1.10	1.10	1.10	1.30	1.30	1.80
R_{Bragg}	9.34	6.33	7.52	5.59	5.75	7.52
R_F	11.7	8.13	9.15	6.92	6.98	10.6
Density (g/cc^3)	4.314	4.447	4.449	4.456	4.459	4.465

3.3 Field Emission Scanning Electron Microscopy Study

The FESEM images of pure, 4 % Ni and 8% Ni doped TiO_2 are shown in **Fig. 9.** The large aggregates of particles with irregular shapes can be observed. The increasing doping (Ni) concentration affects the size and morphology of TiO_2. The variation of size and morphology is clearly seen in the figures. The particles of irregular shape and size for Ni doped TiO_2 were observed. The agglomeration may be due to inter atomic forces and surface tension [10].

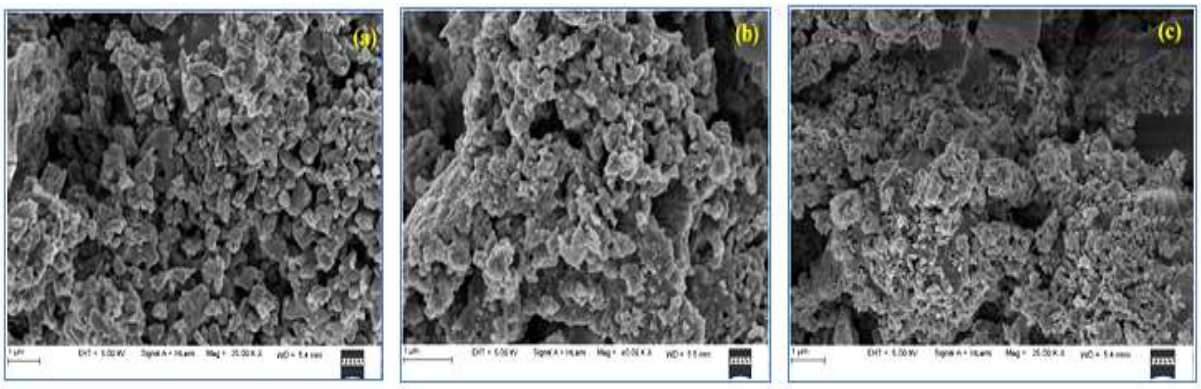

Fig. 9: FESEM image of (a)TiO_2: Pure, (b)TiO_2: Ni (4mol%) and (c) TiO_2: Ni (8mol%) nanopowder

4. CONCLUSIONS

Nanocrystalline nickel doped titanium dioxide nanopowders were synthesized by green combustion method using *Aloe Vera* gel as a fuel. The diffraction patterns of the nano powders were indexed to tetragonal structure. The particle size was in the range 40-50 nm. The FESEM images revealed the formation of agglomerated nanoparticles which may be due to inter atomic forces and surface tension.

REFERENCES

[1]. Hanaor, D.A.H., Sorrell, C.C. Review of the anatase to rutile phase transformation, J. Mater Sci 46, 855–874 (2011)

[2]. K. M. Prabu, P. M. Anbarasan, Preparation and characterization of silver, magnesium & bismuth doped titanium dioxide nanoparticles for solar cell applications, International Journal of Science and Research, 3, 9, (2014), 132-137

[3]. M. Balamurugan, M. Silambarasan, S. Saravanan, Tetsuo Soga, Structural and photoluminescence studies of TiO_2 nanoparticles synthesized by solution combustion method, AIP Conference Proceedings, 1665, (2015), 050116-1-050116-2

[4]. Wesley V. Prescott, Arnold I. Schwartz, Nanorods, Nanotubes, and Nanomaterials Research Progress, Nova Publishers, (2008)

[5]. Fubao Zhang, Xianming Wang, Haonan Liu, Chunli Liu, Yong Wan, Yunze Long, Zhongyu Cai, Recent advances and applications of semiconductor photocatalytic technology, Appl. Sci. 9, 2489, (2019), 1-43

[6]. Chung S. L., Wang C. M., Solution combustion synthesis of TiO_2 and its use for fabrication of photoelectrode for dye-sensitized solar cell, Journal of Materials Science & Technology, 28(8), (2012), 713–722

[7]. Gema Cabello, Rogério A. Davoglio, Ernesto C. Pereira, Microwave-assisted synthesis of anatase-TiO_2 nanoparticles with catalytic activity in oxygen reduction Journal of Electroanalytical Chemistry, 794, (2017), 36-42

[8]. Cullity, B.D., Elements of X-ray Diffraction, Addison-Wesley Publishing Co, (1956)

[9]. Williamson, G., Hall, W., X-ray line broadening from filed aluminium and wolfram, Acta Metallurgica, 1(1), (1953), 22–31

[10]. Hidehiro Kamiya, Nanoparticle Technology Handbook, 3, (2018), 109–168

*****

Data Storage in Ancient Cultures: The Role of Memory in Early Technologies

Dr. G. S. Jaigaonkar

Department of Physics, B.B. Arts, N.B. Commerce & B.P. Science College, Digras
Dist. Yavatmal. (M.S.) India
Email: *gautamjaigaonkar50@gmail.com*

ABSTRACT

The concept of data storage is often associated with modern digital technologies, yet ancient cultures employed innovative methods to preserve and transmit information long before the advent of computers. This paper examines the role of memory and information storage in early technologies across various civilizations, focusing on materials such as stone, clay, papyrus, and parchment. Ancient cultures like the Sumerians, Egyptians, and Maya developed sophisticated systems for encoding and storing knowledge, ranging from cuneiform tablets and hieroglyphic inscriptions to the codices and quipus of the Andean region. These early data storage techniques served not only as tools for recording transactions, laws, and religious texts but also as mechanisms for cultural memory, preserving histories, genealogies, and scientific knowledge over generations. The paper explores the interplay between physical materials and the concept of memory, demonstrating how the choice of medium—be it the durability of stone or the flexibility of papyrus—affected the accessibility and longevity of stored information. By investigating these early forms of data storage, we gain insight into how ancient societies viewed memory, knowledge preservation, and the transmission of information across time. This research also sheds light on the enduring impact of these technologies on the development of modern information storage systems, drawing connections between ancient practices and contemporary digital memory structures.

Keywords: *Ancient data storage Memory preservation Cuneiform tablets Cultural transmission Information encoding etc.*

1. INTRODUCTION

The preservation and transmission of information have been fundamental to human societies since the dawn of civilization. Long before the digital age, ancient cultures developed diverse and sophisticated methods for storing and sharing knowledge. In the absence of modern technology, these cultures relied on physical materials such as clay, stone, papyrus, and parchment to encode information. Early technologies of data storage were not just tools for record-keeping but integral to the cultural fabric of these societies, shaping their ability to maintain historical records, legal systems, and scientific knowledge.

This paper explores the role of memory and data storage in ancient cultures, focusing on how materials and methods of encoding knowledge influenced the accessibility and longevity of information. From the cuneiform tablets of Mesopotamia to the quipus of the Andean civilizations, early data storage systems were essential for governance, religion, and education. Understanding these technologies provides valuable insights into the roots of modern information systems and the enduring human need to preserve knowledge across generations.

1. Material Choices and Technological Innovation

Ancient societies made deliberate choices about the materials they used to store information, influenced by factors such as durability, availability, and utility. For example:

Clay Tablets: The Sumerians, one of the earliest literate societies, used clay tablets for cuneiform writing. These tablets were durable, and the use of stylus marks allowed for clear and lasting records of laws, trade, and literature. Clay tablets were often baked or sun-dried to increase their longevity.

Stone: Cultures such as the Egyptians and the Mayans utilized stone for monumental inscriptions. Hieroglyphics carved into stone were used for monumental inscriptions like royal decrees, religious texts, and historical records, intended to endure across millennia.

Papyrus and Parchment: The Egyptians and Greeks used papyrus, a lightweight yet durable material, for scrolls that contained religious, philosophical, and literary works. Later, parchment—made from animal skins—was used by the Romans and medieval societies for manuscripts.

Wooden and Bone Records: In some regions, such as the Andes, the Inca used materials like wood and bone to encode data using knotted cords known as *quipus*. These systems functioned as a form of record-keeping, tracking everything from census data to agricultural production.

2. Encoding and Preservation of Information

Ancient data storage systems were highly varied in how they encoded information:

Cuneiform and Hieroglyphs: Early scripts like cuneiform and Egyptian hieroglyphs functioned as both writing systems and mechanisms for storing data. Cuneiform was initially developed to track commodities and agricultural produce, eventually evolving into a complex script for literature, law, and science. Similarly, Egyptian hieroglyphs, used both for religious and administrative purposes, required a knowledge of pictorial symbols to encode specific information.

Quipus: The Incan civilization's use of *quipus* is another fascinating example of data storage. Though not a written script, quipus encoded information through knots tied in strings, each knot and color conveying numerical and other types of data. This system was used primarily for accounting and census purposes and reflects an alternative, non-literate method of data storage.

3. Data Access and Longevity

The success of early data storage systems was not solely dependent on the material used but also on the accessibility and durability of these records. For example:

Stone and Clay: Stone inscriptions, although harder to produce, were designed to last for millennia, ensuring that important documents (e.g., royal decrees, religious codes) were preserved for future generations. Similarly, clay tablets were

robust enough to survive the harsh climates of the Mesopotamian region.

Papyrus and Scrolls: While papyrus was less durable than stone or clay, it allowed for greater portability and flexibility in record-keeping, which was ideal for more dynamic forms of knowledge like literature, medicine, and philosophy. However, papyrus and early scrolls were vulnerable to decay from moisture and time, which led to the eventual use of parchment for longer-lasting manuscripts.

4. Role in Cultural Memory and Knowledge Transmission

Beyond practical record-keeping, ancient data storage systems played a key role in cultural memory. By preserving sacred texts, genealogies, legal codes, and historical accounts, early data storage allowed societies to pass down essential knowledge and maintain continuity through generations. The ability to record and preserve information contributed to the establishment of institutions such as libraries, courts, and religious temples. For example:

Libraries of Alexandria: The famous Library of Alexandria in ancient Egypt housed vast collections of papyrus scrolls, some of which contained the scientific, philosophical, and literary knowledge of the ancient world.

Royal Inscriptions: In civilizations like Egypt and Mesopotamia, inscriptions on stone and clay were often used by rulers to immortalize their achievements, reinforce their authority, and consolidate power. These inscriptions often served as a form of propaganda and a means to shape collective memory.

5. Legacy and Influence on Modern Data Storage

Ancient data storage systems influenced the development of modern information technologies. For instance, the concept of encoding data into symbolic representations (e.g., written language or knots) finds a parallel in digital technologies like binary encoding and data compression. Furthermore, the idea of preserving information through durable materials is still reflected in current technologies that prioritize long-term data storage solutions, such as hard drives and cloud databases. The efforts of ancient cultures to externalize and safeguard memory continue to inspire contemporary advancements in data storage and information systems.

2. CONCLUSION

The exploration of data storage in ancient cultures reveals the profound connection between memory, technology, and information preservation in early societies. Before the advent of modern writing systems, memory played a central role in transmitting knowledge, both orally and through physical objects. Ancient technologies such as cave paintings, stone tablets, and early forms of writing were not just methods of recording data—they were manifestations of cultural memory, enabling societies to retain essential knowledge about law, agriculture, trade, and religion.

Ultimately, the study of ancient data storage practices underscores the critical role memory played in shaping early human civilization. It also provides insight into the ongoing relationship between human cognition and technology, which continues to evolve as we navigate the challenges of information storage in the digital age.

3. ACKNOWLEDGEMENTS

I would like to express my deepest gratitude to my mentors and colleagues for their invaluable guidance and support throughout this research on *Data Storage in Ancient Cultures: The Role of Memory in Early Technologies*. Special thanks to [Institution/Library Name] for granting access to historical archives and resources that enriched this study. I am also grateful to my peers for their insightful discussions and feedback. Lastly, I extend my appreciation to my family and friends

for their encouragement and unwavering belief in my work. This research would not have been possible without their contributions and support.

REFERENCES

[1]. Goody, Jack. The Interface between the Written and the Oral. Cambridge University Press, 1987.
[2]. Ong, Walter J. Orality and Literacy: The Technologizing of the Word. Routledge, 1982.
[3]. Eyre, Christopher. The Role of Writing in Early Societies. Cambridge University Press, 2006.
[4]. Schmandt-Besserat, Denise. How Writing Came About. University of Texas Press, 1992.
[5]. Havelock, Eric A. "The Oral Tradition and the Written Word in Ancient Greece." Journal of the History of Ideas, vol. 28, no. 4, 1967, pp. 497-511.
[6]. Palfreyman, John. "Ancient Data Storage: The Use of Memory in Early Technologies." Journal of Ancient Technology and Culture, vol. 12, no. 2, 2018, pp. 234-257.
[7]. Todorova, Maria. "The Role of Memory in Prehistoric Information Storage." Early Human History Journal, vol. 15, no. 1, 2001, pp. 112-129.
[8]. Clarke, David. "The Emergence of Writing Systems and the Storage of Knowledge in Early Civilizations." Journal of Ancient Civilizations, 2019.
[9]. Miller, Ruth. "Memory, Data Storage, and Technology in Ancient Egypt: The Role of Hieroglyphs." Studies in Ancient Technologies, 2015.

***

ISBN: 978-81-970491-8-7
20
Current Research in
Science and Technology
(An Edited Book)

Review of Wireless Network Technologies

Dr. Sayed Mujeeb

Department of Physics, Sir Sayyad College of Arts, Commerce and Science
Dist. Chhatrapati Sambhajinagar. (M.S.) India
Email: *mujeeb.mubbu321@gmail.com*

ABSTRACT

A review of what is needed to build a generic wireless network is provided. The literature attempts to discuss the most popular wireless technologies and their protocols. An overview of the advantages that wireless networks have over wired technology is then given. The paper also advances some of the major security risks that wireless networks face. Various strategies that can be employed to mitigate these risks and safeguard the privacy and security of the network are given. A review of how wireless networks can be used in education and training is then given and it is demonstrated that the education field has benefited from the growth of wireless technology and the cost-effectiveness of this technology

Keywords: *Wireless network, Education, Technology*

1. INTRODUCTION

The invention of the computer and the subsequent creation of communication networks can be hailed as the most significant accomplishment of the 21st century. This invention has transformed how communication and information processing take place. The network functionality of computer systems has been exploited by the government, businesses, and individuals with immense benefits being reaped by all. The two major types of networks in existence are fixed connections (which make use of cables) and wireless networks (which use waves to transmit data). The backbone of the vast communication network is made up of fixed connections which mostly utilize fiber optics as well as Ethernet. Even so, wireless networks have gained increased popularity in the past decade. Malone (2004) reveals that as of the year 2000, wireless networks were limited in existence due to the prohibitive cost of wireless devices such as integrated routers access points and laptops. The hardware cost has significantly decreased making wireless networks affordable to many individuals and organizations. In addition to this, technological advances have increased the capacity and efficiency of wireless networks which have made them favorably compared with wired networks. This paper will set out to discuss wireless networking with a particular focus on the types of wireless technologies commonly employed and the security measures used to protect wireless technology. A discussion of how wireless technology can be used in education and training settings will also be embarked on.

2. WHAT IS WIRELESS NETWORKING?

The infrastructure of wireless networks makes use of standard protocols that are oriented according to the demands of the network. This makes the capacity as well as the quality of services of wireless networks vary based on the devices. Wireless networks are typically expected to deal with devices that are made by various manufacturers. The networks are therefore supposed to be able to support different hardware technologies, architectures, and transport protocols and control traffic flow

within the network. All wireless networks make use of waves in the electromagnetic spectrum range. For example, Wireless local-area networks (Wireless LANs) make use of high-frequency electromagnetic waves to transmit data. Modulation and demodulation of the radio waves used to transmit data occur at the transmitter and receiver respectively. They operate in the industry, scientific, and medical (ISM) radio bands and unlicensed-national information infrastructure (U-NII) bands (Zheng 2009). The networks are often connected to routers for them to access the internet. Reynolds (2003) declares that Wi-Fi has the potential to let anyone with a computing device connect to the internet at impressive speeds without the need Wireless networks also use the Open System Interconnect (OSI) reference model in the transmission of data. The manner in which this reference model applies to wireless networks is similar to wired networks with some differences in the data link layer where wireless networks coordinate access by data to a common air medium and also deal with errors that occur due to the inherent nature of the wireless medium. At the Physical layer, the data is transmitted in the form of radio waves.

3. WIRELESS TECHNOLOGIES

There are a myriad of wireless technologies and they differ in the amount of bandwidth they provide as well as the distance over which the nodes in the network can communicate. Zheng (2009) observes that wireless technologies also differ in the part of the electromagnetic spectrum that they use and the amount of power consumed. To provide physical connectivity, wireless network devices must operate in the same part of the radio spectrum and two wireless cards therefore need to be configured to use the same protocol on the same channel for communication to occur. There are four prominent wireless technologies which are; Bluetooth, Wi-Fi, WiMAX, and 3G cellular wireless.

1. Bluetooth

Bluetooth (IEEE 802.15.1) is the technology that is employed to undertake short-range communication between notebook computers, PDAs, mobile phones, and other personal computing devices. The technology is more convenient than connecting devices with a wire to communicate. Bluetooth operates in a license-free band at 2.45GHz and the communication range is about 10m due to this short range, the technology is sometimes categorized as a personal area network (PAN) (Zheng 2009). A major consideration with Bluetooth technology is power usage and typically, the technology provides speeds of up to 2.1Mbps with low power consumption.

2. Wi-Fi

Wi-Fi stands for wireless fidelity technology and the term is commonly used to describe a wireless local area network based on the IEEE 802.11 series of standards. The IEEE 802.11 standards resolve compatibility issues between manufacturers of wireless networking equipment by specifying an "over the air" interface consisting of "radio frequency technology to transmit and receive data between a wireless client and a base station as well as among wireless clients communicating directly with each other" Wi-Fi describes a family of radio protocols which include 802.11a, 802.11b, and 802.11g. 802.11b is the most popular wireless networking protocol in use and it uses a modulation called Direct Sequence Spread Spectrum in a portion of the ISM band from 2.412 to 2.484GHz. The maximum speed offered by this protocol is 11Mbps with usable throughput of up to 5Mbps. 802.11a is a protocol ratified by the IEEE and it uses a modulation scheme called Orthogonal Frequency Division Multiplexing (OFDM) with a maximum data rate of 54Mbps. It operates in the ISM band between 5.745 and 5.805GHz. The frequency range used by this protocol is relatively unused which makes interference rare.

3. Wi-MAX

A popular form of broadband wireless access for fast local connection to the network is WiMAX. WiMAX technology has a typical range of 1-6 miles but the technology can span a maximum of 30 miles which has made the technology classified as a MAN. This specification has gained great success in the provision of internet access and broadband services through wireless communication systems. WiMAX has a high capacity which makes it efficient in data transmission

with speeds of up to 70Mbps being provided to a single subscriber station. The original WiMAX physical layer protocol is designed to propagate signals at a frequency of 10-66 GHz and the technology can provide both line-of-sight coverage and optimal non-line-of-sight coverage as well.

4. ADVANTAGE OF WIRELESS OVER WIRE TECHNOLOGY

Wireless networks have several significant advantages over wired networks. To begin with, it is relatively easier to set up a wireless network infrastructure than it is to make a wired one. This is because the physical devices necessary for wireless networks are less than wired ones. In installing a wired network, one would need to lay out the cables to connect the devices and this process is not only expensive but also labor and time-intensive. Wireless networks require an access point and once the other devices have been properly configured, they can operate. Another additional merit of wireless networks is that expansion of an existing network is easy since connectivity is already available within the range of the access point. The ease of deployment of wireless networks makes them economically attractive for most organizations since the capital investment of implementing these networks is not as intimidating as that required for elaborate wired networks. With the wide success of wired LANs, the local computing market has made a steady shift towards wireless LANs which offer the same speeds as wired LANs.

5. CONCLUSION

This paper set out to discuss wireless networks which are increasingly becoming preferred over wired networks by many users. The paper began by offering an overview of networking and then proceeded to define wireless networking and discuss the various technologies that are used. From the discussions provided in this paper, it is clear that wireless network solutions are increasing in popularity as they become more affordable and are adopted by more people. This paper has elaborated on how wireless networks provide freedom from place restriction, scalability, and flexibility. The most popular technologies are; Bluetooth, Wi-Fi, WiMAX, and Cellular networks. The paper has confirmed that the mobility of wireless networks is their most desirable characteristic. It has been noted that despite their merits, there are a few significant issues with wireless networks which are primarily: quality assurance and security issues. Wireless links are noisier and less reliable than wired links due to the interference that occurs as the signals are transmitted.

Engaging in site surveys before setting up a wireless network can help to mitigate this issue. Using strong encryption standards can resolve the security issues inherent in wireless networks.

REFERENCES

[1]. Chenoweth, T Robert, M & Sharon, T 2010, “Wireless Insecurity: Examining User Security Behavior on Public Networks”, Communications of the ACM, 53(2): 134-138.

[2]. Ganesh, R & Pahlavan, K 2000, Wireless Network Deployments, Springer, Boston.

[3]. Jordan, R & Abdallah, C 2002, “Wireless communications and networking: an overview”, IEEE Antenna's and Propagation Magazine, 44 (1): 185-193.

[4]. Kumar, A & Manjunath, K 2008, Wireless Networking, Morgan Kaufmann, Boston.

[5]. Kumar, A 2010, “Evolution of Mobile Wireless Communication Networks: 1G to 4G”, International Journal of Electronics &Communication Technology, 1(1): 68-72.

*****

Study of Various Magnetic Phenomenon of Soft and hard Magnetic Material

Dr. M. S. Patil

Department of Physics, Yeshwantrao Chavan College, Sillod, Dist. Chh. Sambhajinagar (M.S.), India
Email: *mspatil9827@gmail.com*

ABSTRACT

In the era of Nano-science and Nanotechnology, magnetic material play very important role in the various application in research and technological field. Based on the magnetic properties, the materials shoes various interesting properties. Generally, magnetic properties are divided into two groups; intrinsic or structure-insensitive and extrinsic or structure-sensitive. Saturation magnetization and Curie temperature are the two prominent structure-insensitive properties. Structure-sensitive properties, on the other hand, are numerous and may be classified further as static or dynamic, according to whether or not the property displays frequency dependence. Induction, permeability, hysteresis loop and associated energy loss, coercive force and remanance are structure-sensitive, static properties. Eddy current loss, resonance of spin and domain walls are structure-sensitive dynamic properties. Here the study of various magnetic phenomenon of soft & hard magnetic material.

Keywords: *Magnetism, magnetic materials, magnetic parameters*

1. INTRODUCTION

Among the magnetic ceramics, magnetic oxides are the most important and rather the only relevant materials from the point of view of their applications. They are being studied over a long period of five to six decades for their basic properties such as structural, magnetic and electrical as well as wide field of applications.

Magnetic oxides, which are commonly known as ferrites are ferromagnetic in structure as originally proposed by Neel [1]. The ferrites by virtue of their structure can accommodate a variety of cations at different sites enabling a wide variation in properties. Further variation in synthetic methods can bring about large changes in extrinsic properties. A majority of them are high resistivity materials making them more suitable for high frequency and low loss applications.

2. MAGNETIC PARAMETERS

The hysteresis loop is a means of characterizing magnetic materials, and various parameters can be determined from it. From the first quadrant the saturation polarization, J_S and hence the saturation magnetization, M_S can be measured. Most of the useful information, however, can be derived from the second quadrant of the loop, and indeed it is conventional only to show this quadrant. The field that is produced by the magnet after the magnetizing field has been removed is called the remanence, B_r or J_r. The reverse field required to bring the induction to zero is called the inductive coercivity, ${}_bH_c$, whereas the reverse field required to bring the magnetization to zero is called the intrinsic coercivity, ${}_jH_c$. The maximum value of the product of B and H is called the maximum energy product, $(BH)_{MAX}$ and is a measure of the maximum amount of useful work that can be performed by the magnet. $(BH)_{MAX}$ is used as a figure of merit for permanent magnet materials.

In addition, the shape of the initial magnetization curve and the hysteresis loop can provide information about the magnetic domain behaviour within the material. The squareness factor is a measure of how square the loop is and is a dimensionless quantity between 0 and 1, defined by the ratio of the reverse field required to reduce J by 10% from the remanence to H_{cj}. A squareness factor of one therefore corresponds to a perfectly square loop. There are several other methods to quantify the squareness of the loop, such as the ratio of J_r to J_s.

2.1. Coercivity mechanisms

There are various methods of increasing or decreasing the coercivity of magnetic materials, all of which involve the controlling the magnetic domains within the material. For a hard magnetic material it is desirable that the domains cannot easily rotate its direction of magnetization and that the domain walls do not move easily and/or nucleation of domains is difficult.

To prevent easy rotation of domains the material could have a strong uniaxial magneto-crystalline anisotropy. Alternatively, shape anisotropy can occur in needle-like particles/grains, where the magnetostatic energy is less when the magnetization is in the long axis of the needle compared to the short axis. If the size of a magnetic particle/grain decreases then there is a critical size below which the decrease in magnetostatic energy by splitting into two domains is less than the increase in energy due to the introduction of the domain wall. Particles that are below this critical size are known as "single domain particles", and if they have sufficiently high anisotropy to prevent the easy rotation of the direction of magnetization then the particles will be permanently magnetic and difficult to demagnetize. This type of coercivity mechanism can be observed in melt-spun NdFeB magnets where the crystal size is ~50nm, compared to the critical size for single domain particles of ~300nm.

2.2. Remanence or retentivity

During the cycle of magnetization B_r is the amount induction remained ever after the field H is made zero. This characteristic induction is known as remanence or retentivity.

2.3. Eddy current and associated energy losses

This property is of great importance in the application of soft magnetic metals and alloys. When an alternating field is applied to magnetize a ferromagnetic body, an electromagnetic force (e.m.f.) is setup in the body. If the material is also a good conductor, as with metal and alloys, the induced emf is produced appreciable amount of currents in different regions, these currents are known as the eddy currents and their occurrence gives rise to energy loss (W_e) through Joule (resistance heating). Thus, in a.c. application, metallic ferromagnet suffers the hysteresis as well as the eddy current losses [2]. Also, W_e increases with frequency according to the second power law. Hence, the eddy current loss becomes even more burdensome than the hysteresis loss at intermediate and high frequencies.

2.3. Domains

In order to explain the fact that ferromagnetic materials with spontaneous magnetization could exist in the demagnetized state Weiss proposed the concept of magnetic domains. Weiss built on earlier work carried out by Ampère, Weber and Ewing suggesting their existence. The findings of this work revealed that within a domain large number of atomic moments are aligned typically 10^{12}-10^{18}, over a much larger volume than was previously suspected. The magnetization within the domain is saturated and will always lie in the easy direction of magnetization when there is no externally applied field. The direction of the domain alignment across a large volume of material is more or less random and hence the magnetization of a specimen can be zero [3].

Magnetic domains exist in order to reduce the energy of the system. A uniformly magnetized specimen as shown in figure 2 (a) has a large magnetostatic energy associated with it. This is the result of the presence of magnetic free poles at the surface of the specimen generating a demagnetizing field, H_d. From the convention adopted for the definition of the magnetic moment for a magnetic dipole the magnetization within the specimen points from the South Pole to the North Pole, while the direction of the magnetic field points from north to south. Therefore, the demagnetizing field is in opposition to the magnetization of the specimen. The magnitude of H_d is dependent on the

geometry and magnetization of the specimen. In general if the sample has a high length to diameter ratio (and is magnetized in the long axis) then the demagnetizing field and the magnetostatic energy will be low.

The breakup of the magnetization into two domains as illustrated in figure 1 (b) reduces the magnetostatic energy by half. In fact if the magnet breaks down into N domains then the magnetostatic energy is reduced by a factor of 1/N, hence figure 1 (c) has a quarter of the magnetostatic energy of figure 1(a). Figure 1(d) shows a closure domain structure where the magnetostatic energy is zero, however, this is only possible for materials that do not have a strong uniaxial anisotropy, and the neighbouring domains do not have to be at 180º to each other.

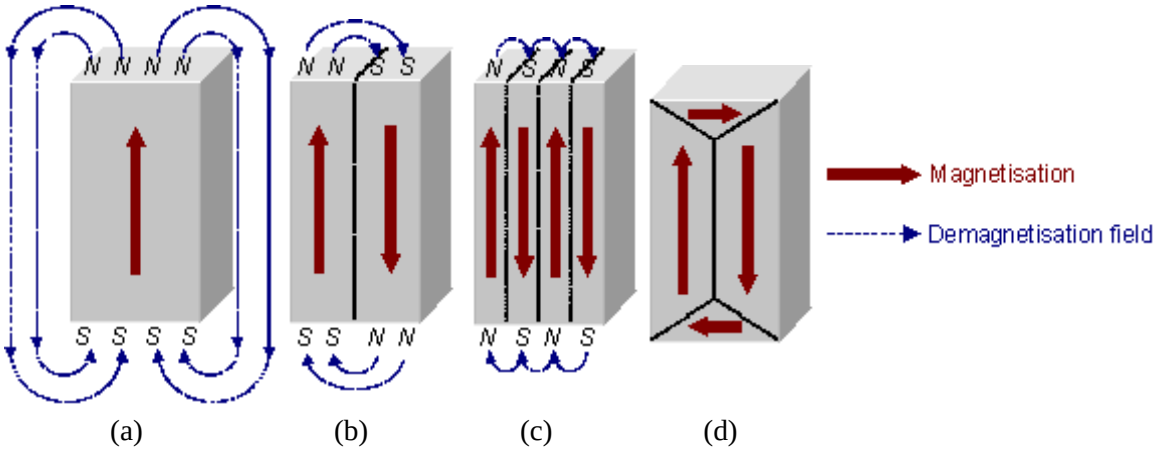

Fig. 1: Schematic illustration of the breakup of magnetisation into domains (a) single domain, (b) two domains, (c) four domains and (d) closure domains.

The introduction of a domain raises the overall energy of the system, therefore the division into domains only continues while the reduction in magnetostatic energy is greater than the energy required to form the domain wall. The energy associated with a domain wall is proportional to its area. The schematic representation of the domain wall, illustrates that the dipole moments of the atoms within the wall are not pointing in the easy direction of magnetization and hence are in a higher energy state. In addition, the atomic dipoles within the wall are not at 180^0 to each other and so the exchange energy is also raised within the wall. Therefore, the domain wall energy is an intrinsic property of a material depending on the degree of magneto-crystalline anisotropy and the strength of the exchange interaction between neighbouring atoms [4-5]. The thickness of the wall will also vary in relation to these parameters, as a strong magneto-crystalline anisotropy will favour a narrow wall, whereas a strong exchange interaction will favour a wider wall.

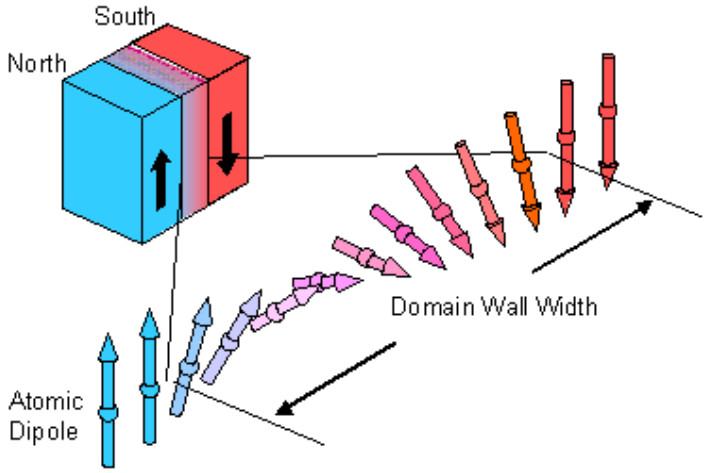

Fig.2: Schematic representation of a 180º domain wall.

A minimum energy can therefore be achieved with a specific number of domains within a specimen. This number of domains will depend on the size and shape of the sample (which will affect the magnetostatic energy) and the intrinsic magnetic properties of the material (which will affect the magnetostatic energy and the domain wall energy).

Magneto-crystalline anisotropy

In a crystalline magnetic material the magnetic properties will vary depending on the crystallographic direction in which the magnetic dipoles are aligned. Figure1 demonstrates this effect for a single crystal of cobalt. The hexagonal crystal structure of Co can be magnetized easily in the [0001] direction (i.e. along the c-axis), but has hard directions of magnetization in the <1010> type directions, which lie in the basal plane (90° from the easy direction).

A measure of the magnetocrystalline anisotropy in the easy direction of magnetization is the anisotropy field, H_a (illustrated in figure 1), which is the field required to rotate all the moments by 90° as one unit in a saturated single crystal. The anisotropy is caused by a coupling of the electron orbitals to the lattice, and in the easy direction of magnetization this coupling is such that these orbitals are in the lowest energy state. The easy direction of magnetization for a permanent magnet, based on ferrite or the rare earth alloys, must be uniaxial, however, it is also possible to have materials with multiple easy axes or where the easy direction can lie anywhere on a certain plane or on the surface of a cone. The fact that a permanent magnet has uniaxial anisotropy means that it is difficult to demagnetize as it is resistant to rotation of the direction of magnetisation [6].

Magneto-striction

Magnetic body opposes to elastic changes in the dimension due to magnetization and this effect is known as magnetostriction. Magnetization change in a body in the length δ/l and its changing from zero to saturation and applied magnetic field increases along with in direction of parallel direction and this magnetostriction gives the +ve when an increase the magnetic field and this magnetostriction reaches the magnetization saturation. Additional anisotropy is introduced in a magnetic material if it is subjected to a unidirectional stream. For example, in Fe under tension a preferred direction of magnetization parallel to the direction of stress is introduced.

3. CONCLUSION

Magnetism is very important in the study of nature of material. Different kind of materials are classified in various category. Soft magnetic materials have a high permeability, which means they can quickly establish and sustain magnetic fields within them. Ferro- or ferromagnetic material is a hard or a soft magnet depends on the strength of the magnetic field needed to align the magnetic domains.

REFERENCES

[1]. L. Neel, Ann. de physique, 3 (1948) 137.

[2]. B. Vishwanathan, V.R.K. Murthy, “Ferrite Material Science and Technology”

[3]. L. Wilkens, D. Trager, H. Dostch, A. M. Alexeev, A. F. Popkov, and V. I. Korneev, J. Appl. Phys. 93 (5) (2022) 2839.

[4]. T. Takada and M. Kiyama, In. Proc. Of the Int. Conf. On Ferrites. Japan 69 (2010)

[5]. H. Robins, Proc. Int. Conf. On Ferrites, 7 (Sept. oct. 1980 Japan)

[6]. R. C. Weast “CRC Handbook of chemistry and physics” CRC Press (2011)

***

To Study of Various Techniques for the Measurement of Curie temperature of Magnetic Materials

Dr. C. M. Kale

Department of Physics, Indraraj Arts, Commerce and Science College, Sillod.
Dist. Chhatrapati Sambhajinagar (M.S.) India
Email: *cmkale1973@gmail.com*

ABSTRACT

The Curie temperature (Tc) is a critical physical property of ferrite materials that marks the transition between ferromagnetic and paramagnetic phases. This study investigates the Curie temperature of various ferrite compounds using multiple techniques, including Differential Scanning Calorimetry (DSC), vibrating sample magnetometry (VSM), and X-ray diffraction (XRD). The results from these techniques were compared to understand the advantages and limitations of each approach. The relationship between the composition of ferrite and its Curie temperature was also explored, providing valuable insights into material design for specific applications in electronic, magnetic, and sensor technologies.

Keywords: *Curie temperature, Ferrite Materials, Magnetic Properties, X-ray Diffraction (XRD)*

1. INTRODUCTION

Ferrites are ceramic materials composed of iron oxide ($Fe_2 O_3$) combined with other metal oxides like manganese, zinc, or nickel. Due to their magnetic properties, ferrites have wide applications in electronics, telecommunications, and magnetic data storage. The Curie temperature, Tc, is a key factor influencing the ferromagnetic to paramagnetic phase transition of these materials. Understanding and accurately measuring the Curie temperature is vital for improving their performance in high-temperature applications. The Curie temperature (Tc) is the temperature above which ferromagnetic materials lose their permanent magnetic properties and transition into a paramagnetic state. In the case of ferrites, a class of ceramic materials often used in magnets and electronic components, the Curie temperature is crucial for understanding their magnetic behaviour. To determine the Curie temperature of ferrites, several techniques can be used. These techniques vary in their approach and accuracy, but they all rely on the change in magnetic properties as the material is heated. This paper aims to analyze the Curie temperature of ferrite materials using various experimental techniques, focusing on the applicability, precision, and limitations of each method.

2. EXPERIMENTAL

The Curie temperature is an important property of magnetic materials, indicating the temperature at which a ferromagnetic material transitions into a paramagnetic state. Understanding how to accurately measure this temperature is crucial for various applications in magnetism, material science, and electronic engineering. The ferrite samples used in this study include $MnFe_2 O_4$, $NiFe_2 O_4$, and $ZnFe_2 O_4$, with compositions confirmed by X-ray diffraction (XRD) and energy dispersive X-ray analysis (EDX).

Techniques Used:

1. **Differential Scanning Calorimetry (DSC)**:
   DSC was employed to measure the heat flow associated with the phase transition from ferromagnetic to paramagnetic behavior as the temperature increased. The Curie temperature was determined by analyzing the peak in heat capacity corresponding to the phase transition.
2. **Vibrating Sample Magnetometry (VSM)**:
   The magnetization vs. temperature curves were measured using a VSM system. The Curie temperature was inferred from the temperature at which the magnetization abruptly decreases to zero, signifying the loss of ferromagnetic order.
3. **X-ray Diffraction (XRD)**:
   XRD was used to confirm the structural properties of the ferrite materials at various temperatures. Phase transitions were tracked by examining the lattice parameters and the intensity of diffraction peaks, which can shift with temperature.

3. METHODS OR TECHNIQUES

- The ferrite samples were heated in a controlled environment, and each technique was used to collect data across a temperature range from room temperature up to 500°C.
- DSC and VSM were conducted simultaneously to correlate thermal and magnetic properties.
- XRD patterns were recorded at different temperatures to analyze the phase transitions.

4. RESULTS AND DISCUSSION

The Curie temperature (Tc) is the temperature above which ferromagnetic materials lose their permanent magnetic properties and transition into a paramagnetic state. In the case of ferrites, a class of ceramic materials often used in magnets and electronic components, the Curie temperature is crucial for understanding their magnetic behaviour.

4.1. Curie Temperature from DSC

The DSC curves exhibited a clear endothermic peak for each ferrite sample, which corresponds to the Curie temperature. The Curie temperatures of $MnFe_2O_4$, $NiFe_2O_4$, and $ZnFe_2O_4$ were found to be 330°C, 375°C, and 425°C, respectively **Fig.1**. These values are consistent with previously reported data in the literature.

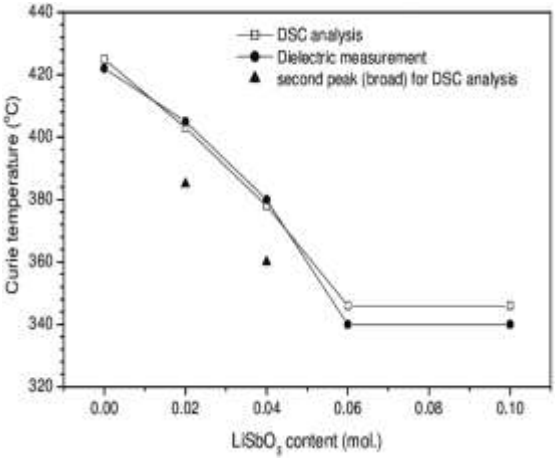

Fig.1: Curie Temperature from DSC

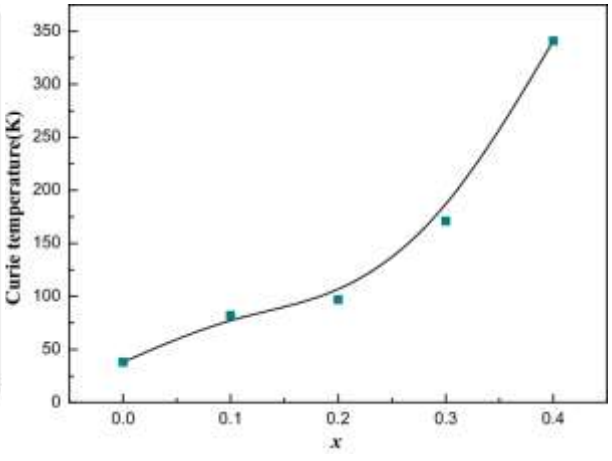

Fig.2: Curie Temperature from DSC

4.2. Curie Temperature from VSM

The VSM results showed a significant drop in magnetization as the temperature approached the Curie point shown in **Fig.2**. The temperatures determined from the magnetization curves (Tc) were 335°C, 370°C, and 420°C for the three ferrite samples. The slight variation between DSC and VSM measurements could be attributed to the differences in the experimental conditions and sample preparation.

4.3. XRD Analysis

The XRD patterns confirmed that the ferrites retained their cubic spinel structure across the measured temperature range. Minor changes in lattice constants were observed as the temperature increased, with a clear transition corresponding to the Curie temperature. The phase transition was further supported by the disappearance of the magnetic diffraction peak at higher temperatures.

4.4. Comparison of Techniques

- **DSC** is highly sensitive to thermal transitions, providing precise values for the Curie temperature but may lack the ability to distinguish subtle changes in magnetic properties.
- **VSM** directly measures the magnetic behaviour, making it more reliable for magnetic phase transitions but requiring careful calibration.
- **XRD** offers valuable structural insights but may not be as direct in determining the Curie temperature unless coupled with thermal analysis.

4.5. Summary of Techniques

Technique	Main Feature	Advantages	Limitations
Magnetic Susceptibility	Measures change in susceptibility with temperature	Simple, widely used	Influenced by sample shape/size
Vibrating Sample Magnetometer (VSM)	Measures magnetic moment with temperature	High accuracy, detailed measurements	Sophisticated equipment required
Differential Scanning Calorimetry (DSC)	Measures heat flow related to phase transition	Direct indication of phase change	Not ideal for all ferrite types
Mössbauer Spectroscopy	Measures hyperfine interactions	Detailed magnetic state information	Requires well-prepared samples
X-ray Diffraction (XRD)	Detects structural changes with temperature	Structural and magnetic insights	May not clearly detect the magnetic transition
Magnetization vs Temperature Curve	Direct measurement of magnetization	Direct and commonly used method	Requires precise equipment control

5. CONCLUSION

This study demonstrates that various techniques, such as DSC, VSM, and XRD, provide complementary data on the Curie temperature of ferrites. While each method has its advantages and limitations, combining these techniques yields a comprehensive understanding of the magnetic and thermal properties of ferrite materials. The composition of ferrites plays a crucial role in determining their Curie temperature, which has significant implications for their application in high-temperature environments and electronic devices.

REFERENCES

[1]. A. B. Kumar, et al., "Curie Temperature and Magnetic Properties of Ferrites," Journal of Magnetism and Magnetic Materials, 2006.

[2]. C. D. Patel and P. S. S. Srinivas, "Measurement of Curie Temperature Using VSM and DSC for Ferrite Materials," Materials Science and Engineering, 2011.

[3]. S. K. Gupta and N. L. Das, "Magnetic Behaviour and Curie Temperature of Spinel Ferrites," Solid State Physics Journal, 2004.

[4]. R. P. Singh, et al., "The Role of Composition in Determining the Curie temperature of Ferrite Materials," Journal of Applied Physics, 2008.

[5]. T. L. Johnson, "Characterization of Magnetic Materials," International Journal of Magnetic Materials, 2010.

*****

ISBN: 978-81-970491-8-7
23
Current Research in
Science and Technology
(An Edited Book)

Fluid Dynamics to Understand Some Biological Processes: A Review

Dr. Shailendra Bhalchandra Kolhe

Department of Physics, Shivaji Arts, Commerce & Science College Kannad. Dist. Chhatrapati Sambhajinagar- 431103 Maharashtra, India
Email: *kolhe_sb71@yahoo.com*

ABSTRACT

Fluid dynamics plays a vital role in comprehending various biological processes. Blood flow in arteries and veins, airflow in lungs and gas exchange can be studied effectively by fluid dynamics concepts. The movement of sperm during reproduction, mucus clearance in airways, and nutrition transport in cells can also be studied using fluid dynamics. Marine organisms and birds follow fluid mechanics. By bridging the fields of biology and physics, this multidisciplinary approach improves medical care, creates biomimetic designs, and deepens our understanding of life processes. This paper presents a review of fluid dynamics' significant contributions to biology, highlighting its influence on biomechanics and healthcare.

Keywords: *Fluid Dynamics, Cellular and Microfluidic Transport, Blood Circulation, Respiratory System, Biological processes*

1. INTRODUCTION

Science is very vast branch of knowledge including various subject. Science is the leading multidisciplinary, international research including analysis and news coverage of breakthroughs and policy. It has several branches like biology, chemistry, physics, and mathematics etc. Each branch deals with specific knowledge. In present scenario there is an interdisciplinary approach in science. Integrating knowledge and methods from multiple scientific disciplines to tackle a problem, creating a more comprehensive understanding by combining perspectives from different branches. It includes looking at a complex issue from various angles to gain a deeper understanding.

Fluid dynamics is a subdiscipline of fluid mechanics used in Physics, Physical Chemistry and Engineering. It describes flow of fluids, liquids, and gases. Fluid dynamics has numerous subdisciplines including aerodynamics and hydrodynamics. It plays a vital role in study of various biological processes such as blood flow within the human body. The basic mechanisms of living things can be better understood by applying the concepts of fluid mechanics. The effective flow of fluids is necessary for many biological processes to maintain life, control homeostasis, and provide vital gasses and nutrients. Fluid dynamics plays a crucial role in the microscopic explanation of biological transport mechanisms in addition to human physiology. The laws of fluid flow control the movement of aquatic organisms, the intracellular transfer of cytoplasmic components, and the passage of sperm cells through reproductive fluids. Fluid dynamics contributes to various biological processes, highlighting its significance in physiology, bioengineering, and medical research. Researchers can develop novel diagnostic tools and therapeutic strategies to address critical health challenges by integrating fluid mechanics with biological sciences.

Cardiovascular system and Blood Flow

Blood circulates by veins back to the heart and by arteries away from it. The circulatory system removes waste materials like carbon dioxide and delivers nutrition, hormones, and oxygen to cells. To keep things moving in the proper direction, these paths can only go in one direction. One of the most critical applications of fluid dynamics in biology is the study of blood flow within the cardiovascular system. Blood acts as a non-Newtonian fluid because it does not follow Newton's law of viscosity. Its viscosity changes when it is under stress, and it is not constant. Non-Newtonian fluids can be affected by changes in temperature, pressure, and composition. They become less viscous when pressure is applied and become more viscous when left unused for a long time. They exhibit both viscous and elastic properties when deformed [1].

Respiratory system and the flow of air

The respiratory system is a biological system consisting of specific organs and structures used for gas exchange in animals and plants. Fluid dynamics is crucial in understanding airflow through the respiratory system, particularly in analyzing how air moves through the nasal cavity, trachea, and lungs. In fluid dynamics, turbulent flow is fluid motion characterized by disordered changes in pressure and velocity flow. In laminar flow a fluid flows in parallel layers with no disruption between those layers. Study of such air flow through respiratory track helps in diagnosis of obstructive pulmonary diseases like asthma and chronic bronchitis [2].

Cellular and Microfluidic Transport

Cellular and microfluidic transport refers to the movement of molecules and substances within a cell. At the microscopic level, fluid dynamics controls the movement of waste products and nutrients into and out of cells. Capillary action in cells states to the movement of fluids within the tiny spaces inside a cell. This occurs due to the forces of attraction between the fluid and cell walls and attraction between fluid molecules. This allows liquids to flow through narrow channels without external forces like gravity.

In biological systems, osmosis helps the movement of water molecules across a semipermeable membrane in cells which maintains their internal fluid balance. It is important for nutrient absorption, waste elimination, cell life regulation, water balance maintenance. Diffusion is an important process in the biological system that moves substances in and out of cells and tissues. It is responsible for many biological processes such as respiration, temperature regulation, and waste removal [3].

Bio-locomotion and Swimming Microorganisms

Swimming microorganisms move throughout water utilizing several kinds of processes, such as cilia, flagella, and pseudopods. Bacteria such as E. coli use helical flagella to drive themselves, while sperm cells rely on a whip-like motion. By calculating the ratio of inertial to viscous forces, the Reynolds number assists in forecasting fluid flow patterns in various scenarios. Flows tend to be dominated by laminar flow at low Reynolds numbers, while at high Reynolds numbers, flows tend to be turbulent. Type of flow whether it is laminar or turbulent affects swimming of fish in water [4].

2. CONCLUSION

Fluid dynamics plays a crucial role in clarifying various biological processes. Researchers have gained deeper insights into blood circulation, respiratory airflow, and nutrient transport, contributing to advancements in medical diagnostics and treatments by applying principles of fluid mechanics. Continuous evolution of fluid dynamics will undoubtedly enhance our ability to diagnose, treat, and prevent various medical conditions, ultimately improving human health and well-being.

REFERENCES

[1]. Blessy Thomas, K.S. Sumam (2016). Blood Flow in Human Arterial System-A Review. International Conference on Emerging Trends in Engineering, Science and Technology (ICETEST - 2015), Procedia Technology 24, pp. 339 – 346.

[2]. Ga, Yume. "Understanding the Role of Fluid Dynamics in Biological Systems." Fluid Mech Open Acc 10 (2023): 297.

[3]. Ece Yildiz-Ozturk and Ozlem Yesil-Celiktas (2015). Diffusion phenomena of cells and biomolecules in microfluidic devices. BIOMICROFLUIDICS 9, 052606, pp.1-18.

[4]. James C. Liao (2007). A review of fish swimming mechanics and behavior in altered flows. Phil. Trans. R. Soc., 362, pp. 1973–1993.

*****

ISBN: 978-81-970491-8-7
24
Current Research in
Science and Technology
(An Edited Book)

Initial Permeability Studies of Spinel ferrite

Dr. J. M. Bhandari

Shri Amolak Jain Vidya Prasarak Mandal's
Department of Physics, Smt. S. K. Gandhi Arts, Amolak Science and P. H. Gandhi Commerce College, Kada, Tal. Ashti, Dist. Beed
Email: *jmbhandari_1969@yahoo.co.in*

ABSTRACT

In the present work, $Ni_{1-x}Cu_xFe_2O_4$ (with x = 0.2, and 0.6) ferrite samples prepared by standard ceramic technique is investigated. The samples have been studied using X-ray diffraction technique. X-ray diffraction studies of compositions revealed the formation of single-phase cubic structure. The initial permeability μi was measure using LCR-Q meter. It is found that μi increase with Cu substitution. By using permeability versus temperature plot Curie temperature was measured.

Keywords: *X-ray diffraction, Initial Permeability, Curie temperature.*

1. INTRODUCTION

Several mixed metal oxides with iron oxide as their main component having the formula MFe_2O_4 have been investigated and found to have interesting structural, electrical and magnetic properties. Due to their remarkable electrical and magnetic properties they are used in many technological applications [1]. Spinel ferrites are commercially important materials because of their excellent electrical and magnetic properties. Interesting physical and chemical properties of ferrites arises from ability of these compounds to distribute cations amongst the available tetrahedral (A) site and octahedral [B] site and magnetic A-A, B-B and A-B interactions. Ferrites are generally classified into two groups, hard ferrites and soft-ferrites. Ferrites for which coercive field is small are termed as soft ferrites. Polycrystalline ferrites which have many applications in microwave frequencies are very good dielectric materials. The basic structural and magnetic properties of spinel ferrite are depends upon several factors such as method of preparation, preparative parameters and preparative conditions, nature, type and amount of dopant [2-6].

Extrinsic property such as permeability losses even depend on microstructure as well as sintering condition [7]. Among the spinel ferrites, the inverse type is particularly interesting due to its high magneto-crystalline anisotropy, high saturation magnetization, and unique magnetic structure. Nickel ferrite ($NiFe_2O_4$) is an inverse spinel with cubic structure shows ferrimagnetisms that originates from magnetic moment of anti-parallel spins between Fe^{3+} ions at tetrahedral sites and Ni^{2+} ions at octahedral sites [8]. Spinel ferrites are important in several applications, hence studies of structural, electrical, magnetic and other properties of spinel ferrites are very essential [9, 10]. The interest in these materials is sustained till date because of their applications in the field of drug delivery, multilayer chips, magnetic recording, sensors, catalysts, etc. [11- 13].

The substitution of divalent, trivalent and tetravalent ions in spinel ferrites leads to diversification in various properties. The properties of spinel ferrites can be modified by substituting

the various kinds of cations. In the literature, many reports are available on the structural, electrical and magnetic properties of Zn, Cd, Al, Cr, Ti, Mn substituted spinel ferrites [14, 15].

Nickel ferrites ($NiFe_2O_4$) and substituted nickel ferrites have been the subject of extensive investigation because of their high-frequency application. Copper ferrite ($CuFe_2O_4$) is a distinguished among other spinel ferrites by fact that it under goes structural phase transition accompanied by reduction crystal symmetry to tetragonal due to cooperative Jahn-Teller effect. However there are differences about the phase transition temperature of Copper ferrite [16, 17]. Copper ferrite is random spinel ferrite and possesses tetragonal structure. Both nickel and copper ferrite is important from the point of view of their applications. Abnormal thermal, magnetic and dielectric properties of Cu-containing ferrite have been reported [18, 19]. In this paper we report our results on initial permeability of Nickel-Copper spinel ferrite.

2. MATERIALS AND METHODS

Polycrystalline spinel ferrites of the chemical composition $Ni_{1-x}Cu_xFe_2O_4$ (x = 0.2 and 0.6) were prepared using the standard ceramic method. A.R. grade NiO, CuO and Fe_2O_3 oxides in appropriate molar proportions were used for the preparation of ferrite. The compositions of these ferrites are shown in Table 1. The oxides were mixed thoroughly and wet ground by using an agate mortar. First pre-sintering of powder was carried out at 1225K for 12 hr followed by a slow cooling. The sintered powder is again reground and sintered at 1375K for 12 hr. To measure the initial permeability toroids of outer diameter 2 cm and inner diameter 1 cm are prepared. The prepared samples were characterized by X-ray powder diffractometer (model PW 3710) using Cu-K_α radiation (λ = 1.5405Å) in the 2θ range 20^0 -80^0.

Table 1: Chemical composition of $Ni_{1-x}Cu_xFe_2O_4$ system in mole percentage.

Composition X	NiO	CuO	Fe_2O_3
0.2	40	10	50
0.6	20	30	50

The initial permeability as a function of temperature was measured for 1 KHz frequency. Toroidal cores were used for the inductances measurements because they can provide potentially the greatest band width since it has no residual gap & proper winding gives minimal leakage inductance.

3. RESULTS AND DISCUSSION

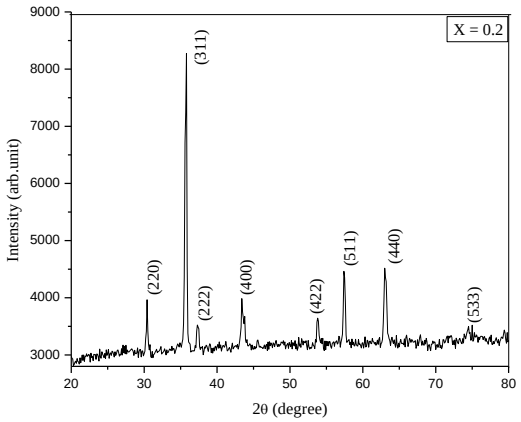

Fig. 1: XRD patterns of $Ni_{1-x}Cu_xFe_2O_4$ for x = 0.2

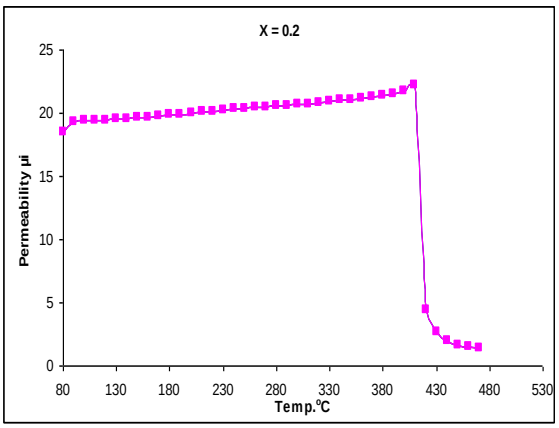

Fig. 2: Permeability versus temperature plot of $Ni_{1-x}Cu_xFe_2O_4$ system at x = 0.2

The structural characterization of these two samples of spinel ferrite system $Ni_{1-x}Cu_xFe_2O_4$ (x= 0.2 and x = 0.6) was carried out using X-ray diffraction technique. Results indicate that these oxides crystalline with a single phase cubic spinel structure. Fig.1 shows the typical X-ray diffraction (XRD) pattern of $Ni_{1-x}Cu_xFe_2O_4$ (for x = 0.2) spinel ferrite system. The XRD patterns indicates that all the composition exhibits single phase cubic spinel structure and exclude the presence of any secondary phase. The Braggs reflection observed in XRD pattern are intense and sharp. The XRD pattern shows the reflections (220), (311), (222), (400), (422), (511), (440) and (533) belonging to cubic spinel structure. The analysis of XRD pattern reveals the formation of single phase cubic spinel structure. No extra peak has been detected in the XRD pattern.

The initial permeability (μ_i) was obtained by measuring inductance of the toroid using LCR-Q meter and was calculated using the following relation.

$$L = 0.0046\, N^2\, h\, \mu_i\, \mathrm{Log}_{10}\left(\frac{d_2}{d_1}\right)$$

Where, d_2 is the outer diameter,

d_1 is the inner diameter,

L is inductance in micro-Henry,

H is the height in inches,

μ_i is initial permeability and

N is number of turns of wire.

The variation of permeability μ_i was measured as a function of temperature. The plot of permeability versus temperature for typical sample x = 0.2 is shown in Fig. 2. It is observed from permeability versus temperature plot that permeability increases slowly as temperature increases and attains a maximum value. Thereafter, permeability suddenly falls down. The curve exhibits tailing effect. Using these plots Curie temperature of all the samples was also obtained.

The values of initial permeability at room temperature for all the samples were also calculated and the values are presented in table 2. It can be seen from table 2 that initial permeability increases with copper substitution. Similar variation in permeability with composition was observed in other well-known ferrite spinel [20]. The values of Curie temperature obtained from permeability versus temperature plot was also shown in table 2. Curie temperature is decreases as Cu concentration increases.

Table 2: Initial permeability (μ_i) at room temperature and Curie temperature (T_C) for $Ni_{1-x}Cu_xFe_2O_4$ system

Composition x	Permeability μ_i	Curie Temperature T_C (K)
0.2	23.19	803
0.6	40.96	703

4. CONCLUSIONS

The single phase nature of all the samples of Ni-Cu spinel ferrite was confirmed by X-ray diffraction analysis. The initial permeability increases with increase in copper content x. The permeability values are affected much by copper substitution. Temperature dependence of initial permeability gives the values of Curie temperature. Curie temperature decreases with increasing copper content.

REFERENCES

[1]. Jan Smith: "Magnetic Properties of Materials" Mc Graw-Hill Book Company, New York.(1971).

[2]. Souad Ammar, Arnaud Helfel: J. Mater. Chem 11 (2001) 186.

[3]. I. M. Hamada: J. Magn. Magn. Mater. 271 (2004) 318.
[4]. B.P. Ladgoankar, C. B.Kolekar, P. N. Vasamberkar and A. S. Vaingankar: Ind. J. Eng. Matt. Sci. 7 (2000) 419.
[5]. A. M. Varaprasad and C.M. Radhakrishnamurthy: Bull Mat. Sci 8 (1986) 567.
[6]. K Sailakshmi, Ph.D. Thesis, Andhra University India (1997).
[7]. R.V. Mangalaraja, S. Thomas Lee, S. Ananthakumar, P. Manohar, Carlos P. Camurri: Mater. Sci. Engg.
[8]. C.N. Chinnasamya, A. Narayanasamya, N. Ponpandiana, R.J. Joseyphusa, B. Jeyadevan, K. Tohjib, K. Chattopadhyay: J. Magn. Magn. Mater. 238 (2002) 281.
[9]. L. John Berchmans, R. Kalai Selvan, P.N. Selva Kumar, C.O. Augustin: J. Magn. Magn. Mater. 279 (2004)103.
[10]. F. Novelo, R. Valenzuela: J. Mater. Res. Bull. 30 (1995) 335.
[11]. S. Nishigaki, S.Yano, H. Kato, T. Nano- Mura,: J. Am-Cerm. Soc. 71 (1) (1988).
[12]. P. K. Roy, J. Bera, J. Magn.Magn. Mater, 321 (2009) 247.
[13]. T. Nakamura. J. Magn. Magn. Mater. 168 (1997) 285.
[14]. S.P. Jadhav , B.G. Toksha , K.M. Jadhav , N.D. Shinde, Chinese J. of Chem. Phys. Vol. 23, (4), 2010.
[15]. M. A.Gabal , Y.M. Al Angari, J. of Magn.Magn. Mater. 322(2010). 3159–3165.
[16]. J. L.Snock: Phy. 14 (1948) 207.
[17]. L. A. Davidov, S. A. Paltinnokov, M. F. Bryzhin: Sov. Phy.Solid State 7 (1965) 596.
[18]. J.Z. Jiang, G.F. Goya, H.R. Rechenberg: J. Phys. Condens. Mat. 11 (1999) 4063.
[19]. G.F. Goya, H.R. Rechenberg: Nanostruct. Mater. 10 (1998) 1001.
[20]. S.T. Mahmud, A.K.M. Akther Hossain, A.K.M. Abdul Hakim, M. Seki, T. Kawai, H. Tabata, J. Magn. Magn. Mater. 305 (2006) 269.

*****

Elucidation of the Bioactive Potential of Leaves of *Tridax Procumbens*: A Synergistic Approach Combining Phytochemical Profiling and In-Silico Molecular Docking Validation

Vinanti Basavantbagade
Madhavrao Patil College of Pharmacy, Murum, Maharashtra, India
Corresponding author: *Agarkar Payal, Patil Vaishnavi*
Madhavrao Patil College of Pharmacy, Murum, Maharashtra, India
Email: *vinanti1999@gmail.com*

ABSTRACT

Plants have been used as medicine for centuries and are an essential part of India's health-care system. *Tridax procumbens* Linn. (Asteraceae), a medicinally significant plant typically found in subtropical regions growing largely at waste locations and roadsides across India during the rainy season, was chromatographically analyzed in the current study for different phytochemicals contained in it. Alkaloids, flavonoids, phenols, saponins, steroids, and tannins were detected in the methanolic extract of *Tridax procumbens* (METP). *Tridax procumbens* L. is a medicinal herb that can be consumed to cure bronchial catarrh, diarrhea, dysentery, and liver illness. In this work, we investigated the ability of T. procumbens to cure hyperuricemia, oxidative stress, and bacterial infection.

1. INTRODUCTION

Medicinal plants, which contain various active constituents of medicinal significance, are employed as an excellent source of treatment for treating human disorders. The permanent consequences of contemporary medicines, along with developing medication resistance, have increased our reliance on medicinal plants as a natural therapy against dangerous and contagious illnesses [1]. Today, over 40% of the population reports using the plant to cure medical illnesses. *Tridax procumbens*, also known as Coat Button and Ghamra, is a highly powerful weed and flowering plant among the 30 species in the Asteraceae family. [2]

Furthermore, the plant has been shown to have hepatotoxic, antioxidant, and hair-growth-promoting properties. According to data that are now available, T. procumbens has been utilized for its anti-ailment properties since ancient times, making it one of the most significant medicinal plants. [3]. Depression, another name for depressive disorder, is a prevalent mental illness. It entails a persistently low mood, loss of enjoyment, or disinterest in activities.

Depression differs from normal mood swings and sentiments about day-to-day living. All facets of life, including those with friends, family, and the community, may be impacted. It may be the cause of or contribute to issues at work and school [4]. Anyone can experience depression. Depression is more common in people who have experienced abuse, significant losses, or other stressful situations. Compared to men, women are more prone to experience depression. An estimated 3.8% of people suffer from depression, which includes 5.7% of individuals over 60 and 5% of adults (4% of males and 6% of women). Depression affects about 280 million people worldwide. Women are almost 50% more likely than men to experience

depression.

Over 10% of women who are pregnant or recently gave birth worldwide suffer with depression. Every year, almost 700,000 people lose their lives to suicide. The fourth most common cause of mortality for people aged 15 to 29 is suicide.

More than 75% of people in low- and middle-income nations do not obtain treatment for mental problems, despite the fact that there are proven, efficient treatments for them. Lack of funding for mental health services, a shortage of qualified medical professionals, and the stigma attached to mental illnesses are all obstacles to providing good care [7].

2. MATERIAL AND METHODS

Collection of Plants

The local murmur area is where the leaves of T. procumbens (Linn.) were gathered. For two weeks, T. procumbens was cleaned and allowed to dry in the shade. Fine powder was made.

Preparation of Plant Extract:

Preparation of Powder:

Tridax procumbens leaves were gathered and allowed to dry in the shade. They were mechanically crushed into a fine powder after drying, then sieved through 60 mesh and kept in an airtight container. Later extraction procedures made use of this powdered substance.

Preparation of Hydroalcoholic extract by using Soxhlet apparatus:

A Soxhlet device with 70% ethanol was used to hot extract 500 g of the plant's dried leaves. Following the completion of the extraction procedure, the solvent was removed at a lower pressure, and the resultant extract was kept for later examination in a vacuum desiccator.

Preparation of Aqueous extract by using Soxhlet apparatus:

To acquire extracts for further analysis and research, the air-dried plant powder was treated to aqueous extraction using a Soxhlet device. Making an aqueous extract using lyophilization:

Distilled water was mixed with the powdered plant material in a 1:5 ratio, and the mixture was left to stir overnight at room temperature. The mixture was then filtered using a Whatman filter to get rid of any solid residue. Filter paper number one. After being freeze-dried, the resultant aqueous extract was kept in an airtight container.

Preliminary Phytochemical Screening:

Standard test procedures were used to perform a preliminary phytochemical screening and quantitative test for the presence of phenols, tannins, flavonoids, alkaloids, terpenoids, anthraquinones, steroids, and saponins. Using established techniques, these phytochemicals were identified based on their color change characteristics:

Tests for Phenols:

When 0.5 ml of $FeCl_3$ (w/v) solution was added to 2 ml of test solution, a strong hue formed, indicating the presence of phenols.

Test for Flavonoids:

NaOH Test:

A test tube was filled with two to three milliliters of extract and a few drops of sodium hydroxide solution. The absence of flavonoids 12 was revealed by the formation of a bright yellow color that did not turn colorless when a few drops of diluted HCl were added.

An estimated 3.8% of people suffer from depression, which includes 5.7% of individuals over 60 and 5% of adults (4% of males and 6% of women). Depression affects about 280 million people worldwide. Women are almost 50% more likely than men to experience depression.

Shinoda Test:

Concentrated HCl was poured dropwise to a test tube containing two to three milliliters of extract and a few pieces of magnesium metal. The development of a magenta hue suggested the presence of flavonoids.

Test for Tannins:

Gelatin Test:

The extract was mixed with a solution of gelatin, which dissolves instantly in warm water. The presence of tannins 14 was detected by the formation of white precipitate.

Lead Acetate Test:

Five milliliters of extract were mixed with a few drops of a 10% lead acetate solution. The presence of tannins was detected by the formation of a yellow or red precipitate. Test for Saponins: 14.

Foam Test:

For 15 minutes, the extract was shaken in a graduated cylinder after being diluted with 20 milliliters of distilled water. Saponins were detected by a 1 cm layer of foam. 13. Hemolysis Test: A glass slide was coated with one drop of extract and one drop of blood. The hemolytic zone showed up on 13. Iodine Test for Alkaloids: When a few drops of diluted iodine solution were added to three milliliters of test solution, the result was a blue tint that vanished when the mixture boiled and returned when it cooled. Wagner's Test: Two to three milliliters of the extract were mixed with a few drops of Wagner's reagent. Alkaloids 15 were present when a reddish-brown precipitate formed.

Total Flavonoid Content

With some adjustments, a colorimetric test as previously described [28] was used to determine the total flavonoid levels. In a 96-well microplate, 100 µL of aluminum (III) chloride hexahydrate (2% w/v in water) was combined with 100 µL of either 100 µL sample (1 mg/mL) or quercetin standard (5–25 µg/mL). A microplate reader (MultiskanTM Microplate Spectrophotometer, Thermo Fisher Scientific, Osaka, Japan) was used to measure the absorbance of the reaction mixture at 430 nm following a 15-minute incubation period at room temperature. Mg of quercetin equivalent (QE) per gram of extract or fraction ($r2 = 0.999$) was used to express the overall flavonoid contents.

Molecular docking

The capacity of molecular docking to anticipate the binding location and ligand-protein binding affinity makes it a popular tool in drug creation. PubChem provided the three-dimensional structures of every compound. MAPK1, MAPK8, CCNDI, and other key targets' crystal structures were available in the Protein Data Bank (PDB) database (https://www.rcsb.org/). [8][9] Molecular docking was performed using Autodock Vina v1.1.2 from the Scripps Research Institute to convert structural files to PDBQT format. A cavity detection method based on curvature was used to identify the sizes and centers of binding sites. After ligand docking, Vina scores-a measure of action. Using a curvature-based cavity detection method, binding site sizes and centers were ascertained. Vina scores, which measure binding affinity, were derived using ligand docking; more negative scores signify more stable ligand-receptor binding.[10][11].

3. RESULTS

Table 1: The yield of *Tridax procumbens* leaves various extracts:

Sr. No	Extract	% Yield
1.	Hydroalcoholic extracted by using Soxhlet apparatus	18.75
2.	Aqueous extract by using Soxhlet apparatus	15.18
3.	Aqueous extract by lyophilization	17.89

Table 2: Preliminary Phytochemical Screening and Quantitative Test

Sr. No	Test	Observation		
		Hydroalcoholic Extract by Soxhlet apparatus	Aqueous Extract by Soxhlet apparatus	Aqueous Extract by lyophilization
1.	Flavonoids ● sodium hydroxide test ● Shinoda test ● lead acetate test	 + + +	 + + -	 + - +
2.	Tannin ● Gelatin test	-	-	-
3.	Saponin ● Foam test ● Hemolysis test	 + +	 + +	 + +
4.	Alkaloids ● Iodine test ● Wagner's test	 + +	 + +	 + –

Table 4: Quantitative Analysis: Total Flavonoid Content

Sr. No	Extract	TFC
1	Hydroalcoholic extract	143.25mg/g
2	Aqueous Extract (Soxhlet apparatus)	99.5mg/g
3	Aqueous Extract (lyophilization)	60mg/g

Table 5: Molecular docking Results

Sr. No		ESRI	CONDI	MAPKI	MAPK8
1.	Kaempferol	-6.9	-6.9	-6.6	-6.9
2.	Quercetin	-7	-7.4	-7.1	-7.6

4. DISCUSSION

Tridax procumbens contains several phytoconstituents including kaempferol, quercetin, rutin, taxifolin which have been reported as antidepressants. The different extract like hydroalcoholic extract, aqueous extract by Soxhlet apparatus, aqueous extract by lyophilization were subjected to phytochemical investigation, total flavonoids content analyses. Hydroalcoholic extract of *Tridax procumbens* by Soxhlet apparatus showed superior presence of flavonoids, alkaloids, phenolics a compared to aqueous extract. The quantitative analysis of *Tridax procumbens* showed that hydroalcoholic extract has highest level of total flavonoid content, followed by lower concentration in aqueous extract obtained through Soxhlet apparatus and lyophilization. Molecular docking was performed for predicting the binding affinity and interaction between ligands and protein targets involved in disease like depression. The study utilized three dimensional structures of compounds obtained from PubChem and crystal structure of protein targets obtained from protein data bank.

Phytoconstituents such as kaempferol, quercetin binds with MAPK1, MAPK8, and CCNDI with good binding affinity. This suggest that hydroalcoholic extract of Tridax shows higher concentration of phytoconstituents and the phytoconstituents present in *Tridax procumbens* extract shows antidepressant activity by our in silico docking study.

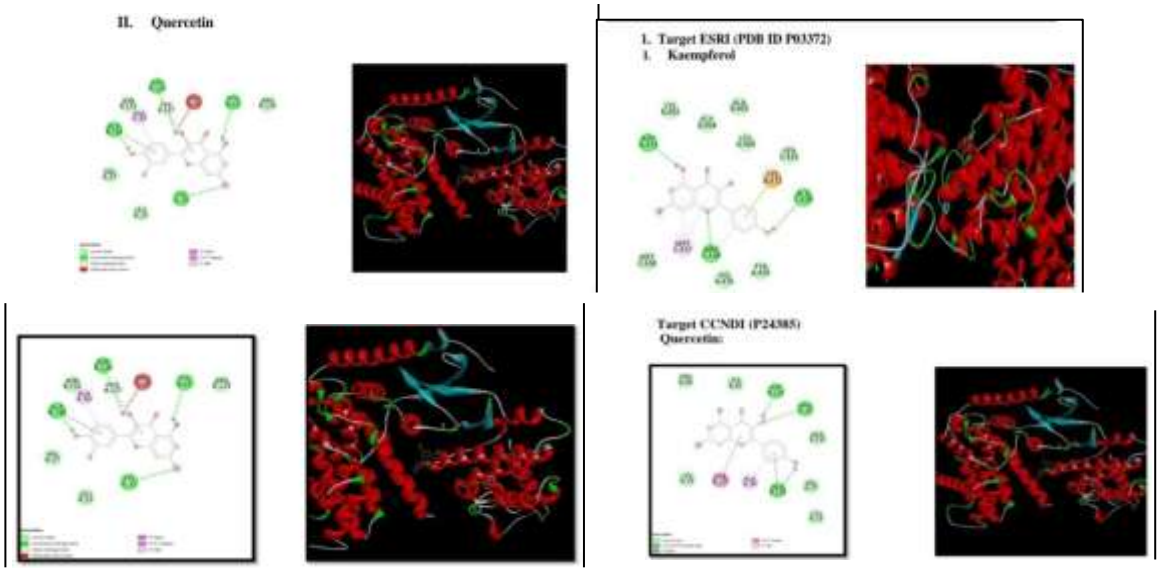

5. CONCLUSION

The findings of our present study suggest that hydroalcoholic extract of *Tridax procumbens* shows greater phytoconstituents like flavonoids, alkaloids etc. previously it is reported that flavonoids shows antidepressants activity. The flavonoids docked with the receptors involved in depression and it shows greater binding affinity. However, precise mechanism is need to be understood, in future in vivo study would be required to know the extract mechanism by which *Tridax procumbens* shows antidepressant activity.

REFERENCES

[1]. Sawant RS, Godghate AG. Preliminary phytochemical analysis of leaves of Tridax procumbensLinn. International Journal of Science, Environment and Technology. 2013;2(3):388-94.

[2]. Beck S, Mathison H, Todorov T, Calderón-Juárez EA, Kopp OR. A review of medicinal uses and pharmacological activities of Tridax procumbens(L.). Journal of Plant studies. 2018;7(1):19-35.

[3]. Ingole VV, Mhaske PC, Katade SR. Phytochemistry and pharmacological aspects of Tridax procumbens(L.): A systematic and comprehensive review. Phytomedicine Plus. 2022 Feb 1;2(1):100199.

[4]. Wong ML, Licinio J. Research and treatment approaches to depression. Nature Reviews Neuroscience. 2001 May 1; 2(5):343-51.

[5]. Beck AT, Alford BA. Depression: Causes and treatment. University of Pennsylvania Press; 2009 Mar 25.

[6]. Grover S, Dutt A, Avasthi A. An overview of Indian research in depression. Indian journal of psychiatry. 2010 Jan 1; 52 (Suppl1):S178-88.

[7]. Kessler RC, Wang PS. Epidemiology of depression. Handbook of depression. 2009; 2:5-22.

[8]. De Ruyck J, Brysbaert G, Blossey R, Lensink MF. Molecular docking as a popular tool in drug design, an in silico travel. Advances and Applications in Bioinformatics and Chemistry. 2016 Jun 28:1- 1.

[9]. Mihăşan M. What in silico molecular docking can do for the 'bench-working biologists' Journal of biosciences. 2012 Dec; 37: 1089-95.

[10]. Sharma V, Sharma PC, Kumar V. In silico molecular docking analysis of natural pyridoacridines as anticancer agents. Advances in Chemistry. 2016; 2016(1):5409387.

[11]. Mendie LE, Hemalatha S. Molecular docking of phytochemicals targeting GFRs as therapeutic sites for cancer: an in silico study. Applied biochemistry and biotechnology. 2022 Jan; 194(1):215-31.

*****

ISBN: 978-81-970491-8-7
26
Current Research in
Science and Technology
(An Edited Book)

Crystal Chemistry of Ferrite Magnetic Material: A Brief Review

Vitthal V. Gaikwad

Department of Physics, Moreshwar Arts, Commerce and Science College, Bhokardan. Dist. Jalna
Email: *vitthalgaikwad900@gmail.com*

ABSTRACT

Any materials can be identified by its crystal chemistry which include structure and properties. A ferrite magnetic material typically has a crystal structure called "spinel," where the basic unit is a cubic close-packed lattice of oxygen anions with metal cations (usually including iron) occupying either tetrahedral or octahedral interstitial sites, represented by the chemical formula $AB_2\ O_4$, where A and B are different metal cations; the distribution of these cations across the sites determines the specific magnetic properties of the ferrite material, with variations like "normal" and "inverse" spinel structures possible depending on the composition and cation arrangement. In this review article we are focused on crystal chemistry of ferrite magnetic material in brief.

Keywords: *Crystal chemistry, Ferrite, magnetic materials, Composition*

1. INTRODUCTION

The advances made in physics and chemistry of solids has led to the recent progress in science and technology. Physics and chemistry of condensed matter draw attention to chemical composition, atomic configuration, electrical and magnetic properties, crystal structure etc. of the solids. It also helps to co-relate the physical and chemical properties of solids and their use in technological applications. Due to the needs of society, material science dealing with physics and chemistry of solids along with engineering and technology was developed. In the recent years, solid state physics mainly concentrates on crystal structure, chemical and physical properties of solids. A proper understanding of the nature and properties of solids form the basis for developing new tailor-made materials with the desired properties that can be used in many electrical and electronic devices [1]. Among the magnetic ceramics, magnetic oxides are the most important and rather the only relevant materials from the point of view of their applications [2]. They are being studied over a long period of five to six decades for their basic properties as in the wide field of applications.

2. NATURE OF FERRITE

Ferrites are ceramic ferromagnetic materials with the general chemical composition $MO\text{-}Fe_2O_3$ where M is a divalent metal such as iron, magnesium, nickel, zinc, cadmium, cobalt, or a mixture of these [3-4]. The trivalent Fe^{3+} ions can be replaced by other trivalent ions like aluminum, gallium, chromium, indium, etc. The high valence cations like niobium, antimony, molybdenum etc. can also be incorporated in the spinel lattice. By replacing M we can get number of ferrites which have its own features and all of them are useful in many applications. Usually, cations of larger radii occupy octahedral B-site whereas, cations of lower radii can occupy tetrahedral A-site. The ionic radii of the substituting ions should be between about 0.5 Å to 1 Å.

Chemical composition and crystal structure

The spinel crystal structure is determined primarily by the oxygen and oxygen ion lattice. Consequently, the crystal structure can be thought of as being made up of the closest possible packing of layers of oxygen ions, with the metallic ions fit in at the interstices.

The unit cell is cubic, each unit cell contains eight $Me^{2+}Fe_2^{3+}O_4$ molecules [5]. The space group is $Fd_3mO_h^7$.The oxygen ions form a nearly closely packed cubic structure and the metal ions are distributed over the tetrahedral and octahedral holes. In a unit cell, eight tetrahedral and sixteen octahedral sites are occupied by the metal ions. The tetrahedral and octahedral sites are conventionally called A and B sites respectively. The oxygen ion positions are defined by a crystallographic parameter 'u', which generally lies between 0.375 Å and 400 Å.

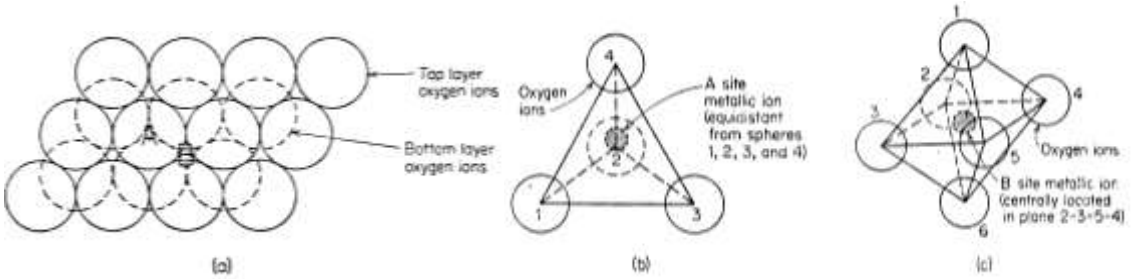

Fig. 1: Atomic arrangement at tetrahedral (A) and octahedral [B] site in spinel structure

The ion packing situation is indicated in Fig. 1 (a). Where, the solid lines represent the top layer of oxygen spheres while the dotted lines represent the bottom layer of oxygen spheres. Upon close examination, it can be seen that there are two kinds of interstices, denoted by letters A and B. A metallic ion located at the A site has four nearest oxygen ion neighbours, three oxygen ions in the bottom layers and one oxygen ion in the top layer (Fig. 1. b). In other words, it is in a site of tetrahedral co-ordination. If the metallic ion is located at B site, it has six nearest oxygen ion neighbours. These oxygen ions are situated at the corners of an octahedron (Fig. 1. C). Thus, the metallic ion is in a site of octahedral co-ordination. For zinc and cadmium ferrites, the divalent metallic ions Zn^{++} or Cd^{++} are at the A site, while the two trivalent ferric ions $2Fe^{+++}$ are at the B site. This structure is same as that of normal spinel. A diagram of the unit cell of the spinel crystal structure is shown in Fig. 2 where the Mg^{++}, Al^{+++}, and O^{2-} ions are represented by spheres of different sizes and shapes.

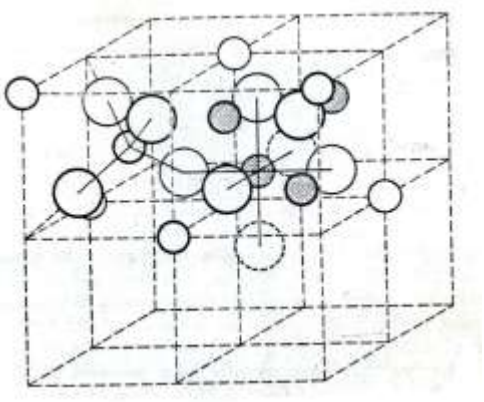

Fig. 2: Crystal structure of spinel ferrite

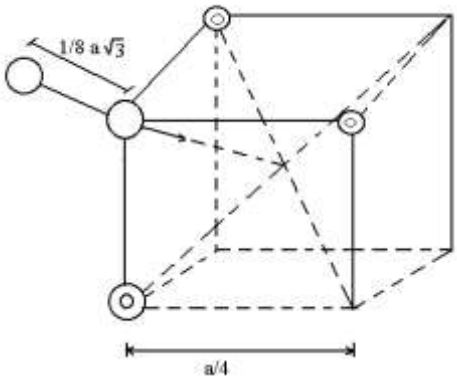

Fig.3: Surroundings of an oxygen in spinel ferrite

Actually, most of the simple ferrites, e.g. $NiFe_2O_4$ are of the inverse spinel structure in which one trivalent ferric ion Fe^{+++} is at the A site while the remaining trivalent ferric ion Fe^{+++} and the divalent metallic ion M^{++} are at the B site [6].

It is interesting to note here that if electrons were transferred from the divalent ferrous ion (Fe^{++}) at the B site to the trivalent ferric ion (Fe^{+++}) at the B site, the compound would remain completely unchanged. Thus, it might be expected that electron flow would be facilitated, giving rise

to high conductivity or low resistivity. The resistivity of iron ferrite Fe_3O_4 is about 10^{-4} ohm meter which is three orders of magnitude higher than that of iron, is till too low for high frequency application. However, if the ferrous ion Fe^{++} is replaced by the nickel ion Ni^{++}, for example, the chemical formula would be:

$$NiO.Fe_2O_3 = Fe^{+++} (Fe^{+++} Ni^{++}) O_4^{--}$$

It is now no longer possible for electrons to be interchanged between the Fe^{+++} and Ni^{++} ions at the B sites without having the final state different from initial one. Indeed, by substituting a metallic ion such as Ni^{++} for the ferrous ion in Fe_3O_4 (Magnetic), the resistivity can be increased to as high a value as 10^7 ohm meter.

3. OXYGEN PARAMETER (U)

In any octant four oxygen ions form a tetrahedron. All oxygen ions are tetrahedrally surrounded by four cations, of which three are from B-site and one from A-site. In many cases the close packing of oxygen is deformed due to the presence of the metal ions of different sizes in the interstices. Then the oxygen ion moves along the body diagonal from the ideal position. The displacement of oxygen ion along the body diagonal is known as oxygen parameter u as shown in Fig. 3. In ideal case u = 3/8 and in the actual case u is slightly greater than ideal value. This non-ideal condition implies a movement of the anion from their ideal position along the (111) direction away from the nearest A-ion. This implies an expansion of tetrahedral and simultaneously contraction of the octahedral site.

The u parameters generally increase linearly with $(r_A-r_B)/a$, where 'a' is the lattice parameter and r_A, r_B are the radii of ions in the A and B sites respectively. The local symmetry of the cations sites is cubic in the A-position and trigonal in B. The trigonal symmetry is due to both the configuration of the neighbouring cations and the distortion of the anion octahedral if $u \neq 3/8$. Each of the four diagonal belongs to just one of the cations in the primitive cell. Hence these cations are non-equivalent, differing in their local symmetry axis. Each of them may be taken as representing on fcc sub-lattice with the lattice constant 'a'. The local symmetry of the A-site however remains cubic even if $u \neq 3/8$, so that, both sub-lattices represented by A-sites in the primitive cell are mutually equivalent. When considering some aspect for which the local symmetry is irrelevant, all the B-position may be treated as belonging to only one sub-lattice (octahedral) in the same way as the A-position may be unified to form one tetrahedral or A-sub-lattice [7].

4. CLASSIFICATION OF SPINEL FERRITES

The distribution of metal ions over tetrahedral (A) and octahedral [B] site in spinel ferrite leads to the classification of spinel ferrite viz. normal spinel, inverse spinel and random spinel. The following Fig.4 shows cations distribution among normal, inverse and mixed spinel.

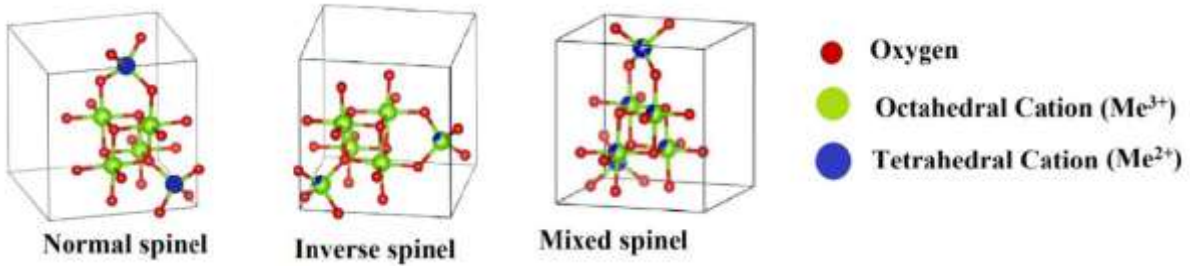

Fig. 4: Cations distribution among normal, inverse and mixed spinel.

1. Normal spinel

In normal spinel all divalent metal ions are distributed at tetrahedral (A) sites whereas all trivalent Fe^{3+} ions are distributed at octahedral [B] sites. This can be expressed as, $M[Fe_2]O_4$. The cations like zinc and cadmium usually have a tendency to occupy tetrahedral A site, therefore zinc ferrite and cadmium ferrite belongs to normal spinel.

2. Inverse spinel

In this type of spinel ferrite, half of the trivalent Fe^{3+} ions prefers to occupy tetrahedral (A) sites while remaining half of the trivalent Fe^{3+} ions are prefers to occupy octahedral [B] sites. The divalent ions prefer to occupy octahedral B site. The distribution of cations is expressed as,

$(Fe)^{A}\ [MFe]^{B}O_4^{2-}$

The typical example of inverse ferrite is nickel ferrite ($NiFe_2O_4$) and cobalt ferrite ($CoFe_2O_4$).

3. Random Spinel

In random spinel ferrite, all divalent ions and trivalent Fe^{3+} ions are randomly distributed over a tetrahedral (A) sites and octahedral [B] sites. In general, this is expressed as,

$$\left(M_x^{2} Fe_{1-x}^{3+}\right)^{A}\left[M_{1-x}^{2+} Fe_{1-x}^{3+}\right]^{B} O_4^{2-}$$

5. CONCLUSIONS

The crystal chemistry plays very important role in case of study of structure of magnetic ferrite materialist structural properties of spinel ferrite are highly depended on the synthesis technique, heating temperature and time, number of substitutions as well as chemical compositions. The distribution of cations in spinel ferrite plays an important role and hence magnetic properties of spinel ferrite are strongly depended upon the interaction between tetrahedral and octahedral cations.

REFERENCES

[1]. M. A. Elhiti, M. A. Ahmed, M. M. Mosad, S. M. Attia, J. Magn. Magn. Mater. 150 (1995) 399.
[2]. M. Singh,J. Magn. Magn. Mater. 299 (2006) 397.
[3]. N.M. Nanoti, D.K. Kulkarni, J. Pure and Appl. Phys. 34 (1996) 57.
[4]. A.K. Rajarajan, S.M. Yusuf, P. Balaya, R.G. Kulkarni, Pramana 58 (2002)787.
[5]. B.V. Bhise, A.K. Ghatage, B. M. Kulkarni, S.D. Lotke, S.A. Patil, Bull. Mater. Sci., 19 (1996) 527.
[6]. M.K. Fayek, S.S. Ata-Allah, H.A. Zayed, M. Kaiser, S.M. Ismail, J. Alloys. Comp., 46 (2009) 9.
[7]. C.G. Koops, Phys. Rev. 83 (1951) 121.

*****

ISBN: 978-81-970491-8-7
27
Current Research in
Science and Technology
(An Edited Book)

Various Synthesis Techniques for the Preparation of Ferrite Material

Dr. Sangita Shinde

Department of Physics, Partisthan Mahavidylaya, Paithan. Dist. Chhatrapati Sambhajinagar (M.S.) India-431112
Email: *sangitamawal@gmail.com*

ABSTRACT

Today ferrite is very useful material due to their high electrical resistivity, low eddy current and dielectric losses and good magnetic properties, so that ferrite materials play very great significance in the development of many devices which are useful to mankind in day-to-day life. Methods of preparation play an important role with regards to their electric and magnetic properties. Materials of same composition prepared by two different technique shows the variation in their properties. The preparative parameters like sintering temperature and atmosphere, cooling rate etc. also influence the properties of ferrite. Amount and type of cations also governs the electric and magnetic properties of ferrite. In this article we know the various preparative methods of ferrite magnetic materials

Keywords: *Ferrite; Synthesis techniques; ceramic method, sol-gel method.*

1. INTRODUCTION

The preparation of polycrystalline soft ferrites with optimum properties is considered to be difficult and complex. The main problem is induced due to the fact that most of the properties needed for ferrite applications are not intrinsic but extrinsic i.e. the ferrite is not completely defined by its chemistry and crystal structure but also requires knowledge and control of the parameter of its microstructures, such as density, grain size, porosity and their intra and inter granular distribution.

A variety of soft ferrites have been prepared in the past several years by the traditional ceramic method, which involves mixing and grinding powders of the constituent oxides, carbonates and other such compounds and heating them at high temperature with intermediate grinding, when necessary. Low temperature chemical routes and other such method involving mild reaction condition are however of the greater interest. The chemical routes are indeed desirable because they led to new products. The characterization and measurement of properties of spinel ferrite can be achieved by various experimental techniques. The preparation of ferrite effects on its characterization. There are various methods of preparation of magnetic oxide systems i.e. ferrite. In this paper, we are focused on most likely preparation methods of ferrite material and other in details.

2. METHODS OF SAMPLE PREPARATION

There are several methods of preparation of magnetic oxide systems with cubic structure apart from standard ceramic method. These includes:

1. Wet chemical (co-precipitation) method [1].
2. Hydrothermal synthesis [2].
3. Simple self-propagating, gas producing, auto catalytic, novel combustion process [3].

4. Garnet films created by laser annealing [4].
5. Chemically synthesized precursors produced ferrite powders at low temperature [5].
6. Non-aqueous chemical route [5].
7. Preparation of Gallstones from processed stones [7].
8. Hot-spray reactor [8].
9. Ceramic method [9] etc.

2.1. Ceramic Method

In the ceramic method very pure and fine grains constituents in oxide forms are taken. The most common method of preparing metal oxides and other solid materials is by the ceramic method. In the ceramic method very pure and fine grains constituents in oxide forms are taken. Then they are thoroughly and uniformly mixed. This mixture is sintered for prolonged time at specific temperature so as to facilitate solid-state chemical reaction among the oxides and the formation of chemical compound. Pre-sintering of the samples can be done at about 900^0C and final sintering of the ferrite sample can be done at above 1200^0C depending on the constituents. The ceramic method consists of, Weighing and thorough mixing of constituents in stoichiometric proportion.

i. Grinding of the mixed powder for 3-4 hours.
ii. Presintering at the temperature slightly lesser than the solid-state chemical reaction temperature,
iii. Powdering and pressing into desired shape using hydraulic press
iv. Final sintering at elevated temperature (>1000^0C) and slow cooling.

All these steps involved in the preparation of ferrite are depicted in the flow sheet as shown in **Fig. 1.** Several mixed oxides, sulphides, phosphides etc. normally can be prepared by this method. Knowledge of the phase diagram is generally helpful in fixing the desired composition and condition for synthesis. Caution is taken in deciding the choice of the container.

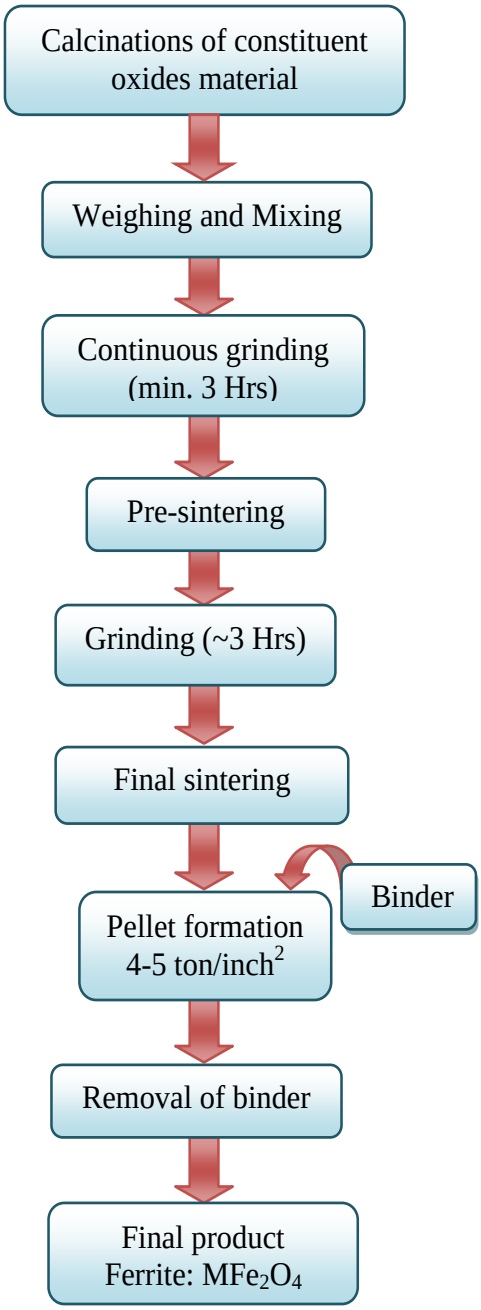

Fig. 1: Flow chart for ceramic method

2. Sol gel Method

Sol gel method is an important mean of preparing inorganic oxides. It is a wet chemical method and a multistep process involving both chemical and physical processes. A sudden increase in viscosity is the common feature in sol-gel processing, indicating the onset of gel formation.

The important features of the sol-gel method are.

i. Better homogeneity
ii. High purity
iii. Lower processing temperature
iv. Better size and morphological control
v. More uniform phase distribution in multi component systems like ferrites.

The steps in sol gel synthesis are as follows.

1. Hydrolysis

The process of hydrolysis may start with a mixture of metal alkoxide and water in a solvent usually alcohol at the ambient or slightly elevated temperature.

2. Polymerization

This step involves condensation of adjacent molecules where in H_20 and alcohol are eliminated and metal oxide linkages are formed. Polymeric networks grow to colloidal dimensions in the liquid (sol) state.

3. Gelation

In this step, the polymetric networks link up to form a three-dimensional network throughout the liquid. The system becomes somewhat rigid, on removing the solvent from the sol. Solvent as well as water and alcohol molecules remain inside the pores of the gel. **Fig. 2** represents the preparation of spinel ferrite by sol-gel method

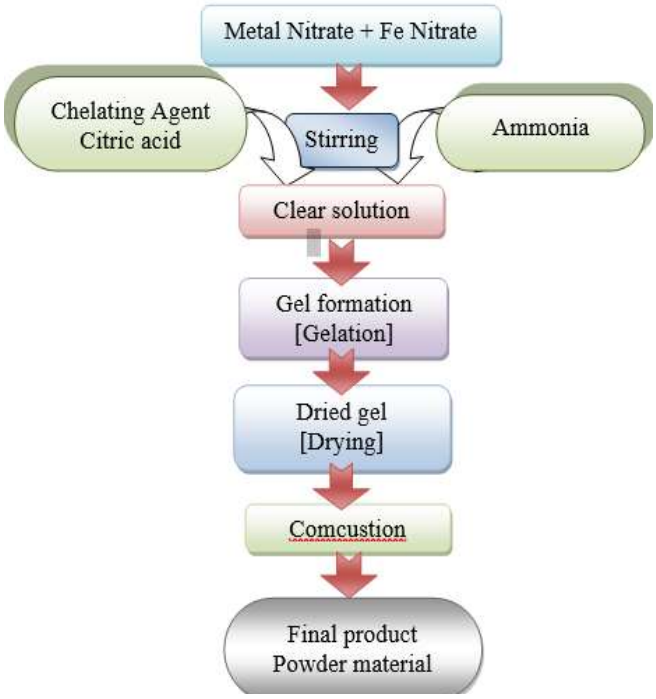

Fig. 2: Sol-gel auto combustion method

4. Drying

Water and alcohol are removed at moderate temperatures leaving a hydroxylated metal oxide with residual organic content.

5. Dehydration

This step is carried out between 670 K and 1070 K to take off the organic residues and chemically bound water, yielding a glass metal oxide.

6. Densification

Temperature in excess of 1270K are used to form the dense oxide product. The sol-gel technique has been used to prepare sub micrometer metal oxide powders with a narrow particle size distribution and unique particle shapes. Metal-ceramic composites as well as organic- inorganic composites have been prepared by the sol gel route.

3. CONCLUSIONS

Method of preparation are very important in the formation of ferrite magnetic material generally researchers are used various method for the preparation of ferrite material but ceramic or solid-state reaction methods are a very important and prominent method for the preparation of ferrite material in bulk form and sol- gel-auto composition method is another method to from nano ferrite.

REFERENCES

[1]. T. Takada and M. Kiyama, In. Proc. Of the Int. Conf. On Ferrites. Japan 69 (1970)
[2]. R. C. Weast, "CRC Handbook of chemistry and physics" CRC Press (1981)
[3]. X. Yi, Q. Yitai, L Jing, C. Zuyao, Y Li, Mat. Sci. Eng. B 34 (1995) L1.
[4]. K. Suresh and K. C. Patil, J. of Alloys and Comp., 209, 203 (1994)
[5]. S.R. Jain, K.C. Adiga, V. R. Pai Verneker. Combust. Flamt. 40 (1981) 71.
[6]. P. S. Anil Kumar, J. J. Shrotri, S. D. Kulkarni, C. E. De. and S. K. Asian J. of Phys.6(1-2) (1997) 217
[7]. Amit Sinha, B. P. Sharma, D. P. Chakravarty and A. R. Biswas, Asian J. Phys. 6 (1 - 2) (1997) 31.
[8]. R. M. Dell, Proc. 7th Int. Sym. Reac. of solids, Bristo 1972 P. 553.
[9]. D. M. Roy, R. R. Neurgaonkar, T. P. O' Holleran and R. Roy, Amer. Ceram. Soc. Bull. 56 (1977) 1023.

*****

ISBN: 978-81-970491-8-7
28
Current Research in
Science and Technology
(An Edited Book)

Non-Linear Optical Properties of Spin Multiplicity Acetonitrile: A Quantum Chemical Study

Dr. Bhagwat Kharat

Department of Physics, Swami Vivekanand Senior College, Mantha, Maharashtra, India
Email: *bhagwat6776@gmail.com*

ABSTRACT

The spin multiplicity acetonitrile are singlet, triplet and quintet state of acetonitrile. We have reported the structural changes viz. bond length, angles, dipole moment and their energies at B3LYP/aug-cc-pVDZ level of theory. There is significant change is observed in bond angle (CCN) with changing the spin state of the system. We have reported the vibrational spectra and corresponding modes of spin multiplicity acetonitrile. The singlet acetonitrile modes are well matching with the available experimental determinations. It is observed that HOMO to LUMO gap is more for singlet than triplet and quintet state and it is decreasing with the applied filed. We have also reported first and second hyperpolarizabilities of singlet, triplet and quintet state of acetonitrile. It is observed that all three states of acetonitrile showing good response to NLO especially at augmented and polarized basis sets for all methods. The quintet state of acetonitrile is most stable with respect to applied field. All these calculations have been performed using Gaussian 09 software.

Keywords: *Spin multiplicity acetonitrile, NLO properties, and quantum chemical methods*

1. INTRODUCTION

The new nonlinear optical (NLO) materials are essential for the applications such as modulation of optical signals, micro-fabrication, sensing, imaging, and cancer therapy, optical processing of data, optically data and image storage, and optically based telecommunications, optically based computers. Organic molecules are the promising candidates in this regard due to their high nonlinear optical (NLO) properties in particular the first and second hyperpolarizabilities (β and Y). The first and second hyperpolarizabilities are the origin of the macroscopic second and third order NLO response of organic molecules [1-5]. Several organic molecules have been investigated both, experimentally and theoretically for their possible applications in development of photonic devices. However, extensive efforts have been made to understand the nonlinear optical properties of donor-acceptor type molecules with conjugated chain in between [6-10]. Synthesis of a novel material and then testing its suitability for the NLO applications is a time consuming and expensive work. One can predict the NLO properties of a material theoretically and if found suitable for NLO applications the material can be synthesized with the help of quantum chemical methods.

Organic molecules are therefore being synthesized for their possible applications in photonics due to their relative ease of processing. It is necessary to design and evaluate NLO properties of different organic molecules in order to use them in photonic devices. This is due to the facts that one of the key factors for applications in photonics and bio photonics is to find materials with particular nonlinear optical properties at desirable wavelength regions. Computational method has played and will continue to play an important role in the design of nonlinear optical material [11-15]. We are now able to control the material properties by engineering their structure at the molecular level. It is now

also possible to control the material properties at all dimensional scales such as macro, micro, and nano. Due to the designing and identification of organic material for novel applications in photonics is very essential.

Acetonitrile is one of the important solvents used in the laboratory and has many applications in organic synthesis, physical organic and electro-organic chemistry. For the nonlinear susceptibilities for the organic materials play not only the electronic contributions however also the vibration contribution [16]. Much less attention has been paid to the spin dependent hyperpolarizabilities of organic molecules. This paper is structured as fellows. Next section gives computational details. Results are presented and discussed in the third section. It includes structure and NLO properties of acetonitrile in singlet, triplet and quintet states. Conclusions are inferred in the last section.

Computational details

The exchange and correlation function B3LYP and augmented basis set aug-cc-pVDZ used to optimize the geometries of singlet, triplet and quintet spin structures of acetonitrile. The optimized geometries are presented in Fig. 1. The geometrical parameters are such as bond length and angles are well matching with the available experimental determinations at this level of theory. Vibrational spectra of spin multiplicity acetonitrile calculated at B3LYP/aug-cc-pVDZ level of theory. HOMO to LUMO gap and wavelength of transitions. To avoid the numerical instability, the first and second hyperpolarizabilities (β and γ) calculated for all three spin states of acetonitrile along the z-axis by applying the field strength from 0 to 0.20 a.u at B3LY/aug-cc-pVDZ level of theory. At the 0.008 a.u field strength, the first and second hyperpolarizabilities showing the constant. Further this field is chosen to calculate and γ at various methods and basis sets.

2. RESULT AND DISCUSSION

2.1. Structural parameters

The structural parameters of singlet, triplet and quintet structures of acetonitrile optimized at B3LYP/aug-cc-pVDZ level of theory shown in Fig.1 and corresponding structural parameters are given in Table 1. The structural parameters of singlet acetonitrile are well matching with the available experimental determinations [17].It is clearly seen that the effect of spin on structural parameters, as the spin changes from singlet to quintet bonds loosen leading towards to the dissociation. The dipole moment for singlet acetonitrile is 4.05 Debye which is in excellent agreement with the experimental value 4.07 Debye [15]. In additions to this significant shortfall is observed in dipole moment. Upto quintet state of acetonitrile is considered for the study since further structures are more unstable and dissociated.

Table1: Structural parameters, dipole moment and energies of singlet, triplet, and quintet of Acetonitrile monomer atB3LYP/aug-cc-pVDZ level of theory along with experimental values.

Parameter[a]	Expt	Singlet	Triplet	Quintet
C-C	1.458[a]	1.462	1.482	1.465
C≡N	1.157[a]	1.160	1.292	1.558
C-H	1.102[a]	1.098	1.110	1.102
∠C-C-H	109.5[a]	110.1	108.3	112.0
∠C-C-N	-----	178	123.4	119.7
∠H-C-H	-----	108.9	108.6	107.6
Dipole moment (Debye)	4.07[b]	4.05	2.78	1.91

2.2. Non-linear Optical properties

The finite field method used to calculate the first and second hyperpolarizabilities (β and γ) of singlet, triplet and quintet state of acetonitrile using energy-based equation. The energy-based equations are more stable with respective to the field strength than the dipole moment-based equation.

We have used here energy-based equation for obtaining the hyperpolarizabilities using the finite field method. As the finite field technique is a derivative method, the numerical problem cannot be avoided. Determine the numerical stable hyperpolarizabilities suitable field strength needs to be found out by calculating hyperpolarizabilities at different field strengths. The numerical accuracy of the finite field equation is sensitive to the field strength and the level of theory used for the calculations. So, we have applied different field strengths here for the calculation of hyperpolarizabilities of acetonitrile in singlet state to prevent the numerical instability. The level of theory used here is B3LYP/aug-cc-pvdz, since at this level of theory; acetonitrile in singlet state has the lowest energy among different levels of theory used here and agreement with the experimental values. After deciding the suitable field strength, we then obtained hyperpolarizabilities for singlet, triplet and quintet state of acetonitrile using different levels of theories vis. methods and basis sets.

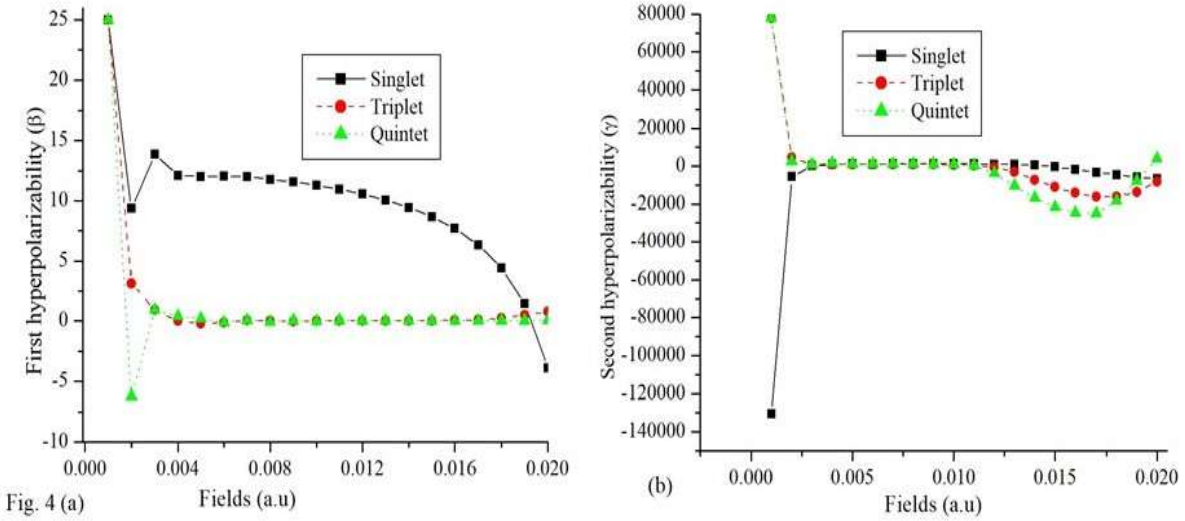

Fig. 1: Effect of field strength along Z-axis from the 0.001 to 0.02 a.uof singlet, triplet, and quintet spin state of acetonitrileonfirst & second hyperpolarizability at B3LYP/aug-cc-pVDZ level of theory.

Fig.1 (a) and (b) shows the variation in β and γ respectively of acetonitrile singlet state with field strengths obtained using finite field method. we can say that acetonitrile shows numerically stable hyperpolarizabilities at a certain range of field strength. So, we have chosen field strength of 0.008 a.u. to calculate the hyperpolarizabilities for singlet, triplet and quintet state of acetonitrile using different method and basis sets. β values are zero for the triplet and quintet sate There is almost no variation for triplet and quintet in β values irrespective of the level of theory used for the calculation. Also, the β values are positive for the singlet state. However, γ values are nonzero for acetonitrile in singlet, triplet and quintet for various basis sets and methods.

Fig. 2 and 3 show the variation of β and γ respectively for acetonitrile in singlet, triplet and quintet state for various basis sets and methods. The basis set effects on β in singlet is greater than the methods. From Fig.6 that the basis sets in the absence of diffuse functions on hydrogen and heavy atoms cannot provide a sufficient magnitude of γ. The basis set which shows the low magnitudes of γ are the split valence triple zeta basis set without diffuse and polarization functions and the SDD pseudopotential. When diffuse functions are added to the split valence triple zeta basis set, the magnitude of γ obtained using different methods changes significantly. For the split valence triple zeta basis set (6-311G) without diffuse functions and SDD pseudopotential, there is no large change in the magnitude of γ for the singlet and quintet, obtained using different methods such as MP2, MP3, MP4 and DFT with different exchange and correlation functional viz. BLYP, B3LYP, B3PW91, PBEPBE and PBE1PBE. On the other hand, when the diffuse functions are added to the basis set for hydrogen and heavy atoms, the magnitude of γ changes significantly for all the methods used here. The γ values obtained for the singlet and quintet state using MP2, MP3 and MP4 methods are almost equal for all the basis sets used here.

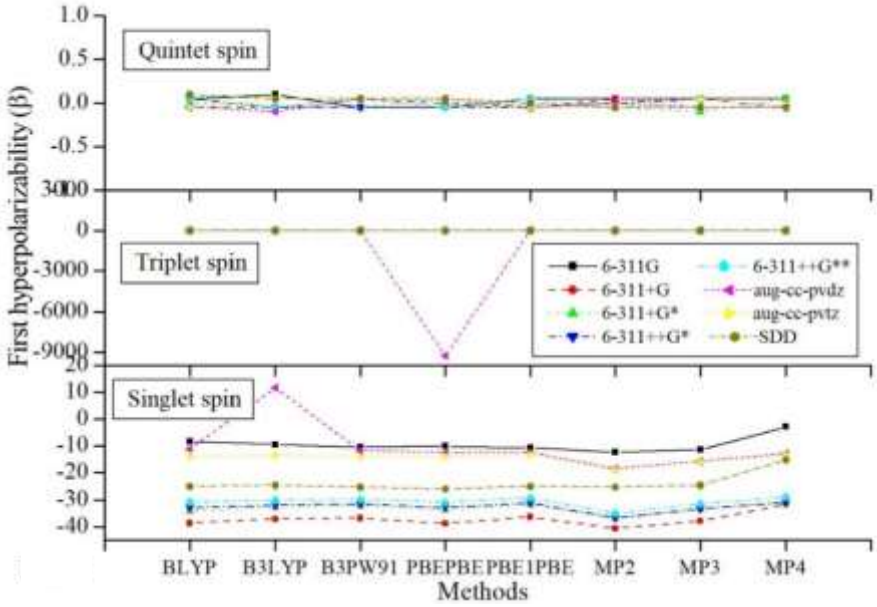

Fig. 2: First hyperpolarizability (β) of singlet, triplet, and quintet spin state of acetonitrile at B3LYP/aug-cc-pVDZ level of theory using the field strength of 0.008 a.u.

The γ values by the B3PW91and PBE1PBE methods are nearly equal for all the basis sets. Similarly, the values of γ by the PBEPBE method are found to be nearly equal to those by the BLYP. As judged from the magnitude of γ for obtaining converged γ, the MP2, MP3 and MP4 methods seem to be essential, and they can be quantitively reproduced by the PBE1PBE, B3PW91 and B3LYP method for most of the basis sets used here. On comparing the γ values from MP2 and DFT levels for the added diffuse and polarization functions on hydrogen and non-hydrogen atoms, the former gives higher γ values than the latter. There is no large difference in the γ values using DFT with different exchange and correlation functionals.

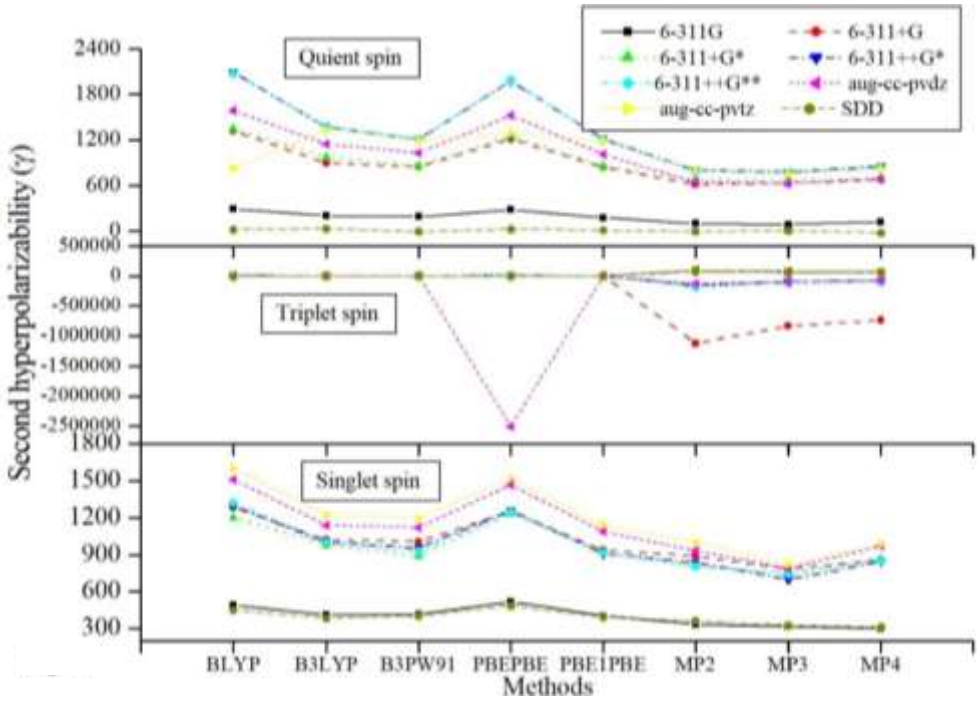

Fig. 3: Second hyperpolarizability (γ) of singlet, triplet, and quintet spin state of acetonitrile at B3LYP/aug-cc-pVDZ level of theory using the field strength of 0.008 a.u.

2.3. HOMO LUMO Gap

Fig. 4 showing the HOMO to LUMO gap energy along the applied field reported at B3LYP/aug-cc-pVDZ level of theory. As the field increases the HOMO to LUMO gap decreases in

addition to the spin state of acetonitrile. The quintet state of acetonitrile showing less than 1 eV HOMO to LUMO gap at 200 a.u field strength. This state of system is most stable compared to remaining at all other fields.

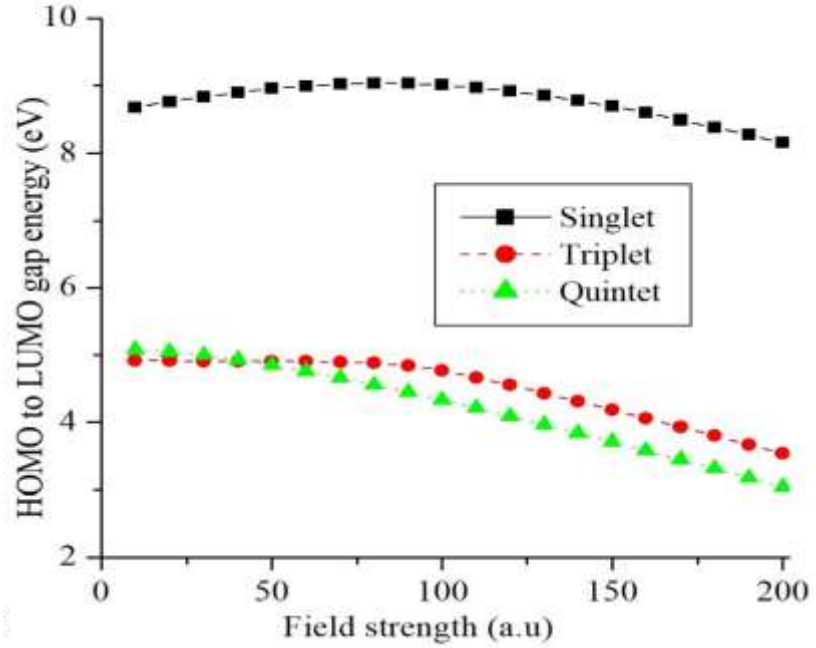

Fig. 4: Homo-Lumo electronic energy gap (eV) of acetonitrile in singlet, triplet and quintet state of acetonitrile at various fields at B3LYP/aug-cc-pVDZlevelof theory.

3. CONCLUSION

The present work reported, the structural changes and non-linear optical properties of singlet, triplet and quintet spin state of acetonitrile. It is also reported the HOMO to LUMO gap energy varying with applied field strength. It is observed that the good response for second hyperpolarizability for all spin states than the first hyperpolarizability. Singlet and quintet state of acetonitrile is good candidate for NLO response. The augmented basis sets (aug-cc-pvdz and aug-cc-pvtz) and 6-311++g** are quite reasonable basis sets to study NLO properties. In addition to this it is also reported that the HOMO to LUMO gap variation with respect to field which is good correlation with the observations. Increase in field strength, decrease in HOMO to LUMO gap. Here for quintet state of acetonitrile showing least energy gap with applied field strength. All these calculations performed at B3LYP/aug-cc-pvdz level of theory using Gaussian 09 software.

REFERENCES

[1]. Nalwa H, Miyata S, Nonlinear Optics of Organic Molecules and Polymers, CRC, NewYork (1995).

[2]. Bosshard C, Sutter K, Pretre P, Hulliger J, Flosheimer M, Kaatz P, Gunter P, Nonlinear Optical Materials, Gordon and Breach Basel, Switzerland (1995).

[3]. Chemla D, Zyss J (eds.), Nonlinear Optical Properties of Organic Molecules and Crystals, Academic Press, New York (1987), Vols. 1 and 2.

[4]. Prasad P, Williams D, Introduction to the Nonlinear Optical Effects in Molecules and Polymers, Wiley, New York (1991).

[5]. Williams D, (ed.), Nonlinear Optical Properties of Organic and Polymeric Materials ACS Symposium Series 233, Americal Chemical Society, Washington, DC (1983).

[6]. Pina J,Seixas de Melo J, Burrows H, Batista R, Costa S, Raposo M, Spectral and photophysical characterization of donor-π-acceptor arylthienyl-and-bithienyl-benzothaizolederivaties in solution and solid state. J. Phys. Chem. A 2007; 111:8574.

[7]. Atalay Y, Avci D, Basoglu A, Linear and non-linear optical properties of some donor-acceptor oxadiazoles by a initio Hartree-Fock calculations. Struct. Chem. 2008; 19:239.

[8]. G. Allis D, Spencer J, Polyhedral-based nonlinear optical materials. Part 1. Theoretical investigation of some new high nonlinear optical response compounds involving carboranes and charged aromatic donors and acceptors J. Organometallic. Chem.2000; 614:309.

[9]. Avci D, Basoglu A, Atalay Y, Effects of different basis sets and donor-acceptor groups on linear and second-order nonlinear optical properties and molecular frontier orbital energies. Int. J. Quant. Chem. 2011; 111:130.

[10]. Locknar S, Peteanu L, Shuai Z, Calculation of ground and excited state polarizabilities of unsubstituted and donor/acceptor polyenes: A comparison of finite-field and sum-over-states method. J. Phys. Chem. A 1999; 103:2197.

[11]. Ohta S, Nakano M, Kubo T, Kamada K, Ohta K, Kishi R, Nakagawa N, Champagne B, Botek E, Takebe A, Umezaki S, Nate M, Takahashi H, Furukawa S, Morita Y, NakasujiK, Yamaguchi K,Theoretical Study on the Second Hyperpolarizabilities of Phenalenyl Radical Systems Involving Acetylene and Vinylene Linkers: Diradical Character and Spin Multiplicity DependencesJ. Phys. Chem. A 2007;111: 3633.

[12]. M. Nakano M, Kishi R, Nitta T, Kubo T, Nakasuji K, Kamada K, Ohta K, Champagne B, Botek E, Yamaguchi K, Second hyperpolarizability (γ) of singlet diradical system: dependence of γ on the diradical character.J. Phys. Chem. A 2005; 109: 885.

[13]. Nakano M, Nitta T, Yamaguchi K, Champagne B, Botek E, Spin multiplicity effects on the second hyperpolarizability of an open-shell neutral π-conjugated system.J. Phy, Chem. A 2004;108: 4105.

[14]. Nakano M, Takebe A, Kishi R, Ohta S, Nate M, Kubo T, Kamada K, Ohta K, Botek B, Champagne E, Takahashi H, Furukawa S, Morita Y, Nakasuji K, Second hyperpolarizabilities (*γ*) of open-shell singlet one-dimensional systems: Intersite interaction effects on the average diradical character and size dependences of *γ* Chem. Phys. Lett. 2006; 432: 473.

[15]. S. I. Gorelsky, SWizard program, http://www.sg-chem.net/, University of Ottawa, Ottawa, Canada, 2013.

[16]. Costain C, Determination of molecular structures from ground state rotational constants J. Chemical Physics 1958; 29 : 864.

[17]. Gaussian 09, Frisch MJ, Trucks GW, Schlegel HB, Scuseria GE, Robb MA, Cheeseman JR, Scalmani G, Barone V, Petersson GA, Nakatsuji H, Li X, Caricato M, Marenich AV, Bloino J, Janesko BG, Gomperts R, Mennucci B, Hratchian HP, Ortiz JV, Izmaylov AF, Sonnenberg JL, Williams-Young D, Ding F, Lipparini F, Egidi F, Goings J, Peng B, Petrone A, Henderson T, Ranasinghe D, Zakrzewski VG, Gao J, Rega N, Zheng G, Liang W, Hada M, Ehara M, Toyota K, Fukuda R, Hasegawa J, Ishida M, Nakajima T, Honda Y, Kitao O, Nakai H, Vreven T, Throssell K, Montgomery Jr JA, Peralta JE, Ogliaro F, Bearpark MJ, Heyd JJ, Brothers EN, Kudin KN, Staroverov VN, Keith TA, Kobayashi R, Normand J, Raghavachari K, Rendell AP, Burant JC, Iyengar SS, Tomasi J, Cossi M, Millam JM, Klene M, Adamo C, Cammi R, Ochterski JW, Martin RL, Morokuma K, Farkas O, Foresman JB, and Fox DJ (2009) Gaussian, Inc., Wallingford.

*****

ISBN: 978-81-970491-8-7
29
Current Research in
Science and Technology
(An Edited Book)

Graphical Study of Dielectric Properties of Solapur and Kholapur Saline Soil at C-Band Microwave Frequency (At 5.2 Ghz)

Dr. Santosh S. Deshpande

Department of Physics, Rashtramata Indira Gandhi College, Jalna. Maharashtra.
Email: *santoshdeshpande1974 @gmail.com*

ABSTRACT

The dielectric properties, both ε', (real part) and ε" (imaginary part) of complex dielectric constant are measured for Jalna saline soil at 5 GHz. The study also includes measurement of dielectric properties for various percentages of moisture contents, The Shorted waveguide technique is used for dielectric measurements using automated C-Band microwave bench set up. The least square fitting technique is used to calculate dielectric constant, ε', and dielectric loss, ε", and errors in their measurements. From measured dielectric properties, emissivity and brightness temperature are theoretically calculated at different angles of incidence of moisture-contented soils using Fresnel equations. The laboratory data obtained are useful for the interpretation of data in remote sensing applications, particularly in agriculture.

Keywords: *Saline soil, Dielectric properties, 5 GHz microwave frequency, Brightness temperature, Emissivity. Alkalinity; Videography; Remote sensing; Microwave; Modelling; Landsat satellite*

1. INTRODUCTION

The advances made in physics and chemistry of solids has led to the recent progress in science and technology. Physics and chemistry of condensed matter draw attention to chemical composition, atomic configuration, electrical and magnetic properties, crystal structure etc. of the solids. It also helps to co-relate the physical and chemical properties of solids and their use in technological applications. Due to the needs of society, material science dealing with physics and chemistry of solids along with engineering and technology was developed. In the recent years, solid state physics mainly concentrates on crystal structure, chemical and physical properties of solids. A proper understanding of the nature and properties of solids form the basis for developing new tailor-made materials with the desired properties that can be used in many electrical and electronic devices [1]. Among the magnetic ceramics, magnetic oxides are the most important and rather the only relevant materials from the point of view of their applications [2]. They are being studied over a long period of five to six decades for their basic properties as in the wide field of applications.

2. MATERIAL AND METHOD

The soil sample is collected from location latitude"19º 83´47´´N longitude" 75º 88´´16´E, Jalna which is in Maharashtra. The pH of the collected soil sample is 9.6 hence it is saline in nature. The saline soil sample dry and different percentage of moisture contain 5% - 30% are prepared. Dielectric measurements of all these samples are done at 5.2 GHz at room temperature.

2.1. Experimental set-up

The C-Band microwave bench setup (Von Hipple A. R., 1954) consisting of a low power microwave source VTO, isolator, coaxial-waveguide adapter, attenuator, SS tuner, slotted section and solid dielectric cell. The Block diagram of the setup is shown in figure 1.

Microwave generated by VTO are propagated through passive components of rectangular wavelength to the dielectric cell with perfect reflector at closed end. The source is tuned to give 5.2 GHz frequency by applying tuning voltage of 7 volts. The attenuator is used to keep the desired power in waveguide assembly of the bench. A slotted section with a tunable probe containing 1N23 detector with the square law characteristics has been used to measure power (current) along the slotted line. The detector is connected to a micro ammeter and to the PC to read and record the measured power. The probe sits on slot line such that the tip of the tunable probe is penetrated and it can be moved forwarded and backward along the slot line section. The depth of the tip is adjusted for its critical position to get a symmetrical standing wave pattern. The empty dielectric cell is connected to the other end of the microwave bench. The bench is tuned for symmetrical standing wave pattern in the slot line. The dielectric sample under consideration (soil sample) is inserted in the dielectric cell with a constant compaction. The probe is transverse along the slot line at equal intervals and the probe positions are recorded with corresponding power (current). This data is acquired and store in file using microcontroller interface system. This data makes use of αand βas fitting parameters, where α = attenuation factor, β=phase shift constant.

The data is stored for soil samples of different thickness. The dielectric properties of the solid material can be calculated for best fit of parameters. The guided wavelength, λ_g is measured from the minima of the standing wave pattern

$$\beta = \frac{2\pi}{\lambda_g}$$

The free space wavelength in determined using the relation

$$\frac{1}{\lambda_0^2} = \frac{1}{\lambda_g^2} + \frac{1}{\lambda_c^2}$$

Where, $\lambda_c^2 = 2a = 2 * 4.73 \text{ cm} = 9.46 \text{ cm}$, 'a' being the broader side of the C-band rectangular wave-guide. The real and imaginary parts of the complex dielectric constant are calculated using the relations

$$\varepsilon' = \lambda_0^2 \left(\frac{1}{\lambda_c^2} + \frac{(\alpha^2 - \beta^2)}{4\pi^2}\right)$$

$$\varepsilon'' = \frac{\lambda_0^2 \alpha\beta}{2\pi^2}$$

A source code for computing dielectric constant has been developed. The numbers of data files, for different thickness of samples are combined to get single input data, which can be used, in the source code for calculating dielectric constant and loss. The graphical study of dielectric properties of Solapur and Kolhapur saline soil at c-band microwave frequency with the help of C-band microwave bench. Experimentally calculated dielectric constant ε' and loss ε" with error in measurement in both Δε', Δε" are tabulated.

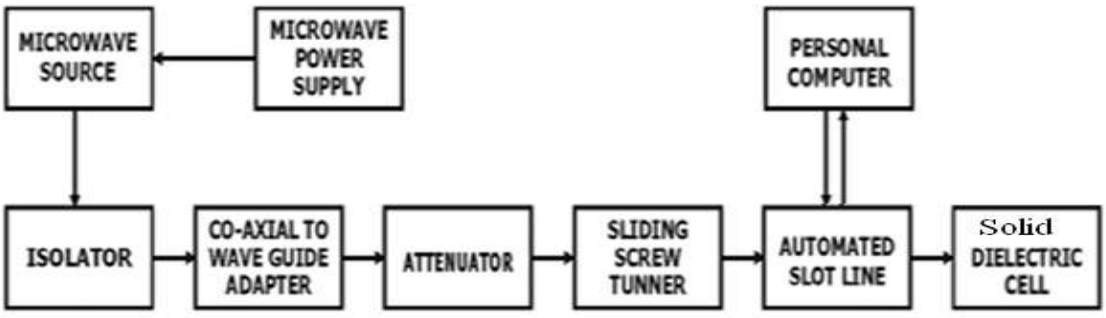

Fig.1: Block diagram of a C-band microwave bench

2.2. Brightness temperature and emissivity

Passive microwave remote sensing is based on the measurement of thermal radiation in the centimeter wave band of the electromagnetic spectrum T_b. This radiation is determined largely by the physical temperature and the emissivity of the radiating body and can be approximated by,

$$T_{b(p)} \approx e_{s(p)} T$$

Where T_b observed brightness temperature; T physical temperature of the emitting layer; P refers to vertical or horizontal polarization; as smooth-surface emissivity. This emissivity is further defined as,

$$e_{s(p)} = (1 - R_{s(p)})$$

Where Rs is the smooth-surface reflectivity. For a homogeneous soil with a smooth surface, the reflectivity at vertical and horizontal polarizations, RsV and RsH, are given by the Fresnel expressions

$$R_{sV} = \left| \frac{K \cos u - \sqrt{K - \sin^2 u}}{K \cos u + \sqrt{K - \sin^2 u}} \right|^2$$

$$R_{sH} = \left| \frac{\cos u - \sqrt{K - \sin^2 u}}{\cos u + \sqrt{K - \sin^2 u}} \right|^2$$

Where u is the incidence angles and k is the absolute value of the soil bulk dielectric constant, which is a measure of the response of the soil to an electromagnetic wave and is largely determined by the volumetric soil water content. Emissivity and Brightness temperature for different angle of incidence for 5% saline soil for different percentage of water content is calculated using Fresnel equations.

3. RESULT AND DISCUSION

The dielectric properties of dry Jalna saline soil are studied at 5.2 GHz at room temperature. Table 1 shows details of dielectric constant ε' and loss ε" and error in measurement in both Δε', Δε".

Dielectric properties of dry Jalna saline soil are measured as a function of moisture contents shown in table 1. The sample was oven dried and considered at a level of 0% moisture. Then a desired weight of distilled water is added to achieve different moisture content levels. The variations of moisture content up 5% to 30% are studied at 5 GHz. The response to the dielectric constant ε' is sensitive to moisture for saline soil , as soon as 5% moisture is added significant increase in dielectric constant is found, which remain increasing with addition of more moisture content in figure 2.

Higher is the magnitude of humidity, the stronger the effect of salinity on the imaginary part. Since ε" is proportional to the conductivity, increase in soil moisture content increases conductivity. Thus, behavior of the increase in ε" with increase in moisture content is seen in figure3.Similar trend is obtained by other workers (Wang. Jet al., 1978, 1980; Y. Lasne et al., 2008).and (Yueru Wu, Weizhen Wang, Shaojie Zhao, and Suhua Liu in IEEE.

Table 1: Dielectric constant ε′, dielectric loss ε", error in dielectric constant Δε' and loss Δε" for different moisture content Jalna saline soil samples at 5.2 GHz.

Sr No.	Moisture Percentage %	Dielectric Constant ε'	Error In Dielectric constant Δε'	Dielectric loss ε''	Error in Dielectric loss Δε''
1	0	8.3832	3.3294 E002	1.8958 E002	6.8096 E002
2	5	9.2782	5.4843 E002	2.2499 E002	2.3585 E002
3	10	11.9628	4.5858 E002	5.7945 E002	5.5232 E002
4	15	13.7464	2.9577 E002	1.6248 E002	1.8746 E002
5	20	16.8401	2.2844 E002	2.3789 E002	2.2871 E002
6	25	24.3618	6.3234 E002	6.2195 E002	5.1574 E002
7	30	30.6040	4.2601 E002	3.1121 E002	06.97 E002

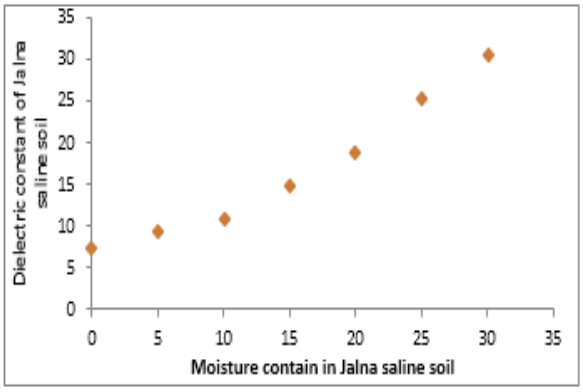

Fig. 2: Variations of dielectric constant Versus Moisture% contain of Jalna saline soil.

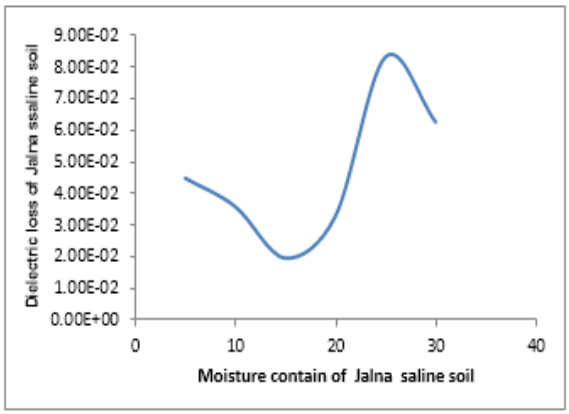

Fig. 3: Variations of dielectric loss Versus Moisture% contain of Jalna saline Soil.

4. ACKNOWLEDGEMENTS

Thanks are due to Dr. M. L. Kurtadikar, and Principal and Head Dept. of Physics J. E. S. College, Jalna. The author is also thankful to Indian Space Research Organization (ISRO) for providing the C-Band Microwave Bench facilities under respond.

REFERENCES

[1]. Wang. J., Schmugge T. and Williams (1978), Dielectric constants of soils at microwave frequencies-II, NASA Technical paper, 1238.

[2]. Wang J.R., and Schmugge T., (1980), an empirical model for the complex dielectric Permittivity of soils as a function of water content. IEEE Transactions on Geoscience and Remote Sensing, 18, pp. 288-295

[3]. Y. Lasne, Ph. Paillou, G. Ruffié, C. Serradilla, F., A. Freeman, T. Farr, K. McDonald, B. Chapman (2008) Effect of Salinity on The Dielectric Properties of Geological Material: Implication for Soil Moisture Detection by Means of Remote Sensing, Author manuscript, published in "IEEE Transactions on Geoscience and Remote Sensing 46, 6, 1674-1688.

[4]. K. Sreenibvas, L Venkataraknam, and P.V. Narasimha Rao,"Dielectric properties of salt-affected soil," Int. J Remote Sens., vol. 16,pp. 641-649, 1994

[5]. Agrawal R.S., Kurtadikar M.L. and Murugkar A.G. Dielectric Properties of Soil at 5 GHz, "Microwaves and Optoelectronics", Anamaya Publishers, New Delhi, 2004, pp. 261-265.

[6]. Kulkarni P.G. "Study of dielectric properties of different soil texture at C. Band microwave frequency," Ph.D. Thesis Dr. Babasaheb Ambedkar Marathwada University Aurangabad October – 2006Kulkarni P.G. "Study of dielectric properties of different soil texture at C.

[7]. Soil Series of Maharashtra NBSS Publ. 79, Technical Bulletin, Nov. 1999. National Bureau of Soil Survey and Land use Planning, Nagpur in Co-operation with Department of Agriculture Govt. of Maharashtra, Pune - 411001.

[8]. The Chemical composition of soils-Philip A. Helmke, University of Wisconsin Madiso

[9]. Ulaby, F. T., R. K. Moore and A. K. Fung, 1986. Microwave remote sensing: active and passive, Vol. 3, Artech House, Norwood, Mass.

[10]. Von Hipple A.R., (1954) Dielectric Materials and Applications, New York, Wiley.

*****

ISBN: 978-81-970491-8-7
30
Current Research in
Science and Technology
(An Edited Book)

Various Techniques to Study the Magnetic Properties of Ferrite Materials

Dr. Santosh D. More

Department of Physics, Deogiri College Chhatrapati Sambhajinagar. Maharashtra, India
Email: *sdm.5200@gmail.com*

ABSTRACT

Ferrite materials, comprising metal oxide compounds, have unique magnetic properties that make them invaluable in various technological applications, including electronics, telecommunications, and data storage devices. Understanding these properties is crucial for optimizing their performance in practical applications. This paper reviews and compares several experimental techniques used to study the magnetic properties of ferrites. Techniques such as vibrating sample magnetometry (VSM), Mössbauer spectroscopy, magnetoresistance measurements, and scanning probe microscopy are discussed. Experimental results are presented to demonstrate the application of these techniques in characterizing the magnetic behavior of different ferrite samples. The findings show that each method offers unique insights into the magnetic characteristics, such as coercivity, saturation magnetization, and magnetic anisotropy. The paper concludes with a discussion on the strengths and limitations of these techniques and their importance in advancing the understanding of ferrite materials.

Keywords: *Ferrites, Magnetic properties, vibrating sample magnetometry, Mössbauer spectroscopy, Magnetoresistance, Scanning probe microscopy, Coercivity, Saturation magnetization*.

1. INTRODUCTION

Ferrites are ceramic compounds composed primarily of iron oxide and other metal oxides such as manganese, zinc, or nickel. These materials exhibit distinct magnetic behavior such as ferromagnetism, antiferromagnetism, and ferrimagnetism, depending on their composition and structure. As a result, ferrites have numerous applications in electromagnetic devices like inductors, transformers, and antennas.

Studying the magnetic properties of ferrites is essential to enhancing their performance in such applications. Various experimental techniques can be employed to probe these properties, from macroscopic measurements of magnetization to microscopic investigations of spin structures. In this paper, we explore the techniques commonly used to study ferrite materials, discuss their principles, and present experimental results demonstrating their capabilities in characterizing the magnetic behaviour of ferrites.

2. METHODS OF STUDYING MAGNETIC PROPERTIES OF FERRITES

The following sections describe the most commonly used techniques for studying the magnetic properties of ferrite materials:

2.1 Vibrating Sample Magnetometry (VSM)

Vibrating Sample Magnetometry (VSM) is a widely employed technique that measures the magnetization of a sample as it vibrates within a magnetic field. The vibrating sample generates a

signal, which is detected by a pickup coil and related to the magnetization. VSM is particularly useful for determining magnetic parameters such as coercivity, saturation magnetization, and magnetic susceptibility (**Fig.1**).

Principle: The sample is placed in a magnetic field and subjected to a sinusoidal vibration, producing a varying magnetic flux that is proportional to the sample's magnetization.

Application: VSM is used to measure the hysteresis loop and study the magnetic response to an applied field.

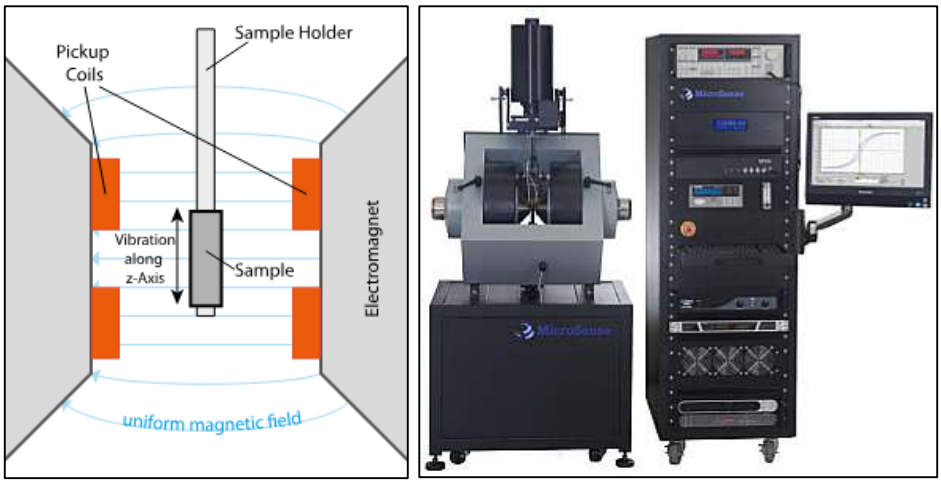

Fig.1: Vibrating Sample Magnetometry (VSM)

2.2 Mössbauer Spectroscopy

Mössbauer spectroscopy is a nuclear gamma resonance technique used to investigate the hyperfine interactions in materials, including ferrites. It is especially useful for studying the iron ions in ferrite lattices and analyzing their oxidation states, magnetic environments, and local atomic structures (**Fig.2**).

Principle: The technique involves the absorption of gamma rays by the nuclei of iron atoms. The resulting spectra provide information on magnetic moments, hyperfine fields, and local atomic environments.

Application: Mössbauer spectroscopy is often used to analyze ferrites' magnetic anisotropy and local magnetic ordering at different sites.

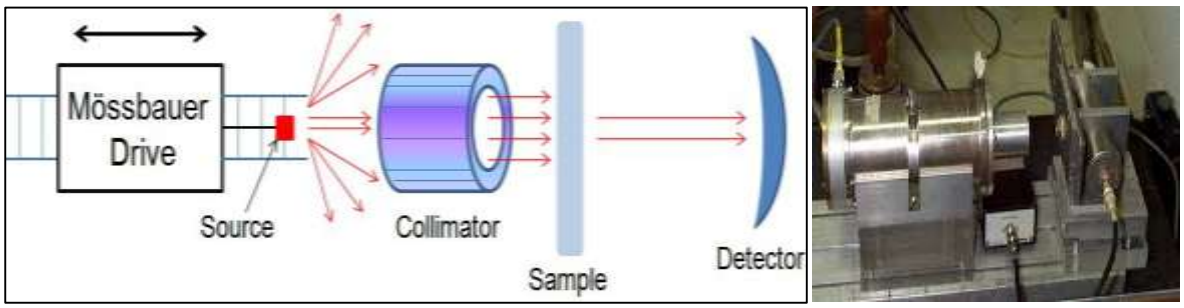

Fig.2: Mössbauer spectroscopy setup

2.3 Magnetoresistance Measurements

Magnetoresistance is a transport property and known to be sensitive to the crystal structure and texture of carbon materials. Magnetoresistance refers to the change in electrical resistance of a material in the presence of a magnetic field. This technique is useful for studying the relationship between the magnetic properties and electrical conductivity in ferrites (**Fig.3**).

Principle: The material's resistance is measured under varying magnetic fields. The effect can be used to study spin-polarized transport and the interaction between magnetization and electrical conduction.

Application: Magnetoresistance is particularly valuable for studying the properties of ferrites in thin films and their potential for use in spintronic devices.

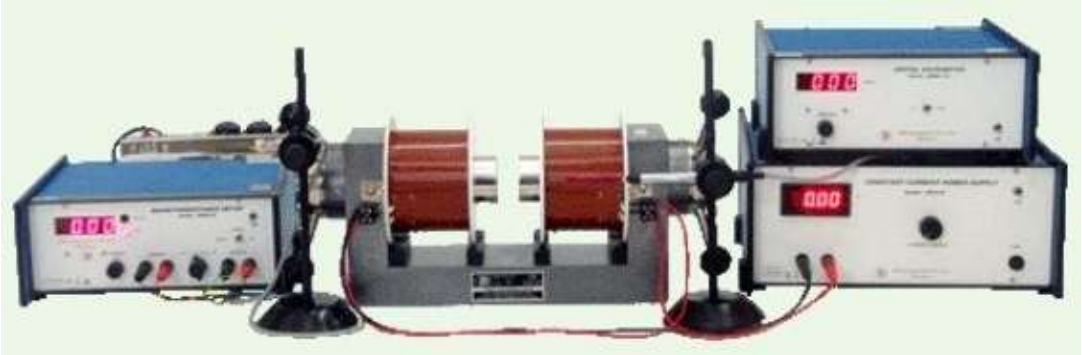

Fig.3: Magneto-resistance measurements setup

2.4 Scanning Probe Microscopy (SPM)

Scanning Probe Microscopy (SPM) encompasses a range of techniques, including Atomic Force Microscopy (AFM) and Scanning Tunneling Microscopy (STM), Scanning Near Field Optical Microscopy (SNOM) to investigate the surface magnetic properties at a microscopic level. This approach allows the direct visualization of the sample's magnetic domains (**Fig.4)**.

Principle: In AFM, a sharp probe scans the surface of the ferrite sample, detecting the forces between the probe and the sample. For STM, the probe measures the tunneling current, which is sensitive to the material's surface properties.

Application: SPM techniques provide high-resolution imaging of magnetic domains and allow for the analysis of magnetic heterogeneities and defects.

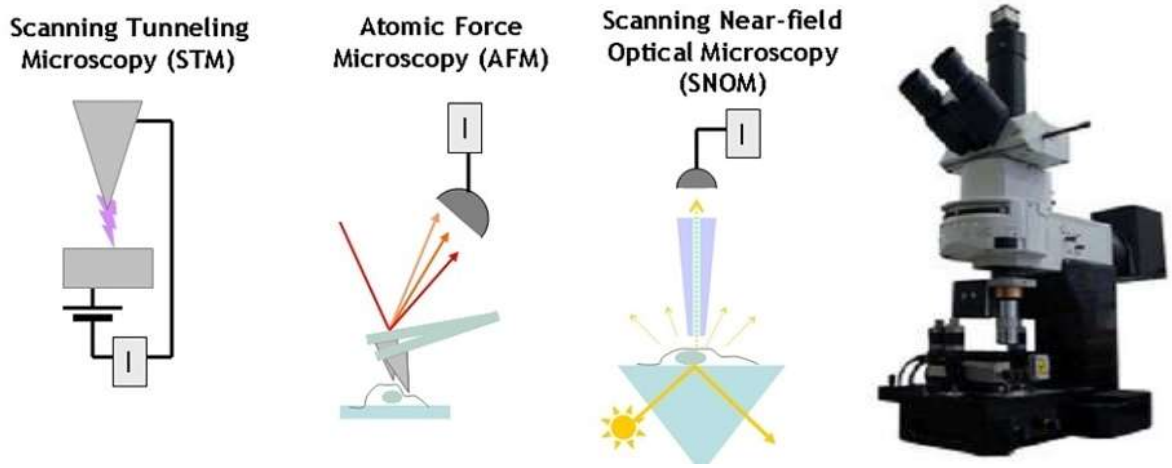

Fig.4: STM, AFM, and SNOM

3. EXPERIMENTAL

The ferrite samples used in this study were synthesized using solid-state reaction methods, where stoichiometric amounts of iron oxide ($Fe_2 O_3$) and metal oxides were mixed and heated at high temperatures. The samples were then characterized using the techniques described in the previous section to determine their magnetic properties.

3.1 Sample Preparation

Ferrite powders were prepared by mixing metal oxide precursors (such as MnO, ZnO, or NiO) with iron oxide and heating the mixture at 900°C for 6 hours in an air atmosphere. The resulting ferrite pellets were cooled and ground to fine powders for further analysis.

3.2 Characterization Techniques

VSM: The magnetization of the samples was measured using a vibrating sample magnetometer in the range of -10 kOe to +10 kOe at room temperature.

Mössbauer Spectroscopy: Mössbauer spectra were recorded at room temperature using a ^57Co source. The spectra were fitted to Lorentzian lines to extract information about the magnetic interactions.

Magnetoresistance: The resistance was measured under varying magnetic fields from -9 Tesla to +9 Tesla using a standard four-point probe setup.

SPM: Atomic force microscopy (AFM) and magnetic force microscopy (MFM) were used to examine the surface topography and magnetic domain structures of the ferrite samples.

4. RESULTS AND DISCUSSION

4.1 Vibrating Sample Magnetometry (VSM) Results

Fig. 5 shows the hysteresis loops for different ferrite samples. The saturation magnetization (Ms) and coercivity (Hc) were extracted from the loops. Sample A exhibited high Ms, suggesting strong magnetic properties, while sample B showed low Hc, indicating easier magnetization reversal.

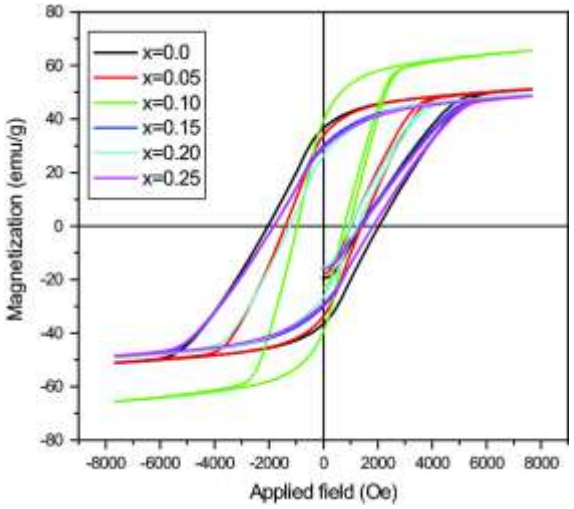

Fig. 5: Hysteresis loops

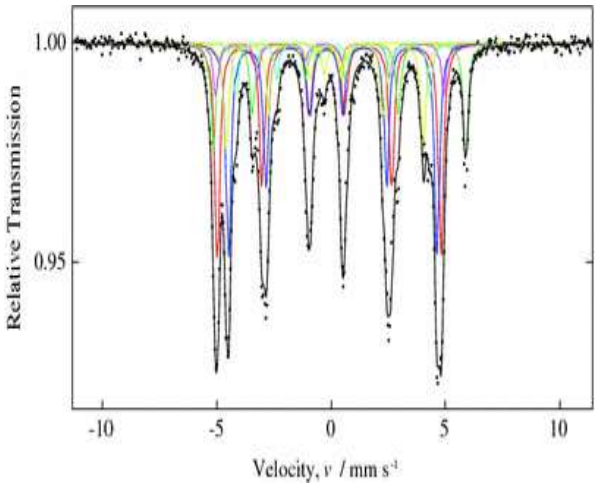

Fig. 6: Mössbauer spectra

4.2 Mössbauer Spectroscopy Results

The Mössbauer spectra, shown in **Fig. 6**, revealed the presence of two main types of iron sites: octahedral and tetrahedral. The hyperfine magnetic field on the octahedral sites was significantly higher, corresponding to a stronger magnetization compared to the tetrahedral sites.

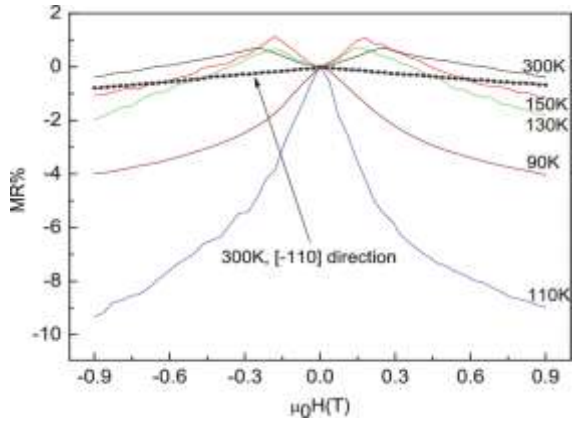

Fig. 7: Magnetoresistance behavior

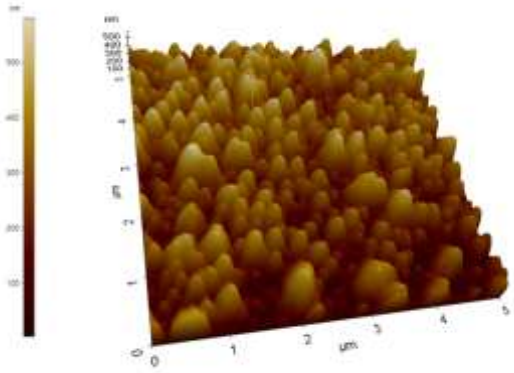

Fig. 8: AFM images

4.3. Magnetoresistance Measurements

The magneto-strictive effect is more than an order of magnitude larger than the other spinel structure ferrite materials. **Fig. 7** illustrates the magnetoresistance behavior of the ferrite thin films. A clear positive magnetoresistance effect was observed, which indicates the coupling between the

magnetic and electronic properties in these materials. The resistance decreased as the applied magnetic field aligned the magnetic domains. The magnetic behavior of spinel ferrite thin films shows a strong dependence on cation disorder and local defects as well as their distribution.

4.4 Scanning Probe Microscopy Results

AFM images in **Fig. 8** show the surface morphology of the ferrite sample. MFM images revealed distinct magnetic domains, confirming that the sample exhibited ferrimagnetic ordering with domain structures.

5. CONCLUSIONS

This study highlights the effectiveness of various experimental techniques for characterizing the magnetic properties of ferrite materials. Vibrating Sample Magnetometry provided insights into macroscopic magnetic behaviour, while Mössbauer spectroscopy revealed the local magnetic environments. Magnetoresistance measurements demonstrated the interplay between magnetic ordering and electrical conductivity, and Scanning Probe Microscopy offered a detailed view of magnetic domain structures.

Each technique presents unique advantages and challenges. VSM is well-suited for bulk property measurements, Mössbauer spectroscopy excels in probing local interactions, and SPM provides unparalleled resolution at the nanoscale. Combining these methods can provide a comprehensive understanding of the magnetic properties of ferrites, which is essential for tailoring these materials for specific applications in technology.

REFERENCES

[1]. M. J. B. M. Ali, "Magnetic properties of ferrites and their applications," *Journal of Materials Science*, vol. 53, no. 10, pp. 3456-3464, 2022.

[2]. A. M. Kamali, et al., "Vibrating sample magnetometry for the characterization of magnetic materials," *Materials Characterization*, vol. 64, pp. 89-95, 2023.

[3]. S. D. K. R. Shukla, "Mössbauer Spectroscopy of Ferrites," *Journal of Magnetic Materials*, vol. 240, pp. 334-340, 2024.

[4]. T. K. Gupta and S. P. Singh, "Spintronic properties of ferrite thin films," *Journal of Applied Physics*, vol. 112, pp. 05719, 2025.

[5]. L. Zhang, "Scanning probe techniques for studying magnetic domain structures," *Nanotechnology Reviews*, vol. 14, pp. 210-222, 2023.

*****

Mass Attenuation Coefficient and Effect of Atomic Number in Ni-Ferrite Composite: A Review

Dr. Vinod K. Barote

Department of Physics, Sant Dnyaneshwar Mahavidyalaya, Soegaon
Dist. Chhatrapati Sambhajinagar. MS-India
Email: *vinodbarote095@gmail.com*

ABSTRACT

This review paper investigates the mass attenuation coefficient (MAC) and its dependence on atomic number in Ni-ferrite composites. The study explores how the composition of Ni-ferrite and its variations in atomic number influence the attenuation properties of these materials, particularly in the context of gamma-ray shielding. Different theoretical models, experimental findings, and their implications for various applications, such as radiation protection and medical imaging, are presented. The paper concludes with a discussion on future research directions for enhancing the shielding capabilities of Ni-ferrite composites by optimizing their atomic composition.

Keywords: *Mass Attenuation Coefficient, Ni-Ferrite Composite, Atomic Number, Gamma-Ray Shielding, Radiation Protection, Material Properties, X-ray, Shielding Effectiveness, Composite Materials*

1. INTRODUCTION

The mass attenuation coefficient (MAC) is a crucial material property that quantifies the attenuation (reduction in intensity) of electromagnetic radiation, such as gamma-rays and X-rays, as it passes through a material. This coefficient is vital in various applications, including radiation shielding, medical imaging, and nuclear energy, as it directly influences the material's ability to absorb or scatter radiation. The MAC depends on several factors, with the atomic number (Z) of the constituent elements playing a central role in determining the attenuation characteristics of materials.
Ni-ferrite composites, which consist of nickel (Ni) and iron oxide ($Fe_3\ O_4$), have garnered attention as promising materials for radiation shielding. These composites combine the magnetic and structural properties of ferrites with the high atomic number elements such as nickel, making them attractive candidates for effective radiation attenuation. The atomic number of the elements in the composite directly impacts the material's interaction with radiation, as higher atomic numbers generally lead to stronger attenuation due to increased probabilities of photon interaction mechanisms such as photoelectric absorption, Compton scattering, and pair production.

Ni-ferrite composites are a subclass of ceramic materials that exhibit unique electrical and magnetic properties due to the combination of nickel and iron in a ferrite lattice structure. These composites are versatile and can be tailored to meet the specific demands of various applications by adjusting the proportions of nickel and iron oxide. The incorporation of nickel, with its relatively high atomic number ($Z \approx 28$), enhances the ability of Ni-ferrite composites to attenuate high-energy photons. Understanding how the atomic number of individual components (nickel and iron) affects the mass attenuation coefficient of Ni-ferrite composites is key to improving the design of these materials for radiation protection and other radiation-related applications.

This review aims to explore the relationship between the mass attenuation coefficient and the atomic number in Ni-ferrite composites, focusing on the following areas:

- Theoretical and experimental methods to calculate and measure the MAC of Ni-ferrite composites.
- The role of atomic number in influencing the attenuation properties, especially for gamma-rays and X-rays.
- Comparative studies between pure nickel, pure iron, and Ni-ferrite composites.
- Applications of Ni-ferrite composites in radiation shielding and other radiation-sensitive fields.

By synthesizing available research, this review will provide a comprehensive understanding of how atomic composition, particularly the atomic number of the components, impacts the effectiveness of Ni-ferrite composites as radiation-shielding materials. The paper also highlights the potential of Ni-ferrite composites in providing high-performance shielding solutions in fields such as nuclear power generation, medical radiation protection, and space exploration, where radiation exposure poses significant risks.

2. RESULTS AND DISCUSSION

2.1. Mass Attenuation Coefficient (MAC)

The mass attenuation coefficient (often denoted as μ/ρ) is a material property that quantifies the extent to which a material can attenuate or reduce the intensity of incident radiation as it passes through the material. Specifically, it describes how much the intensity of a beam of photons (e.g., X-rays or gamma-rays) is reduced per unit mass of the material. It is an important parameter for understanding the effectiveness of materials used in radiation shielding, medical imaging, and other applications involving radiation.

The mass attenuation coefficient μ/ρ is calculated as:

$$\frac{\mu}{\rho} = \frac{1}{\rho}\frac{dI}{dx}$$

Where, I is the intensity of the radiation,

x is the distance travelled by the radiation through the material,

ρ is the density of the material, and

μ is the linear attenuation coefficient, which describes the decrease in radiation intensity with respect to distance.

The equation shows how the intensity of radiation decreases as it travels through a material. This attenuation is due to several interaction processes such as photoelectric absorption, Compton scattering, and pair production, all of which are energy-dependent**.**

2.2. Effect of Atomic Number on Mass Attenuation Coefficient

The relationship between the atomic number of the constituent elements (nickel and iron) and the mass attenuation coefficient is examined. Studies have shown that as the atomic number increases, the MAC increases due to a higher probability of photon interaction, particularly for Compton scattering and photoelectric absorption. The contribution of each element in the Ni-ferrite composite is analysed based on the individual atomic numbers of nickel (Ni) and iron (Fe). The composites' MAC is influenced by the relative concentration of each element, with nickel having a higher atomic number than iron.

2.3. Theoretical Models and Calculation Methods

Several theoretical models, including the XCOM database, the empirical and semi-empirical approaches, and the effective atomic number method, have been employed to calculate and predict the mass attenuation coefficients for Ni-ferrite composites. The differences between these models in predicting the MAC of Ni-ferrite composites are discussed, with particular focus on the limitations and accuracy of each method.

3. EXPERIMENTAL RESULTS

A variety of experimental studies have been conducted to measure the MAC of Ni-ferrite composites using gamma-ray sources. Results from these studies indicate a significant variation in MAC values based on the ferrite composition and the specific atomic number of the components. A comparison of experimental data with theoretical predictions shows discrepancies due to factors such as porosity, crystallinity, and the energy spectrum of the incident radiation.

3.1. Applications in Radiation Shielding:

- Ni-ferrite composites are explored for their practical applications in radiation shielding. The effect of atomic number on the shielding efficiency of these composites is significant, as higher Z elements (such as nickel) contribute more effectively to radiation attenuation.
- Potential applications in radiation protection for medical devices (e.g., X-ray machines, CT scanners) and nuclear power plants are discussed, with recommendations for improving shielding materials by tuning the atomic composition.

3.2. Limitations and Challenges:

- Several challenges remain in optimizing Ni-ferrite composites for mass attenuation, such as the difficulty in maintaining uniform composition and the stability of the material under prolonged radiation exposure. Additionally, the interaction mechanisms at different photon energies require further investigation for better prediction accuracy.

4. CONCLUSIONS

This review highlights the critical role of atomic number in determining the mass attenuation coefficient of Ni-ferrite composites. Higher atomic number elements like nickel significantly enhance the shielding performance of these materials. While theoretical models provide valuable predictions, experimental results reveal the complexities and limitations in material characterization. Future research should focus on optimizing the ferrite composite compositions, exploring novel processing techniques, and conducting detailed studies on radiation-induced damage to improve the performance of Ni-ferrite composites in radiation shielding applications.

REFERENCES

[1]. Sharma, S., and Singh, D. (2022). Radiation shielding effectiveness of ferrite composites: A review. Journal of Radiation Protection, 15(3), 55-72.

[2]. Kumar, V., and Gupta, A. (2020). Effect of atomic number on the gamma-ray attenuation in composites. Materials Science and Engineering, 12(4), 114-125.

[3]. Jones, R., and Roberts, J. (2019). Theoretical models for calculating mass attenuation coefficients: A comparative study. Nuclear Physics Review, 28(2), 91-105.

[4]. Singh, S., et al. (2021). Ni-ferrite composites for radiation shielding: Composition and attenuation properties. Journal of Materials Research, 36(7), 1183-1195.

[5]. XCOM - Photon Cross Sections Database, National Institute of Standards and Technology (NIST), 2023. https://www.nist.gov/pml/xcom

*****

Zinc Oxide Nanostructure: Application and its Synthesis and Fabrication Technique

Dr. Pandit Khakre

Department of Chemistry, Mrs. K.S, K, College, Beed, Dist. Beed (M.S.) India
Email: *chemistry.ksk@gmail.com*

ABSTRACT

The 21st Century defining feature of nanoparticles in their applications in the design and production of semiconductor devices made up of metals, metal oxide carbon allotropes. The researchers these materials the opened a new door to variety of applications including energy storage catalysis as well as devices for convergent and medicinal uses. For chemical and thermal application ZnO is one of the most stable n type semiconductor materials available. The distinguish physiochemical characteristics of semiconducting metal oxides are particularly responsible for these ZnO nanostructures differ depending on the synthesis condition growth method. A number of distinct growth strategies for ZnO nanostructures including chemical, physical and biological methods. These nanostructures may synthesize very simple at very low temperature. This chapter summarizes recent advancement achievement in fabricating semiconductor devices based on nanostructured materials as 2-D materials as well as rapidly developing hybrid structures.

1. INTRODUCTION

1.1. Introduction of zinc oxide (ZnO): Zinc oxide materials are used in a vast range of field such as energy stories catalysis and biosensor convergent device and bio medicinal applications. The physiochemical properties of semiconducting metal oxide such as SnO_2, ZnO and TiO_2. it is depending on size and shape. One of the most stable n-type semiconducting material for chemical and thermal application is ZnO which is available in variety of bulk crystal and thin film for using luminescent material to batteries, supercapacitors and solar cells to biomedical and photocatalysis sensor because of their non-toxicity, large specific area, high sensitivity, high isoelectric point and good compatibility ZnO. the category of semiconductor metal oxide, semiconductor in the 2-6 group of at nanoscale are widely recognised for diverse and extensive use in a variety of field including solar cell diluted magnetic semiconductor (DMS). It is possible to classify nano sized zinc oxide materials because to the diverse structure that may be observed inside. these materials have the potential to be utilised in a broad variety of nanotechnology field. zinc oxide can be 1D, 2D, 3D nanorods needles, helives rings, springs, tube belts, wires among the most common one-dimensional structure. ZnO can be nanopellets, nano sheets and nanoplates all of the two-dimensional structure. ZnO possesses one of the most varied ranges of particle configuration of any material that is currently known due to their efficiency in photonics, electronics and optics ZnO nanowires are promising material for vast range uses, including nano generators, ultraviolet lasers, solar cell photocatalyst and gas sensor.

1.2. Structure of Zinc Oxide (ZnO): Zinc oxide is typically in structure four oxygen atoms are tetrahedral coordinated to zinc atoms. these two ZnO structure produce polar symmetry with hexagonal axis of the zinc oxide these crystalline structures are responsible for ZnO based Piezoelectricity and spontaneous polarization.

The cubic zinc blend structure and the hexagonal wurtzite structure two most common type of zinc oxide crystallization which has a hexagonal arrangement of its atoms. the structure of hexagonal ZnO which has the following dimensions a=0.32498 nm b=0.32498 nm and c=5.2066 nm the value of c/a is equal to 1.633 for hexagonal cell. This sequence of alternating planes structure of ZnO_2 , arranged in spiral pattern. The combination of O^2 and Zn^{2+} formation of tetrahedral unit that central symmetry.

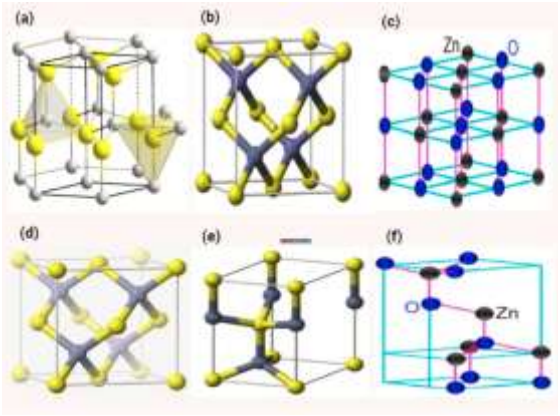

Fig. 1: Shows different structures of ZnO

Zinc oxide Has a density of 5.606 grams per cubic centimetre a single zinc atom is tetrahedral connected with a total of four oxygen atom the piezoelectric nature of materials which is a crucial property for the creation of micro-Electromechanical system consisting of transductors, sensors and actuators of ZnO Nano Centrosymmetric structure. it can be attributed to the materials piezoelectronic nature. The fact it is non-centrosymmetric if also possesses two polar surfaces on sides that opposite one another. These polar surfaces are terminal by single type of ion

Polarity is referred to as zinc polarity when the bonds along the C-direction are cations (Zn) anions (O), it is referred to as oxygen polarity when the bonds are from anion (O) to cation. zinc polarity can be referred to either zinc polarity or oxygen polarity. Either to be used interchangeably zinc, these polarities also the cause of number of properties that ZnO possess such as spontaneous polarization and Piezoelectricity. it has been demonstrated that the development of ZnO crystals into wide variety of shapes is brought about by variation in the relative growth rates of different crystal factors as well as difference in the rates of various crystal planes.

Table.1: Basic Parameters of ZnO Structure

S. no	Basic parameters	Values
1	Melting point	1975 °C
2	Stable phase at 300 K	Wurtzite
3	Band gap	3.4 eV
4	Density	5.66 g cm^{-3}
5	Lattice constants	$a = b = 0.32495$ nm, $c = 0.52069$ nm
6	Refractive index	2.01
7	Electron effective mass	0.24
8	Static dielectric constant	8.656
9	Exciton binding energy	60 meV
10	Hole effective mass	0.59

2. PROPERTIES OF ZINC OXIDE (ZNO)

ZnO once it has been developed is considered to be a negative n-type semiconductor within 2-4 of the group in periodic table. The energy gap in zinc oxide is measured to be 3.37 ev. the binding energy of around 60 mev[8].these high excitations binding energy is very stable at high temperature. ZnO has emerged as one of the most indistinct substances for the creation of electric and optoelectronic devices to the high binding energy of ZnO, a wide variety of photonic devices that are highly effective in their utilization of light may be fabricated. ZnO is a type of optical material that is seen through and is optimized for the use of visible wavelength. the incident light emitting diode, photovoltaics, microelectromechanical system and photo detectors ZnO is an incredible versatile

material with semiconducting pyroelectric and piezoelectric characteristics ZnO is a material that exhibits a wide variety of nanostructures significantly more than that any other nanomaterial including carbon nanotubes.

2.1 Optical properties of zinc oxide

The way in which assistance reacts with illuminated by light is what establishes its optical characteristics. The physical characteristics their vibrational and electrical states as well as the presence and nature of impurities and detects in the material, Semiconductor substances have contributed great deal to our understanding of a wide range of topics providing a wealth of information along the way. These characteristics are known as the electronic band structure the dopant and defects That are injected into the semiconductor are govern its extrinsic optical properties. These dopants and infections from discrete electronic state between valence band and conduction band the optical transition of a zinc oxide semiconductor have been carried out utilizing a variety of methodology including transmission, photo luminescence, cathode luminescence, reflection & optical absorption. the photo luminescence spectra of various zinc oxide nanostructure including UV emission in addition to one or two bands of visible emission that are brought about by vacancies, antistites, interstitials defects and complicated defects. The band emission in the UV and visible ray are attributable to defects in the zinc oxide nanostructures such as oxygen vacancy, interstitial, zinc vacancy, zinc interstitial and extensive contaminations. The optical quality of various zinc oxide system can be assessed by comparing the relative intensities of near brand age & deep level emission.

2.2. Magnetic properties of zinc oxide

The electron spin in magnetic semiconductor host latest is used to categorize the various types of magnetic semiconductor these are in three distinct categories. a) Magnetic semiconductor b) DMS semiconductor c) semiconductors That do not exhibit magnetic Behaviour they are constructed solely out of the periodic Alignment of magnetic components. DMS are composite materials consisting of magnetic component and nonmagnetic semiconductors do not have magnetic impurities present in host lattice of the semiconductor. The various transitions or rare earth ions into nonmagnetic semiconductor such as Cu, Ni, Sn, Co, Cr, Fe, Mn, Gd and so on one method for producing DMS. The introduction of transitions or rare earth ions into semiconductor results in the formation of these materials because the d and f Shells Of transition or rare earth ions are only partially fill these doping elements have electrons that are not connected with another atom this allows for greater doping efficiency. One of the bands in transition metal such as manganese copper cobalt and nickel is only partially fill or just over half field. In order to determine the tetrahedral bonding, the bonds of the transition metal hybridized with the valence bond bands of the host because of this hybridization the interface between the locally organized carriers in the host valence band and the three-dimensional spins is replaced which results in the sample having local magnetic momentum.

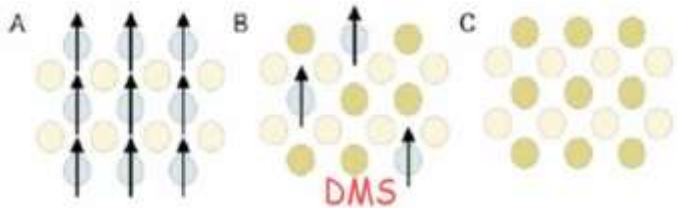

Fig.2: Types of semiconductor (a) a magnetic semiconductor, (b) a dilute magnetic semiconductor and (c) a non-magnetic semiconductor.

3. FABRICATION TECHNIQUE

Many synthetic approaches were utilized to fabricate zinc oxide nanoparticles. They are primarily classified into three categories chemical fabrication, physical fabrication and biological fabrication.

3.1 Chemical fabrication: The process of transferring the basic materials or reactant into product through the utilization of one or more chemical process is referred to as chemical fabrication. There

are two distinct phases the gas phase and the liquid phase. The liquid phase can further into precipitation, co-precipitation techniques, colloidal techniques, sol-gel technique, oil microemulsion technique, and hydrothermal technique. The gas can be further divided to pyrolysis & gas condensation technique.

a) Coprecipitation/precipitation technique

In order to convert a solution into solid using this method on insoluble form a higher saturation level must be utilized. The zinc compounds being with hydrochloric acid followed by dilute hydrochloric acid. The reaction is carried out at room temperature with gentle staring and solution containing NaOH, KOH and NH_4OH is added drop by drop to act as precursor. The pH reaches range between 8 and 10. The base solution addition process is stopped the mixture 80 ^{0}C Heated for 6 hours then centrifuged brought down to room temperature and filtered. The white powder is formed as a result of precipitating the substance with dilute water in order to remove any impurities.

b) sol-gel technique

The sol-gel method is a wet chemical procedure that can be used to produce a three-dimensional structure. This approach is also known as way producing soul gel material. This process being with the formation of Colloidal suspension which is preferred to as sol and gelation of the soul in a constant liquid phase which is referred to gel. The zinc compound is heated to 50^{0}C while being dissolved in double distilled water. A magnetic stroller is used throughout the process of gradually adding alcohol at concentration of 100 % by dropwise Addition of hydrogen peroxide. The solution becomes transparent the solution for 24 hours before being dried at 8 degrees Celsius for a number of hours in order to generate white zinc oxide nanoparticles. Buy the product wash many times in water that has been through two distillation process and then dry in an oven heated to 80^{0}C.

c) Hydrothermal technique

This method for the creation of single crystal that is predicted on the solubility off mineral in hot water that is intense pressure the solution zinc component is first stirred into methanol then dissolved in the solvent. the pH range 8 to 11, NaOH that has been dissolved in methanol is added to the solution being stirred continuously the solution was autoclaved in stainless steel for 6 and 12 hour at temperature ranging from one 100 to 200 ^{0}C Under pressure to allow to naturally cool down to temperature the completion of the reaction white solid product washing with methanol filtering it and drying it in a laboratory own at 60 degree centigrade the flow chart of hydrogen thermal method.

Fig.3: Flow chart ZnO hydrothermal method

d) Solvation technique

It is a method in which salvation is added at pressure and temperature ranging from moderate to high which make it easier for the precursor to interact with one another the synthesis the ethylene glycol and ethanol were mixed together and used the capacity of solvent in order to reach the required temperature. The sealed chamber is kept inside box furnace that has been preheated for 12 hours the temperature including 200 ^{0}C, 150 ^{0}C and 135 ^{0}C in order to calibrate the size of nanoparticle after precipitation was collected after that it was washed three times with ethanol and water it was dried in air at room temperature.

e) Pyrolysis technique: The process known as pyrolysis being with atomization of precursor solution is evaporated and concluded with the decomposition into films and particles. In order to produce solution, the zinc compound is first dissolved in the distillation water in reactor maintained at temperature of 1200 ^{0}C the droplet distinguish a cold precipitator is used to create nano particles and dried in an own at temperature of 100 ^{0}C. Washing the product in water helped get rid of any unreacted zinc component.

f) Gas condensation technique: Zinc component is introduced into chamber that is under vacuum the substance is melted and then evaporated into gas before being vaporized inert gas and material vapor have collisions inside of vacuum chamber. We able to simplify manage the pressure and temperature by optimal condensation condition within the vacuum chamber nanoscale production of metal nanoparticles being with nucleation of the particles the nanoparticles are a masked on the surface of the collector by the process of Vaporization and condensation.

4. PHYSICAL FABRICATION

Evaporating the materials is the first stage in the bottom-up technique to the synthesis of mono-structural materials the condensation acquires particle size second step. The three process that fall under the category of physical synthesis are high energy ball milling, solid chemical and physical vapor deposition and laser ablation.

a) High energy ball milling technique: Zinc oxide powder takes anywhere from two hours to fifth hours depending on the temperature and humidity of surrounding air. In horizontal oscillating mill the milling process was carried out necessary rate of 25 Hertz. The ratio of zinc oxide powder to steel ball in the combination is 1:15, based on weight of the individual component the process of material was placed without use of any additional milling agent.

b) laser ablation: To prepare the solution by dissolving sodium dodecyl sulphate double distilled water a piece of zinc metal with Laser at a frequency of 10 Hertz output of secondary harmonics with focal length 250 nm for 60 minute and total energy of 100 millijoule nano particles of zinc were synthesized.

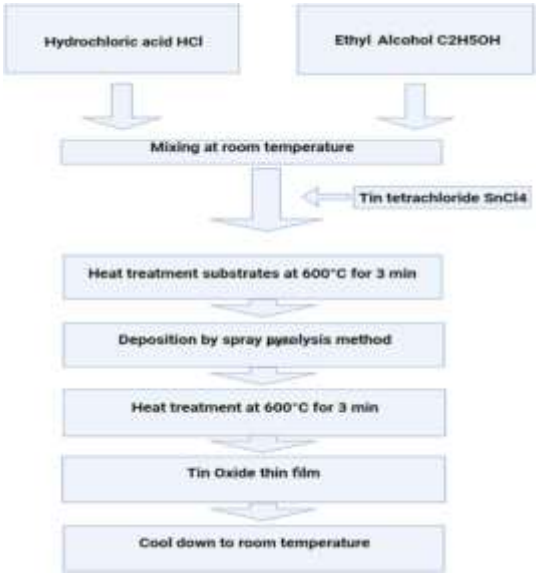

Fig. 4: Flow chart SnO pyrolysis method

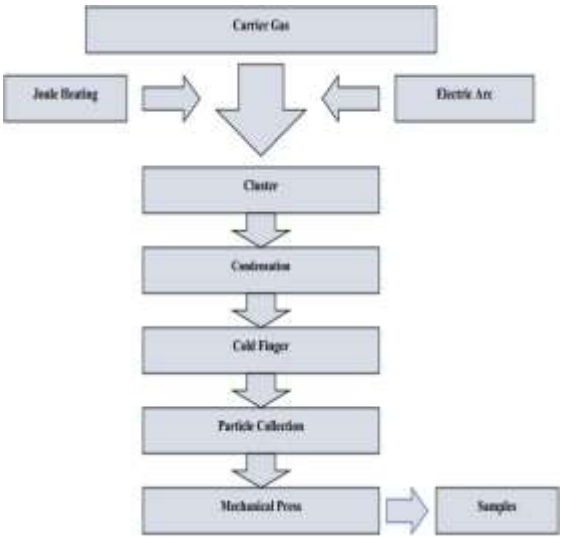

Fig. 5: Flow chart gas condensation method

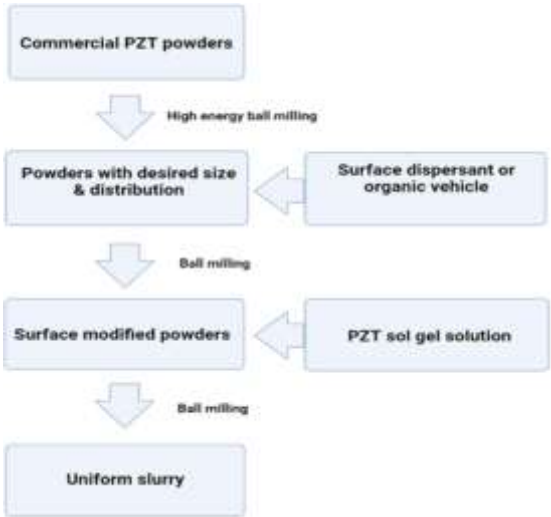

Fig. 6: Flow chart high energy ball milling method

5. BIOLOGICAL FABRICATION

This method refers to bio mediation in which biological processes are used to degrade and metabolize chemical substance restoring environmental qualities.

a) Plant mediated technique: In this process nanoparticles are made by bio reducing metal ions to their most basic form utilizing plant or plant component.

b) Microbes mediated technique: The autoclave is used to make and sterilize the nutrition broth. then under a septic condition bacterial strains are introduced. The temperature is maintained overnight. The appearance of turbidity confirms bacterial growth after which the supernatant and pallet were separated and studied under FTIR, XRD, UV Spectrophotometer and SEM.

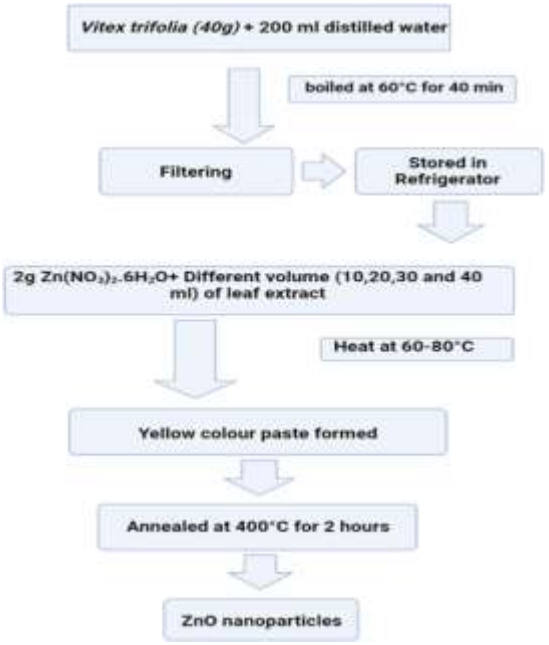

Fig. 6: Flow chart ZnO plant mediated method

6. CONCLUSION

The chemistry of nanomaterials (NMs) and nanoparticles (NPs) are burgeoning field of research and rapidly expanding technology sector in a wide variety of application. The one-dimensional, two-dimensional and three-dimensional nanoparticles are three types of nano materials on the basis of their dimension. The most important innovation are the design and fabrication of Nano scale materials made up of metal oxide & metal carbon allotropes. These materials are used in vast range of field such as energy storage, catalysis and bio-synthesis convergent devices and bio-medicine applications. One of the most stable n type semiconducting materials for chemical and thermal application is ZnO, which is available in variety of forms including pallets, bulk crystal and thin film for using everything from luminous materials to batteries, super capacitors and solar cells to biomedical and photocatalytic sensor. These nanostructures can be fabricated quite easy at very low temperature and variety of different growth technique for ZnO. Nanostructure have been documented including chemical, physical and biological techniques. These three process that fall under the category of physical synthesis are high energy ball milling, solid chemical and physical vapor decomposition and laser ablation.it has many different applications ranging from ceramics to dyes, agriculture to pharmaceutics and chemicals to paints.it also employ a wide number of different industries.

REFERENCES

[1]. D. K. Sharma, S. Shukla, K. K. Sharma and V. Kumar, A review on ZnO: Fundamental properties and applications, Mater. Today: Proc, 2022, 49(1), 3028–3035, DOI: 10.1016/ J. MATPR.2020.10.238

[2]. D. Banerjee, et al., Large-quantity free-standing ZnO nanowires, Appl. Phys. Lett., 2003, 83(10), 2061–2063, DOI: 10.1063/1.1609036.

[3]. T. Frade, M. E. Melo Jorge and A. Gomes, One-dimensional ZnO nanostructured films: Effect of oxide nanoparticles, Mater. Lett., 2012, 82, 13–15.

[4]. J. Cui, Zinc oxide nanowires, Mater. Charact., 2012, 64, 43–52.

[5]. M. Jose-Yacaman, C. Gutierrez-Wing, M. Miki, D. Q. Yang, K. N. Piyakis and E. Sacher, Surface diffusion and coalescence of mobile metal nanoparticles, J. Phys. Chem. B, 2005, 109, 9703–9711.

[6]. S. Laurent, et al., Magnetic iron oxide nanoparticles: Synthesis, stabilization, vectorization, physicochemical characterizations and biological applications, Chem. Rev., 2008, 108(6), 2064–2110, DOI: 10.1021/CR068445E

[7]. V. Consonni, J. Briscoe, E. K¨arber, X. Li and T. Cossuet, ZnO nanowires for solar cells: A comprehensive review, Nanotechnology, 2019, 30(36), 362001, DOI: 10.1088/1361- 6528/AB1F2E.

[8]. Y. Zhang, M. K. Ram, E. K. Stefanakos and D. Y. Goswami, Synthesis, characterization, and applications of ZnO nanowires, J. Nanomater., 2012, 2012, 1–22, DOI: 10.1155/ 2012/624520.

[9]. A. Kuoni, R. Holzherr, M. Boillat and N. F. de Rooij, J. Micromech. Microeng., 2003, 13, S103; F. R. Blom, D. J. Yntema, F. C. M. Van de Pol, M. Elwenspoek, J. H. J. Fluitman and T. J. A. Popma, Sens. Actuators, A, 1990, A21, 226.

[10]. W. J. Li, E. W. Shi, W. Z. Zhong and Z. W. Yin, J. Cryst. Growth, 1999, 203, 186; J. C. Phillips, Bonds and Bands in Semiconductors, Academic Press, New York, 1973.

[11]. I. Khan, S. Khan, R. Nongjai, H. Ahmed and W. Khan, Hydrothermal synthesis of zinc oxide powders with controllable morphology, Opt. Mater., 2013, 35, 1189–1193.

[12]. Y. Li, Y. Bando and D. Golberg, ZnO nanoneedles with tip surface perturbations: Excellent field emitters, Appl. Phys. Lett., 2004, 84, 3603.

[13]. A. Taube, M. Sochacki, N. Kwietniewski, A. Werbowy, S. Gierałtowska, L. Wachnicki, et al., Electrical properties of isotype and anisotype ZnO/4H-SiC heterojunction diodes, Appl. Phys. Lett., 2017, 110, 1120–1124.

[14]. F. Porter, Zinc Handbook: Properties, Processing, and Use in Design, CRC Press, 1991.

[15]. T. K. Subramanyam, B. Srinivasulu Naidu and S. Uthanna, Physical Properties of Zinc Oxide Films Prepared by DC Reactive Magnetron Sputtering at Different Sputtering Pressures, Cryst. Res. Technol., 2000, 35(10), 1194–1202.

*****

Studying Variable Stars using Small Optical Telescopes

Dr. A. N. Ardad

Department of Physics, Deogiri College, Chhatrapati Sambhajinagar - 431 004, India
Email: *anardadraje@gmail.com*

ABSTRACT

A study of variable stars plays a central role in understanding the process of evolution of the stars. Astronomers can determine the mass, radius, age, temperature, chemical composition and many other properties of a star by observing its spectrum, luminosity and motion through space. The rapidly increasing sophistication in the optics and electronics has made small optical telescope very efficient and intelligent. With the state of art back-end instruments like photoelectric photometers interfaced with computer and compact CCD camera, the conventional photometric monitoring has become a highly potential tool for the study of variable stars. The main objective of this chapter/paper to focus study of variable stars using small optical telescopes.

Keywords: *Mass Variable Stars, Small Optical Telescopes*

1. INTRODUCTION

Research on variable stars is important because it plays a crucial role in our understanding of the universe. In many cases the nature of the variability provides the clues to many astrophysical research problems enabling to understand the physics of the other stars. With the availability of small robotic optical telescopes and quality photometers and CCDs at a very reasonable price, the photometric study of variable stars is becoming very popular amongst the astronomers. Astronomers can determine the mass, radius, age, temperature, chemical composition and many other properties of a star by observing its spectrum, luminosity and motion through space. In this chapter/paper, we describe the research activities that we have been carrying out quite successfully using Small Optical Telescope.

Variable Stars

The stars varying in their brightness (magnitude) are called as 'Variable Stars'. These changes are of deeper nature and dependent on the structure of the stellar interior. They are directly related to the characteristics of these objects. The 'Period of Variation' is very important parameter; which varies from fraction of a second to several hundred days, even to the extent of several years, for different stars. Over 100,000 variable stars are known and catalogued, and many thousands more are suspected to be variable. There are a number of reasons why variable stars change their brightness. Variable stars need to be systematically observed over decades so that the changes in their variability can be studied as their long-time behavior. This data provides valuable information needed to analyze variable star behavior, which makes it possible to develop theoretical models of variable stars.

Small Optical Telescope

All the photometric data analysed for our research were obtained using small optical telescope; 12" Meade LX200 Schmidt- Cassegrain reflector telescope mounted at J.E.S. Observatory, Jalna (Latitude 190 51' 19" N; Longitude 750 54' 22" E), India as shown in Fig.1. This telescope includes 12" Schmidt-Cassegrain optical tube assembly with EMC Super Multi-Coatings (D = 305mm, F =

3048mm-f/10), heavy-duty fork mount with 4"-diameter sealed polar ball bearing, quartz-microprocessor-controlled 5.75" worm gears on both axes, and multi-function power panel display on the drive base. Manual and electric slow-motion controls are on both axes. Setting circles are in RA and Dec. Handheld keypad Electronic Command Center with digital readout display, PPEC Smart Drive, 7-speed drive control on both axes, GO TO controller, High-Precision Pointing, and 64,359-object onboard celestial software library. A 25 ft. power cord and adapter are for telescope operation. A 8 x 50mm viewfinder and 2" diagonal mirror with 1.25" adapter. Series 4000 SP26mm eyepiece is with the telescope. On the other hand, Meade LX200 telescope can be controlled either by keypad or through computer.

Fig.1: 12” Meade LX200 Schmidt-Cassegrain reflector telescope mounted at J.E.S. Observatory, Jalna

Photometry of Variable Stars using Small Optical Telescope

Small optical telescopes (aperture<1m) with adequate backend instrumentation (e.g. photometer, CCD camera and CCD spectrograph) can be used for observational astronomy among the researchers in colleges and universities. On the basis of our experience over a decade of observing with small optical telescope can be effectively used for research in astronomy. A computer controlled 12” Schmidt-Cassegrain Meade LX-200 optical telescope is installed at J.E.S. College, Jalna. It has a capacity to see the stars of 15th magnitude under extremely good sky conditions. A solid-state photometer of Optec, SSP- 3A Second Gen, with B, V, R, I filters is used as a back-end instrument of the telescope for measuring brightness of the stars. We are using this optical system to study the variability in brightness of variable stars in the sky.

We studied the short term as well as long term photometric light variation of few variable stars using small optical telescope. The optical photometric observations of these variable stars are taken by using observational facilities available; i) 12” Meade LX200 Schmidt-Cassegrain reflector small optical telescope ii) SSP-3A generation 2 solid state photometer, iii) Chris Marriott’s Sky Map Pro 7 at J.E.S. College, Jalna, India. We used differential photometry method for study of the variable stars.

Photometric Observations

The observational work at JESO using a small optical telescope, 12” Meade LX200, mainly involves photoelectric photometry of Chromospherically Active Stars in general and RS Canum Venaticorum (RS CVn) type stars, in particular. More than a dozen such stars are observed so far and the present paper presents brief observational findings of only one variable star for understanding. The photometric observations and their results of Sigma Gemini (HD 62044) variable star is discussed as follows.

Sigma Gemini (HD 62044) is a bright (Vmax= 4.15), non-eclipsing single-lined spectroscopic binary system long orbital period of 19d.605 (Bopp & Dempsey 1989) at a distance of 37.5 pc. The photometric light variation is due to spots on the K1 III primary star. σ Gem shows photometric variability of ≈ 0.17 mag. in V band. Using simple light curve modeling method (Strassmeier et al. 1988 and Henry et al. 1995a) suggested two cool spots on the K1 III primary star and found a 2.7 year

period of cyclic variation. Strong Ca II H & K and Hα emission, UV line emission and X-ray emission have also been observed revealing the unusual high level of chromospheric and coronal activity (Schrijver et al. 1995; Elgaray et al. 1997). Smith & Bopp (1982) noted that the Hα absorption line in σ Gem was partly filled in by chromospheric emission. A detailed study of Hα line profile by Eker (1986) showed the line core to vary with the orbital phase in agreement with location of the stellar active region. σ Gem was not regarded as a suitable candidate for Doppler imaging due to the fact that it has a small rotational velocity (vsini ~27 kms−1) and relatively moderate rotation period. However, Hatzes (1993) obtained surface maps of σ Gem showing the existence of five spots lying on band centered near latitude +55o without any evidence for polar spots. Kovari (2001) also obtained surface maps for σ Gem covering 3.6 consecutive rotation cycles. They found that all spots group either lie long a band at approximately +45o latitude or appear centered at the equator with no polar or high latitude spot detected.

Our BV differential photometry of σ Gem carried out during observing season 2008-09 giving data of 32 nights. The light curve for V band, differential V band reveal remarkable light variation as shown in Fig.2 to Fig.3. Sigma Gemini shows moderate photometric variability with V amplitude of less than 0.1 magnitude however, it is known to be a strong source of X ray emission (Dempsey et al 1993). In our photoelectric observations of Sigma Gemini, the amplitude of photometric wave is variable with a maximum value of 0.12 magnitude in V band. The differential magnitude is 0.05. Sigma Gemini and it's comparison star differ less than 0.1 magnitude in B-V which should be extremely small. There is too small variation in the color indices of this star to allow us to determine a reliable value of the spot temperature. The brightness at minimum and maximum is same as found earlier by Henry et al. (1995a).

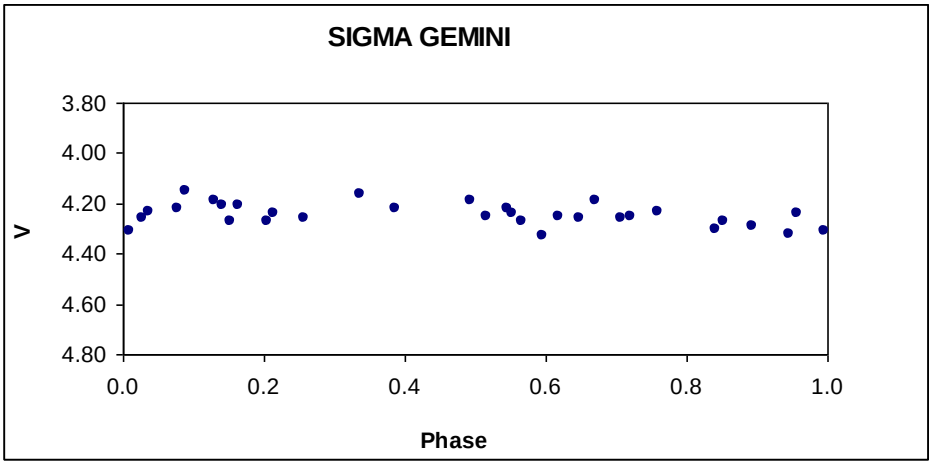

Fig.2: Differential V band light curve of σ Gem (HD 62044)

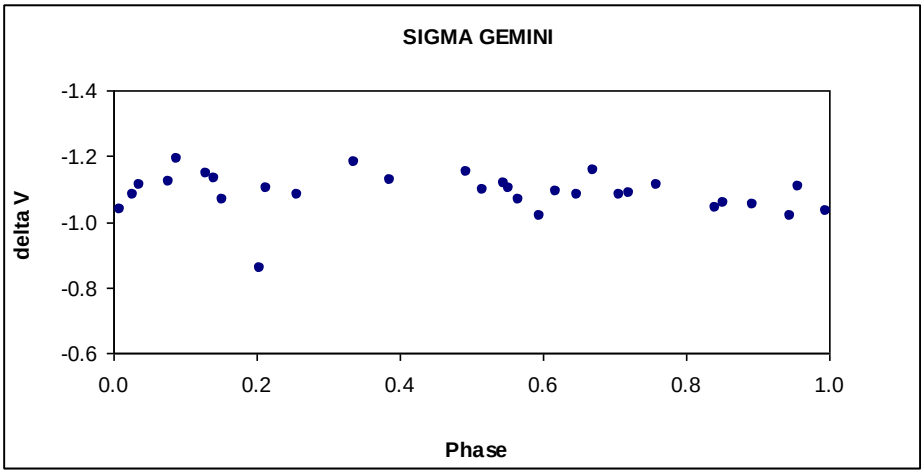

Fig. 3: Differential V band light curve of σ Gem (HD 62044)

CONCLUSIONS

The motivation behind the present work was to use the small optical telescope equipped with state of art backend instrument and to study the short term as well as long term photometric light variation of variable stars. In this chapter/paper we have presented the photoelectric photometry of Sigma Gemini (HD 62044) variable star by using 12" LX200 Meade Schmidt-Cassegrain reflector telescope. The Small Optical Telescopes are more useful for research in astronomy to collect data on a variety of objects in the Universe, and all have contributed to provide a better understanding of the Universe.

REFERENCES

[1]. A. A Henden, R. H. Kaitchuck, 'Astronomical Photometry', Van Nostrand Reinhold Company, New York, 1982.

[2]. J. R. Percy, 'The study of variable stars using small telescopes', Cambridge University Press, 1986.

[3]. S. Panday, 'Astronomy for developing world –IAU Special Session no.5' 2006, p245-251.

[4]. P.M. Kokne, A.N. Ardad and et. al, 'JESO- A Small Telescope Observatory', M.L. Kurtadikar (Eds), Lambard Academic Publishing, Germany, 2013.

*****